

# Azobenzene-Functionalized Materials for Holographic Applications and Nanoimprint Lithography

Dissertation

zur Erlangung des akademischen Grades  
Doktor der Naturwissenschaften (Dr. rer. nat.)  
im Promotionsprogramm „Polymer Science“  
der Bayreuther Graduiertenschule für Mathematik und Naturwissenschaften

vorgelegt von  
Christian Probst  
geboren in Ludwigsburg

Bayreuth, 2016

Die vorliegende Arbeit wurde in der Zeit von August 2011 bis Juni 2016 am Lehrstuhl für Makromolekulare Chemie I der Universität Bayreuth unter der Betreuung von Prof. Dr. Hans-Werner Schmidt angefertigt.

Vollständiger Abdruck der von der Bayreuther Graduiertenschule für Mathematik und Naturwissenschaften (BayNAT) der Universität Bayreuth genehmigten Dissertation zur Erlangung des akademischen Grades eines Doktors der Naturwissenschaften (Dr. rer. nat.).

Datum der Einreichung:	24. Juni 2016
Zulassung durch das Leitungsgremium:	26. Juli 2016
Datum des wissenschaftlichen Kolloquiums:	18. November 2016

Amtierender Direktor: Prof. Dr. Stephan Kümmel

Prüfungsausschuss:

Prof. Dr. Hans-Werner Schmidt (Erstgutachter)

Prof. Dr. Stephan Förster (Zweitgutachter)

Prof. Dr. Matthias Breuning (Vorsitz)

Prof. Dr. Seema Agarwal

*Gewidmet meiner Familie,  
im Gedenken an meinen Vater,  
Albrecht Probst.*

**Table of contents**

1	Introduction.....	1
1.1	The azobenzene chromophore .....	1
1.2	Azobenzene-functionalized polymers.....	4
1.3	Azobenzene-functionalized molecular glasses .....	5
2	Motivation .....	8
3	Synthesis and properties of azobenzene-functionalized molecular glasses .....	10
3.1	Design of azobenzene-functionalized molecular glasses.....	10
3.2	Synthesis of azobenzene-functionalized molecular glasses.....	13
3.2.1	Synthesis of the azobenzene side-groups .....	13
3.2.2	Synthesis of the molecule cores.....	14
3.2.3	Synthesis of the molecular glasses.....	15
3.3	Thermal properties.....	16
3.4	Optical characterization .....	29
3.5	Summary of the chapter .....	33
4	Azobenzene-based nanoimprint lithography.....	34
4.1	Introduction to nanoimprint lithography.....	34
4.2	Azobenzene-based surface patterning .....	37
4.3	Pattern transfer techniques .....	38
4.4	The cavity-filling process .....	40
4.5	Azobenzene-based nanoimprint lithography.....	43
4.5.1	Azobenzene-based nanoimprint lithography - setup.....	44
4.5.2	Azobenzene-based nanoimprint lithography - materials.....	46
4.5.3	Azobenzene-based nanoimprint lithography – experimental parameters.....	48
4.5.4	Micrometer-scale imprinting .....	50
4.6	Influence of the resist material on the imprinting performance .....	60
4.6.1	Azobenzene-functionalized homopolymer .....	60
4.6.2	Azobenzene-functionalized triphenylamine-based derivatives.....	62
4.6.3	Azobenzene-functionalized 1,3,5-benzenetrisamide-based derivatives .....	63
4.6.4	Azobenzene-functionalized spirobichromane-based derivatives .....	66
4.6.5	Imprinting of nanopatterns using azobenzene-functionalized spirobichromane-based derivatives.....	70
4.7	Summary of the chapter .....	84

---

5	Improving Holographic Writing Performance of Photo-Orientable Azobenzene Polymers by Molecular Glasses.....	85
5.1	Introduction .....	85
5.2	Materials .....	88
5.3	Influence of the molecular glass on the writing time .....	92
5.4	Influence of the molecular glass on the refractive-index modulation.....	96
5.5	Influence of annealing on writing time and refractive-index modulation.....	99
5.6	Influence of the molecular glass on the long-term stability of inscribed gratings.....	100
5.7	Summary of the chapter .....	102
6	Photoactive azobenzene-containing polymer nanoparticles.....	103
6.1	Introduction to core/shell block copolymer nanoparticles.....	103
6.1.1	Azobenzene-functionalized nanoobjects .....	108
6.2	Azobenzene-functionalized core/shell polymer nanoparticles .....	110
6.2.1	Materials .....	114
6.2.2	Synthesis of core/shell polymer nanoparticles .....	118
6.3	Synthesis and characterization of non-photoactive poly(4-hydroxystyrene)-b-polystyrene core/shell nanoparticles.....	119
6.3.1	Photoacid generator system .....	120
6.3.2	Thermal acid generator system.....	121
6.3.3	Hydrochloric acid treatment .....	122
6.4	Synthesis and characterization of photoaddressable core/polystyrene shell polymer nanoparticles with polystyrene shell .....	123
6.4.1	Photoacid generator system .....	123
6.4.2	Hydrochloric acid treatment .....	125
6.4.3	Holographic performance of azobenzene-functionalized poly-(4-hydroxystyrene)-b-polystyrene nanoparticles.....	132
6.5	Synthesis and characterization of photoactive polymer nanoparticles with poly-(methyl methacrylate) shell.....	135
6.5.1	Holographic performance of cyano-substituted azobenzene-functionalized poly-(4-hydroxystyrene)-b-poly(methyl methacrylate) nanoparticles.....	139
6.6	Summary of the chapter .....	140
7	Summary.....	141
8	Zusammenfassung.....	145
9	Experimental part.....	149
9.1	Characterization methods (basics).....	149
9.1.1	Dynamic light scattering.....	149

---

9.1.2	Holography .....	151
9.2	Characterization methods .....	152
9.3	Materials .....	156
9.4	Synthesis of azobenzene-functionalized molecular glasses.....	156
9.4.1	General reaction procedures .....	156
9.4.2	Synthesis of molecule cores .....	158
9.4.3	Synthesis of azobenzene moieties .....	158
9.4.4	Synthesis of azobenzene functionalized molecular glasses.....	162
9.5	Block copolymer synthesis .....	166
9.5.1	Purification of solvents and monomers .....	166
9.5.2	Synthesis of poly(4-tert-butoxystyrene)-block-polystyrene .....	166
9.5.3	Polymer analogous reaction.....	167
10	References .....	170

## 1 Introduction

### 1.1 The azobenzene chromophore

Azobenzenes (or diazenes) are molecules, which feature two phenyl rings linked via an N=N “azo”-moiety. The conjugated  $\pi$ -system of the chromophores leads to a strong absorption usually in wavelengths ranging from UV to the (blue/green) visible section of the light spectrum. Most azobenzene molecules exhibit an intense  $\pi$ - $\pi^*$  in the UV and, since the transition is symmetry forbidden, a less intense  $n$ - $\pi^*$  band in the visible region.<sup>[1]</sup> However, their  $n$ - $\pi^*$  and  $\pi$ - $\pi^*$  absorption bands can be tailored by substitution at the phenyl rings, either by an electron-donating or electron-accepting group. This leads to three spectroscopically different classes of azobenzenes: azobenzene-type chromophores, amino-azobenzene-type molecules, and pseudo-stilbenes.<sup>[2]</sup> A schematic depiction of the absorbance spectra of the three different azobenzene classes is shown in Figure 1.

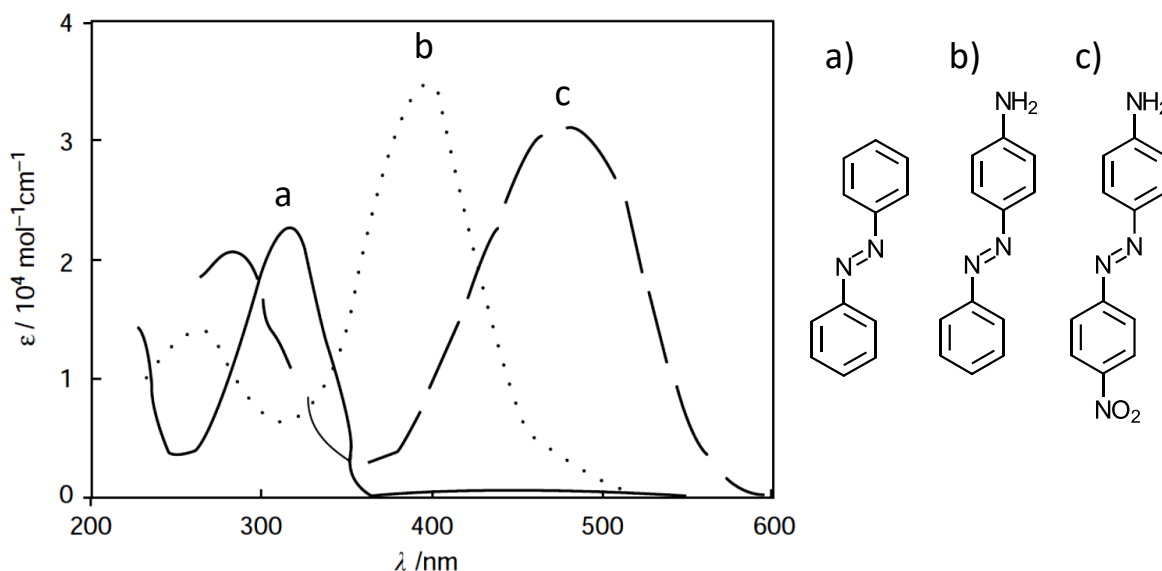


Figure 1: Schematic depiction of absorbance spectra of three different *trans*-azobenzenes. Solid line (a): azobenzene-type molecules with a strong absorption band ( $\pi$ - $\pi^*$ ) in the UV region and a low intensity  $n$ - $\pi^*$  absorption band in the visible region of the light spectrum. Dotted line (b): amino-azobenzene-type molecules have overlapping  $\pi$ - $\pi^*$  and  $n$ - $\pi^*$  absorption bands in the visible region; The same applies for pseudo-stilbenes (dashed line, c).<sup>[3]</sup>

Substituting one of the two phenyl rings with an electron donor, e.g. an amino or a methoxy group, in ortho- or para position leads to a bathochromic, i.e., red shift of the  $\pi$ - $\pi^*$  absorption band. Here, both bands are located close to each other or even superimposed. This type of azobenzene molecules are called amino-azobenzenes. If the azobenzene is substituted at the 4 and 4' positions with both, an electron-donor and an electron-acceptor group, e.g. a nitro group, the  $\pi$ - $\pi^*$  absorption band is also red-shifted, sometimes even beyond the absorption maxima of the  $n$ - $\pi^*$  band. The asymmetric electron distribution causing this shift is referred to as “push-pull” substitution pattern.<sup>[3]</sup> The kind of azobenzene-chromophores featuring such kind of characteristics are called pseudo-stilbenes. The absorption spectrum is also altered when the chromophores are aggregating or packing. One can distinguish two modes of  $\pi$ - $\pi$ -stacking. Parallel packing of the molecules' dipoles yields so-called J-aggregates, and antiparallel stacking so-called H-aggregates.<sup>[3]</sup> The first give rise to a bathochromic shift, whereas the latter (H-aggregates) lead to a hypsochromic

shift (blue shift), of the absorption maxima in comparison to the non-aggregated molecules spectrum. Owing to the anisotropic shape and the rigid structure, azobenzenes are predestinated molecules to exhibit liquid crystalline properties. Hence, many polymers with azobenzene side groups feature LC characteristics.

Azobenzenes have raised a lot of attention in academia for their ability to reversibly isomerize between the two isomeric states, the thermodynamically stable *trans* and the metastable *cis* form. As the *trans* isomer is the stable one, the most prevalent state of azobenzenes in the dark is the *trans*-isomer state. Upon exposure to light of a wavelength located in the absorption band of the chromophore, the *trans*-form will isomerize to the *cis*-form.<sup>[3]</sup> Eventually, the molecule will thermally relax back to the *trans*-form again. The timescale, on which the thermal back-relaxation occurs (from milliseconds to hours, days) is dictated by the substituents on the phenyl rings of the azobenzene molecule and by the environment of the chromophore.<sup>[4–6]</sup> Also, a second photon of an energy corresponding to the wavelength of the *cis*-absorption band can lead to a back-relaxation to the *trans* form. The photo-isomerization usually occurs within femtoseconds and therefore is much quicker than the thermal back-relaxation.<sup>[7]</sup> However, the mechanism underlying the *trans*-to-*cis* isomerization is not yet understood in full detail. The azobenzene molecule either undergoes a rotation (with rupture of the  $\pi$  bond) or an inversion from the *trans*-form to the *cis*-form (see Figure 2).<sup>[8–11]</sup>

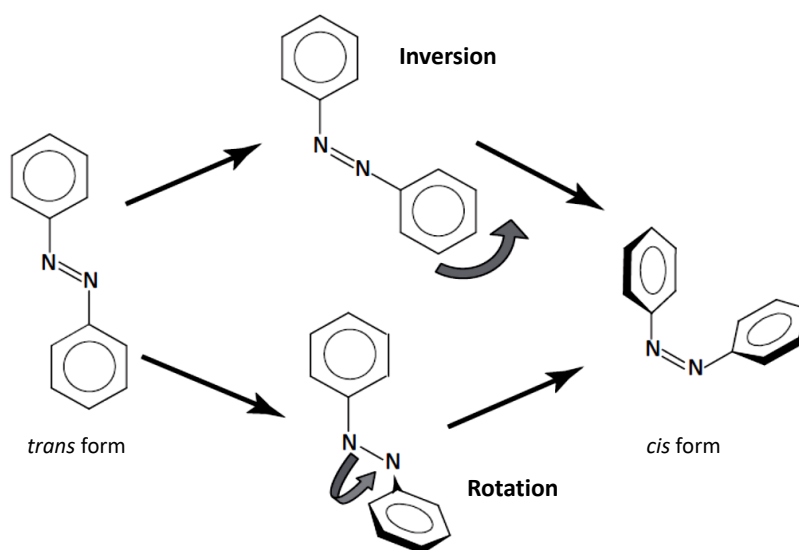


Figure 2: Schematic depiction of the azobenzene isomerization from the *trans* to the *cis*-form. The azobenzene molecule either undergoes a rotation or an inversion.<sup>[3]</sup>

While the thermal back relaxation of the molecule is assumed to be a rotational movement, the photo-induced conversion could either be performed via rotation or inversion of the molecule.<sup>[12]</sup> The absorption spectra of *trans*-rich and *cis*-rich azobenzene samples differ significantly; hence, azobenzene molecules change their color upon irradiation, thus are so-called photochromic molecules. As a consequence, the fraction of *cis* and *trans*-isomers and the thermal back-relaxation in the dark can easily be observed using UV/Vis spectroscopy. Upon irradiation of an azobenzene solution or bulk sample, a photo-stationary state will be reached, in which a steady *cis*-to-*trans* and *trans*-to-*cis* isomerization occurs based on the competing photo-isomerization and thermal back relaxation rates, leading to a certain composition of *cis* to *trans*-state molecules, which depends on the respective azobenzene system.<sup>[3]</sup> In most cases, the predominant form in the photo-stationary state in azobenzene samples is the *cis*-form. However, the composition of this photo-stationary

state can be altered by changing, e.g. the temperature of the system or the intensity and wavelength of the incident light. If the azobenzene molecule is substituted in a way that the two absorption bands ( $n\text{-}\pi^*$  and  $\pi\text{-}\pi^*$ ) overlap, exposure of the chromophore to a single wavelength is enough to spur on both, the forward and the backward reaction between the two isomers, leading to a continuous photo-isomerization of the molecule. This phenomenon is advantageous for photo-induced motion in an azobenzene sample.<sup>[3]</sup>

Owing to their unique photophysical properties, azobenzene-functionalized materials can be used in a variety of applications compiled in the book of “Smart light responsive materials” by Zhao and Ikeda.<sup>[3]</sup> Most of these potential applications make use of the photo-orientation effect, i.e. a re-orientation of azobenzene moieties in the solid state, occurring in films of azobenzene-functionalized materials. As discussed above, exposure of an azobenzene film to light of an appropriate wavelength leads to a photo-stationary state, in which the *cis*-form of the molecule is the prevalent one. Upon irradiation with linearly polarized light of a suitable wavelength, however, multiple *trans-cis-trans* photo-isomerization cycles occur, leading to a so-called trembling motion of the molecules until the transition dipole of the azobenzene is orientated perpendicular to the polarization of the incident light and no further excitation of the chromophore is possible.<sup>[13]</sup> As a consequence of the re-orientation and the shape-anisotropy of the azobenzene moieties, the illuminated area becomes macroscopically birefringent. The exposed area has a different refractive-index modulation compared to the unexposed ones (see Figure 3).

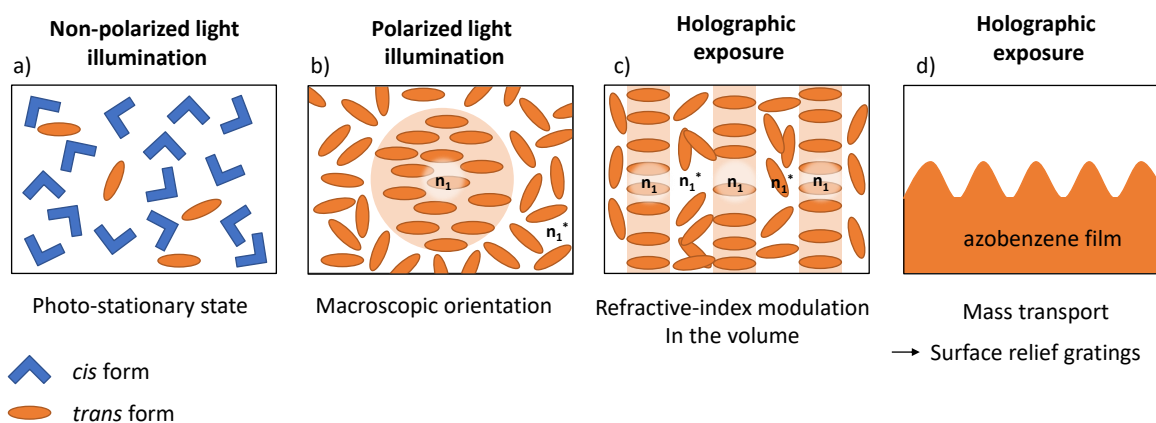


Figure 3: Photo-physics of azobenzenes. a) Exposure to non-polarized visible light leads to a photo-stationary state, in which the *cis*-form of the azobenzene moiety is prevalent. b) Exposure to polarized light leads to a macroscopic orientation with a refractive-index  $n_1$  different to the unexposed areas ( $n_1^*$ ). c) Holographic exposure causes a refractive-index modulation and can eventually cause d) a mass transport leading to surface relief gratings.

In case of a holographic exposure, i.e. exposure of the azobenzene-functionalized material to interfering polarized laser beams, a refractive-index modulation can be obtained, in which the chromophores are oriented perpendicular to the polarization of the incident light in the areas of high light intensities. Hereby, a holographic grating in the volume of the film is formed. If one of the two laser beams used carries information, this effect can be used to store information in the photoactive film. The reversible nature of the photo-isomerization even allows for reversible high-density data storage. Continuing holographic exposure of a suitable azobenzene material with an appropriate polarization can cause a mass transport, which eventually lead to the formation of so-called surface relief gratings (SRGs).<sup>[13]</sup> The different potential applications require tailoring of the azobenzene material.

## 1.2 Azobenzene-functionalized polymers

Side-chain polymers bearing azobenzene moieties linked to the backbone of the polymer via a flexible spacer have been intensively studied since the first synthesis of those by Ringsdorf and Schmidt<sup>[14]</sup> in 1984. Alternatively to this design, guest-host systems, in which azobenzene units are dispersed in a polymeric matrix, or azobenzene main chain polymers bearing the chromophore in the polymer backbone are known. However, for most studies on photoactive polymers, side-chain polymer are used.<sup>[15]</sup> The variety of azobenzene side-chain polymers is large, including, e.g., amorphous, crystalline or liquid crystalline homopolymers, statistical copolymers and block copolymers. The great variety of different photoactive polymeric systems have led to numerous potential applications. For example, they have been investigated or applied as photo-alignment layers, actuators, surface patterning material, photo-switches, photonic crystals or optical data storage material.<sup>[15–20]</sup>

With regard to the use of azobenzene-functionalized polymers as data storage materials, a range of different polymer architectures with varying behavior in holographic experiments (for detailed information about holography see chapter 9.1.2) were examined. In solid films of homopolymers, the azobenzene moieties are in spatial proximity so that the *trans-cis-trans* isomerization can take place in a cooperative manner, resulting in increased writing speeds and enhanced stability of the inscribed volume gratings.<sup>[21,22]</sup> One of the first to study the suitability of homopolymers as data storage material was Ringsdorf et al.<sup>[23]</sup>. In this case, however, the inscribed gratings in films of the liquid crystalline polyester could not be deleted through thermal *trans-cis-trans* isomerization. Further pioneering studies on azobenzene-functionalized homopolymers were performed by Rochon et al.<sup>[24]</sup> and Bieringer et al.<sup>[25]</sup>. Yet, the high optical density of functionalized homopolymers usually prevents them from being used for the inscription of thick volume holograms, since the penetration depth of the light is smaller than the grating period. Only thick recording materials allow for the inscription of multiple holograms in the same volume element owing to their high angular selectivity.<sup>[26]</sup> Alcalá et al. have overcome this issue by blending an azobenzene-functionalized polyester and non-photoactive PMMA.<sup>[27–29]</sup> Up to 20 stable and rewritable gratings in the same volume element have been inscribed in approx. 500  $\mu\text{m}$  thick films using blue and red light irradiation to control the content of hologram-stabilizing *cis* isomers.

Another way to overcome the problem of high optical density in thick films is the use of statistical copolymers instead of homopolymers. Among the first azobenzene-functionalized statistical copolymers liquid crystalline systems were investigated by Schmidt et al.<sup>[14,30]</sup>. Photoactive statistical copolymers were also studied several other groups including for instance Ikeda<sup>[31]</sup>, Stumpe<sup>[32]</sup>, Bieringer<sup>[33]</sup>, Haarer<sup>[34]</sup> and Hvilsted et al.<sup>[35]</sup>. Natansohn et al. were pioneering the examination of applicability of azobenzene-containing statistical copolymers as material for holographic data storage.<sup>[36]</sup> However, using azobenzene-functionalized statistical copolymers in holography experiments, mass transport can occur resulting in surface relief gratings.<sup>[37]</sup> This represents a major drawback of both kind of polymers, homopolymers and statistical copolymers. Besides the inscription of volume gratings, both polymers tend to form SRGs gratings during holographic experiments.<sup>[38]</sup> SRGs are thin gratings and, thus, provide no angular selectivity, so they are detrimental to high-density data storage. Moreover, statistical copolymerization leads to the loss of the beneficial cooperative effect; hence, inscribed gratings are lacking long-term stability.<sup>[22]</sup> Both properties render statistical copolymers to an inadequate material for volume holography

data storage. Since almost all blends of polymers show macro-phase separation resulting in light scattering, they are not suitable for holographic experiments either.

A solution to most of these problems is the use of block copolymers which are composed of an amorphous majority block and an azobenzene-containing minority block and which form uniform micro-phase-separated morphologies with domain sizes well below 100 nm, preventing light scattering. In addition, the confined geometries maintain the spatial proximity of the chromophores and the important cooperative effect which enables the inscription of long-term stable volume gratings in thick samples. Consequently, several research groups have investigated azobenzene-containing block copolymers.<sup>[39–44]</sup> The block copolymers, were either synthesized via anionic polymerization and subsequent polymeranalogous reaction<sup>[45,46]</sup>, or by controlled radical polymerization techniques as for example nitroxide mediated polymerization (NMP)<sup>[47]</sup> or atom transfer radical polymerization (ATRP)<sup>[48–51]</sup>. When it comes to multiplexing holography experiments, the azobenzene-containing block copolymers have to be diluted in a non-photoactive matrix. Schmidt et al.<sup>[52]</sup> have demonstrated multiplexing of 20 volume holograms on millimeter thick samples made from blends of azobenzene-containing block copolymers with polystyrene majority block in non-absorbing polystyrene.<sup>[53]</sup> Diblock copolymers with additional non-photoactive optical density decreasing mesogenic side groups, such as benzoylbiphenyl moieties in the azobenzene-minority block have shown to be suitable for holographic data storage with improved stability of inscribed gratings.<sup>[54]</sup> A general issue of such kind of copolymers, however, is that the improved stability of inscribed gratings usually comes at the cost of decreased writing speed.

### 1.3 Azobenzene-functionalized molecular glasses

Molecular glasses are an emerging materials class and an alternative to polymers. This material class of low-molecular-weight compounds is able to form a stable amorphous phase above room temperature. The first to describe the glassy state of low-molecular-weight compounds was Tammann<sup>[55]</sup> in 1898. Owing to entanglements of polymer chains and as a consequence of numerous possible conformations, polymers can reach a stable glassy state. Instead, molecular glasses can be transferred into a glassy state by non-equilibrium processes such as quick cooling of the melt (quenching), vapor deposition or spin-coating from solution.<sup>[56]</sup> In the following years, only few publications on molecular glasses were published<sup>[57–60]</sup> until research intensified in the late 1980s.<sup>[56]</sup> Unlike most polymers, which exhibit undefined end groups and non-uniform molecular weight, molecular glasses feature a defect-free and well-defined molecular structure and can easily be highly purified using standard methods of organic chemistry, i.e. adsorption chromatography, sublimation or recrystallization.<sup>[61]</sup> Just as amorphous polymers, molecular glasses are able to form smooth, homogeneous and transparent thin films.

Numerous rules of design of molecular glasses have been established by Shirota et al.<sup>[56,62–64]</sup>, Wirth<sup>[65]</sup> and Naito<sup>[66]</sup>. Two vital factors are a non-planar structure and a large number of conformers to prevent packing and hence crystallization of the molecules. As a consequence of steric hindrance, bulky substituents can foster the formation of an amorphous phase. They also reduce rotational and translational motions of the molecule, thus increase the glass transition temperature of the molecular glass. An increase of the  $T_g$  can also be achieved by the introduction of rigid substituents such as biphenyl- or naphthyl moieties. Besides, an introduction of substituents increases the molecular weight, which increases the  $T_g$  of the compound. Lastly, an increased glass

transition temperature can also be achieved by strong intermolecular interactions, i.e. hydrogen bonds or dipolar interactions. However, strong interactions can spur crystallization, especially in rigid molecules. Some of the typical morphologies of molecular glasses are depicted in Figure 4. Most molecular glasses are spiro-linked molecules or compounds based on either star-shaped or a branched topology.<sup>[56,61]</sup> Additionally to these symmetric structures, asymmetric low-molecular-weight molecule structures are known to form amorphous phases owing to the high number of conformers reducing the tendency to crystallize.<sup>[61,67]</sup> Molecular glasses are a material class of increasing research interest can be employed in optical and optoelectronic devices, and photolithographic and nanoimprint processes.<sup>[68–72]</sup> Besides, they find use in photoconductor drums.<sup>[73]</sup>

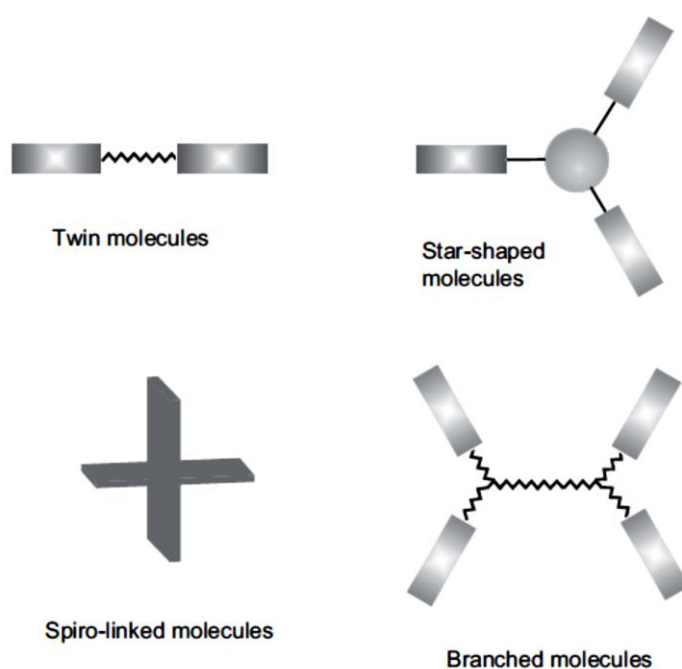


Figure 4: Topologies of molecular glasses.<sup>[61]</sup>

Azobenzene-functionalized, e.g. photochromic molecular glasses, were first investigated by Shirota et al.<sup>[5]</sup> They can potentially be applied in the same way as the photoactive polymer equivalents, but were mainly investigated in the field of SRG formation.<sup>[74,75]</sup> Shirota et al. have investigated the influence of substituents on the photochromic response of several photochromic molecular glasses.<sup>[76,77]</sup> Substituents also influence the SRG formation.<sup>[78–80]</sup> However, owing to the absence of entanglements which hamper the mass transport, the SRG formation is mostly much faster than in polymeric materials. It was also demonstrated that bulk birefringence, i.e. an optically induced reorientation of the azobenzene chromophores, takes place in thin films of photo-responsive molecular glasses, the formation rate being faster than in polymers.<sup>[81–85]</sup> As in the case of polymers, stable volume gratings were only obtained if the azobenzene moieties are decoupled from the rigid molecular core.<sup>[86]</sup> Some examples of structures of azobenzene-functionalized molecular glasses based on different design approaches are shown in Figure 5.

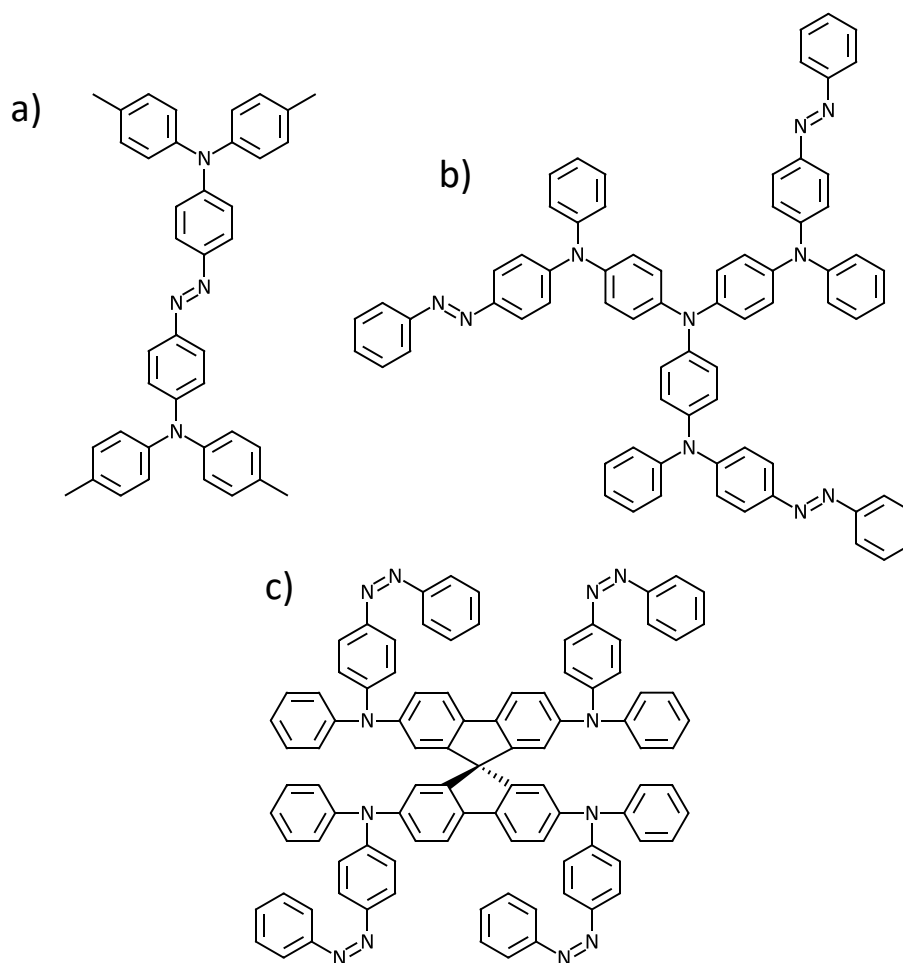


Figure 5: Chemical structures of molecular glasses based on different design strategies. a) twin molecule 4,4'-bis[bis(4-methylphenyl)amino]azobenzene (BBMAB)<sup>[56]</sup>; b) star-shaped tris[(4-(phenylazo)-diphenylamine)-phenylamine] (TPPA)<sup>[87]</sup>; c) spiro-linked 2,2',7,7'-tetrakis(4-phenylazodiphenylamino)-9,9'-spirobifluorene (Spiro-ADA)<sup>[88]</sup>.

In the 1990's, Shirota et al. have published a series of novel photochromic molecular glasses including the linear shaped BBMAB.<sup>[56,76,89]</sup> The azobenzene-functionalized low-molecular weight compound features a stable amorphous phase with a glass transition temperature of 79 °C. The bulky substitution led to a low fraction of *cis* isomers after irradiation with 450 nm and 550 nm light for 1 minute. The thermal back-relaxation on the other hand is also hindered.<sup>[76]</sup> Star-shaped tris[(4-(phenylazo)-diphenylamine)-phenylamine] (TPPA)<sup>[87]</sup> shows good film-forming properties when processed either by vacuum evaporation methods or spin coating technique. Its glass transition temperature is 80 °C. TPPA has been used to generate SRGs using an interfering Ar<sup>+</sup>-laser with an intensity of 50 mW/cm<sup>2</sup>. After 25 min a diffraction efficiency of 23 % and a surface modulation depth of 250 nm was reached.<sup>[87]</sup> The diffraction efficiency reported for spiro-linked Spiro-ADA is even higher (38 %).<sup>[88]</sup> Owing to the non-planarity of the triphenylamines and the spiro-linkage the tendency to form a stable amorphous phase and the glass transition temperature (147 °C) are greatly increased. The bulky and rod-like azobenzene moieties additionally increase the amorphous character of the compound.

## 2 Motivation

The aims of this thesis are to design, synthesize, identify and apply azobenzene-functionalized molecular glasses and polymeric compounds. These compounds are then to be employed in holography and its applications as well to improve the recording performance of established polymers for holographic volume gratings. Furthermore, it is targeted to make use of the athermal photofluidization effect to develop novel approaches in nanoimprint lithography.

Four different, yet intertwined subjects are discussed within four chapters of this thesis. It covers the synthesis and investigation of azobenzene-functionalized molecular glasses, to their application in newly developed azobenzene-based nanoimprint lithography, and blends of such low-molecular-weight compounds with photo-orientable polymers to improve their holographic writing performance. Finally, the synthesis of novel azobenzene-functionalized polymer nanoparticles and their investigation in holographic experiments is demonstrated.

### *Synthesis and properties of azobenzene-functionalized molecular glasses*

Molecular glasses are an emerging material class of low-molecular-weight compounds, which are able to form a stable amorphous phase at and above room temperature. Azobenzene-functionalized molecular glasses have proven to be an alternative to comparable polymeric systems, to be suitable to be employed in holographic applications and to be able to form stable volume or surface gratings. An appropriate choice of the molecule core should allow for the synthesis of high- $T_g$  molecular glasses featuring a stable amorphous phase. Since these compounds feature no entanglements, the mobility of these systems is higher than in polymers. Substitution at the para-position of the azobenzene-moieties should enable tailoring their photophysical and wettability behavior.

The main objectives of this chapter are:

- I. Synthesis of high- $T_g$  azobenzene-functionalized molecular glasses on the basis of spirobichromane and 1,3,5-benzenetrisamide molecule cores with perfluoroalkyl- and methoxy-substituted azobenzene moieties.
- II. Thermal characterization of azobenzene-functionalized molecular glasses via DSC and POM and TGA.
- III. Optical characterization of the molecular glasses via UV/Vis spectroscopy.

### *Azobenzene-based nanoimprint lithography (azo-NIL)*

Nanoimprint lithography techniques allow for high-throughput surface patterning and are a low-cost alternative to photolithographic structuring techniques. Conventional imprint techniques, e.g. UV-NIL or thermal NIL, are based on either crosslinking reactions or heating/cooling cycles making shrinkage almost inevitable. In this chapter, a novel nanoimprint approach based on the athermal photofluidization effect of azobenzene-functionalized materials, which should avoid shrinkage is planned, investigated and optimized.

The main objectives of this chapter are:

- I. Revealing the optimal process conditions for azo-NIL regarding, e.g., light source, fluence, film thickness, stamp and pattern size.

- II. Imprinting of structures ranging from the micrometer-scale down to 100 nm under optimized conditions.
- III. Variation of the resist and evaluation of the influence of the molecule core or substituents on the imprinting process.

*Improving the holographic recording performance of photo-orientable polymers with an azobenzene-containing molecular glass*

Azobenzene-functionalized polymers are an appealing material class for the application in holographic data storage or as security feature. A general problem of azobenzene-containing polymers, however, is that the stability of inscribed gratings usually comes at the cost of a decreased writing speed. Here, a promising approach to improve the holographic recording speed of photo-orientable polymers is presented by blending them with an azobenzene-containing molecular glass acting as photo-orientable plasticizer. In contrast to conventional plasticizers, the photochromic molecular glass is plasticized upon exposure solely; this should enable the azobenzene moieties of the polymers to orient more quickly and to maintain the long-term stability of inscribed gratings.

The main objectives of this chapter are:

- I. Identification of suitable photo-orientable polymers to be blended with an appropriate azobenzene-functionalized molecular glass.
- II. Determination of the influence of blending the investigated polymers with the molecular glass regarding the writing speed, the refractive index-modulation and the long-term stability of inscribed gratings.

*Photoactive azobenzene-containing polymer nanoparticles*

For volume holography with high angular selectivity, thick samples in the range of millimeters are required. Up to now, only block copolymers show satisfyingly good properties to fulfill this requirement of being processed to samples of such a thickness with a suitable optical density between 0.3 – 0.7 by blending them with a non-photoactive polymer. In this chapter, a synthetic strategy for novel photoactive azobenzene-containing core/shell polymer nanoparticles, featuring the same ability to be processed to thick samples while retaining their initial morphology determined by the block ratio of the non-photoactive block and the azobenzene-functionalized block, will be discussed. The crosslinking of the block copolymers used to generate the nanoparticles is performed in micro-phase separated films of the polymers, to which a commercially available acid-labile crosslinking agent is added.

The main objectives of this chapter are:

- I. Identification of a suitable proton source for the activation of the crosslinker in a non-photoactive and photoactive partially azobenzene-functionalized poly(4-hydroxystyrene)-block-polystyrene block copolymer.
- II. Synthesis of non-photoactive and photoactive nanoparticles with PMMA shell.
- III. Processing of nanoparticles to thick samples via blending them with either PS or PMMA depending on their shell using injection-molding technique and investigation of the samples in holographic experiments.

### 3 Synthesis and properties of azobenzene-functionalized molecular glasses

In this thesis, a series of azobenzene-functionalized molecular glasses are designed, synthesized and investigated with the aim to apply them in azobenzene-based nanoimprint lithography (azo-NIL). As this method requires thin films of a photoactive material with a stable amorphous phase, good film forming properties and a high mobility of the material, molecular glasses have been chosen.

#### 3.1 Design of azobenzene-functionalized molecular glasses

The design of the azobenzene-functionalized molecular glasses is chosen to be star-shaped featuring a sterically demanding core, to which 3 to 4 azobenzene units can be linked to. The azobenzene moieties can be substituted to alter the photophysical properties. In general, 11 different molecular glasses with three varying molecular cores will be investigated. The three different central cores of the molecular glasses have substantially different properties and therefore a significant impact on the properties of the resulting molecular glass. On the one hand, the rigidity of the core is increasing from the triphenylamine- to the spirobichromane-based core. The 1,3,5-benzenetrisamide core on the other hand features H-bonds, which introduce secondary intermolecular interactions. These should have a significant impact on the mobility of the molecules. Additionally, the cores are either twisted, as it is the case of the spirobichromane or triphenylamine core, or, in case of the 1,3,5-benzenetrisamide core, planar. The twisted molecule cores should promote a readily transfer of the molecules to an amorphous phase. The molecules are tri- and tetra-functional, i.e. three or four azobenzene moieties are attached to the molecule core via an amide or an ester group. The high molecular weight of the tetra-functionalized molecules as well as the intermolecular H-bonds in derivatives based on 1,3,5-benzenetrisamide are expected to promote a relatively high glass transition temperature. This is another important factor for the molecular glasses in their usage as material for azo-NIL, since the temperature in potential etching steps can be as high as 70 °C or 80 °C. Thus, a suitable material has to feature a  $T_g$  as high as 80 °C or above to assure the stability of the amorphous phase.

The azobenzene moieties provide photo-addressability, which here refers to the ability to show mobility and to be photo-orientable upon exposure to an appropriate wavelength and light polarization. The design of the molecular glasses is chosen to feature the azobenzene units on the periphery of the molecular glass to assure the mobility of the low-molecular weight compounds as azobenzene moieties in the center of the structure would most probably have a low *trans*- to *cis* isomerization rate due to the confinement caused by heavy substituents.

The substituents on the para-position of the azobenzene chromophores alter the photophysical properties of the molecular glasses and influence their level of hydrophobicity. As substituents a hydrogen atom, a methoxy-group or perfluoroalkyl chains of different lengths have been chosen. As described in chapter 1.1, the electron donating methoxy substituent is expected to shift the  $n-\pi^*$  and  $\pi-\pi^*$  absorption bands, so that both bands are located close to each other or even superimpose. This would be advantageous for the azobenzene-based nanoimprint lithography (azo-NIL) discussed in chapter 4, as overlapping absorption bands would allow for a continuous conversion of the azobenzene molecule upon exposure to a single wavelength being beneficial for

photo-induced motion in an azobenzene film.<sup>[3]</sup> Figure 6 depicts a schematic representation of the molecule design.

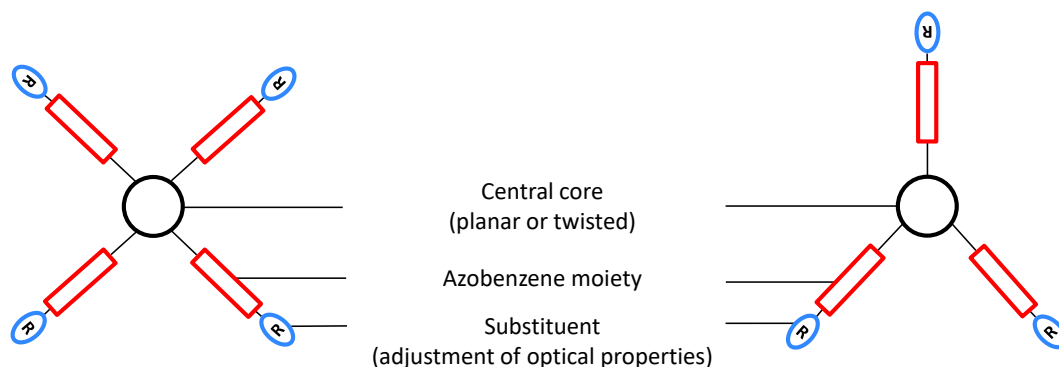
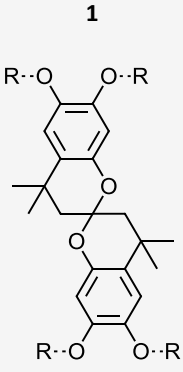
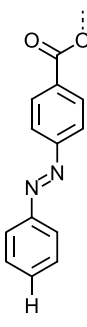
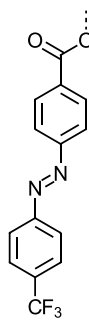
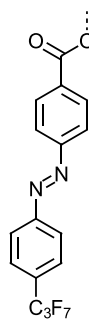
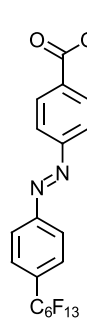
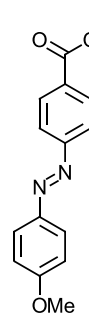
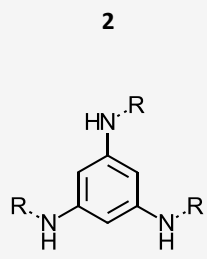
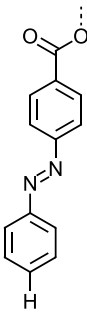
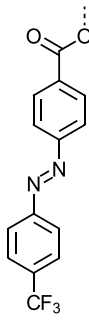
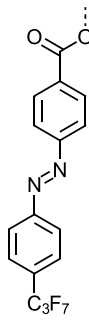
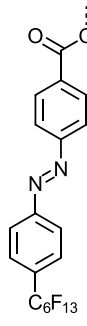
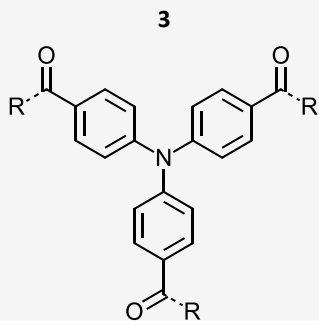
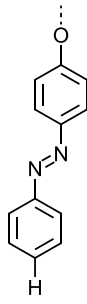
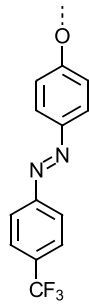


Figure 6: Schematic representation of the molecule design of azobenzene-functionalized molecular glasses.

The perfluoroalkyl substituents are not expected to influence the absorption spectrum of the chromophore significantly. However, they change the hydrophobicity of the molecule; the influence increasing with ascending chain length. The change in hydrophobicity of the molecules is anticipated to have an impact on the film forming properties and more interestingly on the wetting behavior of the stamps used in azo-NIL. Table 1 is an overview of the, in the course of this thesis investigated azobenzene-functionalized molecular glasses.

Table 1: Synthesized and investigated azobenzene-functionalized molecular glasses.

Core / Core#	Compound name	1a	1b	1c	1d	1e
<p style="text-align: center;"><b>1</b></p> 	Substituent R					
	Compound Name	<b>2a</b>	<b>2b</b>	<b>2c</b>	<b>2d</b>	
<p style="text-align: center;"><b>2</b></p> 	Substituent R					
	Compound Name	<b>3f</b>	<b>3g</b>			
<p style="text-align: center;"><b>3</b></p> 	Substituent R					

## 3.2 Synthesis of azobenzene-functionalized molecular glasses

### 3.2.1 Synthesis of the azobenzene side-groups

In this work, the azobenzene chromophores are synthesized via a synthesis route known as the “Mills reaction”: A condensation reaction of a para-nitrosobenzoic acid and an aniline derivative. Unlike in the common synthesis route towards azobenzenes, which involves the diazotization of an aniline derivative requiring strict temperature control, the educts in the Mills reaction are stable at room temperature and the reaction can be performed as a one-pot synthesis. Two different approaches were used to synthesize the azobenzene moieties depending on the availability of the aniline derivatives with different substituents. The reaction with the individual steps of the synthesis route towards the azobenzene chromophores is depicted in Figure 7.

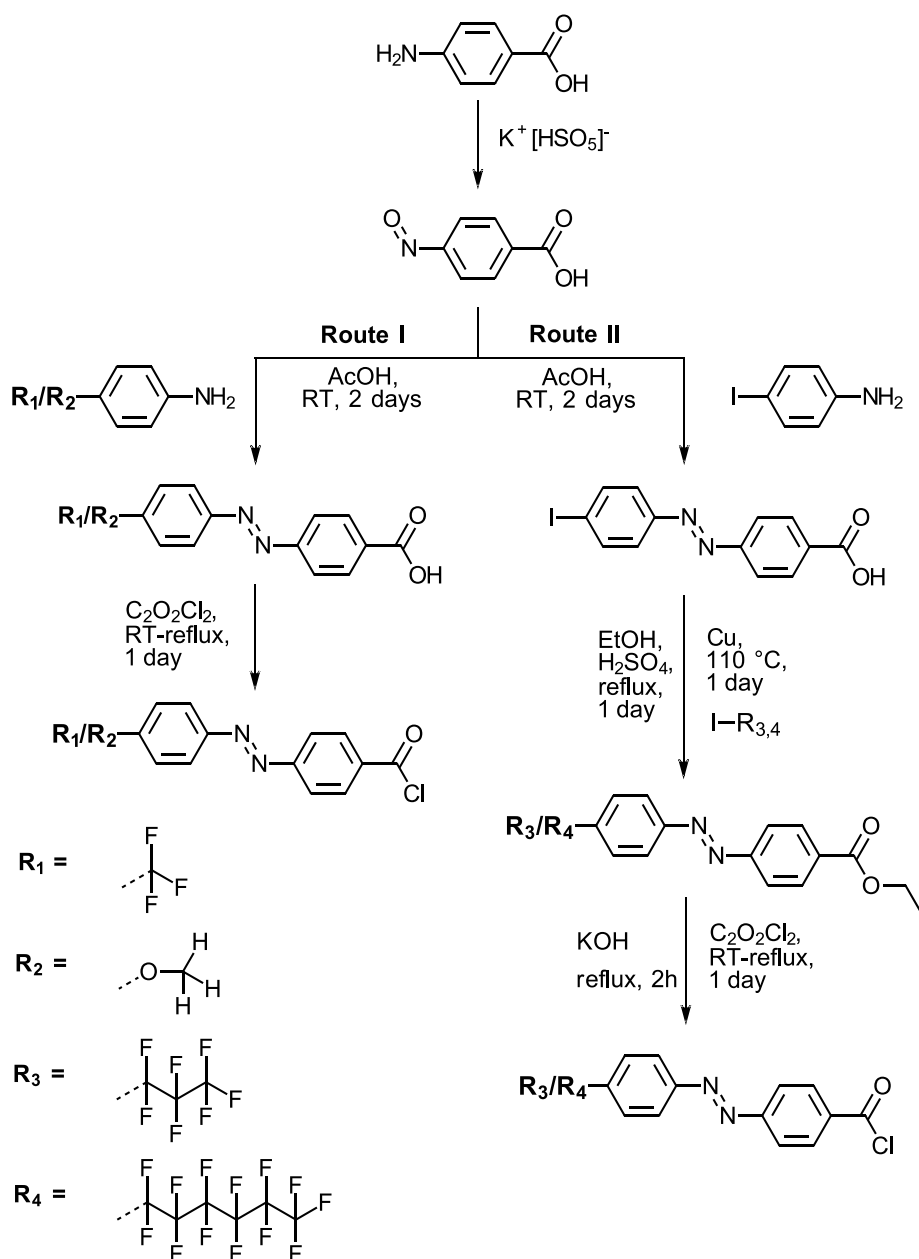


Figure 7: Reaction scheme of the synthesis of azobenzene moieties used to synthesize the targeted azobenzene-functionalized molecular glasses.

In both cases, 4-aminobenzoic acid is dissolved in dichloromethane (DCM). To this solution, an aqueous solution of  $K^+[HSO_5]^-$ , and oxidative persulfate, is added at room temperature under vigorous stirring. The reaction progress is monitored via thin-layer chromatography. When the reaction is finished, the oxidized product, a nitroso derivative, is filtered off and dried under vacuum. As small impurities of the nitro compounds formed by the oxidation of the amines do not interfere the Mills reaction to azobenzene, no purification step is necessary at this stage of the synthesis.<sup>[90]</sup>

The first route includes a Mills-reaction with a commercially available aniline derivative bearing methoxy- or  $CF_3$  substituents, and the chlorination step to the corresponding acid chloride, which is used for the synthesis of the molecular glasses. In detail, in a first step, the Mills reaction is carried out at room temperature, in which the nitrosobenzoic acid condensates with the amine derivative in presence of an acid (AcOH) for about 48 h to yield the azobenzene derivative. The methoxy-azobenzene product could directly be subjected to the chlorination step after a purification step via recrystallization in EtOH.

The second route includes a Mills-reaction with an iodine-substituted aniline derivative, an esterification step, an "Ullmann reaction", a deprotection step and a final chlorination step. In detail, in a first step, an azobenzene derivative with an iodine at the para-position is generated via Mills reaction of 4-iodoaniline with the para-nitrosobenzoic acid under the same conditions as in case of the methoxy- and trifluoromethyl substituted derivatives. Before the conversion of the synthesized para-iodine-substituted 4-(phenylazo)benzoic acids, the acid has to be converted to the corresponding ethyl ester. After the esterification reaction, the formed iodine-substituted 4-(phenylazo)benzoic acid ethyl ester is subjected to a copper-catalyzed Ullmann coupling reaction with a perfluoroalkyl iodide derivative featuring the iodine at the end of the perfluoroalkyl chain. The nucleophilic aromatic substitution reaction is performed at 100 °C and is nearly quantitative. After a purification step, the azobenzoic acid ester can be converted to an acid again and then be subjected to the chlorination step. Chlorination of the acids is performed with oxalyl chloride, since the excess of the chlorination compound can readily be removed under high vacuum.

### 3.2.2 Synthesis of the molecule cores

In this chapter, eleven different molecular glasses based on three different molecule cores are investigated. As the two triphenylamine-based molecular glasses have been synthesized by R. Walker and as the 6,6',7,7'-tetrahydroxy-4,4,4',4'-tetramethylbis-2,2'-spirobichroman molecule core is commercially available, only the synthesis of the molecule core of the 1,3,5-benzenetrisamide-based is discussed in detail.

For the synthesis of the 1,3,5-benzenetrisamine, 3,5-dinitroaniline is reduced with palladium on activated charcoal (Pd/C; 10% Pd) in a solvent mixture of THF/MeOH. The reaction is stirred at 35°C in an autoclave with a  $H_2$  pressure of 3.5 bar for 24 h. Afterwards, the catalyst is filtered off and the solvent is evaporated under reduced pressure. The dried product needs no further purification. Since the product is sensitive to oxidation, it has to be stored under inert gas.

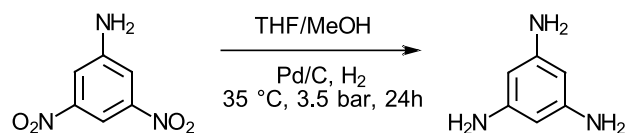


Figure 8: Reduction of 3,5-dinitroaniline to 1,3,5-benzenetrisamine.

### 3.2.3 Synthesis of the molecular glasses

In a final step, the activated, i.e. chlorinated azobenzoic acid derivatives were attached to the 1,3,5-triamino benzene or the tetra-functional spirobichromane core in an amidation or an esterification reaction, respectively. Prior to the amidation reactions of the azobenzene derivatives with the triamino benzene core, a 3,5-Dinitroaniline was reduced to the tri-functional amino derivative using palladium on active carbon in a high-pressure reactor at a pressure of 3 bar overnight. After thorough drying of the educt under high vacuum the core is ready for the amidation reaction. The spirobichromane core was used as received, but also was dried under high vacuum at 60 °C overnight prior to the esterification. Figure 9 depicts the reaction scheme of the conversion of the azobenzene derivatives with the respective molecule cores to yield the azobenzene-functionalized molecular glasses.

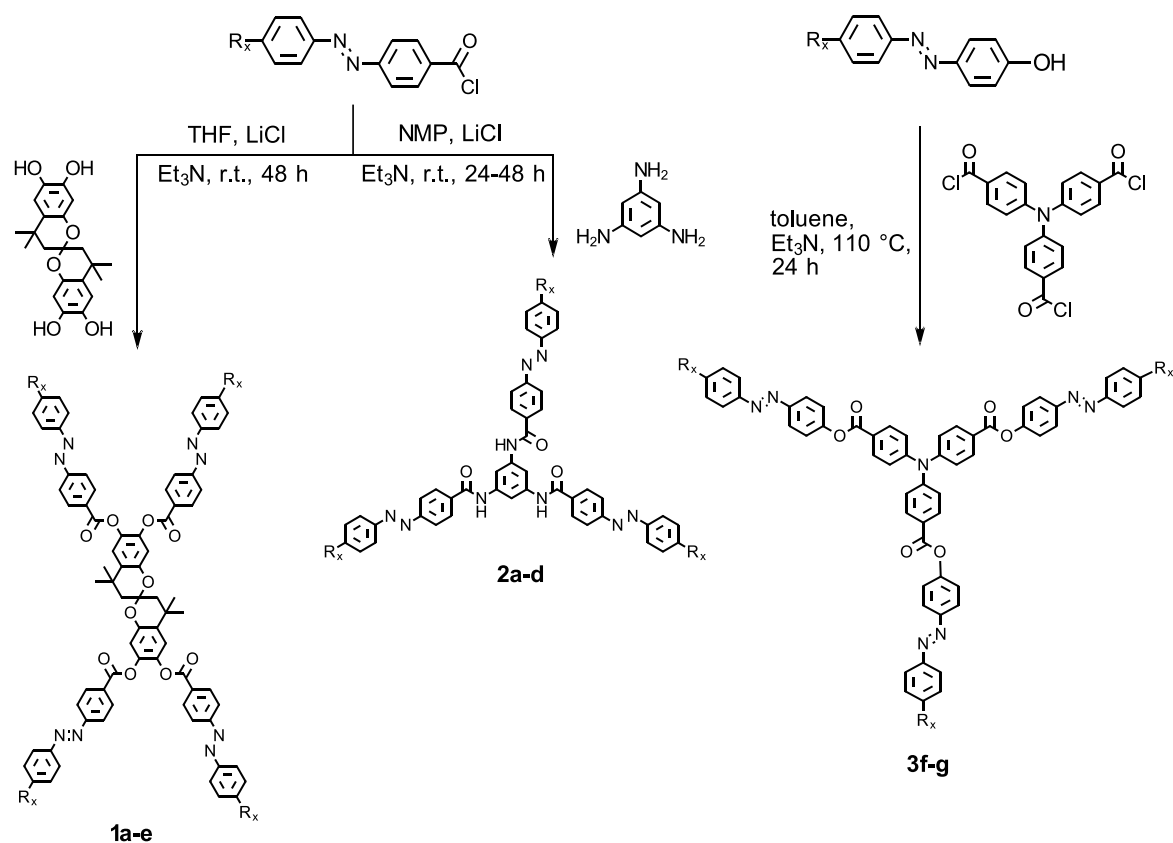


Figure 9: Reaction scheme of the conversion of azobenzene derivatives with the respective molecule cores to yield the azobenzene-functionalized molecular glasses.

To avoid oxidation of the azobenzene acid chloride derivative, the amidation reaction of the 1,3,5-benzenetrisamine with the respective azobenzene acid chloride derivative to yield the azobenzene-functionalized 1,3,5-benzenetrisamide-based molecular glass is carried out under inert atmosphere in dry solvents and flame-dried Schlenk flasks. In a first step, the azobenzene acid chloride derivative is dissolved in dry NMP, to which dried LiCl is added to increase the solubility of the resulting molecular glass. As base, an excess of triethylamine is used. To reduce the reaction speed

the solution is cooled down to 0°C prior to adding 1,3,5-triaminobenzene to the reaction mixture. The reaction mixture is then carried out at room temperature for 24 h. The reaction can be monitored by TLC. The crude reaction products could be purified using one or more of the typical purification methods of organic chemistry, e.g. column chromatography or re-crystallization.

As in case of the amidation reaction, the esterification reaction of the 6,6',7,7'-tetrahydroxy-4,4',4'-tetramethylbis-2,2'-spirobichroman with the respective azobenzene acid chloride derivative is carried out under inert atmosphere in dry solvents. In a first step, the azobenzene acid chloride derivative is dissolved in dry THF, to which dried LiCl is added and an excess of triethylamine is added. To reduce the reaction speed the solution is cooled down to 0°C prior to adding the spirobichromane core to the reaction mixture. The reaction mixture is then carried out at room temperature for 24 h-48 h. Also here, the crude reaction products could be purified using one or more of the typical purification methods of organic chemistry, e.g. column chromatography or re-crystallization.

The esterification of the triphenylamine to yield the azobenzene-functionalized triphenylamine-based molecular glasses was carried out by R. Walker (University of Bayreuth) according to Y. Shirota et al..<sup>[91]</sup>

### 3.3 Thermal properties

The thermal properties of the molecular glasses investigated in this thesis are determined using dynamic scanning calorimetry (DSC), thermogravimetric analysis (TGA) and polarization microscopy (POM). Hereto, the compounds were firstly examined in the DSC at a scan rate of 10 K/min under inert gas. In a second step, the compound were investigated with a polarization microscope at the same scan rate and pictures were taken at key temperatures. To this end, the powdery compounds were used as received from synthesis, put between two glass slides and were heated on an air-cooled hot-stage. In addition, to assess the glass-forming ability of all compounds, thin films were prepared by spin-coating and were optically evaluated with regard to their homogeneity and transparency. The results will be discussed along with the DSC and POM results, which also provide information about the phase behavior of the respective compound.

The results of the thermogravimetric analysis is summarized in Table 2 at the end of the thermal characterization chapter. In the DSC and POM experiments, the maximum temperature is kept at least 20 K below  $T_{-5wt.-%}$ , i.e. the temperature, at which 5 % of the weight of the compound is gone upon heating in the TGA experiment.

#### Azobenzene-functionalized spirobichromane derivatives

The first compounds to be investigated were the spirobichromane-based azobenzene-functionalized molecular glasses, which will be discussed in the following. Figure 10 depicts the DSC traces and POM images of unsubstituted azobenzene-functionalized compound **1a** during three heating and cooling cycles at a scan rate of 10 K/min.

Upon first heating, the freshly re-crystallized compound features a polymorphic melting behavior in a temperature range between 235 and 250 °C. Upon first cooling, **1a** shows a glass transition temperature of 108 °C. In the second heating scan, the  $T_g$  is located between 108 and 110 °C. Between 200 and 230 °C the compound recrystallizes before it melts at a temperature of 249 °C.

This behavior is reproducible, although the heat of fusion is steadily decreasing. Since the melting point does not decrease during the thermal steps, no decomposition of **1a** occurs. This finding is confirmed by TLC.

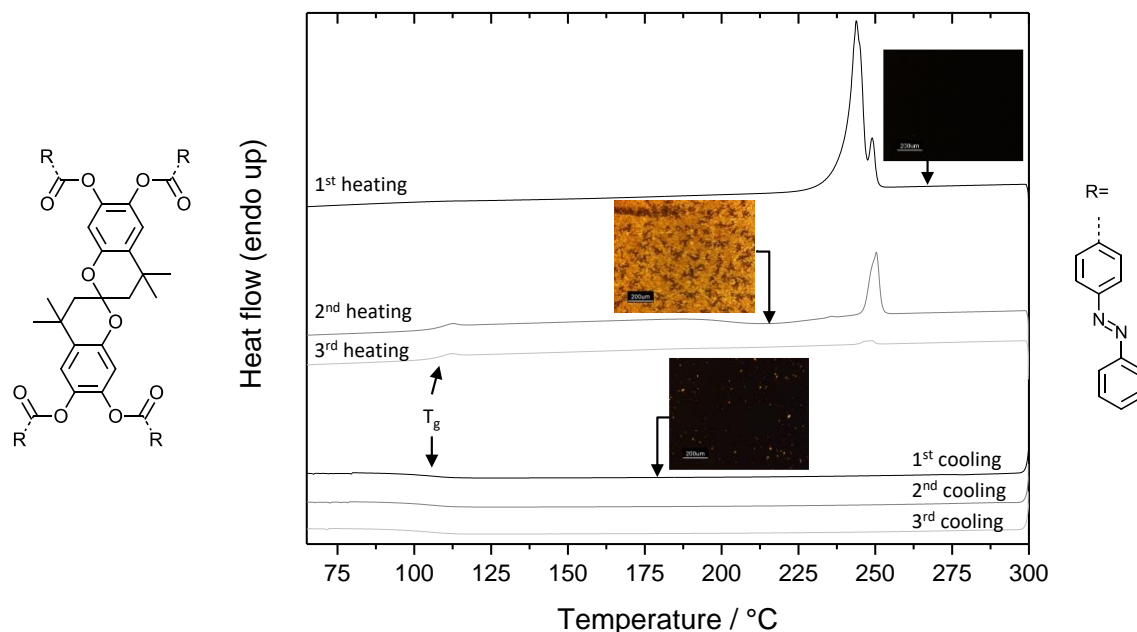


Figure 10: DSC traces of compound **1a** during three heating and cooling cycles at a scan rate of 10 K/min under a  $N_2$ -flow of 50 mL/min. Insets: Polarizing microscopy images between crossed polarizers. The scan rate in POM experiment is 10 K/min. Arrows mark the temperature at which the image was taken.

The POM experiments confirm the DSC scans. Quenching from melt on a or spin-coating from solution readily transfers the compound **1a** into a stable amorphous phase at room temperature and surprisingly above the  $T_g$  of the compound.

Figure 11 shows the DSC traces and POM images of trifluoromethyl-substituted azobenzene-functionalized compound **1b** during three heating and cooling cycles at a scan rate of 10 K/min. Upon first heating, the glass transition temperature at 126 °C is observable. Further heating reveals a polymorphic melting behavior in a temperature range between 290 °C and 330 °C. Upon first cooling, the compound crystallizes at 329 °C. The reason for this behavior is most probably an incomplete melting of the compound during the first heating step, so that remaining crystalline structures could serve as nucleus for the molecules in the melt. However, further heating to avoid this phenomenon would not be reasonable since the compound begins to decompose at a temperature of 330 °C. After the crystallization, a weak but still observable glass transition at 120 °C is visible in the DSC trace of the first cooling step. During second heating, the compound seems to recrystallize in a temperature range between 275 °C and 330 °C. This phenomenon most probably appears for the same reason as described in the first cooling step. The following cooling and heating steps show no phase transitions anymore.

The polarization optical microscopy investigation confirms the DSC experiment in the first heating step.

As in case of compound **1a**, quenching the compound by spin-coating from solution transfers **1b** into a stable amorphous phase. Even though changes to **1a** are small, the influence of the  $CF_3$  group

is significant. Compared to the unsubstituted **1a**, the glass transition temperature as well as the melting temperature are increased. The ability to form a stable amorphous phase, however, is not influenced.

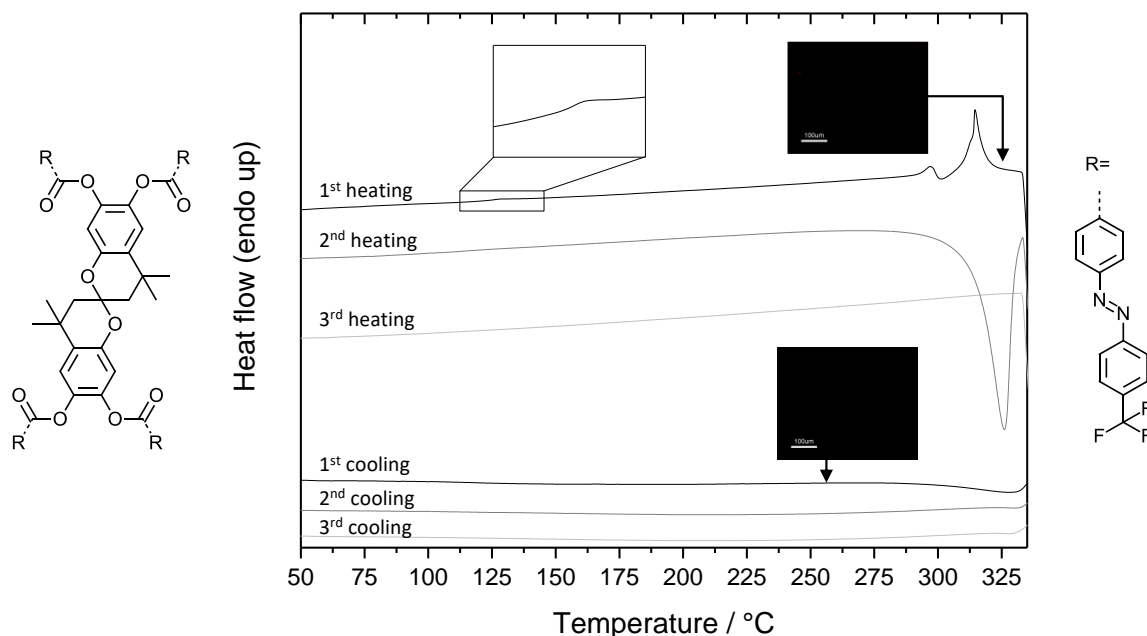


Figure 11: DSC traces of compound **1b** during three heating and cooling cycles at a scan rate of 10 K/min under a  $N_2$ -flow of 50 mL/min measured in a high pressure pan. Insets: Magnification of the first heating curve in a temperature range between 110 °C and 140 °C; Polarizing microscopy images between crossed polarizers. The scan rate in POM experiment is 10 K/min. Arrows mark the temperature at which the image was taken.

Figure 12 depicts the DSC traces and POM images of perfluoropropyl-substituted azobenzene-functionalized spirobichromane-based compound **1c** during the three heating and cooling cycles. In the first heating scan of the DSC experiment, a melting point featuring a small shoulder is observable at a temperature of approx. 322 °C. Upon first cooling, crystallization is observable in the DSC experiment between a temperature of 250 and 230 °C. Second heating reveals a broader melting peak in a temperature range between 230 °C and 330 °C. Since the melting is incomplete during the heating step, crystallization in the second cooling step occurs earlier than in the first cooling step at a temperature of approx. 325 °C. This crystallization, however, seems to be incomplete as in the third heating step re-crystallization is observable, which is setting in at a temperature of approx. 250 °C. A glass transition temperature is neither visible upon heating nor upon cooling of the compound. Also, DSC experiments at higher scan rates could not reveal the  $T_g$  of the compound.

The POM experiment performed at first heating of the compound confirms the isotropic melt of **1c** upon heating. During first cooling, they reveal an crystallization at about 250 °C. Further cooling the compound reveals cracks in the crystallized film at a temperature of ca. 105 °C, which could indicate a glass transition temperature. At a cooling rate as low as 10 K/min the compound tends to crystallize. However, spin-coating from solution yields transparent films with a stable amorphous phase at room temperature.

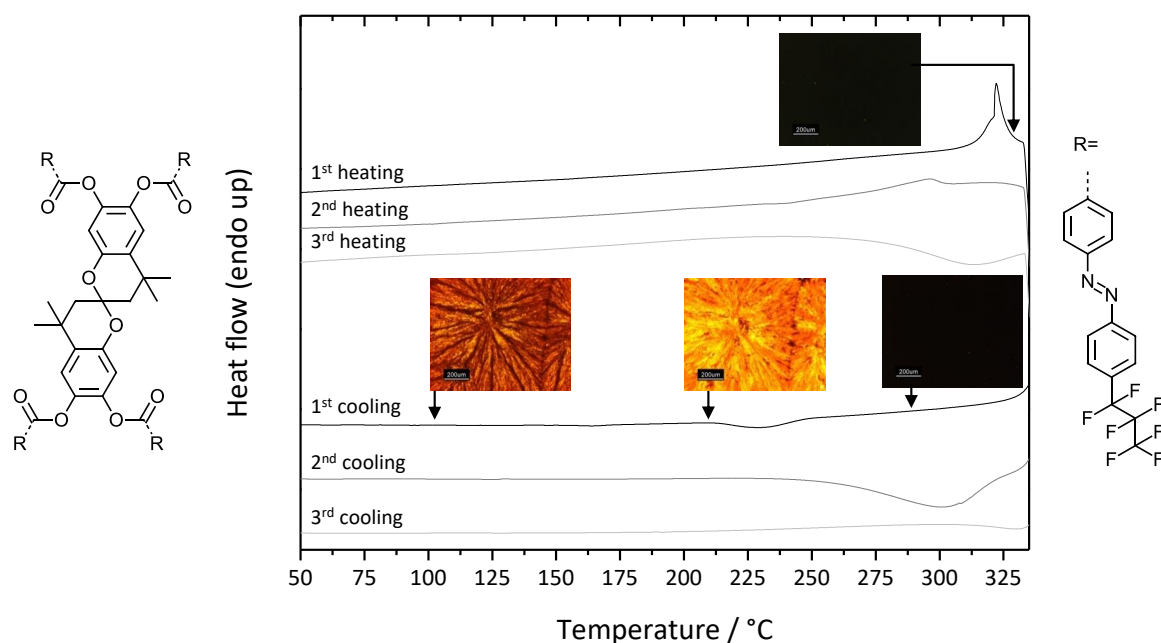


Figure 12: DSC traces of compound **1c** during three heating and cooling cycles at a scan rate of 10 K/min under a  $N_2$ -flow of 50 mL/min measured in a high pressure pan. Insets: Polarizing microscopy images between crossed polarizers. The scan rate in POM experiment is 10 K/min. Arrows mark the temperature at which the image was taken.

The DSC traces and POM images of perfluorohexyl-substituted azobenzene-functionalized spirobichromane-based compound **1d** during the three heating and cooling cycles is shown in Figure 13.

During first heating, a complex polymorphic behavior with several melting peaks at 233 °C, 240 °C and 273 °C can be observed. This implies a polycrystalline crystallization. Hence, upon cooling, several crystallization peaks show up at 269 °C, 222 °C and 210 °C. The following heating/cooling steps confirm the first two DSC scans. The isotropic phase above 280 °C is confirmed by POM. Even though the crystallization peaks are very sharp and reproducible, a liquid crystalline phase cannot clearly be assigned, since POM experiments did not show typical textures of a liquid crystal and no mobility of the phase. No transparent amorphous film could be generated using **1d** in quenching experiments or by spin-coating.

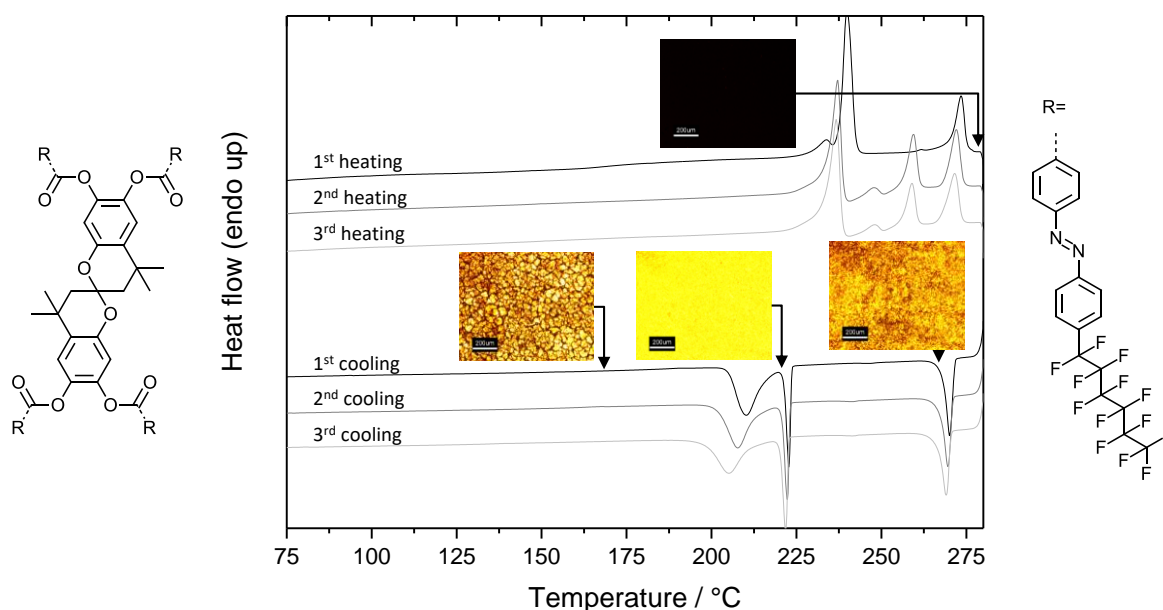


Figure 13: DSC traces of compound **1d** during three heating and cooling cycles at a scan rate of 10 K/min under a N<sub>2</sub>-flow of 50 mL/min. Insets: Polarizing microscopy images between crossed polarizers. The scan rate in POM experiment is 10 K/min. Arrows mark the temperature at which the image was taken.

Figure 14 depicts the DSC traces and POM image of methoxy-substituted azobenzene-functionalized spirobichromane-based compound **1e** during the three heating and cooling cycles.

**1e** features a melting point at 239 °C upon first heating. **1e** vitrifies upon cooling without crystallization and can be considered a molecular glass. The glass transition temperature is reached at approx. 105 °C. Upon second heating, **1e** shows the glass transition at 107 °C. This is just 1 °C above the  $T_g$  of unsubstituted **1a**. This result is expected, as studies in our workgroup have already shown that a methoxy-substitution at the para-position of the azobenzene moiety has no significant influence on the glass transition temperature of the compound.<sup>[92]</sup> Further heating reveals two re-crystallization peaks at 170 °C and 190 °C before the compound melts at a temperature of approx. 136 °C. The following DSC scans confirm this behavior. POM investigations confirm the DSC experiments. **1e** is readily transferred to a stable amorphous phase in quenching or spin-coating experiments.

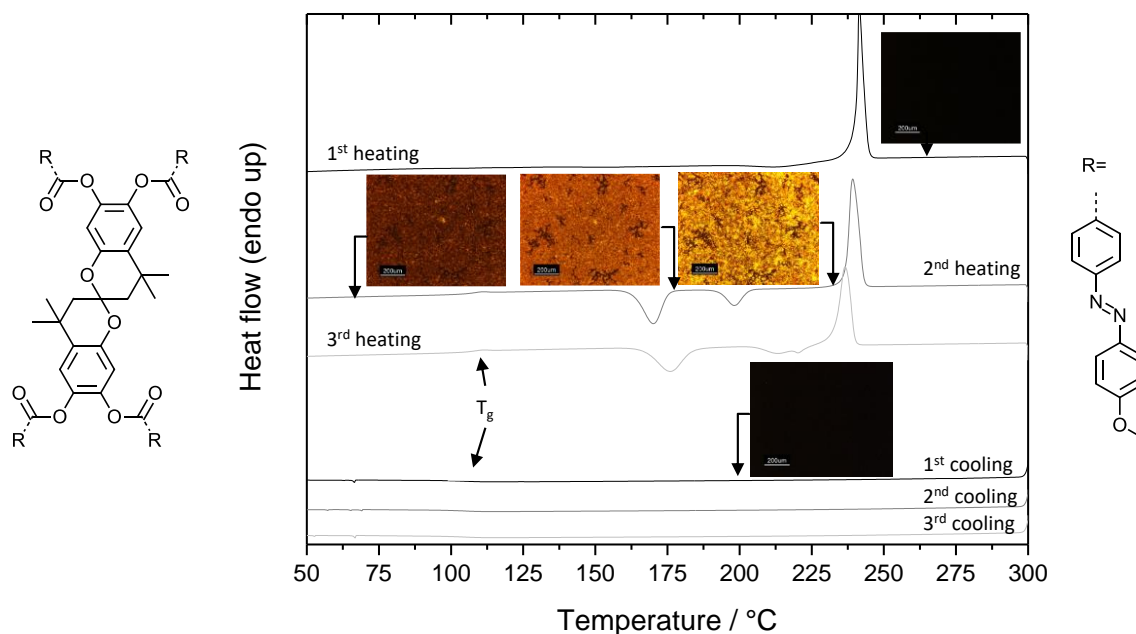


Figure 14: DSC traces of compound **1e** during three heating and cooling cycles at a scan rate of 10 K/min under a N<sub>2</sub>-flow of 50 mL/min measured in a high pressure pan. Insets: Polarizing microscopy images between crossed polarizers. The scan rate in POM experiment is 10 K/min. Arrows mark the temperature at which the image was taken.

#### Azobenzene-functionalized 1,3,5-benzenetrisamide derivatives

Owing to the ability to form hydrogen bridge bonds, trisamide derivative are expected to feature higher glass transition temperatures compared to spirobichromane-based equivalents. Besides, intermolecular hydrogen bonding was demonstrated to potentially enhance the stability of the amorphous phase.<sup>[93]</sup>

Figure 15 depicts the DSC traces and POM images of azobenzene-functionalized 1,3,5-benzenetrisamide-based compound **2a** during the heating and cooling cycles in the DSC experiment.

Prior to the first heating, the compound was molten and quenched inside the aluminum pan in order to observe the glass transition of the compound. Upon heating at a rate of 10 K/min, the glass transition is visible at a temperature of 136 °C. Further heating leads to a re-crystallization of the compound at 173 °C and 225 °C, before the compound melts at 252 °C. During cooling, the isotropic melt crystallizes at a temperature of 214 °C. Upon second heating, no glass transition or re-crystallization is observable. The melting point as well as the crystallization temperatures are confirmed in the following DSC scans. The POM experiments confirm the DSC measurements. When the glass transition temperature is reached, POM images show that the birefringent film forms cracks, which suggests that the film becomes more brittle. It was found, that **2a** is a highly crystalline substance. Despite the tendency to crystallize, **2a** can readily form a transparent amorphous film by spin-coating from solution or by quenching of the melt.

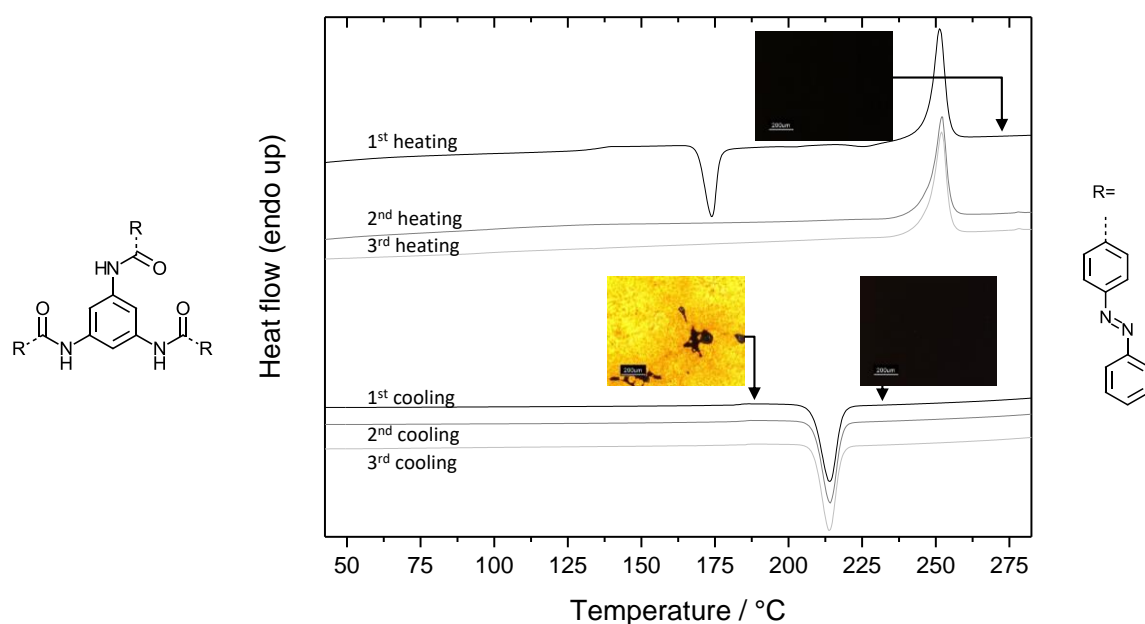


Figure 15: DSC traces of compound **2a** during three heating and cooling cycles at a scan rate of 10 K/min under a N<sub>2</sub>-flow of 50 mL/min. The compound was molten in a DSC pan at 300°C for 1 min and quenched in liquid nitrogen prior to the DSC experiment. Insets: Polarizing microscopy images between crossed polarizers. The scan rate in POM experiment is 10 K/min. Arrows mark the temperature at which the image was taken.

The DSC traces and POM images of CF<sub>3</sub>-substituted azobenzene-functionalized trisamide-based compound **1b** during the heating and cooling cycles is shown in Figure 16.

Prior to the DSC measurement, the compound has been dissolved in THF and dropped into the aluminum pan in order to increase the amount of material in the DSC measurements. Subsequently, the solvent is evaporated off at a temperature of ca. 80 °C for 5 min. Upon first heating, the glass transition is not observable in the DSC measurement. Further heating results in melting of the powder at 315 °C. In the first cooling step, the compound seems to crystallize immediately. However, it is not clear if the first peak during first cooling is a measurement artefact or recrystallization of the compound. In the further cycles, neither melting nor crystallization or glass transitions could be observed. Upon second heating, the melting of the compound occurs in a temperature range between 325 and 335 °C according to POM experiments. Upon cooling the film on the POM hot stage, crystallization of **1b** can be observed. At a temperature of about 128 °C, movement in the film is noticeable suggesting a glass transition. Albeit to the tendency to crystallize, the compound can be vitrified in a spin-coating experiment.

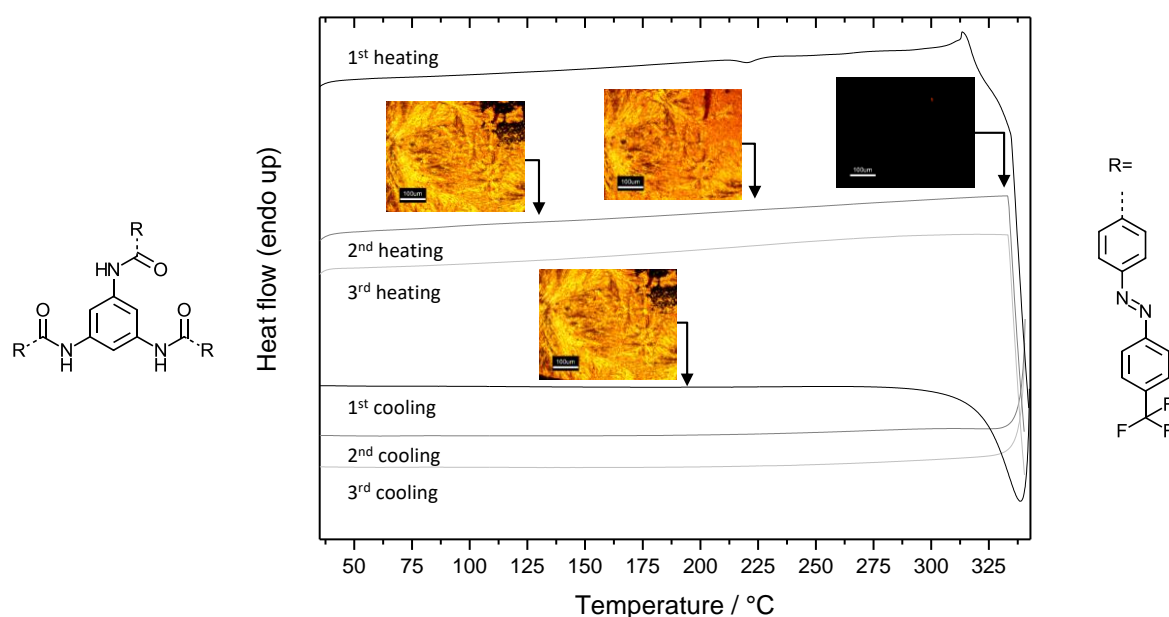


Figure 16: DSC traces of compound **2b** during three heating and cooling cycles at a scan rate of 10 K/min under a N<sub>2</sub>-flow of 50 mL/min measured in a high pressure pan. Insets: Polarizing microscopy images between crossed polarizers. The scan rate in POM experiment is 10 K/min. Arrows mark the temperature at which the image was taken.

Figure 17 shows the DSC traces and POM images of perfluoropropyl-substituted azobenzene-functionalized trisamide-based compound **2c** during the heating and cooling cycles in the DSC experiment. According to TGA measurements, the onset for decomposition of compound **2c** is already starting at a temperature of 240 °C. Therefore, DSC measurements had to be performed in a high pressure pan. The maximum temperature was set to 290 °C.

Upon first heating, compound **2c** shows neither a glass transition nor a melting point. Hence, upon cooling no tendency to crystallize is observable in the DSC measurement. However, during POM experiments, the powder starts melting at about 200 °C. Yet, in the POM experiments, the film starts to generate cracks just above 105 °C suggesting a glass transition. As in case of the other two 1,3,5-benzenetrisamides, transparent films could be obtained by spin-coating from a THF solution.

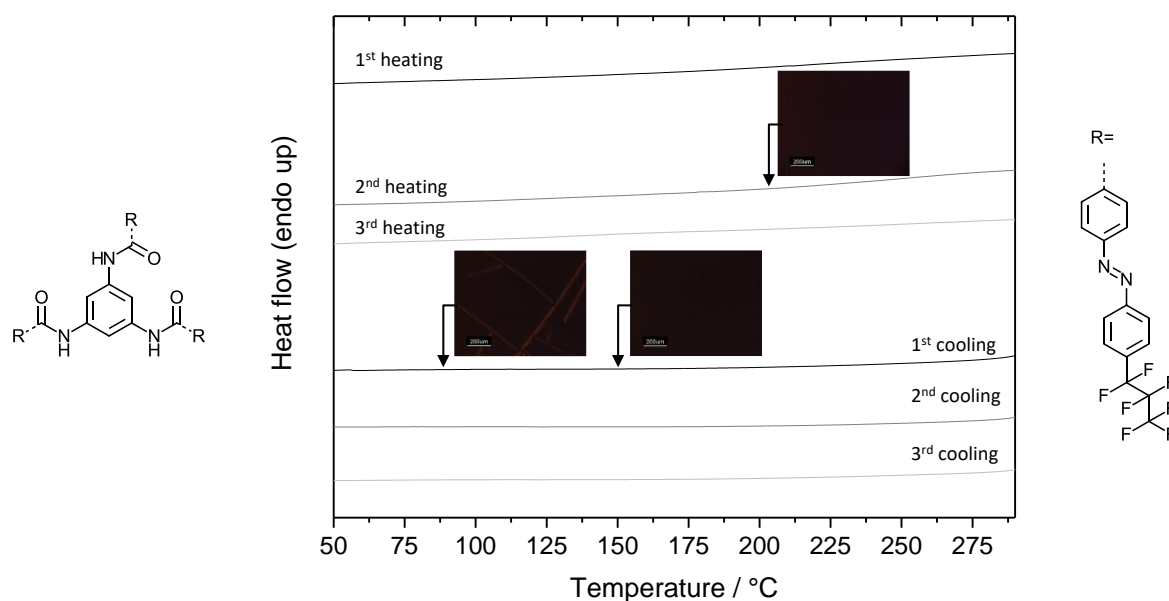


Figure 17: DSC traces of compound **2c** during three heating and cooling cycles at a scan rate of 10 K/min under a N<sub>2</sub>-flow of 50 mL/min measured in a high pressure pan. Insets: Polarizing microscopy images between crossed polarizers. The scan rate in POM experiment is 10 K/min. Arrows mark the temperature at which the image was taken.

The DSC traces and POM images of the final compound of the 1,3,5-benzenetrisamide series, the perfluorohexyl-substituted azobenzene-functionalized 1,3,5-benzenetrisamide compound **2d** during the heating and cooling cycles is shown in Figure 18.

In case of trisamide compound **2d**, the melting peak at approx. 275 °C features a very low heat of fusion. Upon cooling the melt, the compound crystallizes at around 250 °C. In the DSC traces, no glass transition is observable. All other scans are highly reproducible, indicating that no decomposition occurs during the DSC experiments. During cooling of the film in the POM experiment, however, the film became brittle as indicated by cracks in the film at a temperature of 112 °C implying a glass transition at this temperature. Regarding the spirochromane compounds, perfluorohexyl-substituted **1d** was the derivative with the most pronounced tendency to crystallize. No homogeneous thin films could be generated with compound **1d**, neither by quenching from melt nor by spin-coating from solution, as a solution dewets from untreated and surface-treated glass and silicon wafer substrates.

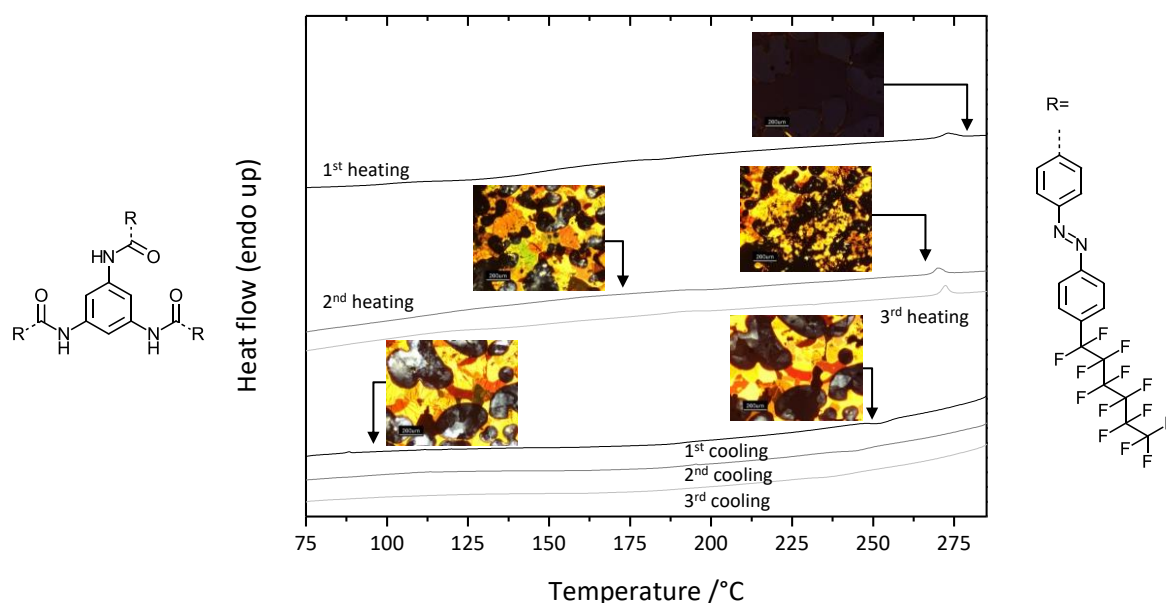


Figure 18: DSC traces of compound **2d** during three heating and cooling cycles at a scan rate of 10 K/min under a  $N_2$ -flow of 50 mL/min. Insets: Polarizing microscopy images between crossed polarizers. The scan rate in POM experiment is 10 K/min. Arrows mark the temperature at which the image was taken.

#### Azobenzene-functionalized triphenylamine derivatives

As the last compound class, the phase behavior of the triphenylamine derivatives were studied via DSC and POM experiments. Since the triphenylamine derivatives cannot interact with other molecules via hydrogen bonding, the glass transition temperature as well as the melting points are expected to be lower than in case of the 1,3,5-benzenetrisamides. The first compound to be investigated is H-substituted azobenzene derivative **3f** (see Figure 19).

Upon first heating of **3f**, the compound shows a  $T_g$  of 92 °C. Further heating leads to polymorphic melting of the compound at a temperature of 160 °C and 174 °C. Upon cooling, no crystallization can be observed. Further scans show no other phase transitions except the glass transition. In contrast, POM experiments showed still some birefringent fractions in the sample, which were present up to a temperature of 330 °C. Heating beyond this leads to decomposition of the compound. As a consequence, the sample remains birefringent during cooling. After cooling down below the  $T_g$ , the film forms cracks. Upon quenching by spin-coating from solution, **3f** did not form transparent films but slightly light scattering ones instead.

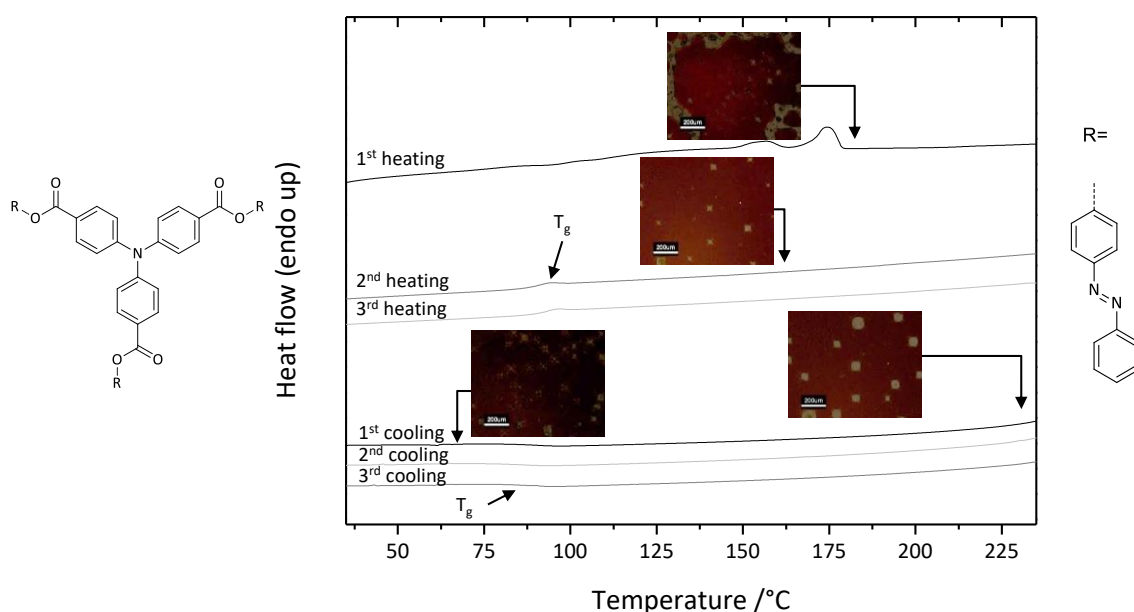


Figure 19: DSC traces of compound **3f** during three heating and cooling cycles at a scan rate of 10 K/min under a  $N_2$ -flow of 50 mL/min. Insets: Polarizing microscopy images between crossed polarizers. The scan rate in POM experiment is 10 K/min. Arrows mark the temperature at which the image was taken.

Figure 20 shows the DSC traces and POM images of  $CF_3$ -substituted azobenzene-functionalized triphenylamine-based compound **3g** during the heating and cooling cycles in the DSC experiment.

During the first heating scan, compound **3g** shows a complicated phase behavior due to the thermal history. At a temperature of 99 °C, a glass transition can be observed. After a recrystallization at 121 °C, a polymorphic melting behavior can be observed at a temperature of 146 °C. Further heating reveals a second melting point at 223 °C. Upon cooling, the compound crystallizes twice, separately at 143 °C and 119 °C before the  $T_g$  is reached at approx. 96 °C. In the second heating process, a glass transition temperature at 100 °C as well as the polymorphic melting at 145 °C can be seen. This behavior is fully reproducible. Similar to compound **3f**, the POM experiments show a small birefringence after the melting point, which cannot be eliminated through further heating without getting too close to the decomposition temperature. This birefringence is not attributed to a crystalline sample, but rather to impurities arising from purification of the compound by column chromatography. Consequently, films of compound **3g** showed slight light scattering after spin coating.

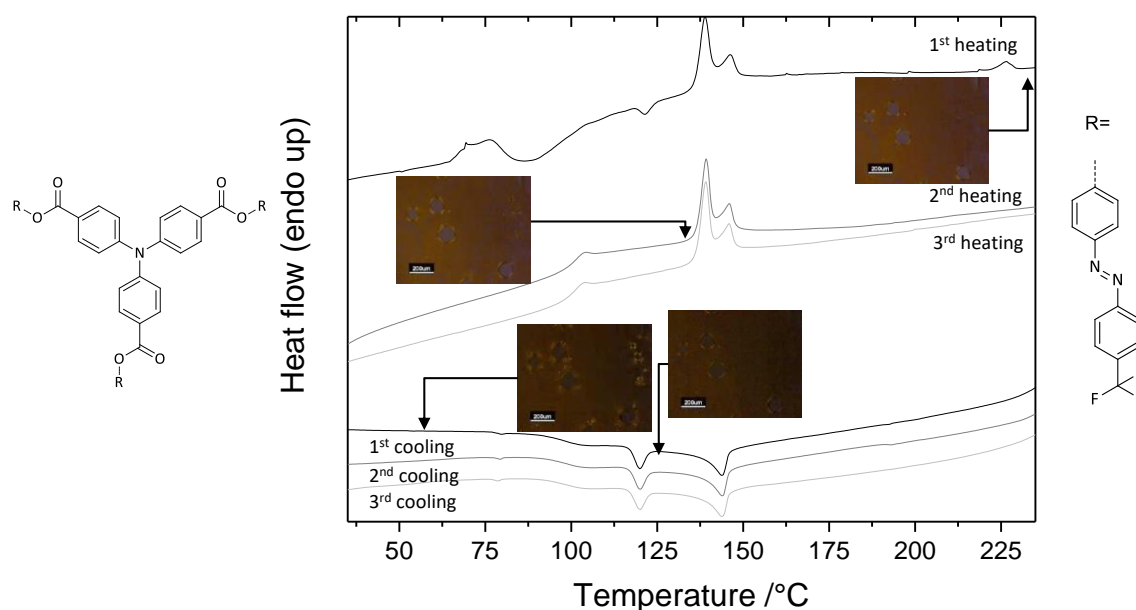


Figure 20: DSC traces of compound **3g** during three heating and cooling cycles at a scan rate of 10 K/min under a  $N_2$ -flow of 50 mL/min. Insets: Polarizing microscopy images between crossed polarizers. The scan rate in POM experiment is 10 K/min. Arrows mark the temperature at which the image was taken.

### Summary of the thermal properties

In this chapter, 11 azobenzene-functionalized low-molecular compounds were investigated with respect to their thermal stability, phase behavior and glass forming ability. Thermogravimetric analysis revealed that all compounds possess a good thermal stability of more than 350 °C. 7 out of 11 feature a  $T_g$  in the range between 92-136 °C as observed by DSC. The glass transition temperature clearly correlates with the structure of the molecule core. The triphenylamine derivatives feature a  $T_g$  in the temperature range between 92-99 °C, whereas the spirobichromane derivatives possess a  $T_g$  in the range between 107-126 °C. The 1,3,5-benzenetrisamide derivatives feature the highest glass transition temperatures with  $T_g$ s between 128 °C and 136 °C. The reason for the increasing glass transition temperatures within the series of different molecular glasses is the increase in rigidity from the triphenylamine core to the spirobichromane core. In case of the 1,3,5-benzenetrisamide derivatives, secondary interactions (H-bonds) are introduced, which increase the glass transition even further (see Figure 21). Surprisingly, compounds with  $C_3F_7$  and  $C_6F_{13}$  substituents do not show  $T_g$ s in DSC/POM experiments. Roughly, the glass transition temperature correlates with the melting temperature, which depends on the molecule core as well as with the substituent at the para position of the azobenzene moiety.  $CF_3$  and  $C_3F_6$ -substituted compounds feature surprisingly high melting points close to the decomposition temperature, whereas the other compounds possess  $T_m$ s below 300 °C. Except for the  $C_6F_{13}$ -substituted compounds **1d** and **2d**, all compounds are capable of forming stable, homogenous transparent films.

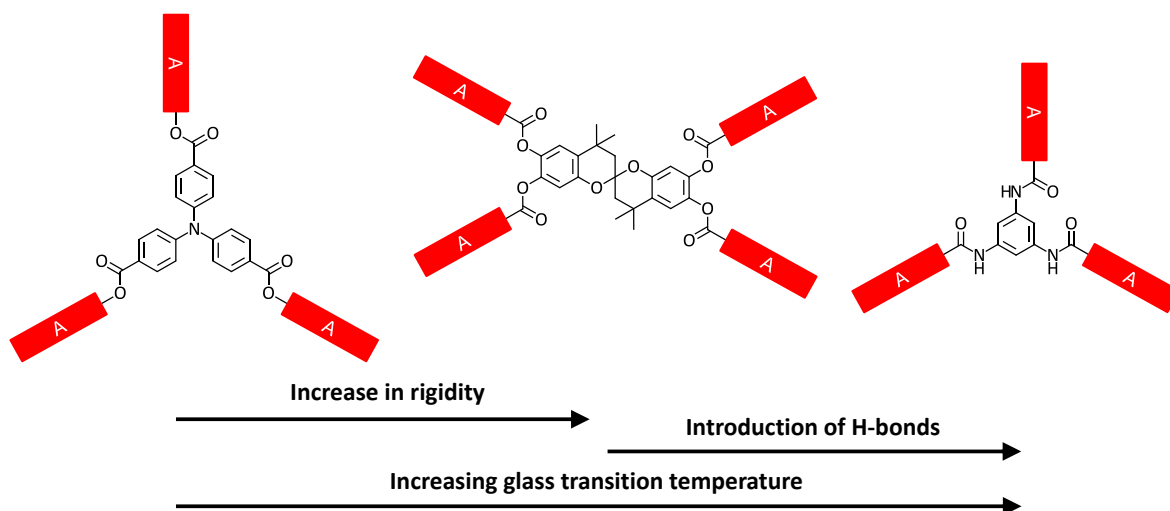


Figure 21: Schematic representation of the synthesized azobenzene-functionalized molecular glasses with different molecule cores. The rigidity of the molecule cores is increasing from triphenylamine-based to spirobichromane-based molecular glasses. In case of 1,3,5-benzenetrisamide derivatives, intermolecular H-bond-formation capability is introduced. The glass transition temperature increases from left to right. The red rectangles represent the azobenzene chromophores.

The thermal stability, phase behavior and glass forming ability of the azobenzene-functionalized molecular glasses are summarized in Table 2.

Table 2: Thermal characteristics of the investigated azobenzene functionalized molecular glasses.

Compound	Structure	R	T <sub>g</sub> / °C <sup>a)</sup>	T <sub>m</sub> / °C <sup>a)</sup>	T <sub>-5 wt.%</sub> / °C <sup>b)</sup>	Stable amorphous phase <sup>d)</sup>
1a		-H	108	249	365	yes
1b		-CF <sub>3</sub>	126	314 (decomp.)	366	yes
1c		-C <sub>3</sub> F <sub>7</sub>	-	322 (decomp.)	366	yes
1d		-C <sub>6</sub> F <sub>13</sub>	-	272	360	no
1e		-OCH <sub>3</sub>	107	239	360	yes
2a		-H	136	252	400	yes
2b		-CF <sub>3</sub>	128 <sup>c)</sup>	315 (decomp.)	375	yes
2c		-C <sub>3</sub> F <sub>7</sub>	-	-(decomp.)	344	yes
2d		-C <sub>6</sub> F <sub>13</sub>	-	275	370	no
3f		-H	92	174	372	yes
3g		-CF <sub>3</sub>	99	146	366	yes

a) determined in DSC measurements; b) determined in thermogravimetric analysis; c) determined in POM experiments; d) at room temperature after spin coating from solution.

### 3.4 Optical characterization

Since in the following chapters (4-6), primarily the photo-isomerization of the azobenzene moieties is exploited, the knowledge absorption in thin film architectures is of crucial importance. Thus, the optical characterization of all compounds is performed via UV/Vis spectroscopy in THF solutions and thin films of the respective compounds. The concentration of the solutions was approx. 0.01 mg/ml. The thicknesses of the transparent homogenous films range from about 20 - 50 nm.

#### Azobenzene-functionalized spirobichromane derivatives

The UV/Vis characterization of THF solutions and thin films of the spirobichromane-based compounds **1a-1e** is shown in Figure 22.

The absorption spectrum of the solution of spirobichromane derivative **1a** features a  $\pi$ - $\pi^*$ -absorption band with a shoulder and a maximum at 325 nm and an n- $\pi^*$ -transition maximum at ca 461 nm. In comparison, the  $\pi$ - $\pi^*$ -absorption bands of the molecular glasses featuring fluoroalkyl-substituted azobenzene moieties (**1b-1d**) are slightly blue shifted to 319 nm, which can be explained by the electron-withdrawing characteristics of the substituents. Methoxy-substituted compound **1e** is characterized by a significant red-shift of the  $\pi$ - $\pi^*$ -absorption band to a wavelength of 359 nm. Since the MeO group at the para position of the azobenzene moieties is an electron-donating group, this shift was expected. The shift results in a stronger overlap of the  $\pi$ - $\pi^*$ - with the n- $\pi^*$ -absorption band at about 443 nm.

The films feature similar trends and broadened peaks owing to the higher degree of disorder and the possible formation of H- and J-aggregates in the respective system compared to the solutions. The maxima of the  $\pi$ - $\pi^*$ -absorption band of compound **1a** is still at 325 nm, while the perfluoroalkyl-substituted compounds show a slight trend to further shifting to lower wavelength with increasing chain length from 315 nm (CF<sub>3</sub> substituent) to 309 nm (perfluorohexyl substituent). A trend, which was almost not observable in the films. This observation could be explained by worsening solubility of the molecules in THF with increasing chain length, leading to the formation of aggregates, which could, in case of H-aggregates, lead to a blue-shift of the absorption maximum. As expected, the maximum of the n- $\pi^*$ -absorption peak, however, remains almost unchanged at a wavelength of ca. 455 nm for each compound as this absorption represents the non-bonding state.

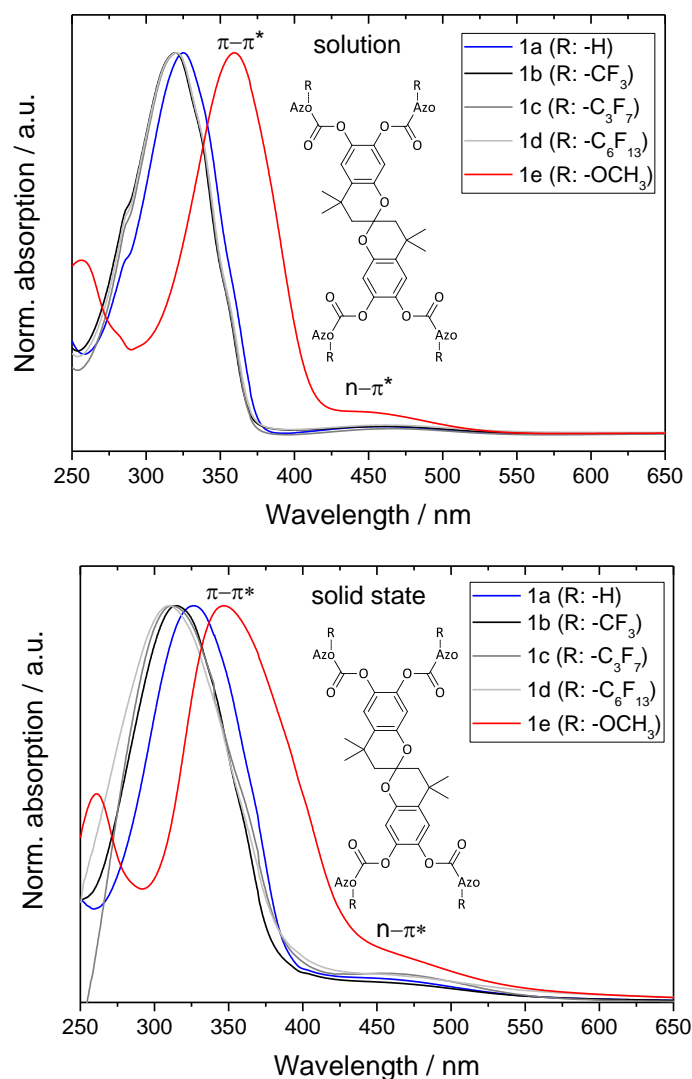


Figure 22: Normalized UV/Vis-spectra of solutions of non-substituted and perfluoroalkyl-substituted azobenzene functionalized spirobichromane-based derivatives (compounds **1a-1e**) in solution (top) and as films (bottom). Film thicknesses range from 20 to 45 nm. Solution concentrations: 0.01 mg/ml.

### Azobenzene-functionalized 1,3,5-benzenetrisamide derivatives

Figure 23 shows the UV/Vis characterization of THF solutions and thin films of the 1,3,5-benzenetrisamide-based compounds **2a-2d**.

The solutions of the 1,3,5-benzenetrisamide-based compounds feature a  $\pi-\pi^*$ -absorption maximum at around 330 nm and an  $n-\pi^*$ -transition at 455 nm. Compared to the width of the  $\pi-\pi^*$ -absorption bands in the thin films of the 1,3,5-benzenetrisamide-based compounds, the width of the  $\pi-\pi^*$ -absorption bands in the solutions is smaller, implying more separated molecules in solution than it is the case in the films. As a consequence of the narrower  $\pi-\pi^*$ -bands, the overlap with the  $n-\pi^*$ -transition is decreased. In contrast to the spirobichromane derivatives, the absorption maxima of the  $\pi-\pi^*$ -transition of the perfluoroalkyl-substituted compounds are shifted slightly to lower wavelength compared to the unsubstituted **2a**.

Compared to thin films of the spirobichromane-based compounds **1a-1e**, the  $\pi-\pi^*$ -absorption bands of the trisamide derivatives **2a-2d** feature a more pronounced shoulder at about 270 nm,

which might be attributed to the molecule core. The maxima of the  $\pi$ - $\pi^*$ -absorption bands are located at a wavelength of about 322 nm, is broadened and has a distinct overlap with the  $n$ - $\pi^*$ -absorption band at ca. 450 nm. As in case of the spirobichromane derivatives, the substitution of the azobenzene moieties with a perfluorinated alkyl chain has no substantial influence of the absorption spectrum of the molecular glasses.

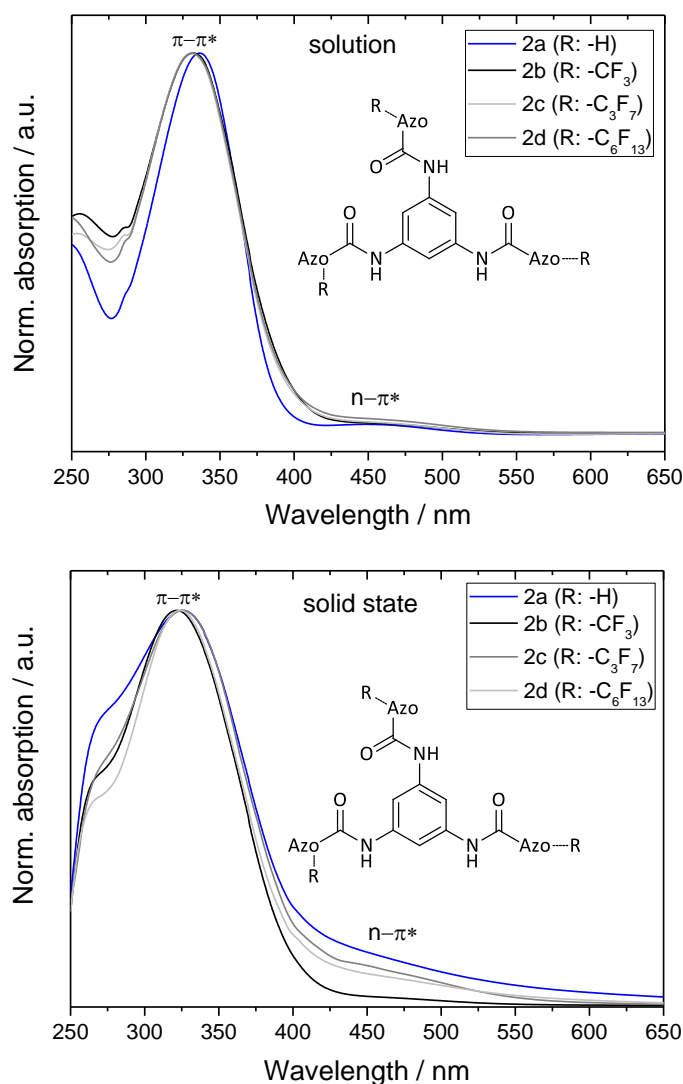


Figure 23: Normalized UV/Vis spectra of solutions of non-substituted and perfluoroalkyl-substituted azobenzene functionalized 1,3,5-benzenetrisamides-based compounds (compounds **2a-2d**) in solution (top) and as films (bottom). Film thicknesses range from 30 to 50 nm. Solution concentrations: 0.01 mg/ml.

#### Azobenzene-functionalized triphenylamine derivatives

The UV/Vis characterization of THF solutions and thin films of the triphenylamine-based compounds **3f** and **3b** are depicted in Figure 24.

The solutions of the triphenylamine-based compounds feature a large absorption peak originating from the molecule core at 357 nm (as evidenced by a reference compound), which overlaps the  $\pi$ - $\pi^*$ -absorption maximum at 318 nm. The  $n$ - $\pi^*$ -absorption band is located at 442 nm. In solution, the  $\pi$ - $\pi^*$ -absorption bands is not significantly overlapping with the  $n$ - $\pi^*$ -absorption band. Unlike in case of the other molecular glasses, the absorption maxima of the  $\pi$ - $\pi^*$ -transition of the CF<sub>3</sub>-

substituted compounds are not significantly shifted to a lower wavelength compared to the unsubstituted compound **3f**. This result is not surprising as the shift is more distinct with increasing chain length.

The  $\pi$ - $\pi^*$ -absorption bands of both triphenylamine derivatives **3f** and **3g** feature a shoulder. The maxima are located at a wavelength of about 366 nm, and therefore are located closer to the  $n$ - $\pi^*$ -absorption band at ca. 450 nm and both bands overlap. As in case of the other molecular glasses investigated so far, the substitution of the azobenzene moieties with the  $\text{CF}_3$  group has no substantial influence of the absorption spectrum of the molecular glasses.

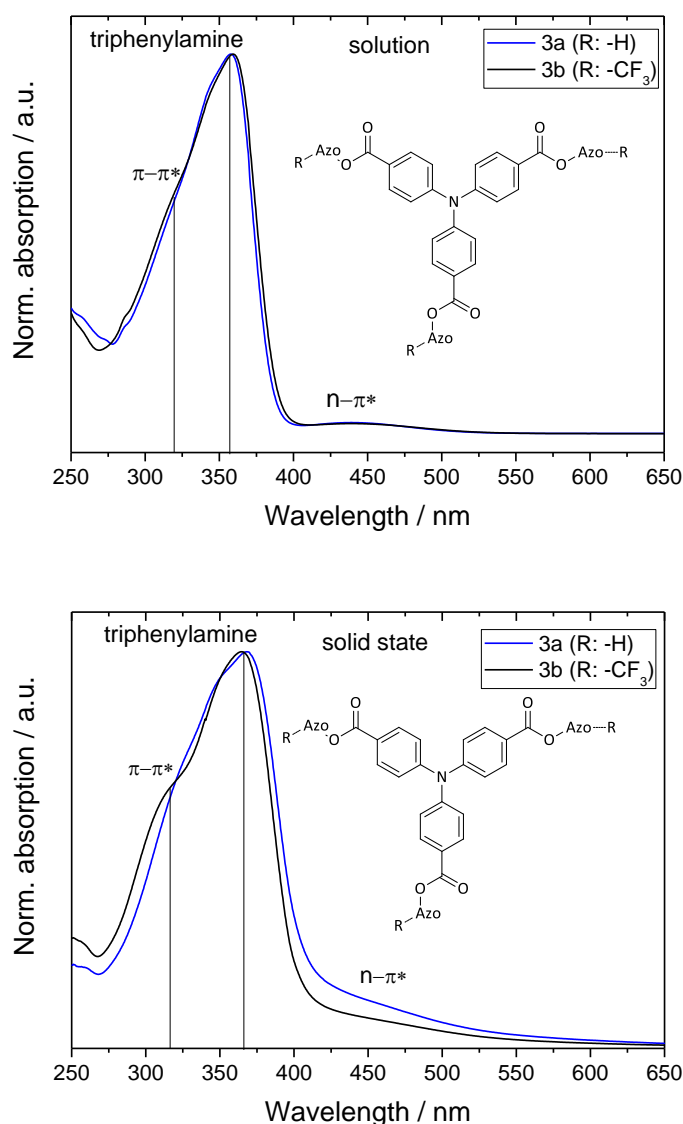


Figure 24: Normalized UV/Vis-spectra of solutions of non-substituted and perfluoroalkyl-substituted azobenzene functionalized triphenylamine-based compounds (compounds **3f**, **3g**) in solution (top) and as films (bottom). Film thicknesses are 40 nm (**3f**) and 20 nm (**3g**). Solution concentrations: 0.01 mg/ml.

### 3.5 Summary of the chapter

In this chapter, the synthesis and thermal as well as optical characterization of azobenzene-functionalized molecular glasses is presented.

The star-shaped molecules are designed to be either tri- or tetra-functional, i.e. three or four azobenzene moieties are attached to the molecule core via an amide or an ester group. The twisted spirobichromane or triphenylamine molecule cores promote an easy transfer of the molecules to an amorphous phase. From triphenylamine-based compounds to the spirobichromane-based derivatives, the rigidity of the structure increases. In case of the 1,3,5-benzenetrisamide-based derivatives, additional secondary intermolecular interactions (H-bonds) are introduced. The molecule cores carry azobenzene substituents, which are substituted on the para-position of the azo group to adjust the level of hydrophobicity or influence the absorption spectrum of the molecules.

Azobenzene moieties are synthesized via two different routes depending on the commercial availability of the educts. In general, the chromophores are synthesized via a so-called "Mills reaction", i.e. a condensation reaction of a para-nitrosobenzoic acid and an aniline derivative. In order to synthesize perfluoroalkyl-chain-substituted azobenzene derivatives, an "Ullmann reaction" with two iodine-substituted derivatives is used. Using the combination of both reactions and an esterification reaction of chlorinated azobenzoic acid with the hydroxyl and amine groups of the molecule cores, the synthesis of azobenzene-functionalized molecular glasses based on 1,3,5-benzenetrisamide and spirobichromane core with CF<sub>3</sub>, perfluoropropyl and perfluorohexyl substituents was possible. Besides, a methoxy-azobenzene spirobichromane-based azobenzene molecular glass was synthesized.

The thermal characterization is conducted via differential scanning calorimetry (DSC), thermal gravimetric analysis (TGA) and polarization microscopy (POM). The compounds are thermally stable to a temperature above 350 °C. 7 out of 11 compounds feature a glass transition temperature. In general, the compounds feature glass transition temperatures higher than 90 °C. As the rigidity increases from triphenylamine-based compounds to the spirobichromane-based derivatives, the glass transition temperature of the respective derivatives increases. In case of the 1,3,5-benzenetrisamide-based derivatives, additional secondary intermolecular interactions (H-bonds) are introduced, which further increase the T<sub>g</sub>. Spin coating and quenching experiments showed that the low-molecular-weight compounds can readily be transferred into an amorphous phase. The perfluorohexyl-substituted molecular glasses, however, possess the tendency to crystallize and dewet from glassy or silicon surfaces.

The optical properties are investigated using UV/Vis spectroscopy. In the solid state, the absorption maxima are broadened in comparison to the maxima in solution. The substitution with perfluorohexyl chains in para-position to the azobenzene moieties has no substantial influence on the position of the  $\pi$ - $\pi^*$ - and  $n$ - $\pi^*$  absorption band maxima. Substitution with the electron-donating methoxy group, however, leads to a shift of the  $n$ - $\pi^*$  and  $\pi$ - $\pi^*$  absorption bands, so that both bands are located closer to each other. This optical property is advantageous for its application in azo-NIL, as overlapping absorption bands allow for a continuous conversion of the azobenzene molecule upon exposure to a single wavelength being beneficial for photo-induced motion in an azobenzene film.

## 4 Azobenzene-based nanoimprint lithography<sup>1</sup>

### 4.1 Introduction to nanoimprint lithography

Micro- and nanopatterning techniques are key processes in the fabrication of modern optics or microelectronics and are becoming increasingly important for biological applications.<sup>[95–97]</sup> One of the most prominent examples is photolithography, a common technique to produce integrated circuits. This technique, however, is facing technical and economic limits with decreasing pattern sizes. A problem, that needs to be overcome by technological innovations or by the identification of alternative patterning techniques. Nanoimprint lithography (NIL) is a method with the potential to solve these issues. Figure 25 gives an overview of the main nanoimprint lithography techniques.

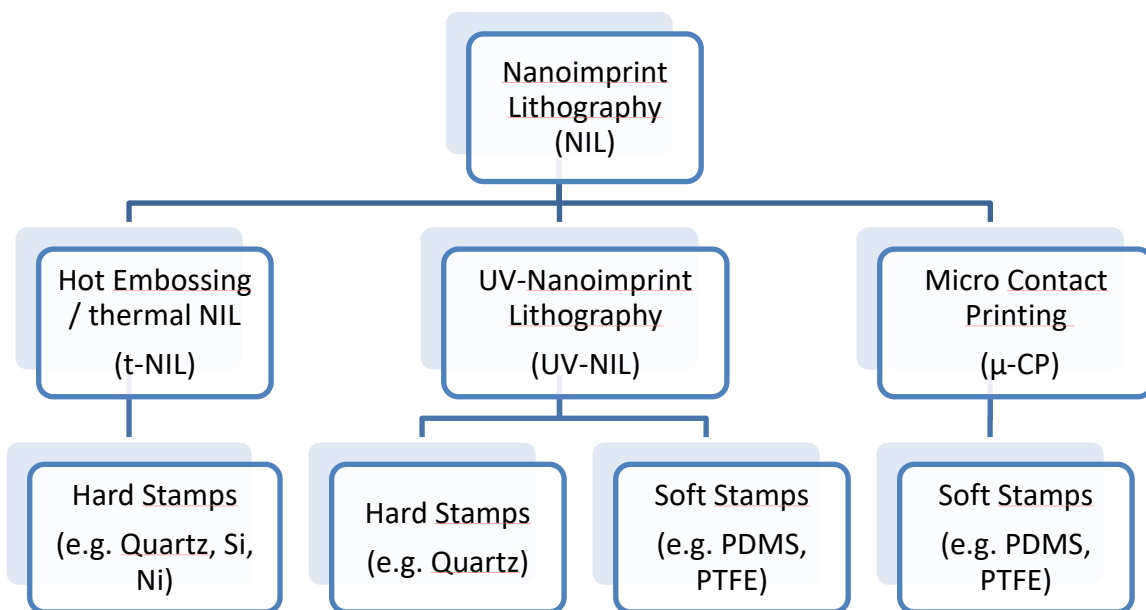


Figure 25: Overview: Main nanoimprint lithography methods.<sup>[98]</sup>

NIL, an alternative to well-established lithographic processes, is a cost-effective high-throughput micro- and nanopatterning technique whose basic principle was developed by Chou et al. in 1995.<sup>[99]</sup> The NIL process consists of two basic steps (see Figure 26). At first, a stamp (mold) with features in the nanometer regime is pressed into a resist, e.g. a polymethyl methacrylate (PMMA).<sup>[99]</sup> The pressure applied and the temperature needed for the process depends on the resist material. In this case, the temperature for the imprint process was adjusted to 200 °C and the pressure to 131 bar. As a consequence, the material flows into the cavities of the mold. After cooling the resist below its  $T_g$  of 105 °C, the stamp is lifted-off (released) and the negative-type pattern of the mold is imprinted into the PMMA film. Pillars with a diameter of 25 nm were successfully transferred from the mold to the resist. In a second step, the residual layer on the patterned silicon wafer was etched using oxygen gas in a reactive ion etching (RIE) process. In 1997, Chou et al. even

<sup>1</sup> Parts of this chapter have been published in the Journal of Advanced Materials.

C. Probst, C. Meichner, K. Kreger, L. Kador, C. Neuber, H.-W. Schmidt, *Adv. Mater.* **2016**, *28*, 2624.<sup>[94]</sup>

presented patterns with a structure size down to 10 nm. Since heat is necessary, this technique is often referred to as thermal NIL (t-NIL). Among the main advantages of this technique, the low cost and the large area that can be patterned are the most outstanding ones. Major drawbacks are the processing time needed and thermal expansion and shrinkage during heating and cooling cycles leading to distortions of the involved resist and mold materials.<sup>[100]</sup>

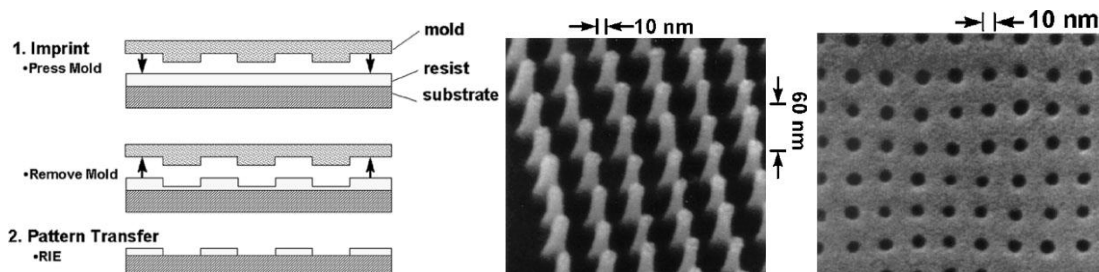


Figure 26: Left: Schematic of the nanoimprint lithography process: (1.) pressing the mold into the PMMA film to create a thickness contrast in the resist; release of the mold, and (2.) reactive ion etching of the resist to transfer the pattern from the template into the resist. Middle: SEM micrograph the mold used for the imprinting process. Right: SEM image of the replicated structures of the mold in a PMMA film.<sup>[101]</sup>

Ultraviolet nanoimprint lithography (UV-NIL) allows for imprinting of nanopatterns at room temperature. In this case, a low viscous UV curable fluid is placed onto a substrate by dispensing or spin-coating. After pressing the UV-transparent stamp onto the thin film, the resist is crosslinked by exposure to UV light (see Figure 27). The applied pressure is much lower than in case of t-NIL (between 0-5 bar) and no heating of the substrate is necessary.<sup>[100]</sup> While in t-NIL rigid stamps (quartz, Si, nickel, etc.) are common, flexible stamps (e.g. PDMS or fluorinated polymers) can be used in UV-NIL processes. Nanoimprinting methods using flexible or soft stamps are embraced by the term *soft lithography*. Since soft stamps simplify the release procedure due to their flexibility and low surface energy, defects are reduced compared to methods working with rigid stamps.<sup>[96]</sup> Another advantage of UV-NIL towards t-NIL is the significantly shortened cycle time. Since no heating or cooling is needed, the average duration for the imprinting process is below 1 min.<sup>[100]</sup> However, one of the drawbacks of this technique is the material shrinkage occurring during the crosslinking step in which the material solidifies. This curing shrinkage is most pronounced in curing systems utilizing radical initiators.<sup>[102]</sup>

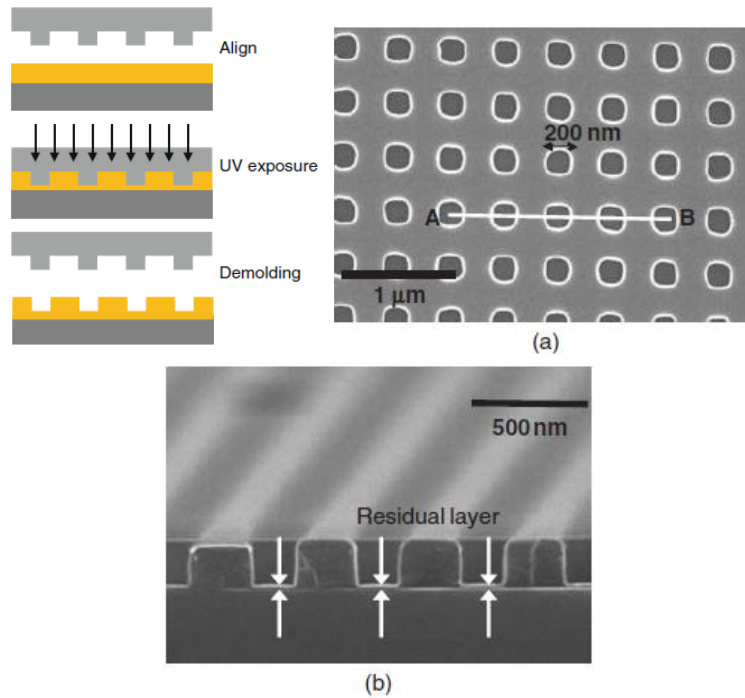


Figure 27: Left: Schematic of the UV-NIL process: the resist is coated on a substrate and aligned; the stamp is imprinted into the resist and cured by exposure to UV light; Separation of stamp and substrate. Middle and Right: SEM images of UV-NIL imprinted samples. a) top view; b) cross-sectional view along line A-B in a).<sup>[102,103]</sup>

In 2001 Hong H. Lee et al. developed an interesting patterning technique that combines the main features of conventional t-NIL with the advantages of soft lithography methods.<sup>[104]</sup> In the so-called capillary force lithography (CFL), a spin-coated polymer film (e.g. PS or SBS) is heated above its  $T_g$  while an elastomeric mold is placed onto it (see Figure 28). During the whole imprinting process, no pressure is applied to the mold. A prerequisite for CFL to function is that the free energy of the system is lowered by the polymer, which wets the walls of the PDMS mold. If the effect of gravity is neglected, the viscosity of the polymer melt  $\eta$  and its surface tension  $\gamma_{\text{polymer/air}}$  as well as the size of the capillary determine the rate of the flow of the polymer into the cavities of the mold. The time  $t$ , to fill the mold is given by:

$$t = \frac{2\eta z^2}{R\gamma_{\text{polymer/air}}\cos\theta} \quad (4.1)$$

Where  $z$  is the length of the capillary to be filled,  $R$  the hydraulic radius (ratio of the volume of the liquid like polymer in the capillary to the solid/polymer interface) and  $\theta$  the contact angle at the resist/mold interface. In the experiments presented, the time for the SBS triblock copolymer to completely fill cavities with a height of 600 nm and a width of 400 nm was about 30 minutes at a temperature of 100°C. Since no pressure is applied to the highly-viscous polymer film (viscosity  $\approx 10^6$  Pa s), the time needed for the imprinting process becomes extremely high. The long time period needed for the process is the biggest drawback of this technique.

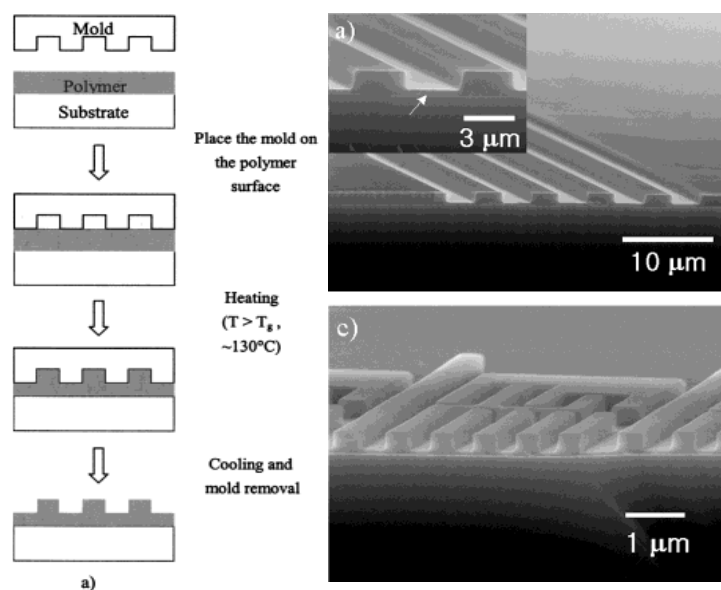


Figure 28: Left: Schematic representation of the function principle of CFL. Right: SEM micrographs of imprinted microstructures via CFL patterning technique. The arrow indicates the residual layer.<sup>[104]</sup>

## 4.2 Azobenzene-based surface patterning

Surface patterning techniques utilizing azobenzene-based materials have been intensively studied in the past decade.<sup>[13,18,105,106]</sup> There are different ways to pattern azobenzene-functionalized materials. Since azobenzene materials possess unique photophysical properties, the function principle of these techniques differs strongly from conventional surface patterning methods. Azobenzenes reversibly isomerize from the thermodynamically stable *trans*-form to the meta-stable *cis*-form when exposed to light in its  $\pi$ - $\pi^*$  absorption band in the UV region. By exposure to visible light at the wavelength of the  $n$ - $\pi^*$  absorption band of the azobenzene molecule, or by thermal stimulus, the *trans*-form is restored again.<sup>[3]</sup> This photophysical behavior allows for the induction of repeated *cis-trans*-isomerization cycles in the azobenzene-functionalized material that lead to a trembling motion of the molecules and, upon holographic exposure to light of an appropriate polarization, to rearrangements in the material. These can induce local differences in the refractive index. Such abilities make these compounds interesting for applications like holographic data storage or as security feature.<sup>[3,107]</sup>

In azobenzene-based surface patterning techniques a film consisting of an appropriate azobenzene-functionalized material is exposed to an interference pattern, which is generated either by two superimposed laser beams or by a phase mask.<sup>[108,109]</sup> In both cases, *cis-trans*-isomerization cycles are induced, which allow for a movement of the azobenzene-functionalized molecules in either the illuminated or the non-illuminated regions, which is referred to as mass transport. As a consequence of the mass transport, which takes place far below the  $T_g$  of the material, surface relief gratings (SRGs) are generated (see Figure 29).

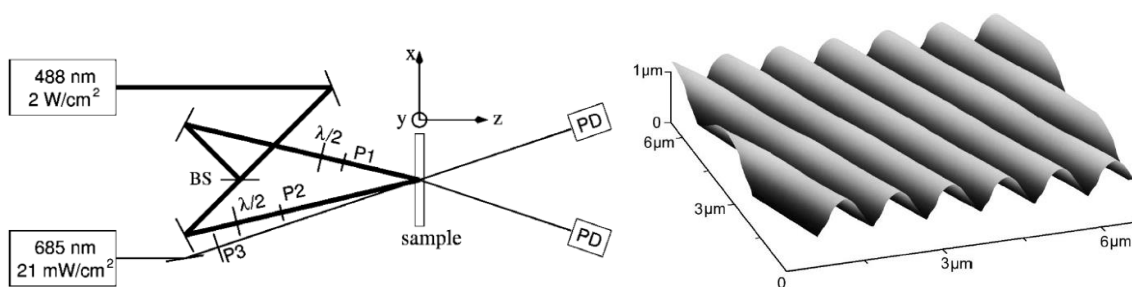


Figure 29: Left: Schematic representation of a typical holographic setup.  $\lambda$ -plates are used to generate different polarization states. P: polarizer; PD: photodiode; BS: beam splitter; Right: AFM image of a SRG inscribed in a film of an azobenzene-functionalized molecular glass.<sup>[110]</sup>

### 4.3 Pattern transfer techniques

For most applications, the patterning process is not finished when the nanoimprint lithography patterning process is completed. Instead, the pattern has to be transferred into another material, e.g., silicon. Figure 30 depicts schematic representations of common pattern transfer processes. The pattern can be transferred by either metal lift-off or etching procedures. When an etching process is used, the resist has to be transformed into a masking layer by homogeneously removing the residual layer after the imprinting process. Only the features that had a higher structure height than the residual layer remain on the underlying substrate. In a next step, the regions, in which the bare substrate is showing (openings), are modified by dry etching, e.g. reactive ion etching, wet chemical etching (etching solutions) or other methods. In NIL, both steps, removing the residual layer as well as the pattern transfer can be performed by etching techniques.<sup>[111,111,112]</sup> It is of vital importance that during the pattern transfer process, the lateral size of the pattern is preserved.

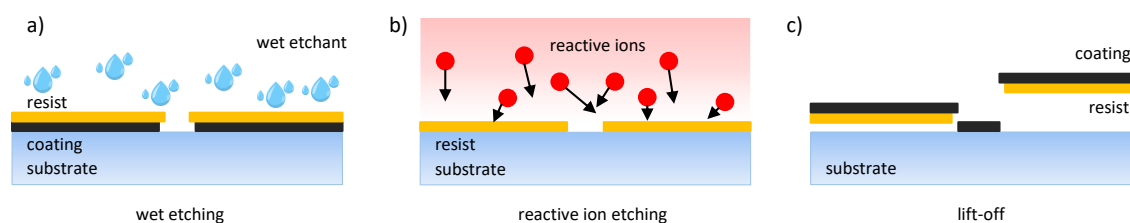


Figure 30: Schematic representation of common pattern transfer processes a) wet etching, b) reactive ion etching and c) lift-off process.

Wet etching is the predecessor of dry etching techniques and is not very common in NIL. Here, a selective wet etchant is deposited on the resist layer. The layer underneath the resist layer (e.g.  $\text{SiO}_2$  layer on a Si-Wafer) is then etched by the wet etchant (e.g. buffered hydrofluoric acid). Due to issues with lateral undercuts, however, the minimum achievable feature size is limited to  $3 \mu\text{m}$ .<sup>[113]</sup> Mostly, the etchant is an isotropic etchant, i.e. the etching process takes place at the same speed in all directions. More common in NIL is the use of dry etching methods like reactive ion etching (RIE). The basic principle of a dry etching process, like RIE, includes the ionization of a gas to generate highly reactive, charged species. During the RIE process these species, which were formed in the plasma of the process gases (e.g.  $\text{O}_2$ ), diffuse into the material which is to be etched. Then volatile products are formed, which can be removed from the reaction chamber.<sup>[114]</sup> Compared to wet etching techniques, this method has several advantages. Since etching is more anisotropic than in wet etching, a higher aspect ratio of etched features is achievable. Furthermore, smaller patterns can be obtained using RIE.<sup>[113]</sup> Yet, the etch rate can be relatively low compared to wet etching processes. Prior to a lift-off process, an etching step has to be performed. Then a thin layer of a

solid material (e.g. metal) is deposited on the resist layer and the openings on the substrate. The resist layer also is a so-called sacrificial layer that is then dissolved and the deposited metal layer is remaining at the former opening spots. The lift-off process is useful when direct etching of the structured resist would affect the substrate in a negative manner. Recently, Kravchenko et al.<sup>[115]</sup> have demonstrated that azobenzene-functionalized polymers can be used as soft mask in etching processes (see Figure 31).

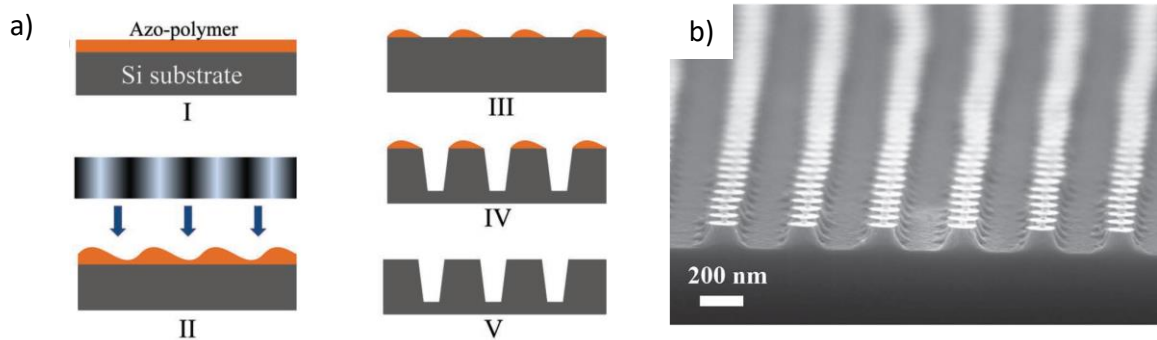


Figure 31: a) Schematic representation of an etching process using an azobenzene-functionalized polymer (poly(disperse red 1 methacrylate)) as soft mask. I: spin-coated azobenzene-functionalized polymer on a Si substrate. II: Patterning of the azobenzene film using an interference pattern with areas of high and low light intensity. III: Partial etching of the azobenzene resist using  $O_2$ . IV: dry etching of Si. V: the mask is stripped off the substrate. b) SEM image of an etched silicon wafer. The pattern is obtained by two orthogonal exposures.<sup>[115]</sup>

Figure 31 depicts a straightforward approach to etch an azobenzene-functionalized material. In a first step, the polymer material is spin-coated onto a silicon wafer (I). Afterwards, SRGs are generated on the polymer film (II), which is then partially etched using  $O_2$  (III). In a next step, the Si wafer is dry etched (IV) before, in the last step, the azobenzene film is washed from the Si substrate (V). Since this simple approach yielded rather trapezoidal profiles, the fabrication process had to be improved by adding an intermediate hard mask (5 nm thick  $Al_2O_3$  layer). Using this additional layer and conventional dry etching techniques (RIE), highly homogenous patterns on Si wafers were demonstrated. However, due to the fact that the patterning was done in a SRG fabrication process, the design of the patterns is limited in its complexity and feature size. Furthermore the resist layer thickness was limited to 100 nm since thicker films led to undesired secondary interference patterns.

#### 4.4 The cavity-filling process

To understand the pattern formation behavior of the various NIL techniques, it is important to comprehend the process of cavity-filling during an imprinting experiment. In literature, most studies deal with the flow of polymers in t-NIL experiments from the micrometer to the nanometer scale.<sup>[116–118]</sup> For large cavities, the process does not differ from the rather simple and well-known hot embossing technique, in which a polymer is heated above its glass transition temperature and then formed by a rigid mold. However, with decreasing cavity sizes and more complex stamp patterns, the process itself and particularly the material flow below the stamp starts to become more complex. In a thin polymer film, a small vertical movement of the stamp can cause a significant horizontal (or lateral) flow – the so-called squeeze flow - of the resist.<sup>[113]</sup> Heydemann et al.<sup>[117]</sup> described the flow behavior of thin polymer films in imprinting processes and illustrated the forces acting on a polymer during an imprinting process (see Figure 32).

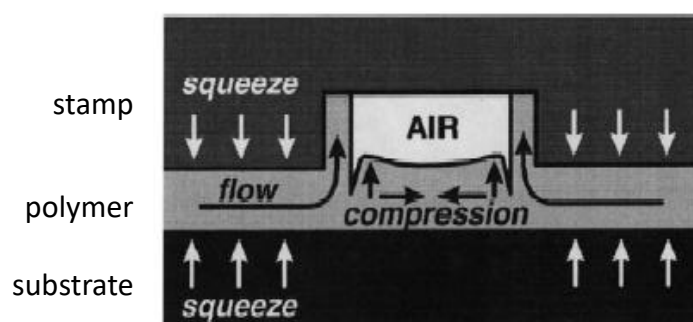


Figure 32: Schematic representation of the forces acting on the resist during the imprinting process.<sup>[117]</sup>

At first, the material is wetting the walls of the cavity and flows along them. The material in the center of the cavity is under compression and a material flow is starting to fill up the cavity. However, the material must not necessarily show a dual peak deformation but can also flow as single peak depending on factors like for example the initial film thickness or the mold geometry (see Figure 33). Rowland et al.<sup>[119]</sup> have investigated the parameters influencing the cavity filling process, such as the mold geometry, the polymers properties and film thickness by numerical simulation. Figure 33 depicts the influence of the cavity geometry and the film thickness on filling times and on the polymer deformation. For each configuration, four different polymer deformations at four different times are shown. The times indicate the start of the imprinting process  $t_i$ , the time needed to the half of the onset of filling  $t_h$ , to the onset of filling  $t_o$  and the time when the polymer has covered half the cavities roof  $t_f$ . The onset of filling is reached, when the polymer peak first touches the roof of the cavity.

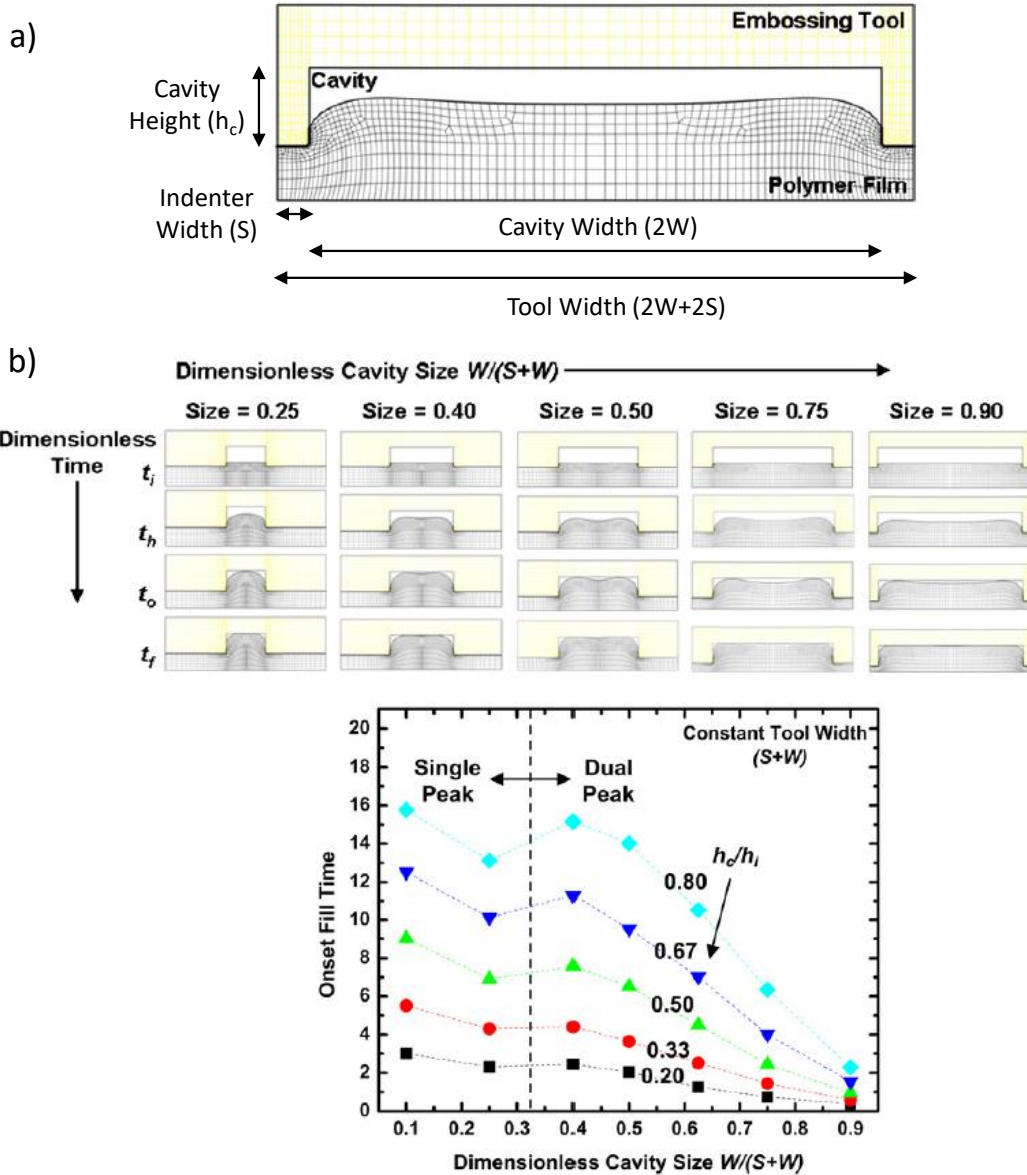


Figure 33: a) Schematic representation of an embossing tool, stamp cavity and polymer deformation in an imprinting process. Indicated are the geometrical variables in the simulation. b) Influence of the cavity geometry (indenter width and cavity height) and film thickness on the cavity filling times.

As the cavity width increases, the deformation of the polymer changes from single to dual peak deformation. The same was found for decreasing initial film thicknesses  $h_i$ . This change has an impact on the cavity filling time as the shear in the polymer is changed. When it comes to the filling speed, wider cavities will fill faster than narrower cavities at a given initial film thickness. If the ratio of cavity height to initial film thickness increases, for example if the initial film thickness is decreasing for a given cavity height, the imprinting speed will decrease significantly.

The squeeze flow underneath the indenter (raised structure) of the stamp can be expressed mathematically. If several assumptions are made, e.g. the polymer is treated as incompressible liquid and that nonslip conditions, i.e. no material velocity at solid boundaries, prevail at the stamp and substrate surfaces, an expression known as the Stefan equation is valid:

$$\frac{1}{h^2(t)} = \frac{1}{h_i^2} + \frac{2F}{\eta LS^3} t \quad (4.2)$$

with  $\eta$  being the resist viscosity,  $h_i$  the initial film thickness,  $F$  the imprinting force applied to the indenters of the mold,  $L$  being the cavity length and  $S$  the indenter width. If the final film thickness  $h_f$  ( $\equiv h(t_f)$ ) is inserted and the same pressure  $p$  underneath every single indenter is assumed, the Stefan equation yields the imprinting time  $t_f$ :

$$t_f = \frac{\eta S^2}{2p} \left( \frac{1}{h_f^2} - \frac{1}{h_i^2} \right) \quad (4.3)$$

From the equation it can be deduced that smaller indenter widths  $S$  would yield a quicker filling of the cavity. Small indenter widths in the nanometer regime would favor a quick filling in a time range of less than a second whereas micrometer-scaled indenters would yield filling times of some hours using standard NIL conditions.<sup>[113]</sup> It also becomes clear that the applied pressure has not such a big influence on the filling time as for example the cavity geometry or the initial film thickness have. Since in the case of a thick initial film the polymer can move more freely towards the cavities without being hindered by friction on the surfaces of the stamp or substrate, the imprinting process time can be significantly reduced by simply increasing the initial film thickness.<sup>[113]</sup> However this would yield in a thick residual layer, which for certain applications is undesirable. Figure 34 depicts another direct consequence from Stefan equation. With ongoing filling of the stamps cavities, the stamp continues to sink into the film but the rate is slowing down as the film thickness is decreasing from the initial film thickness  $h_0$  to the final thickness of the residual layer  $h_f$ .

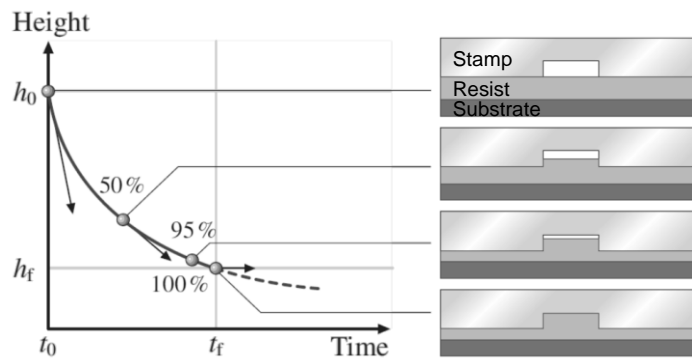


Figure 34: Right: Schematic representation of an imprinting process. Left: Film height as a function of the imprinting time.

Another very intuitive factor influencing the imprinting speed is the viscosity of the resist material. Since in t-NIL polymers are used as resist material, the viscosity is inherently high. This issue can be overcome by heating the polymer significantly above its glass transition temperature. Yet, this increases the cycle time drastically. A solution to this problem could be the use of polymers of a lower molecular weight, since the glass transition temperature is directly proportional to the molecular weight. However, polymers below a certain molecular weight would lose the entanglements, and therefore tend to be brittle and not suited for imprinting processes anymore. An elegant solution is the usage of low-molecular-weight compounds, which are able to form stable amorphous phases well above the ambient temperature. This approach is used in azobenzene-based nanoimprint lithography.

## 4.5 Azobenzene-based nanoimprint lithography

In this thesis, for the first time, a novel, straightforward method for micro- and nano-structuring of surfaces - azobenzene-based nanoimprint lithography - or “azo-NIL” is demonstrated. It will be shown, that this technique carries the potential to achieve complex 2D structures of any design while avoiding shrinking issues related to established NIL methods such as UV-NIL. Azo-NIL combines the unique ability of azobenzenes to be athermally photofluidized with the principles of nanoimprint lithography. Compared to photoresist-based imprinting methods as for instance UV-NIL, the handling of the resist is facilitated in azo-NIL. Whereas in photoresist-based processes the patterning has to be performed at controlled light conditions, imprinting with azobenzene-containing materials can be done at ambient conditions without destroying the exposure process. Typical commercial photoresists are sensitive to wavelengths below 430 nm, and thus necessarily have to be illuminated in the UV region.<sup>[115]</sup> When it comes to azobenzenes, *trans-cis-trans*-isomerization cycles, which are essential for the azobenzene-based imprinting process to take place, can be induced at any wavelength of the absorption bands of the azobenzene. This allows for the use of easier accessible and cheaper light sources. Additionally, an appropriately tailored azobenzene-containing material is not sensitive to humidity or room temperature and it tolerates overexposure. Compared to radical polymerization resins in UV-NIL, azobenzene-functionalized resists are not endangered by cure inhibition due to oxygen. In contrast to most conventional photoresists, the imprinted patterns do not need an additional wet-processing step after the exposure is finished.<sup>[115]</sup>

The basic principle of the azo-NIL process is depicted in Figure 35. In a first step, a solid amorphous azobenzene-containing film is deposited on a substrate by spin coating. The freshly prepared film is composed predominantly of azobenzene molecules in the thermodynamically stable *trans* state with a small share of molecules in the *cis* state.

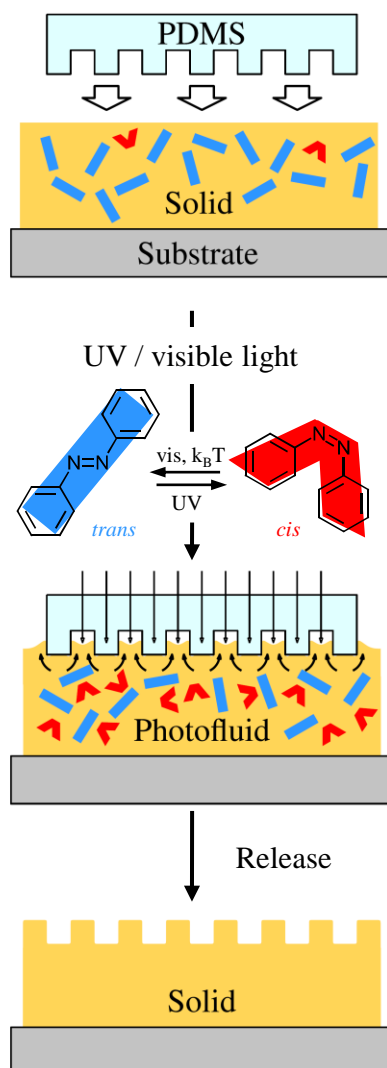


Figure 35: Schematic representation of the basic principle of azobenzene-based nanoimprint lithography.

In the next step, an elastomeric stamp (e.g. PDMS or fluorinated polymer) is placed onto the resist. When the film is illuminated with light of suitable wavelength and intensity, *trans-cis-trans*-isomerization cycles are induced causing a trembling motion of the molecules leading to a photofluidization of the material. The bulk  $T_g$  of the material, however, is unaffected by exposure.<sup>[120]</sup> Capillarity causes the resist to flow into the cavities of the stamp without the need to apply heat or pressure. At the moment the light source is switched off the material flow is terminated. After releasing the stamp the negative type pattern is imprinted into the resist. During the whole process no crosslinking occurs, so that the process could be repeated to restructure the film.

#### 4.5.1 Azobenzene-based nanoimprint lithography - setup

For the azo-NIL experiments two different setups were used as depicted in Figure 36 and Figure 37. The first setup, here referred to as “vertical setup”, is used for experiments at ambient conditions. Here, the stamp is positioned on an azobenzene film on a vertically positioned glass substrate with respect to the ground. The stamp is either fixed by adhesion forces only, or can be hold in place with magnets. During imprinting, the azobenzene-containing film is exposed through the glass substrate. Structures are imprinted using either a 488 nm diode pumped solid state laser source

(intensity:  $1 \text{ W/cm}^2$ ), an UV light LED (intensity:  $0.3 \text{ W/cm}^2$ ), a blue light LED (intensity:  $0.42 \text{ W/cm}^2$ ), or the combination of both LEDs.

### Top view:

#### „vertical setup“

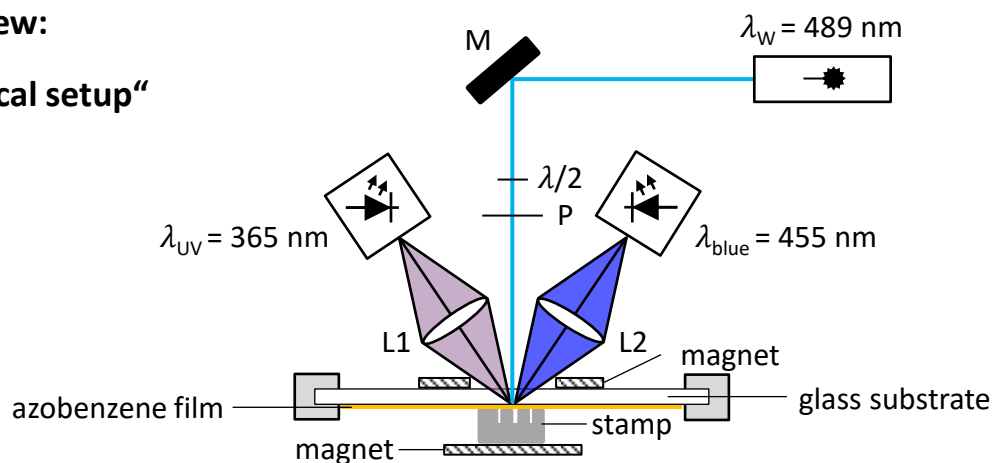


Figure 36: Scheme of the setup for nanoimprint lithography experiments at room temperature through the substrate. Two high power diodes (365 nm and 455 nm) are focused onto the sample by the lenses L1 and L2. The diode intensities at the position of the azobenzene film are  $0.3 \text{ Wcm}^{-2}$  and  $0.42 \text{ Wcm}^{-2}$ , respectively. The laser (488 nm) intensity is adjusted by a lambda half plate ( $\lambda/2$ ) and a polarizer (P) to  $1.0 \text{ Wcm}^{-2}$ . In case the stamp does not adhere to the stamp, magnets were used to hold the stamp. (top view; L1-2: focus lens, P: Polarizer, M: mirror,  $\lambda/2$ : half-wave plate, magnets are optional).

Experiments at elevated temperatures were performed using the so-called “horizontal setup” depicted in Figure 37. Here, the stamp is placed on the horizontally oriented substrate, which is positioned on a hot stage able to heat the substrate precisely to temperatures between room temperature and  $300^\circ\text{C}$ . In this setup the film is illuminated through the stamp. This is possible, since PDMS stamps are transparent to the wavelengths used in the azo-NIL experiments.

### Side view:

#### „horizontal setup“

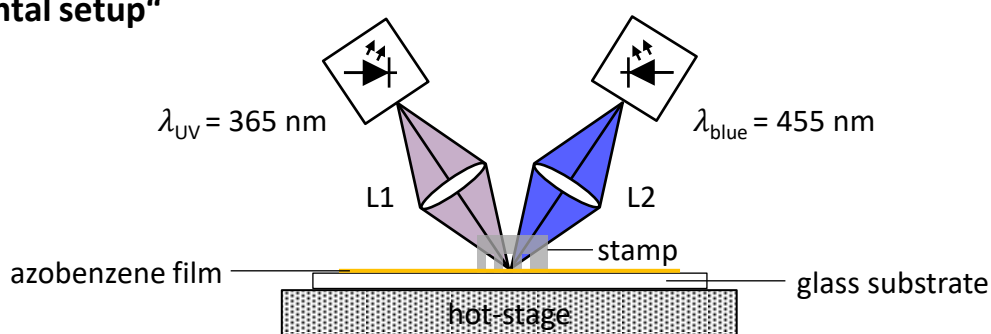


Figure 37: Scheme of the setup for temperature dependent nanoimprint lithography experiments. Exposure of the azobenzene film through the stamp (top view; L1-2: focus lens). Two high power diodes (365 nm and 455 nm) are focused onto the sample. The diode intensities at the position of the azobenzene film are  $0.3 \text{ Wcm}^{-2}$  and  $0.42 \text{ Wcm}^{-2}$ , respectively.

#### 4.5.2 Azobenzene-based nanoimprint lithography - materials

Resist materials used in conventional and established NIL techniques, e.g., t-NIL, are most often polymers with high-molecular-weight and high glass transition and melting temperatures as low-molecular-weight polymers would lower the mechanical properties of the material and thus rendering it unfitting for the use as hard resist for pattern transfer.<sup>[113]</sup> However, high-molecular-weight polymers are expected to move into small mold cavities less easily than polymers of lower molecular weight. Therefore, a trade-off in imprinting performance in terms of imprinting speed and the resists mechanical properties is inevitable. Apart from issues related to their mobility, polymers also limit the minimum feature size possible. In NIL processes, polymers with molecular weights typically of some tens of kg/mol are patterned.<sup>[121]</sup> A typical resist for t-NIL would be a PMMA polymer of a molecular weight of 25 kg/mol. If the polymer is treated as a solid sphere, one can estimate a radius of around 2 nm.<sup>[113]</sup> As polymers are normally present as coils, this approach is rather underestimating the space occupied by the polymer.

The driving force to fill the stamp with resist material in azobenzene-based nanoimprint lithography is capillary force. Due to the absence of entanglements low molecular-weight compounds are potentially low viscous materials. Additionally, the lack of entanglements leads to a more efficient mass transport in azobenzene-containing molecular glasses than in films of comparable polymers.<sup>[122]</sup> Therefore, azobenzene-functionalized molecular glasses are chosen as resist material for the investigation of the azo-NIL technique. Figure 38 shows the chemical structures of the investigated materials.

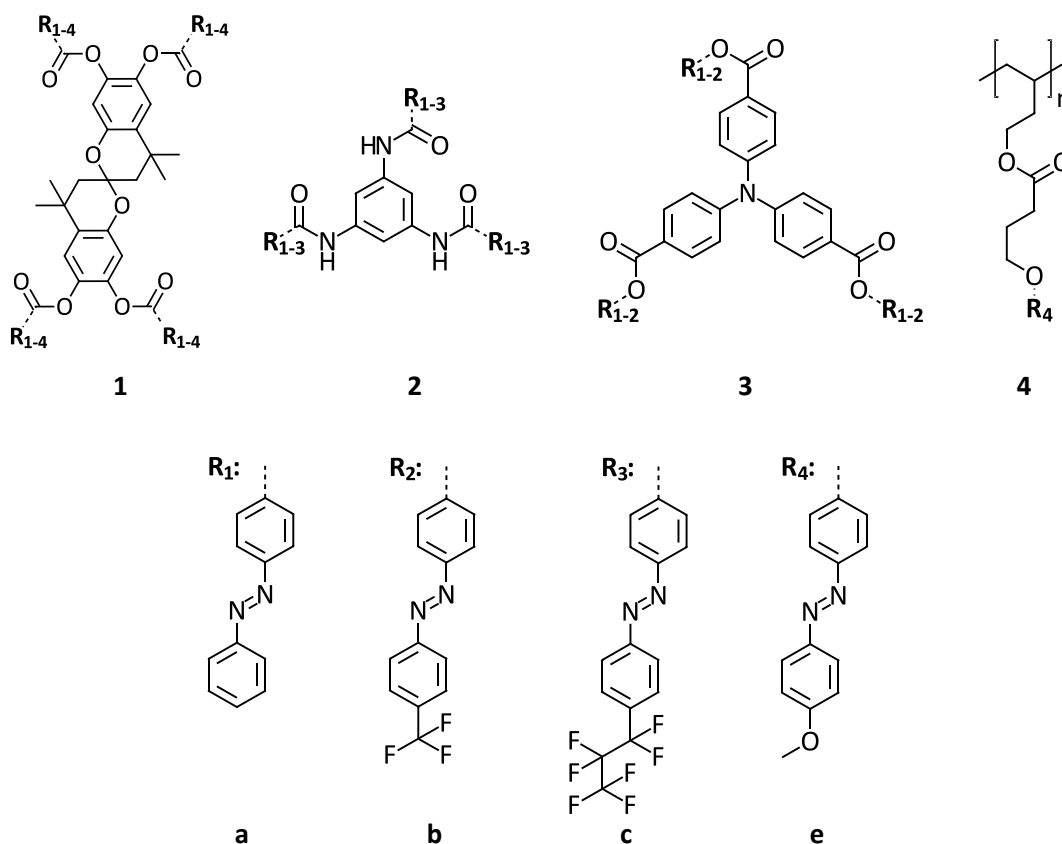


Figure 38: Top: Chemical structure of the cores of the investigated molecular glasses (1-3) and the backbone of the investigated homopolymer (4). Bottom: Chemical structures of the investigated azobenzene substituents (a-e) linked to the different cores.

In this chapter, 9 different azobenzene-functionalized molecular glasses and one azobenzene-functionalized homopolymer are investigated. The design of the azobenzene-functionalized molecular glasses features a sterically demanding core, to which 3 to 4 azobenzene units can be attached to. As described in detail in chapter 3, the three different cores of the molecular glasses have a significant impact on the properties of the molecular glass. The increasing rigidity of the core from triphenylamine- to spirobichromane-based molecular glasses leads to an increased  $T_g$  from an average of approx. 95 °C to an average  $T_g$  of around 110 °C. The intermolecular H-bonds formed in films of 1,3,5-benzenetrisamide-based compounds increase the glass transition temperature even further to a temperature of about 128 °C. This should have a significant impact on the performance in the azo-NIL process. The azobenzene moieties on the periphery of the molecular glass provide mobility upon Exposure to an appropriate wavelength and light polarization. The substituents on the para-position of the azobenzene chromophores alter the photophysical properties of the molecular glasses and influence their level of hydrophobicity and the free volume of the compounds. As substituents a hydrogen atom, a methoxy-group or perfluoroalkyl chains of different lengths have been chosen. Compared to the H-substituted azobenzenes, the electron donating methoxy substituent shifts the  $n-\pi^*$  and  $\pi-\pi^*$  absorption bands, so that both bands are located close to each other. This is expected to be advantageous for the azo-NIL process, as overlapping absorption bands are expected to allow for a continuous conversion of the azobenzene molecule upon exposure to a single wavelength being beneficial for photo-induced motion in an azobenzene film.<sup>[3]</sup> As capillary force is the driving force in the azo-NIL process, one of the most important factors influencing the filling process is the wetting behavior of the material on the material/stamp interface.<sup>[123]</sup> A material wetting the stamp well increases the speed of the filling process. However, if the wetting and therefore the interaction between the resist and the stamp becomes too high, there is a risk of destroying imprinted structures at the moment the stamp is released from the resists surface. The hydrophobicity and therefore the interactions with the stamp material are altered by introducing perfluorinated alkyl chains in para-position to the azobenzene moieties.

To investigate the influence of entanglements on the imprinting performance in azo-NIL, an azobenzene-functionalized homopolymer is chosen as reference material to the molecular glasses. The synthesis and characterization of homopolymer **4e** is shown elsewhere.<sup>[126]</sup> The azobenzene moiety was coupled to the backbone via polymer analogous reaction of the azobenzene acid chloride with the hydroxy groups. Due to its flexible poly(1,2-butadiene) backbone and the decoupling spacer, the azobenzene-functionalized homopolymer features the lowest  $T_g$  of all investigated materials (74 °C) even though the molecular weight is high ( $M_n = 3.75 \cdot 10^5$  g/mol). However, spin coating of the investigated compounds led to the formation of stable amorphous films at ambient conditions. The materials  $T_g$ s are shown in Table 3.

Table 3: Thermal properties of the investigated compounds explored with differential scanning calorimetry and polarization optical microscopy.

Compound	$T_g / ^\circ\text{C}$	$T_m / ^\circ\text{C}$
<b>1a</b>	106	249
<b>1b</b>	126	240
<b>1c</b>	-	327 <sup>1</sup>
<b>1e</b>	107	239
<b>2a</b>	136	252
<b>2b</b>	-	335 <sup>1</sup>
<b>2c</b>	-	-
<b>3f</b>	92	174
<b>3g</b>	99	146
<b>4e</b>	74	120

<sup>1</sup> Determined in polarizing microscopy experiment.

### 4.5.3 Azobenzene-based nanoimprint lithography – experimental parameters

In the following, an exemplary imprinting process and theoretical implications will be discussed. The discussion is intended to clarify and define the parameters necessary for the process of azobenzene-based nanoimprinting. Afterwards, factors influencing the imprint process will be investigated. Figure 39 shows a schematic depiction of a typical test series performing azo-NIL experiments. A stamp is positioned on an azobenzene film and is illuminated for a certain amount of time  $t_x$ . Typically, several imprinting experiments with different exposure times are performed on the same film. After the structures are imprinted, the film is investigated using e.g. scanning electron microscopy or atomic force microscopy.

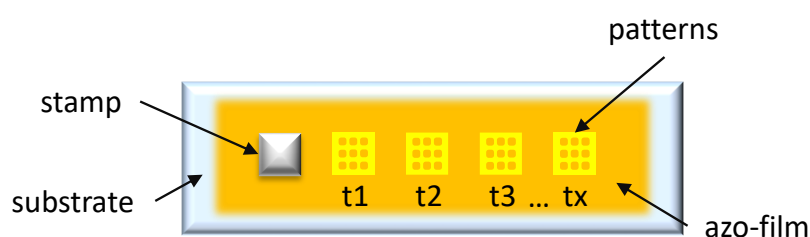


Figure 39: Schematic depiction of a typical test series performing azo-NIL experiments. A stamp is positioned on an azobenzene film and is illuminated for a certain amount of time  $t_x$ . Typically, several imprinting experiments with different exposure times are performed on the same film.

#### 4.5.3.1 Data evaluation in imprinting experiments

An exemplary imprinting process is performed using a micro-structured PDMS stamp positioned on a thin film of compound **1a** in the vertical setup using the two LEDs simultaneously. The transparent and homogenous films of compound **1a** with a film thickness of approx. 540 nm were prepared via spin-coating from a THF solution. Exposure was performed through the glass substrate using the UV light (455 nm) and blue light (365 nm) emitting LEDs at 0.3 mW/cm<sup>2</sup> and 0.42 mW/cm<sup>2</sup> for 75 s and 150 s. The imprinted structures are investigated with an atomic force microscope. From the measurement, the quality of the imprint as well as the height of the features after a given time of imprinting can be evaluated. The height of the features can be evaluated in two different ways.

Figure 40 depicts AFM images and the corresponding height profiles after 75 s and 150 s of imprinting.

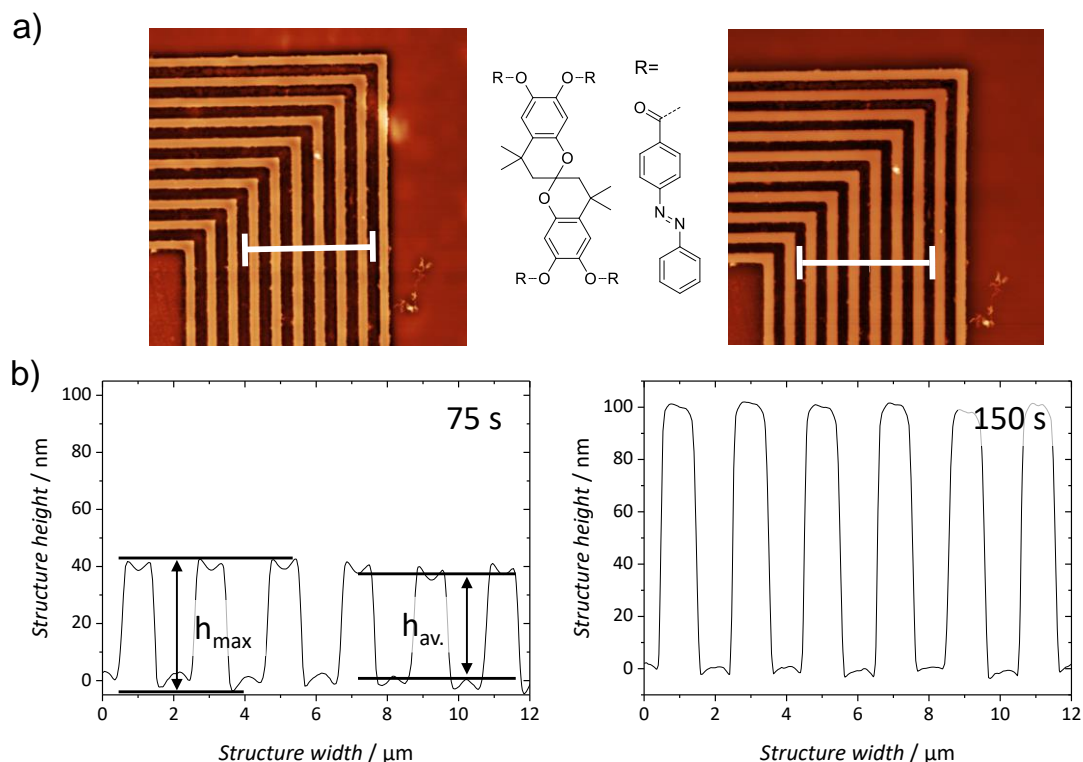


Figure 40: a) L-shaped  $\mu\text{m}$ -scaled structures imprinted into a film of compound **1a**. Film thickness approx. 540 nm. Light source: UV LED and blue light emitting LED simultaneously. Left: AFM image taken after 75 s; right: AFM image taken after 150 s. The white lines indicate the area in which the height of the structures is measured. The height profiles are averaged in the direction of the imprinted lines. b) Averaged height profiles.  $h_{\text{av}}$  is the average height and  $h_{\text{max}}$  is the maximum height of the structures.

If the resist is wetting the stamp, the material preferably moves along the walls of the cavities. During the imprinting process the azobenzene-functionalized material is in a photofluidic state and forms a meniscus in the stamps' cavities. If the maximum height of the cavities is not attained during the time period chosen for the imprinting experiment, these structures may remain. In the evaluation of the feature height, one may now choose between a maximum achieved height and an average height, which will in the following be referred to as  $h_{\text{max}}$  and  $h_{\text{av}}$  (see Figure 40 b, left).

#### 4.5.3.2 The build-up constant $\tau$

As shown before, the structure height reached at the end of an imprinting process is increasing with longer exposure times. In the following chapters, the influence of experimental parameters and the resist material on the structure height growth and structure quality will be investigated. The quantitative parameter to compare the different azo-NIL imprinting experiments is the time needed for the stamps' cavities to be filled. To compare the different imprinting experiments, the build-up constant  $\tau$  is introduced. The constant is set to a point at which about 63 % of the maximum filling height is reached. As a consequence, the build-up constants can only be directly compared among themselves if the maximum filling height of the stamp (in this thesis  $95 \pm 5$  nm for any type of stamp) is reached. Also, the maximum filling height should be mentioned when  $\tau$  is used to describe the time needed for the imprinting process, since lower final structure heights result in lower build-up

constants. If the structures grow exponentially, the results from the measurement of the structure heights can be fitted using the following equation:

$$h(t)=h_0(1-\exp(-t/\tau)) \quad (4.4)$$

where  $t$  is the exposure time,  $h_0$  is the maximum filling height. Additionally to the build-up constant  $\tau$ , a corrected build-up constant  $\tau_{\text{corr}}$  is introduced. The corrected term is the product of  $\tau$  with the quotient of the maximum theoretical filling height of 100 nm and the maximum filling height  $h_0$  and is used to increase comparability of experiments in which the maximum structure height is not reached.

In Figure 41, a typical temporal evolution of the structure growth in an azo-NIL experiment is depicted.

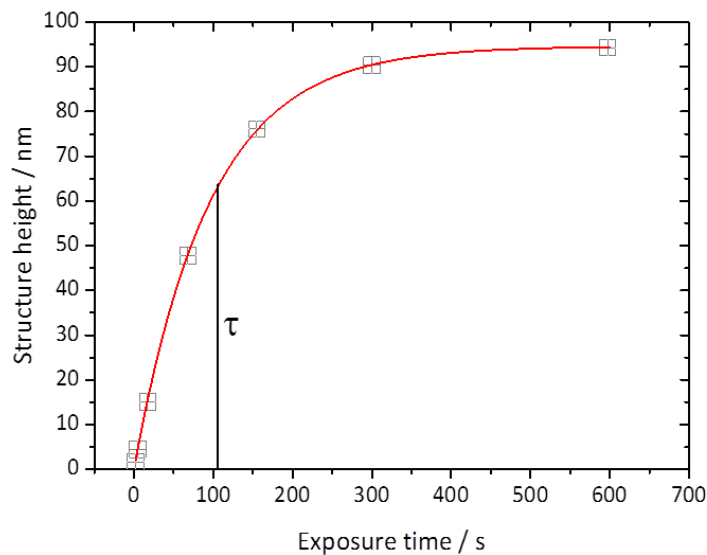


Figure 41: Typical temporal evolution of the structure growth in an azo-NIL experiment. The red line indicates the exponential fit.

#### 4.5.4 Micrometer-scale imprinting

To investigate the basic principles of the novel imprinting technique, first experiments were performed utilizing micrometer scaled patterns. In the following, the different parameters influencing the imprinting performance in the azo-NIL process, such as e.g. the fluence of the incident light, its wavelength or the film thickness are investigated utilizing micro-structured PDMS stamps.

##### 4.5.4.1 Stamp fabrication and characterization

The PDMS stamps were fabricated by casting a structured master. Here, a custom-made master featuring L-shaped line patterns with a line spacing ratio of 1:1, linewidths ranging from 1  $\mu\text{m}$  to 10  $\mu\text{m}$  (1  $\mu\text{m}$ , 1.5  $\mu\text{m}$ , 2  $\mu\text{m}$ , 2.5  $\mu\text{m}$ , 5  $\mu\text{m}$  and 10  $\mu\text{m}$ ) and a height of 100 nm was used. The patterns are distributed over an area of approx. 1  $\text{mm}^2$  (see Figure 42a).

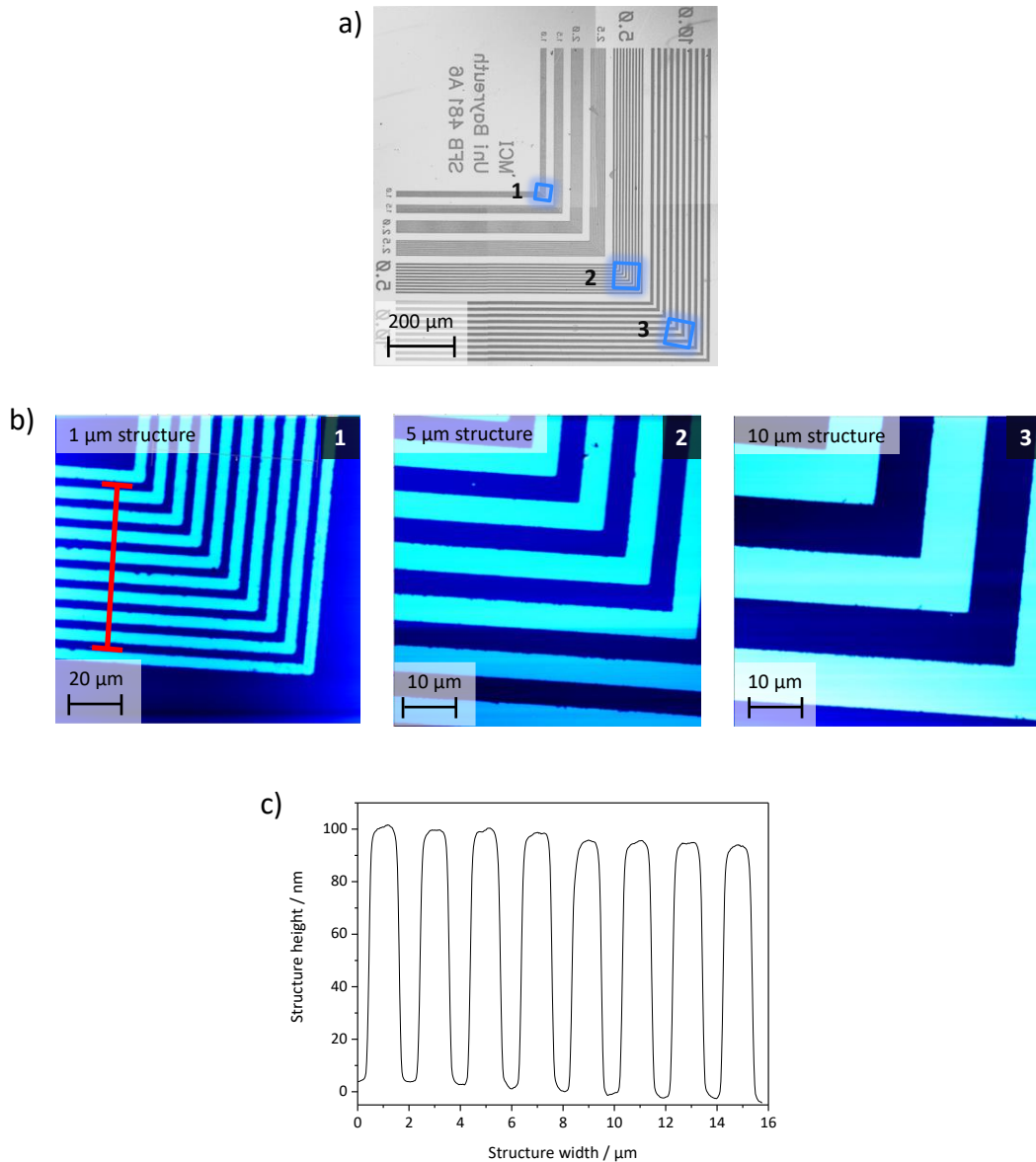


Figure 42: a: Optical micrograph of the micro-scale structured master. Dark areas: glass, bright areas: chrome layer. b: AFM micrographs of a PDMS replica. Structure sizes from left to right: 1µm, 5µm, 10µm. c: Height profile of the casted PDMS replica with a structure size of 1 µm.

The stamps (or replicas) were made from PDMS ELASTOSIL® RT 601. The two component system, consisting of a prepolymer/monomer system and a thermal initiator was mixed in a ratio of 9:1 and was then casted onto the master to crosslink at room temperature for 12 h. The crosslinking reaction was finished in a 2 h heating step at 150°C. Figure 42b shows selected AFM images of 10 µm, 5 µm and 1 µm structures in the PDMS replica. Only minor defects are visible, and the maximum achievable height of around 100 nm is attained in the replication process.

#### 4.5.4.2 Influence of the fluence on the imprinting speed

As the imprinting of structures in azo-NIL is induced by light, the influence of the fluence on the imprinting performance is investigated first. In this experiment, the L-shaped line patterns were illuminated through the vertically fixed glass substrate on which the stamp was positioned on. The film prepared from compound **1a** was illuminated for 15 s by a laser with a maximum power of  $1.0 \text{ Wcm}^{-2}$  and a beam diameter of 1.1 mm at a wavelength of 488 nm.

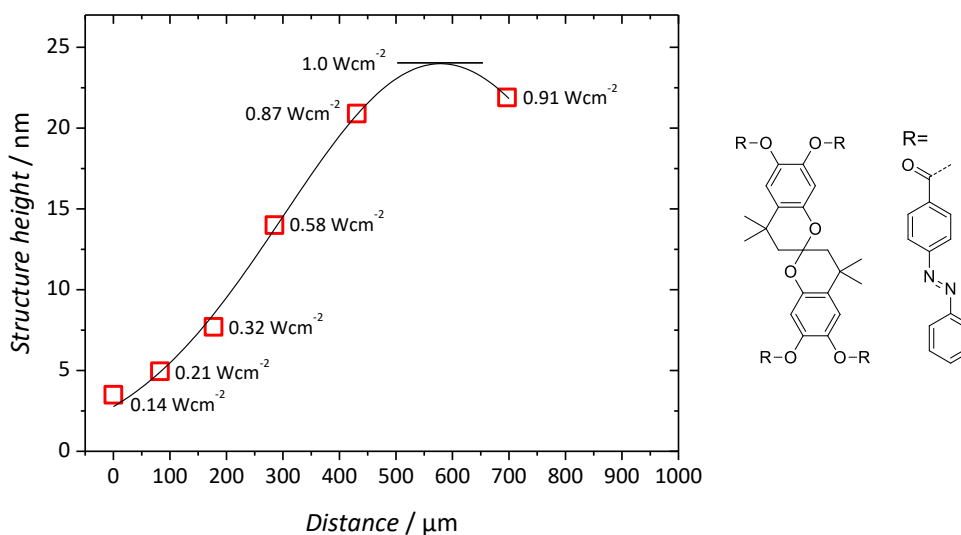


Figure 43: Influence of the fluence on the imprinting performance. Imprinted structure height after 15 seconds imprinting at room temperature as a function of the distance in which the structures were measured. The line fits a Gaussian height distribution mirroring the laser profile. Film thickness  $\approx 500 \text{ nm}$ . Compound **1a**.

In a first step, the attained structure heights in the  $1 \mu\text{m}$ ,  $1.5 \mu\text{m}$ ,  $2 \mu\text{m}$ ,  $2.5 \mu\text{m}$ ,  $5 \mu\text{m}$  and  $10 \mu\text{m}$  sized L-shaped patterns were measured using an atomic force microscope. Due to the low fluence of the laser, the stamp is filled only partially. As it turns out, the maximum attained structure heights measured at different positions of the sample can be fitted using a Gaussian function:

$$h(x) = 24 \text{ nm} \cdot \exp\left(\frac{-2 \cdot (x - 579 \mu\text{m})^2}{(557 \mu\text{m})^2}\right) \quad (4.5)$$

With: 24 nm as maximum structure height; 557  $\mu\text{m}$  as laser beam radius.

The patterned area on the stamp is about as large as  $1 \text{ mm}^2$  and the laser beam diameter is approx. 1.1 mm. As laser beams feature a Gaussian light intensity distribution, and the fit directly mirrors the intensity profile of the laser, the filling speed seems to be directly proportional to the fluence of the incident light. This finding is in good agreement with results found by Fang et al., showing the viscosity of athermally photofluidized azobenzenes to be inversely proportional to the incident intensity.<sup>[127]</sup> Already low intensities ( $0.14 \text{ Wcm}^{-2}$ ) generate a mass flow within a short period of exposure. Higher filling speeds are expected if the intensity is increased above  $1 \text{ Wcm}^{-2}$ .

#### 4.5.4.3 Influence of the pattern size on the filling performance in $\mu\text{m}$ -scaled imprinting

To investigate the influence of the pattern size on the imprinting process, a PDMS stamp featuring micrometer-scaled patterns with a size ranging from  $1\ \mu\text{m}$  to  $10\ \mu\text{m}$  was placed on a thin film containing compound **1a** spin coated on a glass substrate. Subsequently, the film was illuminated using a solid state laser at a wavelength of  $488\ \text{nm}$  and a power of  $1\ \text{W}/\text{cm}^2$  through the substrate for 4 h. To eliminate the influence of gravitational forces, the substrate is mounted vertically. Figure 44 depicts AFM images of imprinted structures of  $1\ \mu\text{m}$ ,  $5\ \mu\text{m}$  and  $10\ \mu\text{m}$  sized L-shaped patterns as well as corresponding height profiles.

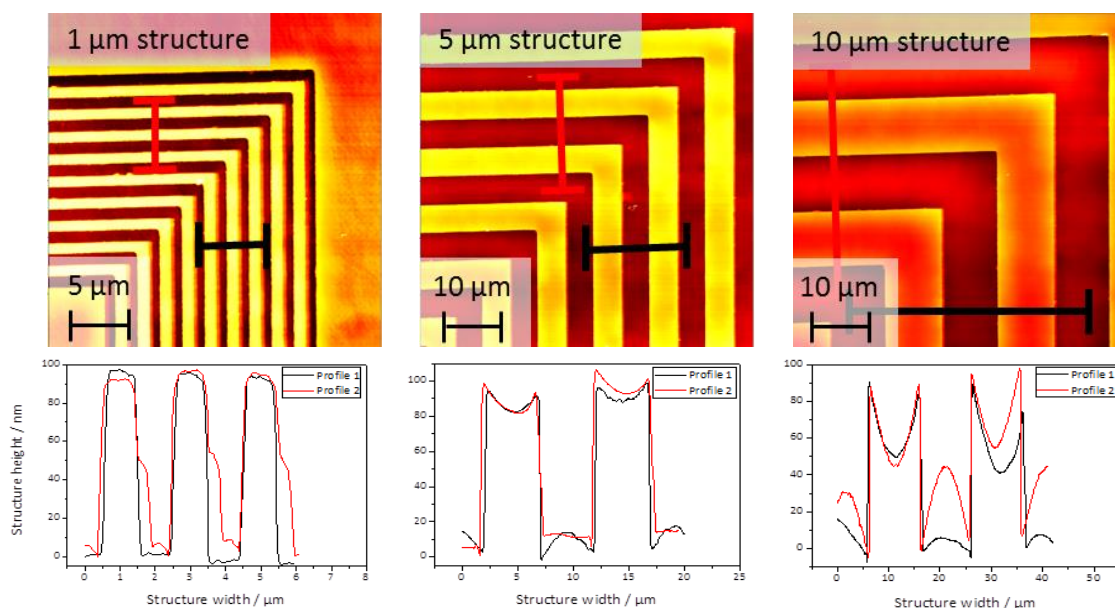


Figure 44: top: AFM micrographs of different structure sizes imprinted in the spin-coated film of **1a** (film thickness  $\approx 480\ \text{nm}$ ; light source:  $\text{Ar}^+$  laser; writing time: 4h). Structure sizes: from left to right:  $1\ \mu\text{m}$ ,  $5\ \mu\text{m}$ ,  $10\ \mu\text{m}$ . The lines indicate the area in which the height profiles were taken. bottom: Height profiles of the imprinted structure. The height is averaged in the direction of the lines.

The AFM investigation on the imprinted structures shows that imprinting of features up to at least  $10\ \mu\text{m}$  is feasible utilizing azo-NIL as imprinting technique. However, with increasing structure size, the cavities of the stamps are filled only partially and the quality of the structure wanes. In case of the  $10\ \mu\text{m}$  sized structures this effect is most pronounced. Here, the major part of the azobenzene material is located at the side of line structures. One reason for this might be a roof collapse of the PDMS stamp onto the film (see Figure 45).

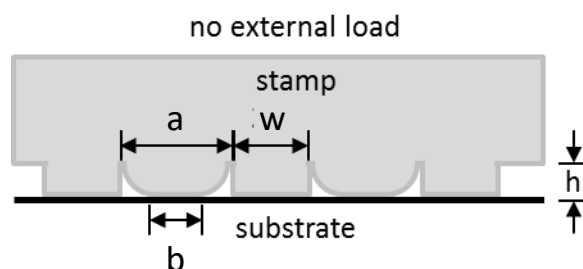


Figure 45: Schematic representation of a roof collapse of a stamp onto a surface. The collapse of the stamp onto the substrate is due to the adhesion between the stamp and substrate without an external load. With the height  $h$ , width  $w$  and spacing  $a$ . The collapse length is  $b$ . Referring to<sup>[128]</sup>.

One criterion for a roof collapse is the ratio of the pattern width  $w$  to the cavity width  $a$ . If  $w/a$  and the height of the structures are low enough, the roof collapses over the length of  $b$ . The height of the stamp cavities is 100 nm and the width is ranging between 1  $\mu\text{m}$  and 10  $\mu\text{m}$ . In our experiments, the ratio of  $w/a$  is constant. However, the ratio of the line width to the height  $h$  exceeds a critical value ( $h \ll a$ ) and the roof collapses, thus the material cannot fill the entire cavity anymore. An exact determination of the cavity height to cavity width ratio necessary for a roof collapse is difficult, since the collapse is controlled by both geometry and material parameters such as the elasticity module and interfacial surface forces.<sup>[128]</sup>

Another reason for the partial filling of the stamp might also be the intensity distribution of the incident laser beam (see section 4.5.4.1 for more details).

#### 4.5.4.4 Influence of the light source on the imprinting speed

To investigate the influence of the wavelength on the imprinting process, two high-power LEDs with peak emission wavelengths of 365 nm and 455 nm as well as a laser (488 nm) were utilized in the following imprinting experiments. These light sources feature wavelengths located at the  $\pi$ - $\pi^*$  and  $n$ - $\pi^*$  absorption bands of the azobenzene moiety (see Figure 46).

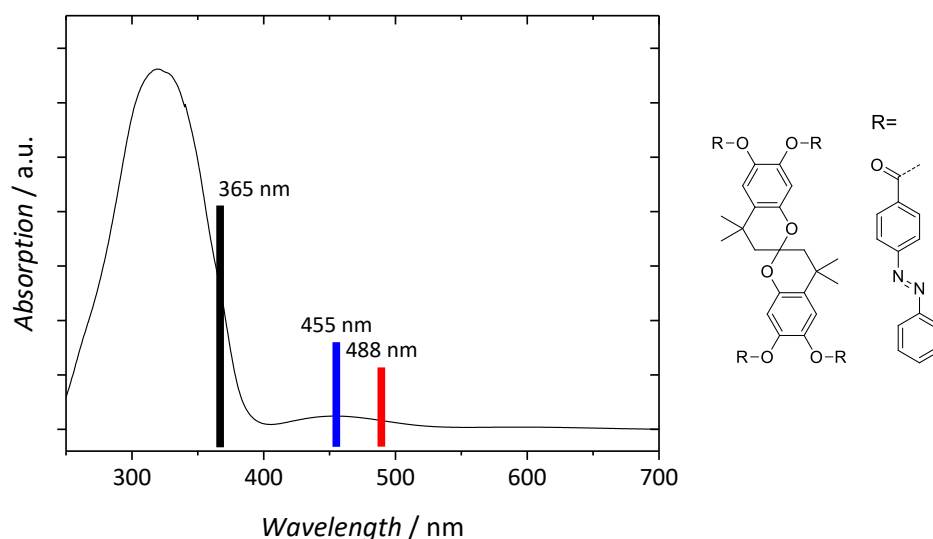


Figure 46: UV/Vis spectrum of a spin coated film of compound **1a** with 500 nm thickness. The wavelengths of the light sources used are depicted as colored lines.

The influence of the wavelength is assessed on films of compound **1a**, which were exposed at different spots for a time period of 15 s to 3600 s and subsequently AFM measurements of the imprinted 1  $\mu\text{m}$  lines were performed at each individual spot. Figure 47 shows that the average structure heights are increasing with increasing exposure time until a plateau is reached. The quick filling of the cavities at the beginning is slowing down when the cavities are filled to 60-70 % of the maximum structure height. The resulting exponential curve shape is in accordance with the theory of squeeze flow of polymers in a conventional t-NIL process (see chapter 4.4).

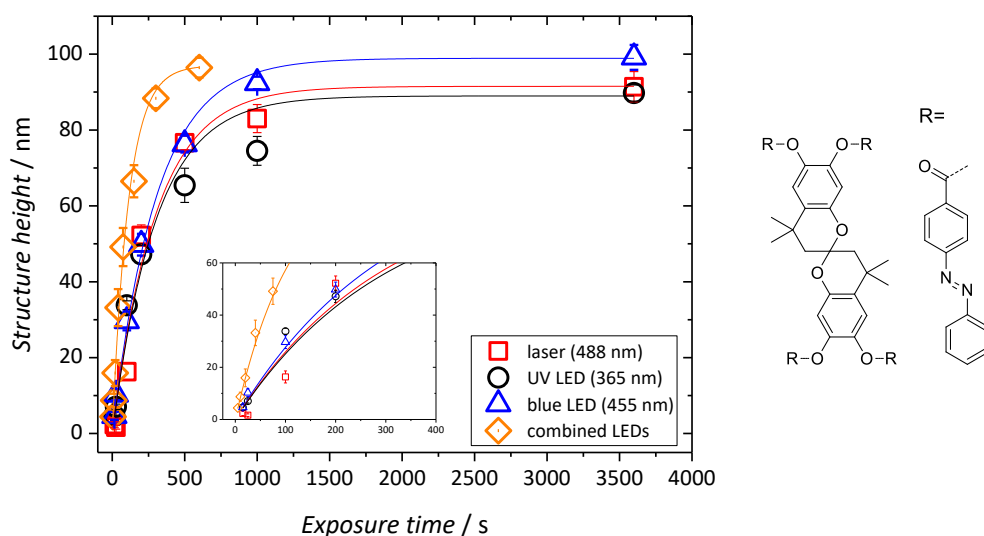


Figure 47: Imprinted structure heights as function of the exposure time for different light sources in films of compound **1a** (film thicknesses: 480-590 nm). The inset shows the first 400 s of the plot enlarged.

The structures of the stamps were filled up to about 90 % within 500 s in any case. The build-up constants are remaining almost constant at values of about 300 s ( $\tau_{UV LED}=301$  s,  $\tau_{blue LED}=305$  s,  $\tau_{laser}=301$  s). The UV and blue LED were operated at their maximum intensities of 0.3 and 0.42  $Wcm^{-2}$ , respectively. The laser needs about twice the power (1  $Wcm^{-2}$ ) to reach the same filling speed as its emitted wavelength is located at the edge of the azobenzenes absorption band (see Figure 48). Exposure at a wavelength in the region of the  $\pi-\pi^*$ -absorption peak predominantly populates the *cis* state, whereas visible light of a wavelength around the  $n-\pi^*$ -absorption peak results in a *trans*-rich state. Therefore, biphotonic exposure, i.e. simultaneous exposure of the azobenzenes in both regions of the absorption bands, may increase the *cis-trans*-isomerization cycle rate and consequently the imprinting speed. With an overall power of 0.72  $Wcm^{-2}$  the time constant decreases to  $\tau_{combined LEDs}=112$  s.

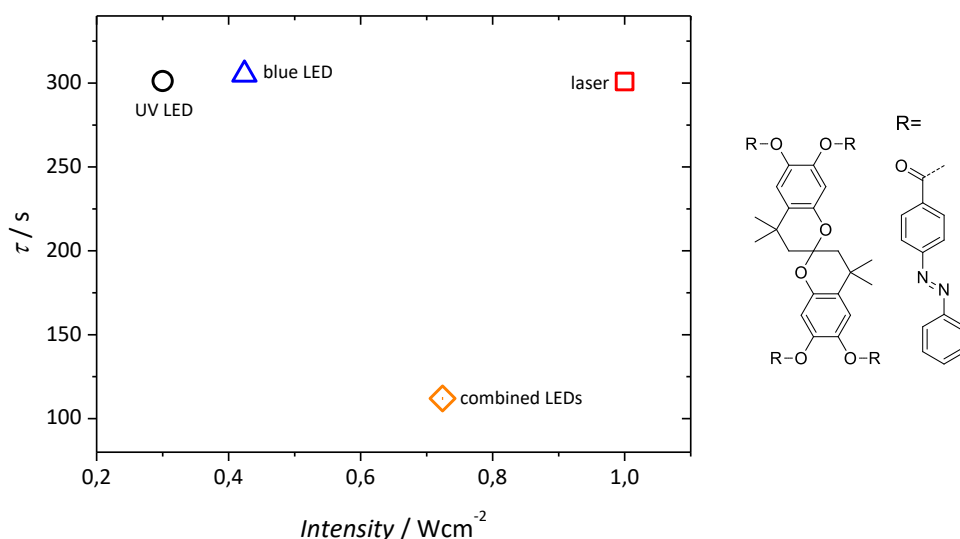


Figure 48: Built-up constants  $\tau$  obtained from fits in Figure 39.

From the Gaussian height distribution of the inscribed structures (see Figure 43, chapter 4.5.4.2), it can be concluded that the structure height  $h$  is proportional to the fluence  $F$ , which is the product of intensity  $I$  and irradiation time  $t$ . This is correct as long as the imprinted structure heights are

small compared to the depth of the indentations of the stamp. Because the stamp geometry confines the structure height, an exponential behavior at longer times is observed. At short times  $h(t) = h_0(1 - \exp(-t/\tau)) \approx h_0 t/\tau = C \cdot F = C \cdot I \cdot t$  applies. Therefore, the time constant  $\tau(I) = h_0/(CI)$  is inversely proportional to intensity of a light source. Because the maximum height  $h_0$  and  $C$  are constant,  $\tau'$  at a different intensity  $I'$  can be calculated by:

$$\tau'(I') = I/I' \cdot \tau(I) \quad (4.6)$$

It can be derived that 1  $\mu\text{m}$  structures have a built up constant of  $\tau'_{\text{UV LED}} (0.72 \text{ Wcm}^{-2}) = 125 \text{ s}$  if irradiated with an UV-LED of same intensity as the combination of both LEDs ( $0.72 \text{ Wcm}^{-2}$ ). A blue LED of this intensity will cause a longer built up time  $\tau'_{\text{blue LED}} (0.72 \text{ Wcm}^{-2}) = 178 \text{ s}$ . Even though the effect is rather low in case of the exposure with UV light, these results imply that the performance of the azo-NIL imprinting process can be improved by biphotonic exposure. Table 4 summarizes the experimental data and results of the experiments performed to investigate the influence of the light source on the imprinting performance in azo-NIL.

Table 4: Summarized experimental series with wavelength used, film thickness,  $h_0$ , build-up constant  $\tau$  and the corrected build-up constant  $\tau_{\text{corr}}$ .

Compound	Wavelength (light source) / nm	Film thickness / nm	Maximum filling height / nm	Build-up $\tau$ / s	Build-up $\tau_{\text{corr}}$ / s
1a	488 (laser)	480	98.9	301	304
1a	455 (blue LED)	490*	91.5	305	333
1a	365 (UV LED)	505*	88.9	301	339
1a	365 and 455 (biphotonic)	505	97.0	112	115

\* Since the experiment had to be performed on two separate substrates, the film thickness is an average of two film thicknesses.

In case of the experimental series investigating the influence of the wavelength used for exposure, the corrected build-up constant is not differing significantly from the uncorrected term. Still, biphotonic exposure is increasing the effectiveness of the process.

#### 4.5.4.5 Influence of the films thickness on the imprinting speed

Most micro- and nanopatterning applications require post processing procedures, such as etching steps, in which a thin residual resist layer is advantageous.<sup>[129]</sup> This means that the film thickness has to be adjustable without impairing the feasibility of the imprinting process. For conventional NIL processes, such as t-NIL, the Stefan equation is valid (see chapter 4.4). As a direct consequence of that equation, one can conclude that decreasing the film thickness leads to a significant increase in the filling time. The effect of the variation in the film thickness on the imprinting speed in azo-NIL is investigated in a series of samples with different film thicknesses. The imprinting process was carried out on films ranging in film thickness from 55-790 nm using both LEDs simultaneously for exposure. Plotting the maximum structure height against the exposure time as a function of the film thickness reveals an exponentially decaying curve trend for any film thickness investigated (see Figure 49 a). The films with a thickness of 505 nm and 790 nm reach the maximum achievable structure height within the time period investigated. For films with thicknesses below 360 nm, the

maximum achievable height of  $95 \pm 5$  nm is not attained anymore. However, for longer exposure times 100 nm could be reached even at this film thickness. Below 180 nm the structure height exponentially decays towards a plateau value for long exposure times and the theoretical maximum structure height of around 100 nm might not be reached anymore even for longer imprinting times. Figure 49 b shows that the structure height reached after 600 s is increasing linearly with the initial film thickness. At an initial film thickness of around 400 nm the maximum structure height is reached. The linear fashion of the initial increase in structure height allows for a simple estimation of attainable structure heights for any film thickness under these experimental conditions.

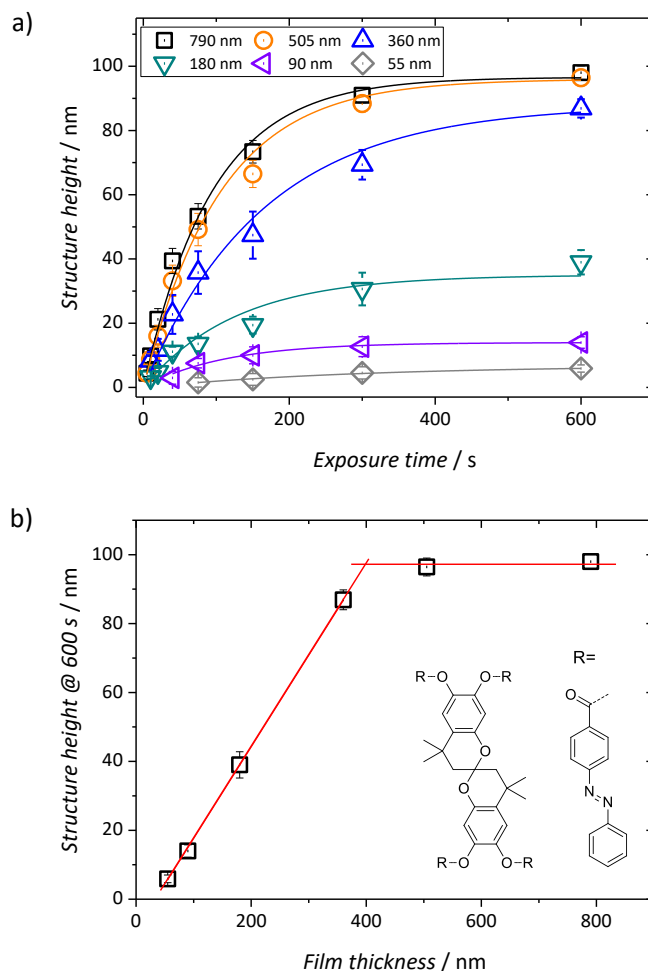


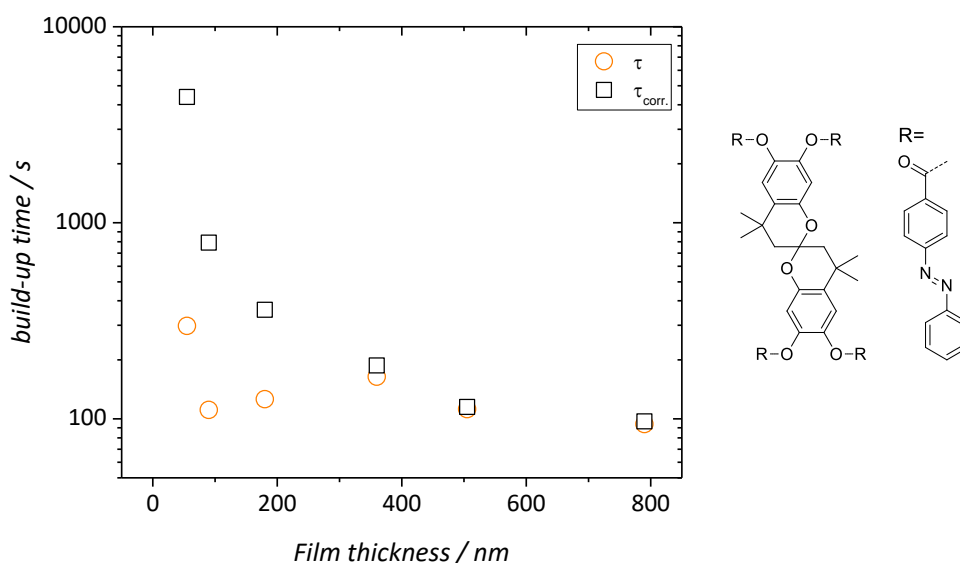
Figure 49: a) Structure height as a function of exposure time in films with varying film thicknesses of compound **1a**. b) Structure height reached after 600 s as a function of the film thickness. The line indicates a linear fit. Light source used for these experiments are combined blue and UV LED (combined power:  $0.7 \text{ W/cm}^2$ ). Structure width is  $1 \mu\text{m}$ ; stamp materials: PDMS. Film thicknesses vary from 790 nm to 55 nm. The chemical structure of the compound used for the series is depicted as inset in b).

Table 5 summarizes the data of the investigation of the influence of the initial film thickness on the imprinting speed.

Table 5: Summarized experimental series with film thickness,  $h_0$ , build-up constant  $\tau$  and the corrected build-up constant  $\tau_{\text{corr}}$ .

Compound	Film thickness / nm	Maximum filling height / nm	Build-up $\tau$ / s	Build-up $\tau_{\text{corr}}$ / s
<b>1a</b>	790	96.6	94	97
<b>1a</b>	505	97.0	112	115
<b>1a</b>	360	87.9	164	187
<b>1a</b>	180	35.0	126	360
<b>1a</b>	90	14.0	111	792
<b>1a</b>	55	6.8	298	4382

As expected, the time to fill up the structures is decreasing with increasing structure height. In this series of experiments, however, the maximum structure height is not reached within 600 s in most cases. Interpreting the build-up constant  $\tau$  is therefore misleading, as it only reflects the time needed to reach around 63 % ( $1-(1/e)$ ) of the maximum structure height in the respective experiment and neglects the theoretical structure maximum of 100 nm. The term  $\tau_{\text{corr}}$  reflects this issue and is the product of  $\tau$  with the quotient of the theoretical structure maximum of 100 nm and the maximum structure height attained in the experiment  $h_0$ . Figure 50 depicts  $\tau$  and the corrected term of the build-up constant  $\tau_{\text{corr}}$  as a function of the film thickness.

Figure 50:  $\tau$  and the corrected build-up constant  $\tau_{\text{corr}}$  as a function of the film thickness. Note the logarithmic scale.

The corrected term of the build-up time  $\tau_{\text{corr}}$  is decreasing with the initial film thickness in an exponential fashion, while  $\tau$  shows no clear trend as soon as the theoretical maximum of the structure height is not reached anymore. For the sake of better comparability of experiments, the corrected term of  $\tau$  has to be used as soon as the structure height achieved is deviating too strongly from 100 nm. Interpreting the corrected term, it can be concluded that the time needed for imprinting is not changing significantly anymore after the film thickness exceeds 500 nm. If possible, the initial film thickness in the upcoming azo-NIL experiments are therefore set to a value of around

500 nm. The lowered imprinting speed for thinner films seems to be a direct consequence of the Stefan equation. Here, the same exponential decay in the imprinting speed with decreasing initial film thicknesses could be observed (see Figure 34). In films thinner than 360 nm increasingly pronounced influence of surface/molecule interactions change in the flow dynamics<sup>[130]</sup> and are hampering the mass transport of the molecules into the structures of the stamp in case of thin films.

#### 4.5.4.6 Influence of the setup on the imprinting performance

Another parameter that may influence the imprinting process is the difference in the two setups used for the azo-NIL experiments performed in this thesis. The setups are schematically depicted in chapter 4.5.1. Due to the different orientations of the azobenzene film, the gravitational force acts in different directions in both setups. Additionally, in the “vertical setup”, in which the substrate is mounted vertically with respect to the ground, the incident light has to travel through the entire azobenzene film before it reaches the surface on which the stamp is located. In the “horizontal setup”, however, the light beam has to travel through the stamp and may be deflected. The influence of the setup was examined using an approx. 500 nm thick film and biphotonic exposure with the UV LED (at 365 nm) and blue LED (at 455 nm) simultaneously (see Figure 51). Despite the slight deviations in the curves, no difference in the build-up time constant  $\tau$  was found.

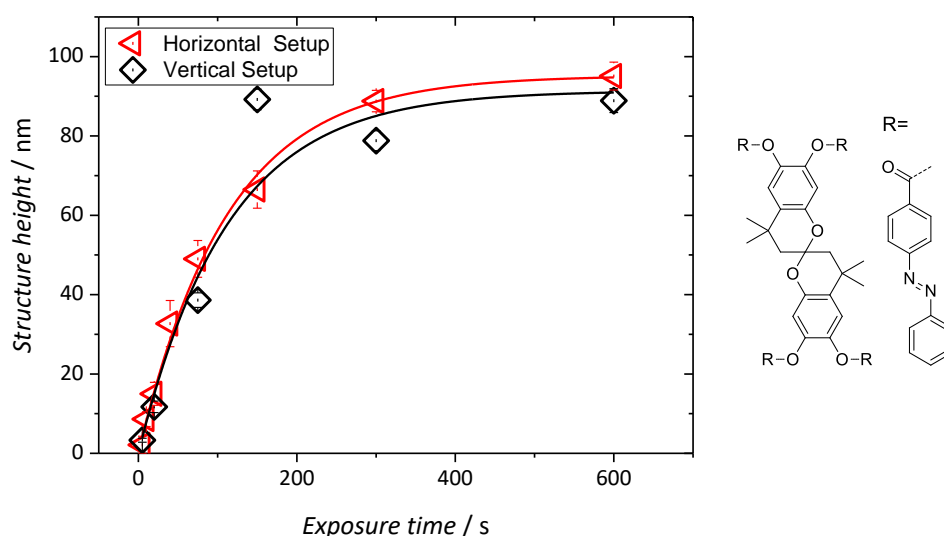


Figure 51: Influence of the nanoimprint setup on the imprinting speed investigated with identical light sources (UV LED and blue LED) at room temperature investigated on compound 1a. Film thickness 505 nm (horizontal setup) and 590 nm (vertical setup).

## 4.6 Influence of the resist material on the imprinting performance

In the following, the influence of the resist material on the azo-NIL process is investigated. As resist material, triphenylamine-, 1,3,5-benzenetrisamide and spirobichromane-based azobenzene-functionalized molecular glasses are investigated. Figure 52 shows the schematic molecular structure of the investigated compounds. The rigidity of the molecule core is increasing from the triphenylamine- over the 1,3,5-benzenetrisamide to the spirobichromane-based compounds. As a consequence the glass transition temperature is increasing in this order. However, since in the 1,3,5-benzenetrisamide-based molecular glasses secondary intermolecular interactions are introduced, these compounds feature the highest  $T_g$ s.

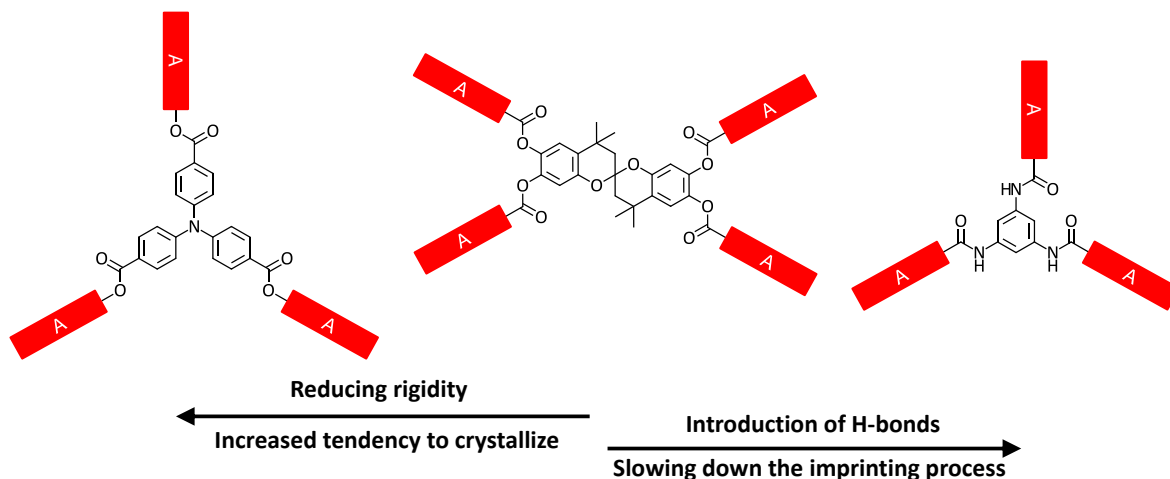


Figure 52: Schematic representation of the synthesized azobenzene-functionalized molecular glasses investigated in this chapter. The rigidity of the molecule cores is decreasing from spirobichromane-based to triphenylamine-based molecular glasses. In case of 1,3,5-benzenetrisamide derivatives, intermolecular H-bond-formation capability is introduced. The red rectangles represent the azobenzene chromophores.

As reference material to the azobenzene-functionalized molecular glasses, a photo-orientable homopolymer with a molecular weight of  $3.75 \cdot 10^5$  g/mol and a  $T_g$  of  $74^\circ\text{C}$  has been chosen. The azobenzene moieties attached to the flexible backbone carry methoxy groups.

### 4.6.1 Azobenzene-functionalized homopolymer

In contrast to low-molecular-weight compounds, polymers with a sufficient chain length can form entanglements. Entangled polymers are physical networks with an increased viscosity compared to compounds of lower molecular weight. Thus, the mobility of high-molecular-weight polymers is constrained. For this reason, molecular glasses have been chosen as ideal material for the azo-NIL process in which a high mobility of the molecules is desired to achieve low imprinting times. Since this method is so novel and the performance of polymers in azo-NIL has not yet been investigated, a series of imprinting experiments has been carried out (see Figure 53).

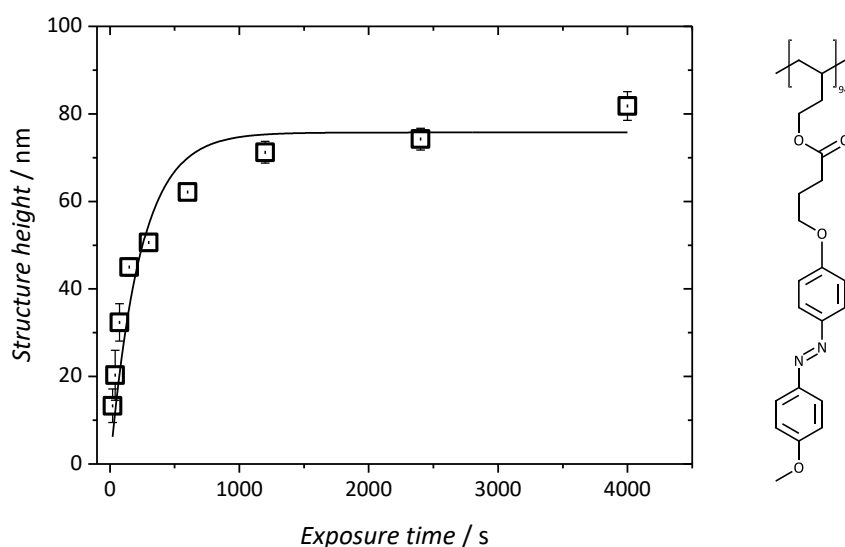


Figure 53: Heights of imprinted structures as function of the exposure time for different light sources in films of polymer **4e** (film thicknesses: 350 nm). The chemical structure is depicted besides the plot. The structures were imprinted using biphotonic exposure at wavelengths of 365 nm and 455 nm at a power of  $0.3 \text{ mWcm}^{-2}$  and  $0.42 \text{ mWcm}^{-2}$ , respectively.

Because both compounds have identical azobenzene moieties, the photophysical preconditions are comparable to low-molecular-weight compound **1e**. The molecular weight  $M_n$  of polymer **4e**, however, is  $3.75 \cdot 10^5 \text{ g/mol}$ , thus roughly 300 times higher than the molecular weight of compound **1e**. Yet, the glass transition temperatures of both compounds is in a comparable temperature range ( $T_{g(4e)} = 74^\circ\text{C}$ ,  $T_{g(1e)} = 107^\circ\text{C}$ ). Despite the high molecular weight of the polymer, the cavities of the stamp are filled in a relatively short period of time. The build-up constant of just 234 s is attributed to the flexible polymer backbone and the spacer decoupling the azobenzene moiety from it. However, the maximum filling height has not exceeded a value of 82 nm, thus the corrected build-up of 308 s is more accurate to assess the performance of the polymer. Figure 54 depicts an exemplary AFM image of the pattern imprinted in a thin film of polymer **4e** and a vertical section generated from this image.

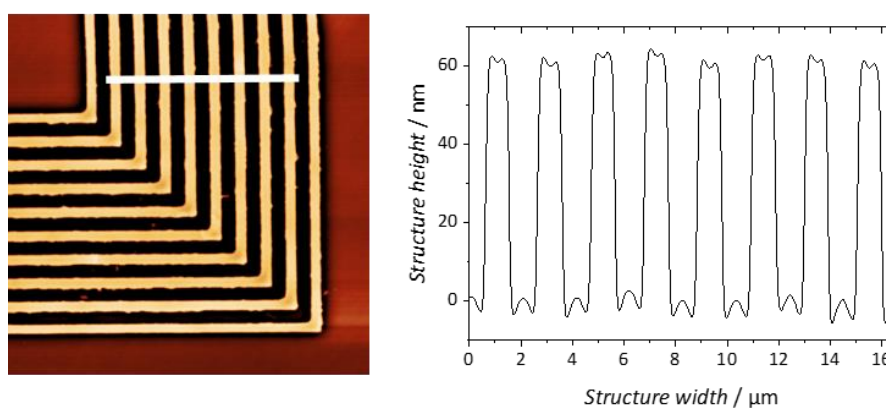


Figure 54: Left: AFM image of imprinted micrometer-scaled L-shaped patterns in a thin film of polymer **4e** (film thickness: 350 nm). The structure was imprinted for 600 s using biphotonic exposure at wavelengths of 365 nm and 455 nm at a power of  $0.3 \text{ mWcm}^{-2}$  and  $0.42 \text{ mWcm}^{-2}$ , respectively. The white line indicates the area in which the vertical section was generated. Left: Vertical sections were generated from the AFM images above.

The polymer compound shows the same filling behavior as the equivalent low-molecular-weight compound **1e**. Since the polymer has a good solubility in THF, no crystallites are visible. Also, no crystallization occurs even after long exposure times. DSC experiments have shown that **4e** tends to recrystallize when the glass transition temperature is reached. This is a proof that the macroscopic temperature is not raised to such high values.

#### 4.6.2 Azobenzene-functionalized triphenylamine-based derivatives

As the first material to investigate the influence of the resist on the azo-NIL process, the flexible triphenylamine-based derivatives are examined. The low-molecular-weight materials have been chosen and synthesized to have high imprinting speeds. The flexible molecule core is expected to increase the mobility of these molecular glasses and therefore the imprinting speed even further. As an indicator for a high filling speed in azo-NIL, the performance in SRG experiments can be applied. The compounds **3f** and **3g** were reported to have relatively low built-up constants, i.e. a high SRG-built up speed while still fulfilling the requirement to have a  $T_g$  higher than  $80^\circ\text{C}$ .<sup>[92]</sup> Figure 55 shows imprinted  $1\ \mu\text{m}$  sized L-shaped structures in thin films of **3f** (film thickness 500 nm) and **3g** (film thickness 750 nm). The film has been illuminated using the blue LED at 455 nm and the UV LED at 365 nm at the same time. For the experiments, a PDMS stamp has been used. The AFM images were taken after 600 s of imprinting. They suggest that in both experiments a crystallization of the material has taken place upon irradiation.

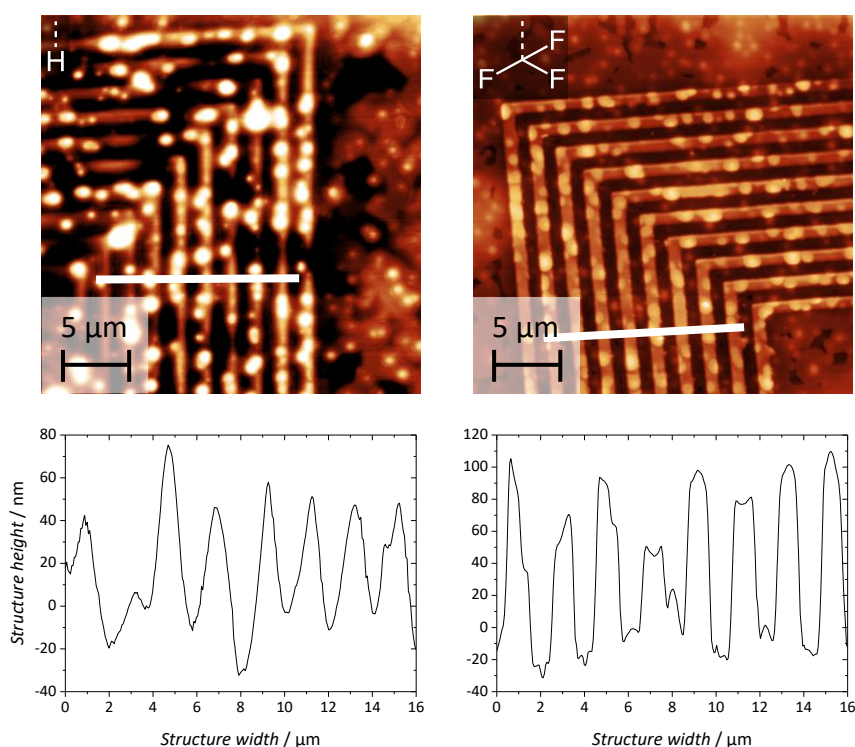


Figure 55: Top: AFM images of imprinted micrometer-scaled L-shaped patterns in thin films of the triphenylamine compounds **3f** (film thickness: 500 nm, left) and **3g** (film thickness: 750 nm, right). The structures were imprinted for 600 s using two LEDs at wavelengths of 365 nm and 455 nm at a power of  $0.3\ \text{mWcm}^{-2}$  and  $0.42\ \text{mWcm}^{-2}$ , respectively. The substituent attached to the azobenzene moiety is depicted on the top left corner of each image. The white line indicates the area in which the vertical section was generated. Bottom: Vertical sections were generated from the AFM images above.

The 3D AFM images show the poor quality of the annealed thin films of both triphenylamine derivatives on the microscopic scale (see Figure 56). In case of the thin film of **3f**, small several

micrometers wide dents with a height of a few nanometers up to 200 nanometers are visible on the 3D AFM image, which might be caused by impurities on the glass substrate. The amorphous phase of compound **3g** featuring the CF<sub>3</sub> substituted azobenzene moieties is more stable than the unsubstituted equivalent **3f**. The film quality of **3g** still is not perfect, neither on the macroscopic nor on the microscopic scale. Even though no crystallization occurs, small holes have formed leading to slightly grayish appearance of the film on the macroscopic scale. The small holes are most likely a consequence of dewetting of the material on the glass substrate. This issue could be solved by changing the solvent or altering the polarity of the surface of the substrate. Since the material crystallizes during biphotonic exposure, no further effort has been made into solving it.

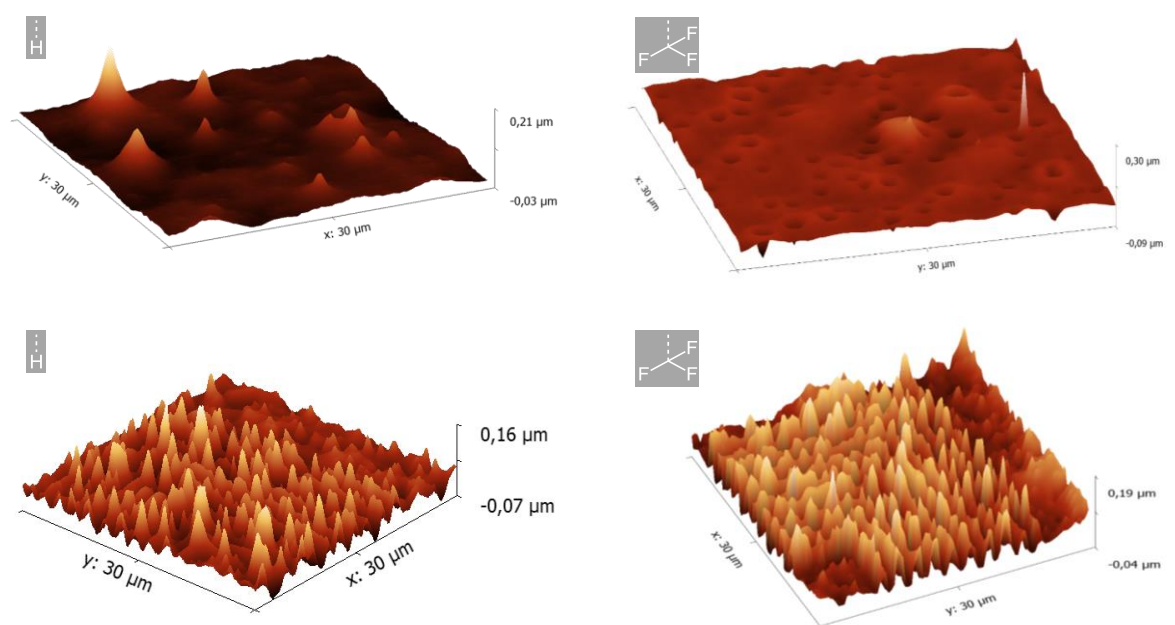


Figure 56: Top: 3D AFM images freshly prepared and annealed thin films of triphenylamine compounds **3f** (film thickness: 500 nm, left) and **3g** (film thickness: 750 nm, right). Bottom: 3D AFM images of imprinted micrometer-scaled L-shaped patterns. The structures were imprinted for 600 s using two LEDs at wavelengths of 365 nm and 455 nm at a power of 0.3 mWcm<sup>-2</sup> and 0.42 mWcm<sup>-2</sup>, respectively.

Both triphenylamine compounds have shown not to be suitable for the use in azo-NIL. The crystallization upon exposure is partly attributed to the high flexibility of the molecule core, which can promote mobility but also packing. Therefore, a new class of compounds with a more rigid core is investigated in the next section.

#### 4.6.3 Azobenzene-functionalized 1,3,5-benzenetrisamide-based derivatives

In the following the trisamide derivative with H-substituted azobenzene moieties (**2a**) as well as the equivalent derivatives with CF<sub>3</sub> (**2b**) and perfluoropropyl substituents (**2c**) in para-position to the azo-group are investigated in azo-NIL imprint experiments. The trisamide core is more rigid than the triphenylamine core and the amide bonds introduce stabilizing secondary interactions. Therefore, a more stable amorphous phase is expected and no crystallization should occur during exposure.

All trisamide derivatives synthesized in this work could be processed to amorphous thin films with films of good optical quality. Into these films, micrometer-scaled L-shaped patterns were imprinted using a PDMS stamp and the two LEDs with wavelengths of 365 nm and 455 nm simultaneously.

The setup used for this series of experiments was the setup here referred to as ‘vertical setup’, in which the substrate is positioned vertically and the film is illuminated through the stamp. The thickness of films of **2a** was around 250 nm. The films of the other two derivatives attained a thickness of around 500 nm. Figure 57 depicts the structure heights reached in the described azo-NIL experiment as a function of the exposure time for the three different trisamide compounds.

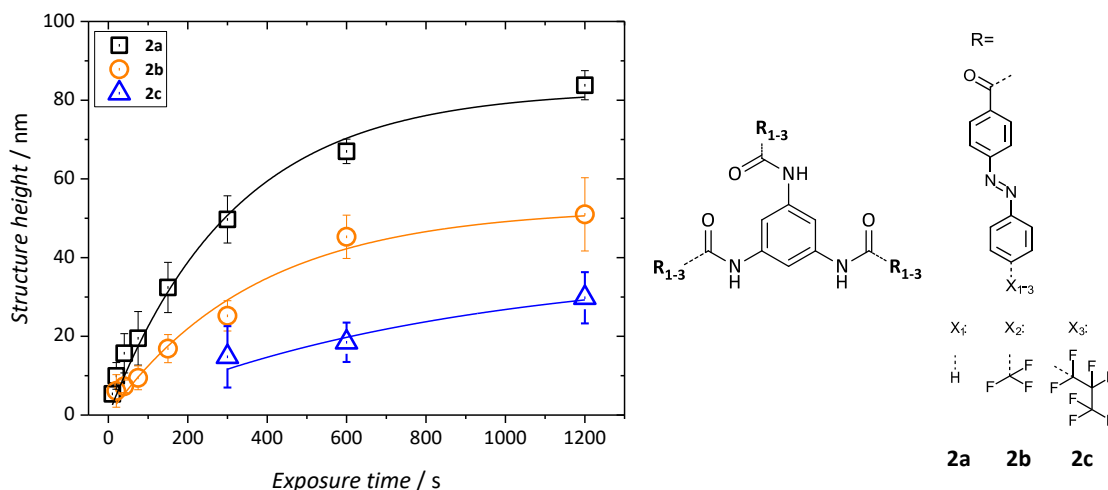


Figure 57: Heights of imprinted structures in films of trisamide compounds **2a-2c** (film thicknesses: 250 nm (**2a**), 500 nm (**2b**) and 430 nm (**2c**)) as function of the exposure time. The chemical structure is depicted besides the plot. The structures were imprinted using biphotonic exposure at wavelengths of 365 nm and 455 nm at a power of  $0.3 \text{ mWcm}^{-2}$  and  $0.42 \text{ mWcm}^{-2}$ , respectively.

Although the imprinting process is slower than under ideal conditions, the imprinting of micrometer-scaled structures into the 250 nm thick films of **2a** was successful and the maximum structure height attained is about  $84 \text{ nm} \pm 3 \text{ nm}$ . The compounds carrying perfluoroalkyl chains do not reach the maximum filling height within 1200 s. After the imprint process compound **2b** reaches an imprinting height of around 51 nm, whereas **2c** attains a height of about 30 nm. In case of the perfluoropropyl-substituted azobenzene carrying compound **2c**, no structures could be detected under 300 s. There are two possible reasons that may explain this phenomenon. On the one hand, the fluorination of the compounds could have led to a decreased wetting of the PDMS stamp. As the time to fill up the cavities is inversely proportional to the contact angle, this would lead to a decreased filling speed. On the other hand, the bulkiness of the fluorinated substituents could have caused a decrease in the isomerization rate of the azobenzene. Table 6 summarizes the data of the performance of 1,3,5-benzenetrisamides in azo-NIL. The high build-up constants of **2b** and **2c**, show that the perfluorinated substituents hinder the imprint process and lead to a drastic decrease in imprint speed substantially.

Table 6: Summarized experimental series with film thickness, maximum filling height  $h_0$ , build-up constant  $\tau$  and the corrected build-up constant  $\tau_{\text{corr}}$ .

Compound	Film thickness / nm	Maximum filling height / nm	Build-up $\tau$ / s	Build-up $\tau_{\text{corr}}$ / s
<b>2a</b>	250	82.6	315	381
<b>2b</b>	500	52.7	371	704
<b>2c</b>	430	38.1	821	2155

Figure 58 depicts exemplary AFM images of the micrometer-scaled patterns imprinted through azo-NIL in thin films of the trisamide compounds **2a-c** and vertical sections generated from these pictures.

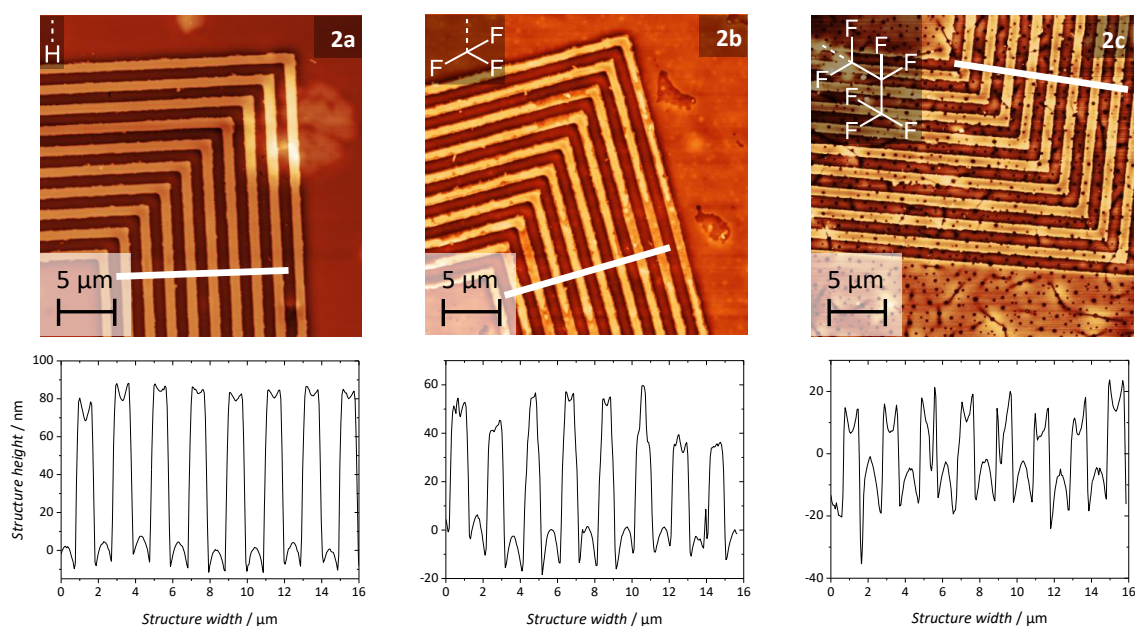


Figure 58: Top: AFM images of imprinted micrometer-scaled L-shaped patterns in thin films of the trisamide compounds **2a** (film thickness: 250 nm, left), **2b** (film thickness: 500 nm, middle) and **2c** (film thickness: 430 nm, right). The structures were imprinted for 1200 s using two LEDs at wavelengths of 365 nm and 455 nm at a power of  $0.3 \text{ mWcm}^{-2}$  and  $0.42 \text{ mWcm}^{-2}$ , respectively. The substituent attached to the azobenzene moiety is depicted on the top left corner of each image. The white line indicates the area in which the vertical section was generated. Bottom: Vertical sections were generated from the AFM images above.

Apart from a dent underneath the top right edge of the structure, the L-shaped  $1 \mu\text{m}$ -sized patterns in the 250 nm thin film of compound **2a** are a qualitatively very good imprinted negative type structure of the PDMS stamp. The dent is not attributed to the compound and is most probably caused by impurities on the substrate. As can be seen from the vertical profile of the pattern (see below), the compound wets the PDMS stamp. The shape of the cross-section of the lines, however, can not only be explained by the wetting behavior of the material, but also by the forces acting on it (see chapter 4.4). While the wetting behavior forms the typical “positive” or concave meniscus shape of the resist at the top of the structures, the “negative” or convex shape of the meniscus at the bottom of the stamp is most likely caused by a complex flow of the material triggered by compression of the resist material. The wetting behavior of compound **2b** seems to be changed significantly. In this case, the concave meniscus has not formed along the entire pattern. As a consequence the filling heights are very inhomogeneous throughout the pattern. In this case, rather the bad wetting behavior, than the bulky substituent is decisive for the worsened imprinting

performance in terms of quality and speed. Interestingly, considering the shape of the meniscus, compound **2c** appears to wet the stamp better than its less fluorinated equivalent **2b**. However, the macroscopically good film quality turns out to have a poor quality on the micrometer scale. As a consequence of a poor wetting behavior of the compound on the glass substrate, holes and cracks have formed throughout the film. This issue might be solved by changing the surface/resist interactions e.g. by fluorination of the glass substrate and/or by varying the spin coating parameters, e.g. the solvent. Since the imprinting speed has turned out to be so low, no further investigations on solving this issue have been carried out so far.

#### 4.6.4 Azobenzene-functionalized spirobichromane-based derivatives

All spirobichromane derivatives synthesized in this work could be processed to amorphous thin films of very good optical quality. The rigid core promotes the formation of a stable amorphous phase as packing is hindered. However, the perfluorohexyl-substituted spirobichromane compound (**1d**) could not be processed to a thin film since it crystallized immediately after spin coating. Therefore, no SRG or azo-NIL experiments were performed with this compound.

In the following the spirobichromane derivatives featuring unsubstituted azobenzene moieties (**1a**), derivatives with  $\text{CF}_3$  (**1b**), perfluoropropyl (**1c**) and methoxy (**1e**) substituents were investigated. As in previous experiments, micrometer-scaled L-shaped patterns were imprinted in the spin coated thin films using a PDMS stamp and biphotonic exposure on the 'vertical setup'. All spirobichromane compounds showed a good solubility in common organic solvents (here THF and cyclopentanone) and the film thickness achieved was around the optimum of 500 nm. Figure 59 shows the structure heights attained as a function of the exposure time for the different spirobichromane compounds.

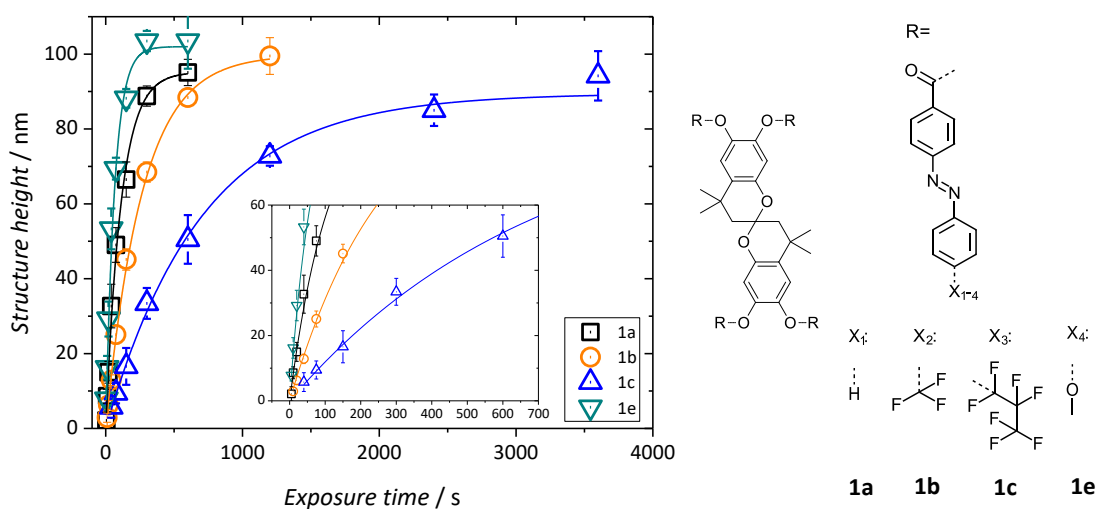


Figure 59: Heights of imprinted structures in films of spirobichromane compounds **1a-1e** (film thicknesses: 505 nm (**1a**), 625 nm (**1b**), 500 nm (**1c**) and 560 nm (**1d**)) as function of the exposure time. The structures were imprinted using biphotonic exposure at wavelengths of 365 nm and 455 nm at a power of  $0.3 \text{ mWcm}^{-2}$  and  $0.42 \text{ mWcm}^{-2}$ , respectively. The chemical structures of the molecule core, as well as the azobenzene moieties with their substituents are depicted besides the plot. The inset shows the first 700 s of the imprinting process.

In this set of experiments the exposure time was chosen in a way that any compound could attain the maximum theoretical structure height of the replica of about 100 nm. Like in the case of the trisamide compounds, the derivatives featuring perfluoroalkyl chains have a lower imprinting performance in terms of speed. However, compound **1e**, which has already proven to be very efficient and quick when it comes to SRG formation experiments, has performed well in azo-NIL, too.<sup>[92,132]</sup> The methoxy substituted compound is nearly twice as fast ( $\tau = 64$  s) as the unsubstituted spirobichromane equivalent ( $\tau = 112$  s). This finding could be explained by the significant red shift of the  $\pi$ - $\pi^*$ -absorption maxima caused by the electron donating MeO group. This shift causes an overlap of the two absorption bands ( $n$ - $\pi^*$  and  $\pi$ - $\pi^*$ ) and efficiently triggers isomerization cycles. Moreover, the maxima of the absorption bands is nearer to the emitting wavelengths of the two LEDs contributing to a more efficient imprinting process. Compared to the azobenzene-functionalized homopolymer **4e**, which carries the same methoxy substituent as molecular glass **1e** does, the imprinting speed is 5 times higher. Table 7 depicts the data of the performance of the investigated spirobichromanes in azo-NIL.

Table 7: Summarized experimental series with film thickness, maximum filling height  $h_0$ , build-up constant  $\tau$  and the corrected build-up constant  $\tau_{corr}$ .

Compound	Film thickness / nm	Maximum filling height / nm	Build-up $\tau$ / s	Build-up $\tau_{corr}$ / s
<b>1a</b>	505	95	112	118
<b>1b</b>	625	99	266	269
<b>1c</b>	500	89	699	785
<b>1e</b>	560	102	65	64

Figure 60 depicts exemplary AFM images and vertical sections of the micrometer-scaled patterns imprinted in thin films of the spirobichromane compounds **1a-e** using azo-NIL.

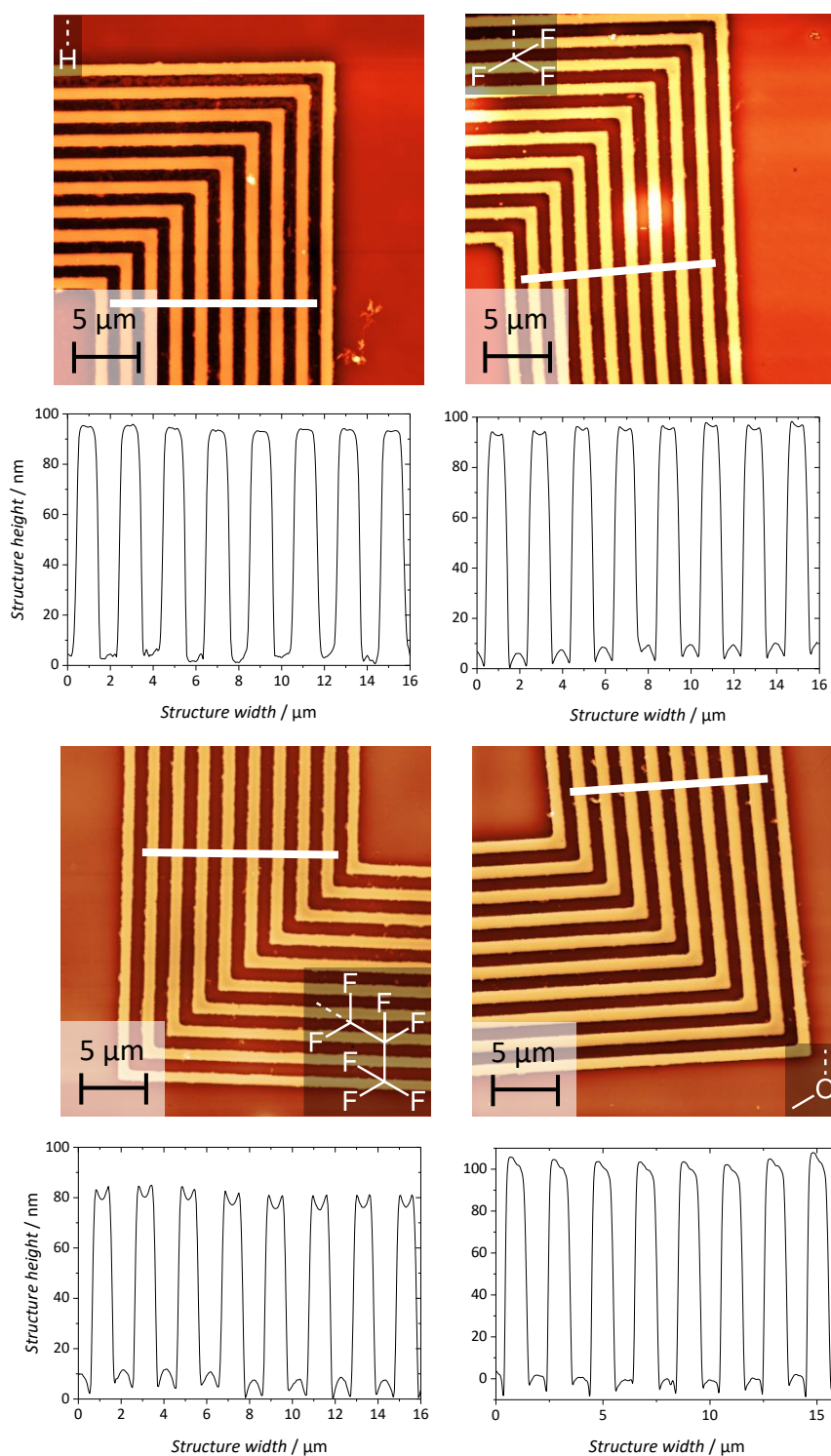


Figure 60: AFM images of imprinted micrometer-scaled L-shaped patterns in thin films of spirobichromane compounds **1a** (film thickness: 505 nm, top left), **1b** (film thickness: 625 nm, top right), **1c** (film thickness: 500 nm, bottom left) and **1e** (film thickness: 560 nm, bottom right). The structures were imprinted for 600 s (**1a** and **1b**), 1200 s (**1c**) and 300 s (**1e**) using two LEDs at wavelengths of 365 nm and 455 nm at a power of  $0.3 \text{ mWcm}^{-2}$  and  $0.42 \text{ mWcm}^{-2}$ , respectively. The substituent attached to the azobenzene moiety is depicted on the bottom right corner of each image. The white line indicates the area in which the vertical section was generated. Bottom: Vertical sections were generated from the AFM images above.

Apart from dents in the film of compound **1b**, the L-shaped 1  $\mu\text{m}$ -sized patterns in all thin film of the spirobichromane compounds are qualitatively very good imprints. As it is the case of the 1,3,5-benzenetrisamide-based compound **2a**, crystallization can be excluded as reason for the phenomenon and most probably dust particles or similar has caused the dents. In contrast to the 1,3,5-benzenetrisamide-based perfluoropropyl substituted equivalent, the spirobichromane compound **2c** does not dewet from the substrate and spin coating yields a perfectly clean film, which is not negatively affected by the exposure during the imprinting process. From the vertical profiles, it can be concluded that all compounds wet the PDMS material of the stamps. The vertical profiles are similar to the ones observed in case of the trisamide compounds.

#### 4.6.4.1 Micrometer-scale imprinting – summary

In the previous section, the influence of the resist material on the azo-NIL process, especially the imprinting speed, has been investigated. As resist materials, a photo-orientable homopolymer and 9 different azobenzene molecular glasses based on three different molecule cores were chosen. The three molecule cores triphenylamine, 1,3,5-benzenetrisamide and spirobichromane increase in their rigidity in this order, hence, their azobenzene-functionalized derivatives become more likely to yield stable amorphous phases.

The most flexible derivatives, which are based on the triphenylamine core **3f** and **3g** crystallized upon exposure. As a consequence these compounds are no suitable resist materials for azo-NIL. The azobenzene-functionalized 1,3,5-benzenetrisamide derivatives feature a more rigid core and additional secondary interactions through H-bonds. Consequently, these compounds did not crystallize and showed good imprinting results. The derivative, which carries unsubstituted azobenzene moieties **2a** featured a corrected imprinting time constant  $\tau_{\text{corr}}$  is 381 s. The derivatives with  $\text{CF}_3$  (**2b**) and  $\text{C}_3\text{F}_7$  (**2c**) substituents in the para position of the azo-group feature much higher time constants of 704 s and 2155 s. Obviously, substitution with the electron-withdrawing  $\text{CF}_3$  group has a negative impact. The introduction of a stiff, fluorinated alkyl chain additionally decreased the imprinting performance. As the spirobichromane-based molecular glasses feature the most rigid core, the amorphous phase of the compounds was stable throughout the imprinting process. The missing secondary interactions have led to a significant improvement of the imprinting speed, as the unsubstituted azobenzene-functionalized derivative **1a** features a  $\tau_{\text{corr}}$  of just 118 s, which is an improvement of a factor of 3 compared to the corresponding 1,3,5-benzenetrisamide derivative **2a**. As in case of the trisamides, the electron-withdrawing  $\text{CF}_3$  group and a fluorinated alkyl chain decreases the imprinting speed. The electron-donating methoxy group of compound spirobichromane-based compound **3e** features the best imprinting performance. Its corrected time constant is 64 s, hence better by more than a factor of 2 than the unsubstituted derivative **2a**. The methoxy-substituted azobenzene moiety carrying homopolymer **4e** featured a surprisingly good imprinting speed. Despite the high molecular weight of  $3.75 \cdot 10^5$  g/mol, the homopolymer **4e** the time constant  $\tau_{\text{corr}}$  is just 308 s. However, compared to the corresponding low-molecular-weight compound with the same MeO substituent, this is slower by a factor of 5.

#### 4.6.5 Imprinting of nanopatterns using azobenzene-functionalized spirobichromane-based derivatives

In the following the imprinting of nanometer-scaled patterns is investigated. As they were identified as most promising resist material for azobenzene-based nanoimprint lithography, the spirobichromane-based derivatives were chosen for this purpose. Moreover, the knowledge gained in the studies of imprinting micrometer-scaled patterns will be applied in the following experiments including the ideal experimental setup with biphotonic exposure of films and the adjustment of an ideal film thickness of about 500 nm whenever possible.

##### 4.6.5.1 Stamp fabrication and characterization

Azobenzene-based imprinting of nanostructures has been performed with stamps casted from a commercially available nano-structured master from the manufacturer *NIL Technology*. The fused silica master was designed for testing nanoimprint processes and has feature sizes down to 100 nm. The stamp features eight quadratic areas of two different types with four squares each. The two different types differ in the line-spacing ratio (also referred to as *spacing*), i.e. the ratio of the size of raised structures to the space in between the raised structures (also referred to as *pitch*). In this case it is either 1:1 (type I) or 1:2 (type II). Each quadratic area features nine squares, which each have a size of  $200 \mu\text{m}^2$ . Each of these quadratic areas feature three different patterns in three different line widths (see Figure 61).

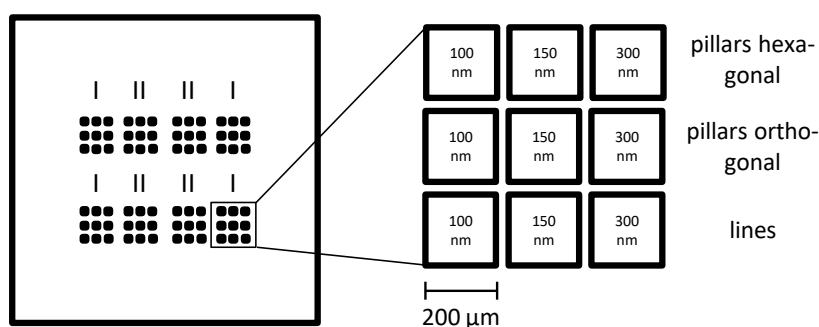


Figure 61: Schematic representation of the layout of the master used for imprinting nano-structures via azo-NIL.

For the imprinting experiments, the polymer replica was cut into eight pieces and one of these eight squares was selected as stamp in a series of experiments. The pattern design, which each of the eight quadratic patterned areas contain are pillars (rounded squares), arranged in an orthogonal or hexagonal way, or lines. The line width are 100 nm, 150 nm and 300 nm and the cavity depth is 100 nm with a tolerance of 10 % as specified from the manufacturer. Figure 62 depicts AFM images of the described patterns.

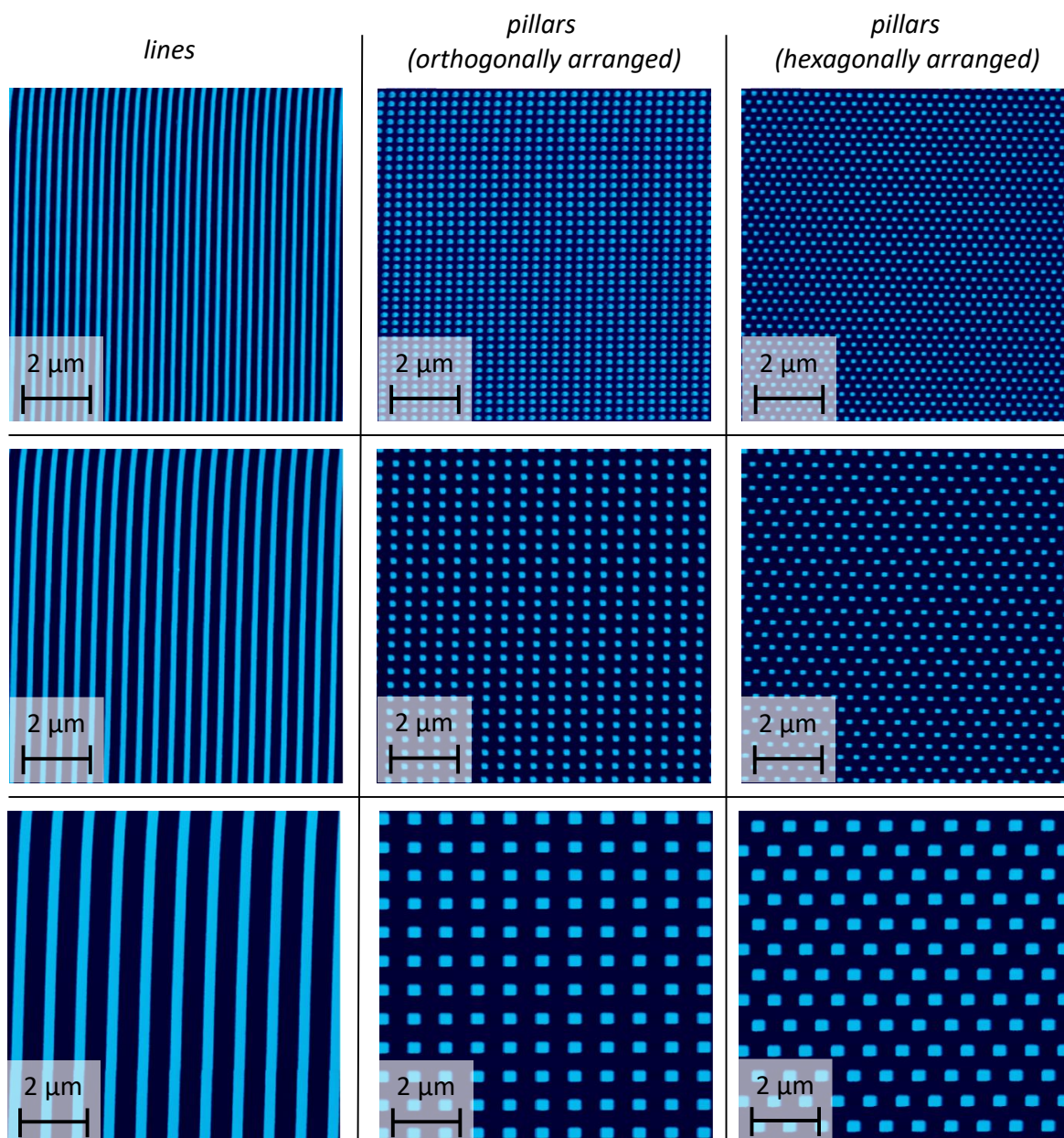


Figure 62: AFM images of the nanometer-scaled fused silica master (type II square). The structure height is 103 nm. Spacing = 1:2.

The stamps are made by casting a crosslinkable 2 component system on the master yielding flexible stamps after curing. As stamp material, three different materials (two different PDMS grades and a partly fluorinated polymer) were tested.

#### *PDMS stamps*

The two PDMS stamps, made from the two commercially available PDMS two component systems SYLGARD® 184 and ELASTOSIL® RT 601 were produced following a typical procedure: In a first step, prepared the surface of the nano-structured master was silanized by treatment with hexamethyldisilazane vapor. The temperature curable two component systems (ELASTOSIL® RT 601, or SYLGARD® 184) were then mixed in a ratio of prepolymer:initiator = 9:1 and were then casted onto the master. The crosslinking was performed at room temperature for 12 h and with a subsequent crosslinking reaction at 150°C for another 2 h (for details see experimental section). AFM images reveal that, when it comes to 100 nm line structures, none of the two PDMS

grades did yield stable stamps (see Figure 63). When cured at room temperature for 12 h and subsequent 1-2 h at 80°C, the two PDMS systems have quite similar elastic moduli or Young's moduli of around 1.5 MPa<sup>[134]</sup> and therefore it is not surprising that both materials behave similar as the phenomenon of so called lateral collapse is strongly dependent on the Young's modulus.<sup>[135]</sup> Increasing the curing temperature can raise the Young's modulus.<sup>[136]</sup> However, experiments with curing temperatures up to 150°C did not solve the issue of lateral collapse.

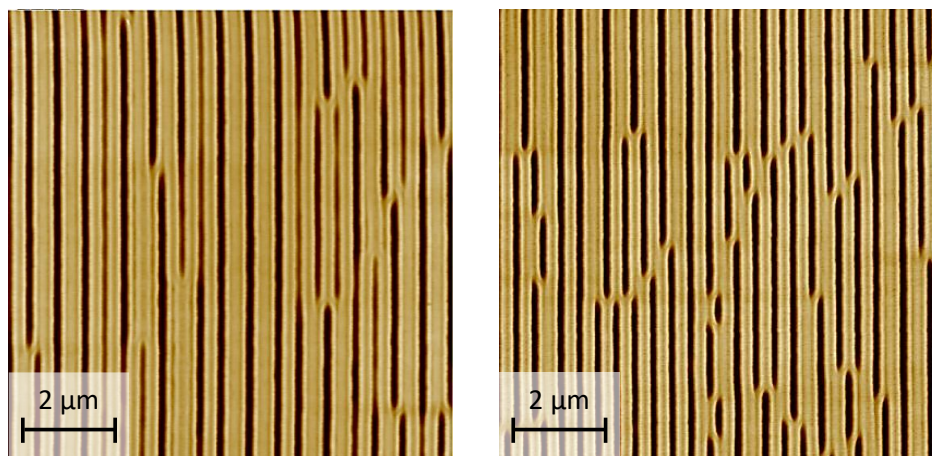


Figure 63: AFM images of replicas of the 100 nm lines from the nanometer-scaled fused silica master. Left: ELASTOSIL® RT 601 (PDMS); Right: SYLGARD® 184 (PDMS).

#### *Fluorinated polymer stamps (EVG stamps)*

Using the commercially available fluorinated polymer system from the manufacturer EVG® solved the problem of lateral collapse of the 100 nm line structures. EVG® polymer replicas were prepared from a mixture of a UV curable prepolymer with 2 wt.-% UV initiator, which was then casted on the master and exposed to UV light. Obviously, the fluorinated polymer features a higher Young's modulus. Therefore, the 100 nm structures are more stable and show no line collapse. Thus, the stamps made from the EVG® polymer are favorable when it comes to patterns below a structure size of 300 nm.

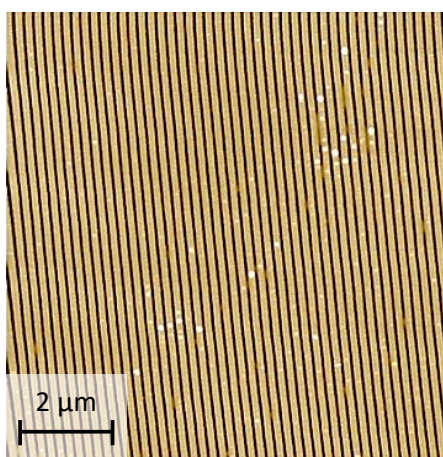


Figure 64: AFM images of replicas of the 100 nm lines from the nanometer-scaled fused silica master. EVG® polymer replica.

### Spacing

While differences in the spacing are no issue with EVG<sup>®</sup> polymer stamps, line spacing gets relevant when it comes to 150 nm structures on PDMS stamps. Figure 65 shows the result of imprinting 150 nm structures with a spacing of 1:1 in one case and 1:2 spacing in the other. In case of the 1:1 spacing, the ratio between cavity height and structure width is exactly 1. Due to the low Young's modulus of PDMS, this ratio is too low and lateral collapse occurs. When the line spacing is increased to 1:2, the lateral collapse does not occur anymore and the structures can be imprinted accurately.

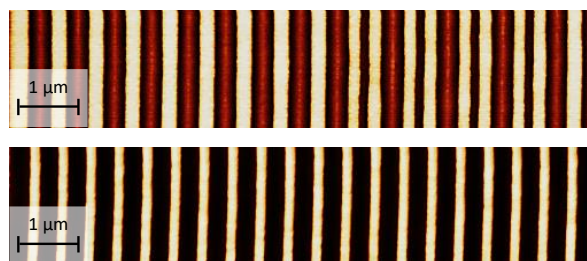


Figure 65: 150 nm line structures with different line spacing ratios imprinted into thin films of spirobichromane derivatives **1e** (top) and **1a** (bottom). Top: spacing: 1:1; bottom: spacing: 1:2. The ELASTOSIL<sup>®</sup> RT 601 PDMS stamps used were cured at 150°C.

#### 4.6.5.2 Influence of the stamp material and experimental setup on the imprinting performance

In the following, the impact of the stamp material and changes in the experimental setup will be investigated. In this set of experiments, nanometer-structured PDMS stamps and equivalent stamps made from EVG<sup>®</sup> polymer have been chosen. To ensure good contact between stamp and resist film, also referred to as *conformal contact*, the EVG<sup>®</sup> stamps had to be fixed with two magnets, which apply pressure on the stamps. Since the pressure originating from the two magnets is rather negligible on the nanometer scale, the influence of the change in the experimental setup should not be significant. The major differences between the experiments performed with PDMS and those performed with the fluorinated EVG<sup>®</sup> stamp should be differences in the interaction between the film and the stamp material. Figure 66 depicts the imprinted structure heights in thin films of compound **1a** as a function of exposure time for different stamp materials and setups.

Owing to its flexibility, PDMS stamps can adapt the surface of the resist and, thus, provide a conformal contact between the film surface and the stamp. As a consequence, the structure height is exponentially increasing in the beginning of the imprinting process and decaying towards a plateau value. Since the EVG<sup>®</sup> polymer stamps are more rigid than the PDMS stamps, the conformal contact is not provided in any case and must be ensured by external pressure. If no magnets are used, the azo-NIL process is significantly slowed down. However, with magnets to ensure conformal contact, the performance of the imprinting process with the EVG<sup>®</sup> stamp is as good as or even slightly better than the comparable PDMS stamp experiment.

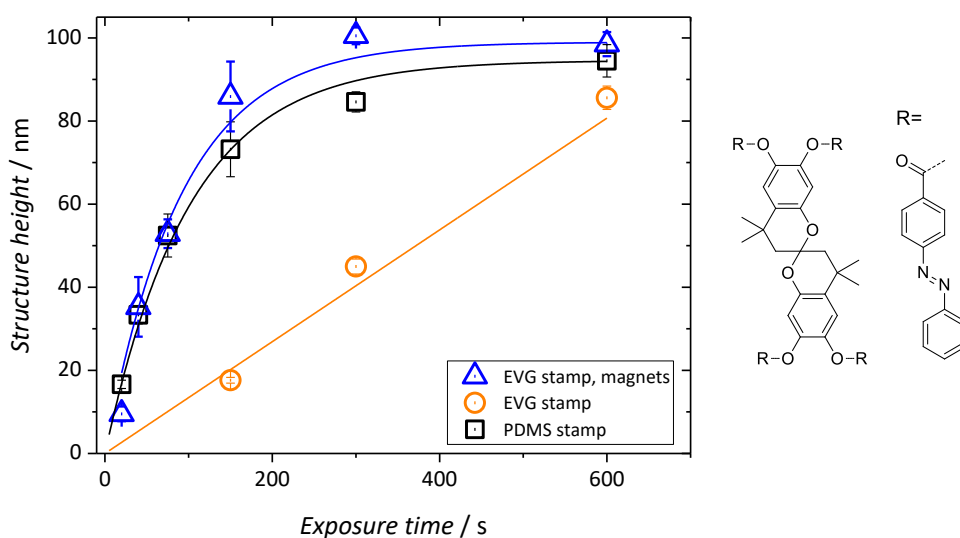


Figure 66: Imprinted 300 nm sized structures in films of spirobichromane compound **1a**. Film thicknesses: 500 nm (EVG<sup>®</sup> with magnets/pressure), 570 nm (EVG<sup>®</sup> without magnets), 550 nm (PDMS). The reproducibility was tested on a 560 nm thick film. Structure height as function of the exposure time. The structures were imprinted using biphotonic exposure at wavelengths of 365 nm and 455 nm at a power of 0.3 mWcm<sup>-2</sup> and 0.42 mWcm<sup>-2</sup>, respectively. The chemical structures of the molecule core, as well as the azobenzene moiety with its substituent is depicted besides the plot.

Figure 67 depicts exemplary AFM images of imprinted nanopatterns scaling from 100 nm to 300 nm of the three different patterns (lines and pillars) with a spacing of 1:1 using an EVG<sup>®</sup> polymer stamp in the experimental setup without the use of magnets. Despite very few defects, which most likely result from handling the stamp and the film and thus the release manually, almost all structures of a size of 300 nm and 150 nm are of very good quality and defect free. Only in the case of the orthogonally arranged pillars large areas with defects can appear. Obviously, this arrangement of the pillars can be torn off easier at release of the stamp.

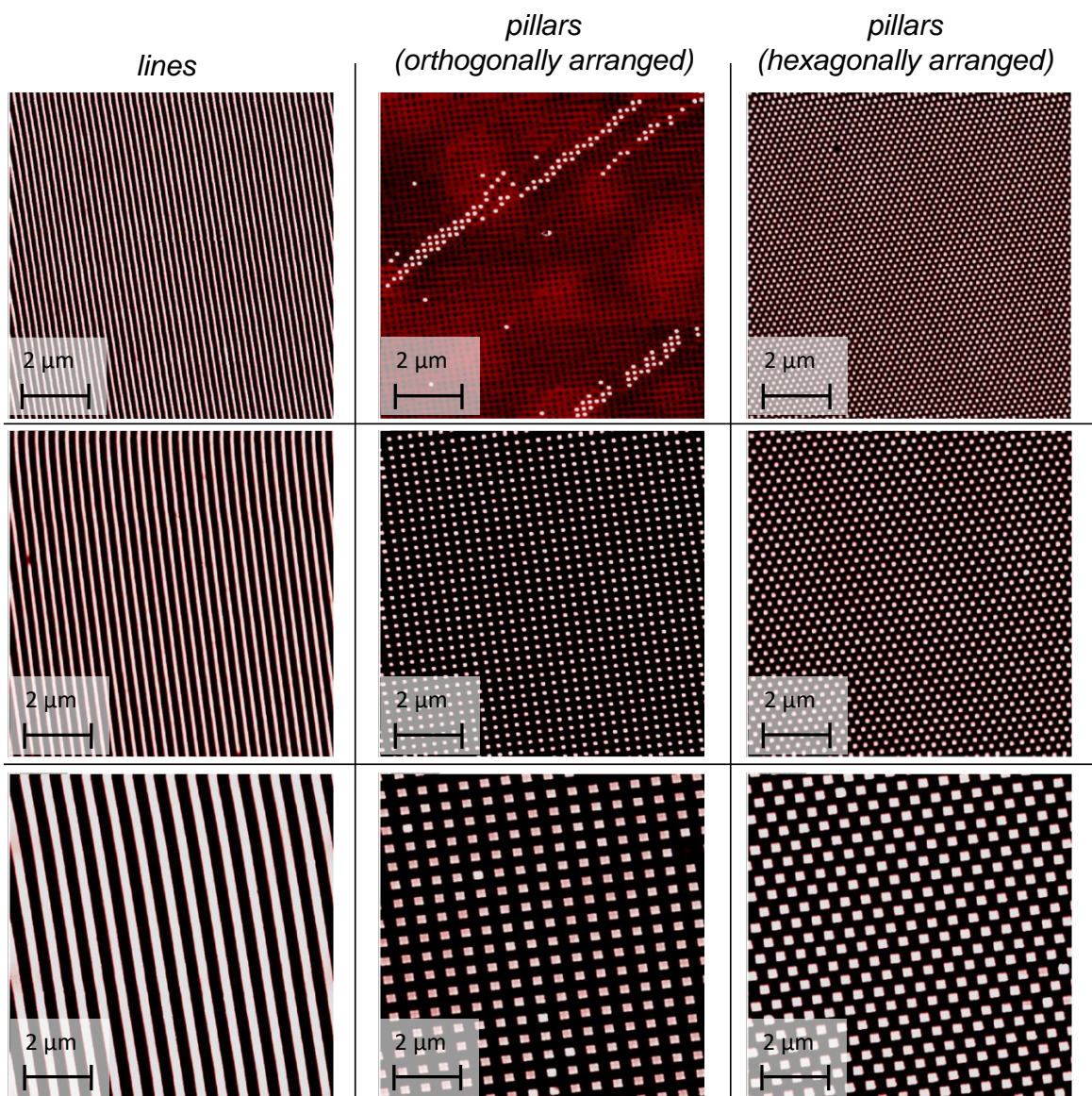


Figure 67: AFM images of nanometer-scaled structures imprinted in a spin-coated film of **1a** at room temperature using the standard setup without external pressure, an EVG polymer stamp and both LEDs. The structure ranges from 55 to 80 nm. Almost all structures are defect free with the exception of the orthogonally arranged pillars.

The quality of imprinted structure using a PDMS stamp is also investigated on a thin film of compound **1a**. As in the experiment with the EVG<sup>®</sup> stamp the 500 nm thick film is illuminated through the stamp with both LEDs simultaneously for 600 s at their maximum intensities. Figure 68 depicts representative SEM micrographs of imprinted lines and pillars pattern sizes between 100 and 300 nm.

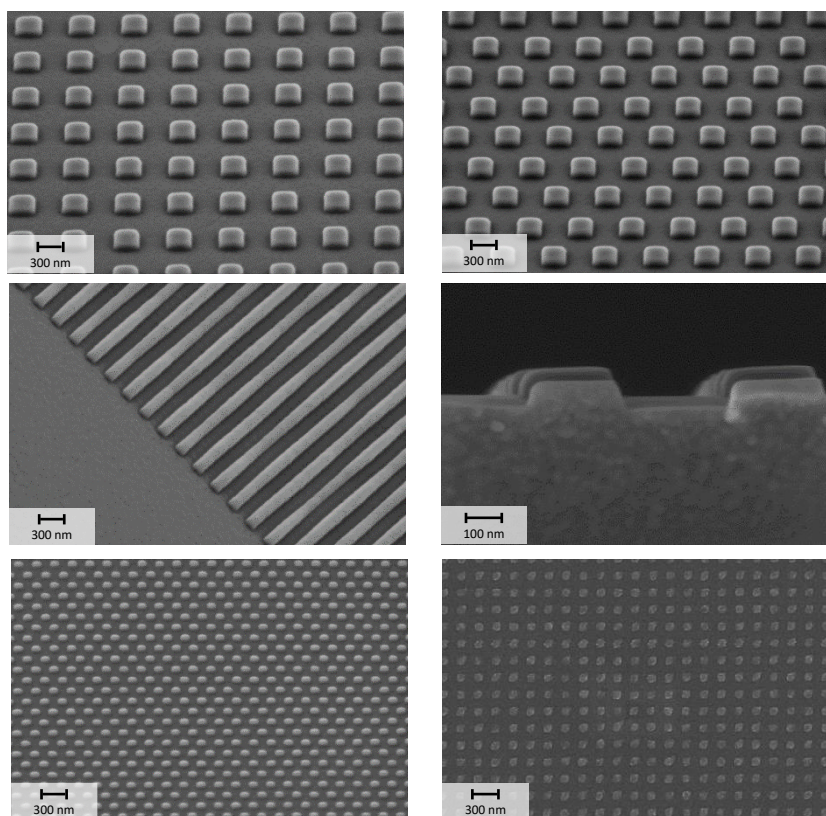


Figure 68: Tilted and non-tilted SEM micrographs of different nanopatterns imprinted into films of compound **1a**; top: 300 nm structures (tilted 45°); middle left: 150 nm structures (tilted 45°); middle right: 150 nm structures (tilted 90°); bottom: 100 nm structures (left: tilted 45°). The thickness of the film is approximately 500 nm. The line spacing ratio is 1:1.

The SEM images show that azo-NIL using a PDMS stamp allows for accurate imprinting of structures in the nanometer regime. The cross-sectional SEM image (middle left) reveals a homogeneous bulk material in the film and in the imprinted structure as well. There are no indications of a boundary layer. However, compared to the imprinting experiments with the stiffer EVG<sup>®</sup> stamp, the edges of the imprinted structures using the PDMS stamp show undesired curved edges. Consequently, the pattern from the master could not perfectly be replicated. Even though the 100 nm sized structures are not torn-off by the stamp, thus are nearly defect free, the structures could only reach non-satisfactory height of around 20 nm in the experiments conducted. This is due to the collapse of the 100 nm sized structures on PDMS stamps.

To conclude, the two types of stamps have both advantages and drawbacks. The EVG<sup>®</sup> stamp allows for more accurate replication of the masters pattern down to 100 nm, even for 100 nm line structures. However, its stiffness leads to problems in the conformal contact which can cause uneven and patchy structure heights and sometimes poor reproducibility of the experiments. Furthermore, the 100 nm pillar structures are likely to be torn-off. When a certain structure height is reached, the likelihood of defects increases drastically. The PDMS stamp is flexible and allows for conformal contact even on uneven surfaces. The structure height therefore is very consistent in most cases. Owing to its flexibility, the structures are not torn-off so easily as compared to the EVG<sup>®</sup> stamp. On the other hand, imprinting of structures with a size of 100 nm is not possible due to lateral collapse.

#### 4.6.5.3 Influence of the structure size and geometry on the imprinting speed

In a previous chapter, the lateral collapse of structures with a size of 100 nm on PDMS stamps has been discussed. To interpret how the structure size is influencing the imprinting performance in the transition between 1 micrometer-scaled patterns and 100 nm structures, PDMS stamps were used to ensure the comparability of the interactions between the film and the stamp material within the different experiments. The structures were imprinted in spin-coated thin films of compound **1a** featuring film thicknesses between 500 and 550 nm. The films featured a good optical quality. Imprinting was performed using biphotonic exposure and both LEDs at maximum power. Figure 69 depicts the temporal evolution of the structure height as a function of the exposure time in dependence of the structure size in thin films of compound **1a**. The imprinting speed is not influenced significantly by decreasing the structure size from 1  $\mu\text{m}$  to 300 nm. However, if the structure size is further decreased, the imprinting speed is reduced substantially to  $\tau_{150\text{ nm}} = 262\text{ s}$  and  $\tau_{100\text{ nm}} = 213$ , respectively. The slightly higher imprinting speed in the case of the 100 nm sized cavities is unexpected, but should not be overrated since the issue of lateral line collapse on PDMS stamps influences the results.

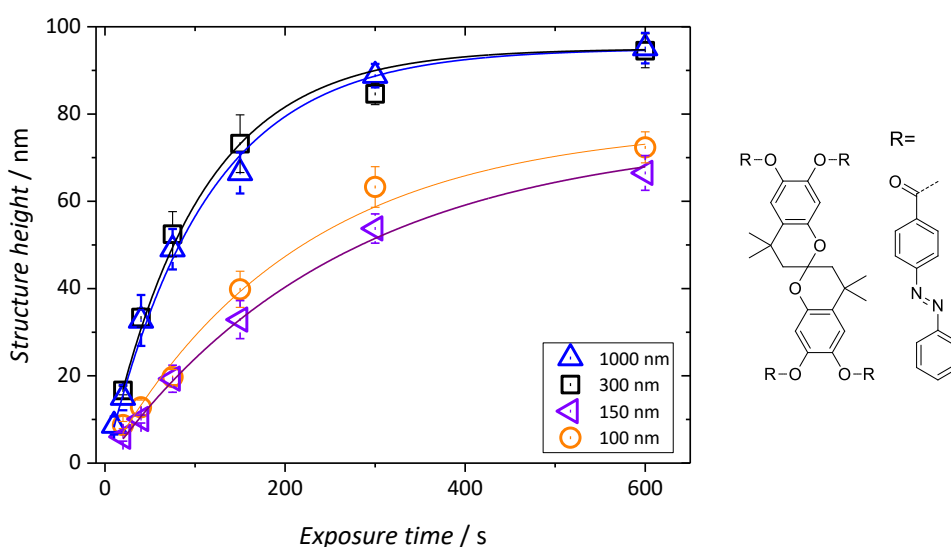


Figure 69: Heights of imprinted structures in films of spirobichromane compound **1a** (film thicknesses: 505 nm (1000nm lines), 550 nm (300 and 100 nm lines) and 550 nm for 150 nm lines and 300 nm reproducibility) as function of the exposure time. The data points connected with dashed lines are an experiment to test the reproducibility. The chemical structure is depicted besides the plot. The structures were imprinted using biphotonic exposure at wavelengths of 365 nm and 455 nm at a power of  $0.3\text{ mWcm}^{-2}$  and  $0.42\text{ mWcm}^{-2}$ , respectively. The stamp material is PDMS.

As reported earlier, the issue of lateral collapse was solved by using the partly fluorinated polymer form EVG<sup>®</sup> as stamp material. Imprinting with this stamp material allows for an accurate investigation of influences on the imprinting speed at cavity widths below 1  $\mu\text{m}$  (see Figure 70). The structures were imprinted in a spin-coated thin film of compound **1a** featuring a film thickness 625 nm. The film featured a good optical quality. Imprinting was performed using biphotonic exposure. Here, the “horizontal setup” with the two magnets is used, so that external pressure is applied onto the EVG<sup>®</sup> stamp and conformal contact is ensured.

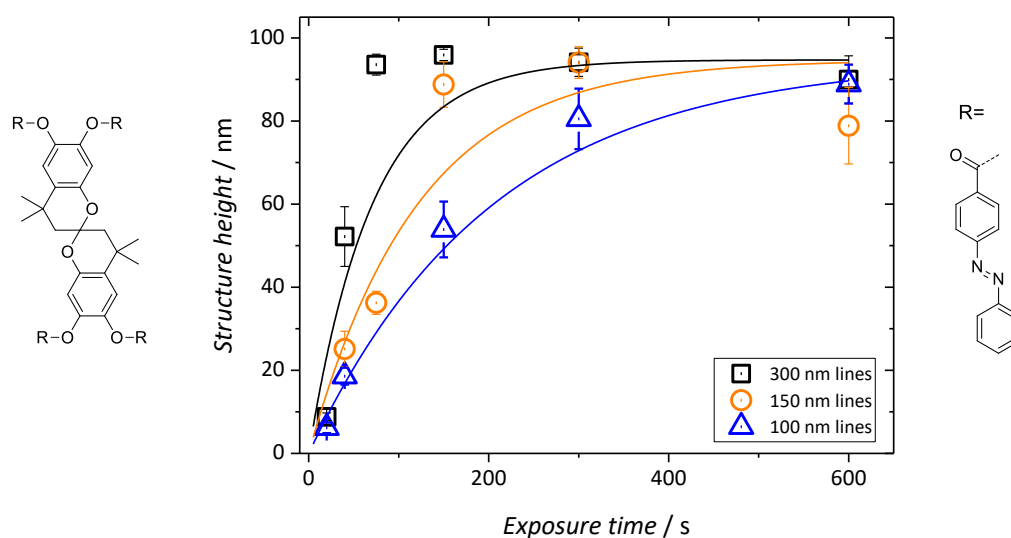


Figure 70: Heights of imprinted structures in films of spirobichromane compound **1a** (film thickness  $\approx 625$  nm) as function of the exposure time. The chemical structure is depicted besides the plot. The structures were imprinted using biphotonic exposure at wavelengths of 365 nm and 455 nm at a power of  $0.3 \text{ mWcm}^{-2}$  and  $0.42 \text{ mWcm}^{-2}$ , respectively. The stamp material is the fluorinated polymer from EVG®.

As in the case of the PDMS stamp, reducing the linewidth from 300 nm to 100 nm means a decrease of the filling speed. The time constant increases from  $\tau_{300 \text{ nm}} = 48 \text{ s}$  over  $\tau_{150 \text{ nm}} = 103 \text{ s}$  to  $\tau_{100 \text{ nm}} = 176 \text{ s}$ . With respect to the PDMS stamp experiment, the imprinting speed is remarkably high. In case of the 300 nm structures, the imprinting speed is more than doubled compared to the  $1 \mu\text{m}$  structure. Since the pressure applied by the magnets can be considered as rather low, the major effect most probably derive from the changed wetting behavior.

Having investigated the influence of a decreasing structure size on the imprinting performance, the influence of the imprinted structure geometry (lines, or differently arranged pillars) is examined next. The same compound has been spin coated under the same conditions and the experimental setup (EVG® polymer stamp hold in place by magnets) have been chosen, so that comparable results should be obtained. Figure 71 shows the temporal evolution of the structure height as a function of the exposure time in imprinting processes of 300 nm to 100 nm sized structures featuring different geometries imprinted into a thin film of compound **1a**.

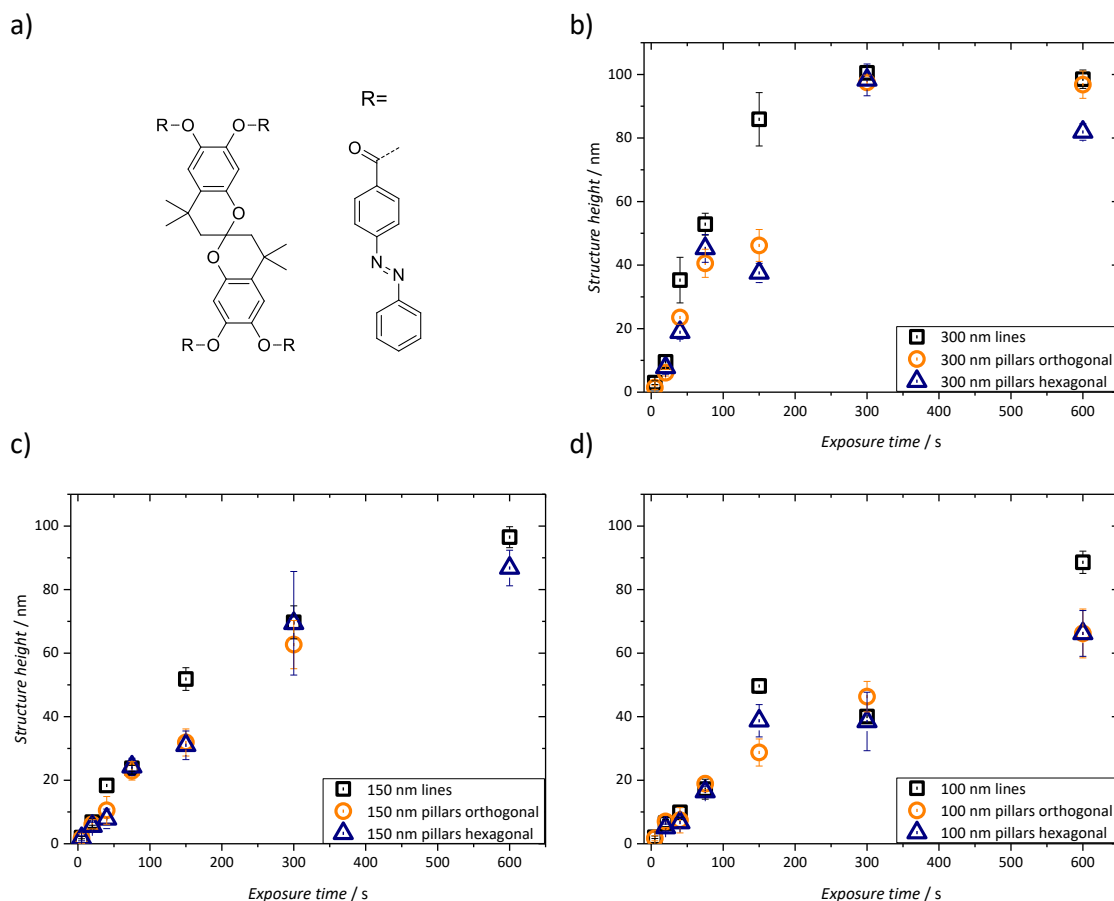


Figure 71: Heights of imprinted structures in a film of spirobichromane-based compound **1a** (film thickness = 560 nm) as function of the exposure time. a) Chemical structure of compound **1a**. b) 300 nm structures, c) 150 nm structures, d) 100 nm structures. The structures were imprinted using biphotonic exposure at wavelengths of 365 nm and 455 nm at a power of  $0.3 \text{ mWcm}^{-2}$  and  $0.42 \text{ mWcm}^{-2}$ , respectively. The stamp material is the fluorinated polymer from EVG®.

The data plotted in this figure is resulting from a reproduction of the experiment discussed on the basis of Figure 70. With decreasing pattern size, the speed, in which the cavities are filled, is decreasing. The values of the absolute values of the build-up constants for the imprinting of 100 nm line structures, the speed is nearly halved compared to preceding experiment. The rather poor reproducibility is most probably arising from difficult handling of the rigid EVG® polymer stamps compared to their elastic PDMS counterparts. The stiffness of the EVG® stamps can also lead to problems at the lift-off of the stamp from the resist after the imprinting process. Especially in case of the 100 nm sized pillars, wide areas of the structures are torn upon release which manifests itself in big error bars and, compared to the 100 nm line structure, low maximum height reached.

The geometry does not affect the imprinting performance significantly. Compared to the pillar structures, the line structures tend to fill up slightly faster (see Table 8).

Table 8: Influence of the structure size and geometry on the imprinting performance in a film of spirobichromane-based compound **1a**. Summarized maximum filling heights  $h_0$ , build-up constant  $\tau$  and the corrected build-up constant  $\tau_{\text{corr}}$  calculated from the data obtained in the set of experiments.

Structure width / nm	Structure geometry	Maximum filling height / nm	Build-up $\tau$ / s	Build-up $\tau_{\text{corr}}$ / s
300	lines	103	98	95
300	pillars orthogonal	105	182	173
300	pillars hexagonal	92	156	170
150	lines	105	251	239
150	pillars orthogonal	100	328	328
150	pillars hexagonal	107	342	320
100	lines	114	443	389
100	pillars orthogonal	69	251	364
100	pillars hexagonal	73	290	397

#### 4.6.5.4 Influence of the temperature on the imprinting speed

Azo-NIL is an athermal process based on the photofluidization effect of azobenzenes below  $T_g$ . Upon irradiation the glass transition temperature of the bulk material is almost unaffected.<sup>[120]</sup> However, processing times at room temperature in the region of 100 s or more are relatively high. In an attempt to lower the imprinting time and to investigate the limit of imprinting speed, the compounds that have proven to be the fastest in imprinting at room temperature, the spirobichromane compounds **1a** and **1e**, have been chosen to be studied in elevated temperature azo-NIL experiments. For this purpose, the spin-coated thin films are heated on a hot-stage to a temperature 10°C below the glass transition temperature of the material ( $T_g \approx 108$  °C). No phase transition occurs during this isothermal treatment and the dimensional stability is not impaired significantly. After heating the film to the desired temperature, the stamp is placed on the film, which is positioned in the horizontal setup. Consequently, exposure occurs through the stamp. During the experiment series, in which several spots of the film are illuminated for different periods of time, the film stays on the hot-stage at elevated temperatures. One spot of the film is used to test if the pattern is imprinted into the film without illuminating it. To this end, the stamp is placed on the film for 20 min. In none of the performed experiments a pattern could be found on these spots in AFM investigations. Figure 72 depicts the temporal evolution of the structure height as a function of the exposure time in imprinting experiments at elevated temperatures performed on thin films of **1a** and **1e** using the micrometer-scale-patterned PDMS stamps and the nanometer-scaled EVG® stamp.

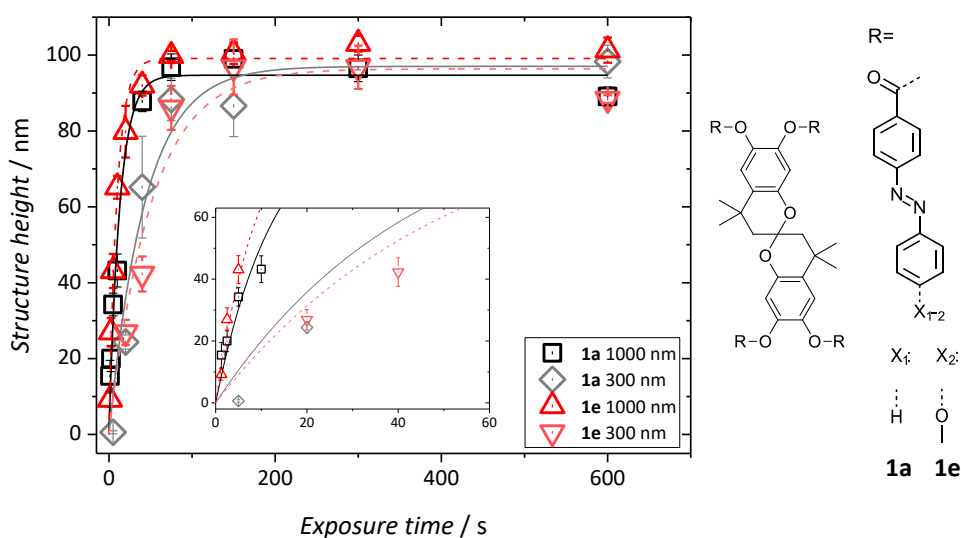


Figure 72: Heights of imprinted structures at elevated temperatures in films of spirobichromane compounds **1a** and **1e** (film thicknesses: 500 nm-540 nm) as function of the exposure time. The structures were imprinted using biphotonic exposure at wavelengths of 365 nm and 455 nm at a power of  $0.3 \text{ mWcm}^{-2}$  and  $0.42 \text{ mWcm}^{-2}$ , respectively. The temperature of the hot-stage was adjusted to  $98^\circ\text{C}$  (**1a**) and to  $97^\circ\text{C}$  (**1e**). The chemical structures of the molecule core, as well as the azobenzene moieties with their substituents are depicted besides the plot. The inset shows the first 700 s of the imprinting process.

As for the imprinting of the L-shaped microstructures, imprinting at temperatures  $10^\circ\text{C}$  below the glass transition of the materials increased the imprinting speed of the two tested compounds. In case of the methoxy-substituted spirobichromane compound **1e**, the  $1 \mu\text{m}$  line structure height reaches around 10 nm after just 1 second. Compared to imprinting at room temperature, the build-up constant of compound **1a**  $\tau_{1 \mu\text{m},1a}$  decreases by an order of magnitude from 112 s to 13 s. Despite micrometer-scaled imprinting in thin films of **1e** at room temperature ( $\tau_{1 \mu\text{m},1e} = 64\text{s}$ ), is twice as fast as in films of **1a**, the build-up constant of **1e** at  $97^\circ\text{C}$  is merely lower at a value of 9 s. The imprinting of  $1 \mu\text{m}$  structures therefore is around 10 times faster in case of compound **1a** and around 6 times faster in case of compound **1e**. Surprisingly, the imprinting performance of 300 nm lines is not improved significantly. With a build-up constant of 43 s at  $98^\circ\text{C}$ , the build-up constant for compound **1a** is just 1.5-2 times lower than at room temperature. The build-up constant of compound **1e** is with 50 s in the same range as **1a**.

#### 4.6.5.5 Performance of substituted spirobichromane derivatives in imprinting of nanostructures

As a final experimental series, the influence of substituents at the azobenzene moieties is investigated in imprinting of nanostructures. Figure 73 depicts the temporal evolution of structure heights as a function of the exposure time in films of the substituted spirobichromane derivatives as a function of the exposure time.

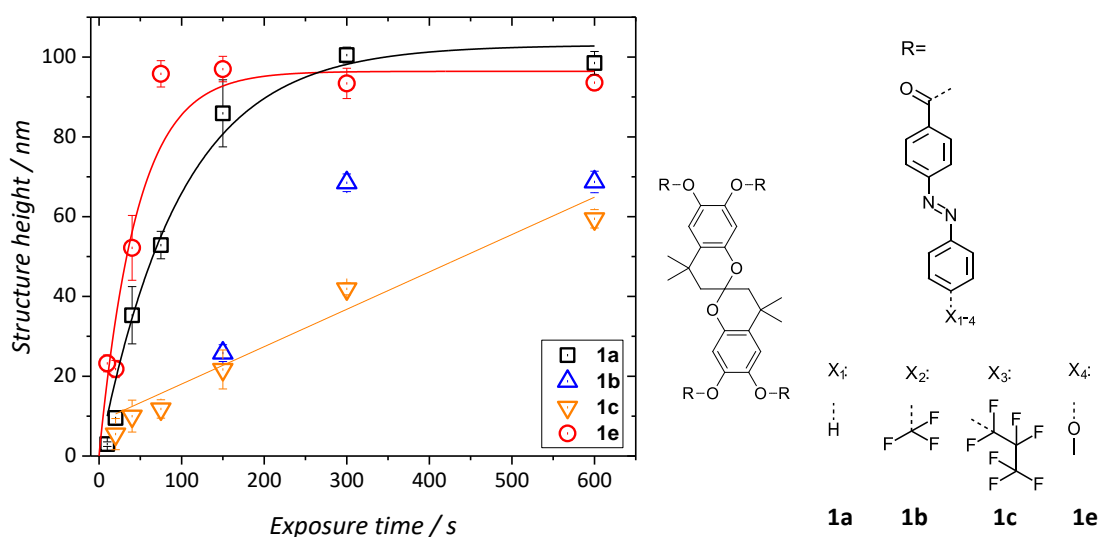


Figure 73: Heights of imprinted 300 nm line structures in films of spirobichromane compounds **1a-1e** (film thicknesses: 560 nm (**1a**), 330 nm (**1b**), 340 nm (**1c**) and 540 nm (**1e**)) as function of the exposure time. The structures were imprinted using biphotonic exposure at wavelengths of 365 nm and 455 nm at a power of  $0.3 \text{ mWcm}^{-2}$  and  $0.42 \text{ mWcm}^{-2}$ , respectively. The chemical structures of the molecule core, as well as the azobenzene moieties with their substituents are depicted besides the plot.

Compound **1e** was designed to be faster in the imprinting process than the unsubstituted equivalent **1a**. In micrometer-scaled imprinting, the compound was about twice as fast as **1a**. Here, the build-up constant also decreases by a factor of 2 from  $\tau_{1a, 300 \text{ nm}} = 95 \text{ s}$  to  $\tau_{\text{corr}, 1e, 300 \text{ nm}} = 46 \pm 10 \text{ s}$ . The other two compounds were designed to have improved release properties than the fluorinated compounds. The fluorination, however, leads to an increased imprinting time. Since the two data plots of compound **1b** and **1c** could not be fitted using equation 4.2, no exact time for the imprinting of 300 nm scaled line patterns can be provided. In general, the same trends terms of imprinting speed in imprinting of micrometer-scaled structures can be seen in imprinting of nanometer-scaled structures.

To study the quality of the imprinted structures, EVG® stamps were chosen. Due to issues at the release at which structures were torn-off, significant differences in quality are visible in the imprinting of 100 nm scaled orthogonally arranged pillars. Figure 74 depicts exemplary AFM images of 100 nm scaled orthogonally arranged pillars imprinted in thin films of spirobichromane derivatives with compound **1a** as comparison.

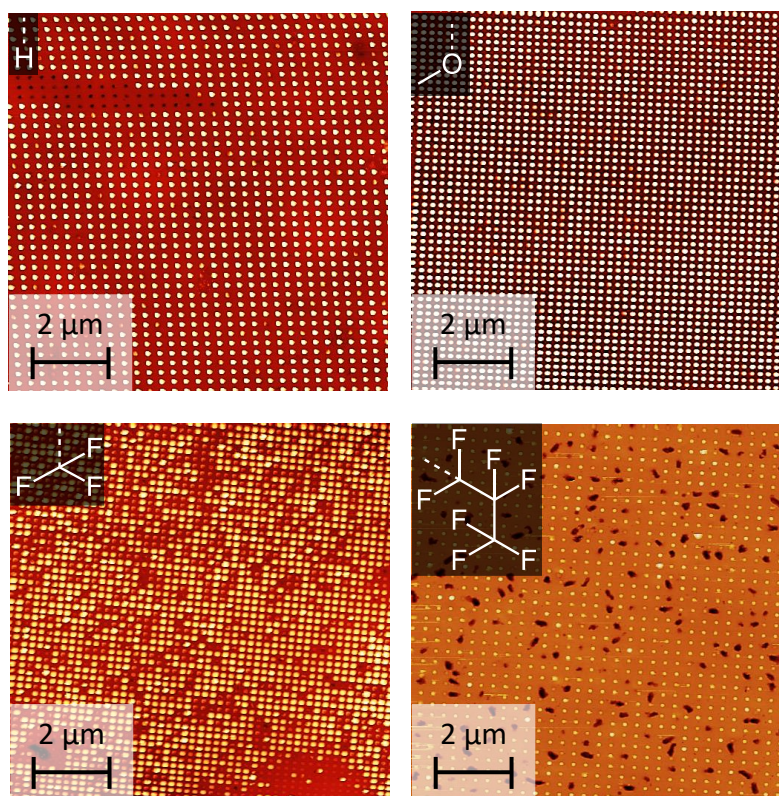


Figure 74: AFM images of imprinted 100 nm scaled orthogonally arranged pillars in thin films of spirobichromane compounds **1a** (film thickness: 560 nm, top left), **1e** (film thickness: 550 nm, top right), **1b** (film thickness: 520 nm, bottom left) and **1c** (film thickness: 430 nm, bottom right). The structures were imprinted for 300 s (**1a**), 600 s (**1e**) and 3600 s (**1b**, **1c**) using two LEDs at wavelengths of 365 nm and 455 nm at a power of 0.3 mWcm<sup>-2</sup> and 0.42 mWcm<sup>-2</sup>, respectively. The EVG<sup>®</sup> stamps were fixed using magnets. The substituent attached to the azobenzene moiety is depicted on the bottom right corner of each image.

The quality of the imprinted structures in films of the compounds **1a** and especially **1e** is satisfyingly good. Since the interactions of H-substituted **1a**, CF<sub>3</sub>-substituted **1b** and MeO-substituted **1e** with the fluorinated stamp should be comparable, no significant changes in the quality of the imprinted pattern is expected. Consequently, the quality of the pattern in the film of CF<sub>3</sub> substituted spirobichromane derivative is only merely inferior to that of the unsubstituted **1a** or the methoxy-substituted **1e**. The perfluoropropyl substitution on the other hand should have significantly altered interactions with the stamp material. This can be seen when placing the fluorinated stamp on the fluorinated film of **1c**. In this case, the adhesion of the stamp so low that the stamp has to be hold in place by fixation with one or two magnets, hence the interaction between stamp and resist are lowered and the release should be easier. The quality of the imprinted structure, however, has worsened compared to the other materials.

## 4.7 Summary of the chapter

In this chapter, for the first time, a straightforward NIL method, permitting the fabrication of non-periodic complex micro and nanostructures, here referred to as azobenzene-based nanoimprint lithography or *azo-NIL*, is presented. The method combines the unique properties of athermal photofluidization of azobenzenes with the principles of nanoimprint lithography. Hence, neither crosslinking reactions nor heating is needed, so that shrinkage issues of already established NIL techniques are avoided. Upon irradiation of the azobenzene-containing film, on top of which a patterned stamp is placed, *trans-cis-trans* cycles are induced and the photo-fluidized resist in filling the cavities of the stamp as a result of capillary forces.

The basic parameters influencing the performance of azo-NIL, such as the wavelength of the incident light, the fluence or the film thickness are comprehensively studied on the basis of low-molecular-weight photochromic molecular glass **1a**, which features a spirobichromane core with four H-substituted azobenzene moieties attached to it. Imprinting of micrometer-scaled patterns has revealed, that the ideal conditions for azo-NIL comprise the use of biphotonic exposure with two LEDs at wavelengths of 365 nm and 455 nm and a film thickness of at least 500 nm. Moreover, it was found that the fluence is directly proportional to the imprinting speed.

The influence of the resist material on the quality of the imprinted structures and on the imprinting speed is investigated based on 9 different azobenzene-functionalized molecular glasses and a photo-orientable homopolymer. The molecular glasses are based on three different molecule cores: triphenylamine, 1,3,5-benzenetrisamide and spirobichromane, which feature increasing rigidity in this order. Additionally, secondary interactions (H-bonds) are introduced in case of the 1,3,5-benzenetrisamide-based molecular glasses. The molecular glasses based on the triphenylamine core, which are the most flexible compounds in the study, have shown not to be suitable for azo-NIL. Imprinting studies have shown, that exposure triggers crystallization of the material. Azobenzene-containing molecular glasses based on a 1,3,5-benzenetrisamide core have shown to feature a more stable amorphous phase and do not crystallize. However, due to secondary interactions, these compounds are slower than the spirobichromane equivalents and even the photo-orientable homopolymer. The built up constant  $\tau$  (the time at which 63 % of the maximum structure height is reached) for H-substituted trisamide derivative **2a** is 381 s, whereas the homopolymer takes just 308 s and the H-substituted spirobichromane compound **1a** just 118 s. The fastest and most precise replication of patterns was realized with the spirobichromane-based molecular glasses. With a  $\tau$  of just 64 s, the methoxy-substituted derivative **1e** featuring optimal photophysical properties for fast isomerization cycles, is about 5 times faster than a comparable polymer.

As the spirobichromane-based derivatives have proven to be best suited for azo-NIL, investigations on the influence of the pattern size were conducted with these compounds. Studies revealed, that azo-NIL allows for the imprinting of structure sizes ranging from 10  $\mu\text{m}$  to 100 nm. As a consequence of hindered flow dynamics, the imprinting speed decreases at structure widths below 300 nm. Deficits in imprinting speed, however, can be eliminated by imprinting at elevated temperatures (10 °C below the resist's  $T_g$ ). Compared to imprinting at room temperature, the build-up constant of compound **1a**  $\tau$  decreases by an order of magnitude from 112 s to 13 s. Under these conditions, imprinting of structures with resist **1e** takes even just 9 s. In both cases, the amorphous phase is stable and no indications of crystallization are noticeable.

## 5 Improving Holographic Writing Performance of Photo-Orientable Azobenzene Polymers by Molecular Glasses<sup>2</sup>

### 5.1 Introduction

The remarkable photophysical properties of azobenzene-containing materials have risen the interest of several research groups, which, have mainly focused on optical holographic data storage. Besides the proposed use as a data storage medium, polymeric or low-molecular-weight azobenzene-containing materials also have the potential to see use as security feature. In particular volume gratings are considered forgery-proof, since complex equipment is needed to form such types of gratings.<sup>[137]</sup>

Upon irradiation in the absorption bands of the azobenzene chromophores, azobenzenes undergo repeated *trans-cis-trans* isomerization cycles. These repeated isomerization cycles of the chromophore leads to a so-called trembling motion resulting in a light-induced plastification<sup>[138]</sup>, also referred to as athermal photofluidization<sup>[72,139]</sup> of the material. Furthermore, exposure with polarized light leads to cooperative rearrangements, which eventually result in an orientation of the azobenzenes perpendicular to the polarization of the incident light.<sup>[21]</sup> Superposition of two polarized laser beams may give rise to the formation of holographic gratings in the volume of the material. These volume gratings feature a refractive-index modulation, which is caused by different refractive indices between the oriented and non-oriented areas. Depending on the material used and on the polarization of the laser, holographic gratings can also be formed by mass transport of the material of an azobenzene-containing film to yield so-called surface relief gratings (SRGs).

Azobenzene-containing materials in general can be divided into two classes; low-molecular-weight and polymeric azobenzene-containing materials. The photoactive polymers can be divided into homopolymers, copolymers and block copolymers. In films of homopolymers, the azobenzene moieties are in spatial proximity, and, hence, the *trans-cis-trans* isomerization is performed cooperatively leading to an enhanced stabilization of the inscribed volume gratings.<sup>[21,22]</sup> However, due to their high optical density, azobenzene-functionalized homopolymers cannot be used in thick samples as the incident light could not penetrate the entire medium. Yet, thick samples with thicknesses much larger than the grating period feature a high angular selectivity, which in turn would allow for the inscription of multiple holograms in the same volume element.<sup>[26]</sup> Consequently, the high optical density of homopolymers prevents them from being used in high density optical data storage (HDS). To decrease the optical density, statistical copolymers can be employed. Like homopolymers, albeit to a smaller degree, these polymers tend to form SRGs.<sup>[38]</sup> SRGs, however, neither provide angular selectivity nor store the polarization state of the writing light. Furthermore, in statistical copolymers the cooperative effect is lost, so that the inscribed gratings are not long-term stable.<sup>[22]</sup> Most blends of polymers result in a macrophase separation leading to light scattering, which makes polymer blends unsuitable for holographic experiments. Since block copolymers, composed of an amorphous majority block and an azobenzene-containing minority block form uniform microphase-separated morphologies with a domain size well below 100 nm, no scattering of visible light occurs in those systems. Moreover, the confined geometries

---

<sup>2</sup> Parts of this chapter have been accepted for publication by C. Probst, C. Meichner, H. Audorff, R. Walker, K. Kreger, L. Kador and H.-W. Schmidt in the Journal of Polymer Science, Part B: Polymer Physics, **2016**.

maintain the spatial proximity of the chromophores. Hence, the preserved cooperative effect and the reasonable low optical density renders block copolymers the most promising polymer class to efficiently inscribe long-term stable volume gratings into thick samples. Consequently, several research groups have investigated azobenzene-containing block copolymers.<sup>[39–44]</sup> A general problem of azobenzene-containing polymers, however, is that the improved stability of inscribed gratings usually comes at the cost of a decreased writing speed. Very recently, an interesting approach to increase the formation speed of holographic gratings by doping an azopolymer with a low-molecular-weight plasticizer was demonstrated (see Figure 75).<sup>[140]</sup>

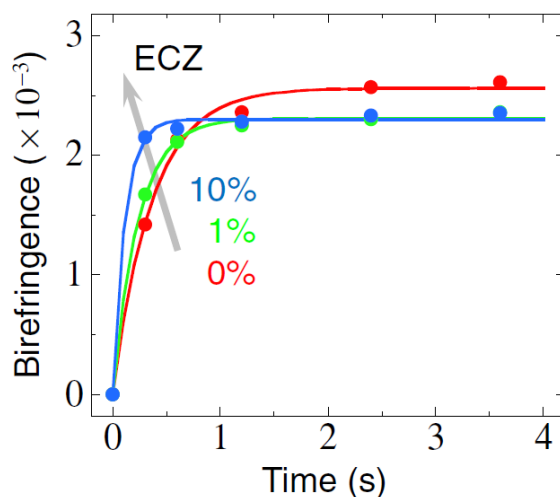


Figure 75: Temporal evolution of the photo-induced birefringence in dependence of the amount of plasticizer added to the azobenzene-functionalized polymer (solid lines: fitted curves).<sup>[141]</sup>

The addition of 0, 1, and 10 wt.-% of plasticizer to the azobenzene-functionalized polymer decreased the inscription time from 0.36 over 0.24 to 0.11 s, respectively. Thus, the addition of plasticizer significantly improved the writing speed by plasticizing the polymer matrix. However, the long-term stability of the inscribed gratings was negatively affected.

Molecular glasses can be employed in optical and optoelectronic devices, and photo-lithographic and nanoimprint processes.<sup>[68–72]</sup> Typically, these compounds feature high glass transition temperatures  $T_g$  and form stable amorphous phases. In contrast to functional polymers, molecular glasses feature a well-defined molecular structure without structural defects and undefined end groups. Photochromic molecular glasses were mainly investigated to study SRG formation.<sup>[74,75]</sup> Usually, owing to the absence of entanglements which hamper the mass transport, the SRG formation is much faster than in polymeric materials. It was also demonstrated that bulk birefringence, i.e., an optically induced reorientation of the azobenzene chromophores, takes place in thin films of photo-responsive molecular glasses, also the formation rate being faster than in polymers.<sup>[81–85]</sup> As in the case of polymers, stable volume gratings were only obtained if the azobenzene moieties are decoupled from the rigid molecular core, which allows for the formation of a LC phase.<sup>[86]</sup>

Here, a promising approach to improve the holographic recording speed of photo-orientable polymers is presented by blending them with an azobenzene-containing molecular glass acting as photo-orientable plasticizer. In contrast to conventional plasticizers, the photochromic molecular glass is plasticized upon exposure only, thus enabling the azobenzene moieties of the polymers to orient more quickly during exposure. After switching-off the writing laser light, the molecular glass hardens again and the long-term stability of the inscribed gratings is retained. This concept is

comprehensively studied by blending polymers such as photoinactive polystyrene, an azobenzene-containing homopolymer as well as two different photo-orientable block copolymers with a molecular glass. In polystyrene and in the photo-active homopolymer, the molecular glass is distributed randomly, whereas in block copolymers the low-molecular-weight compound is expected to accumulate in the azobenzene minority phase. A schematic depiction of the concept is shown in Figure 76.

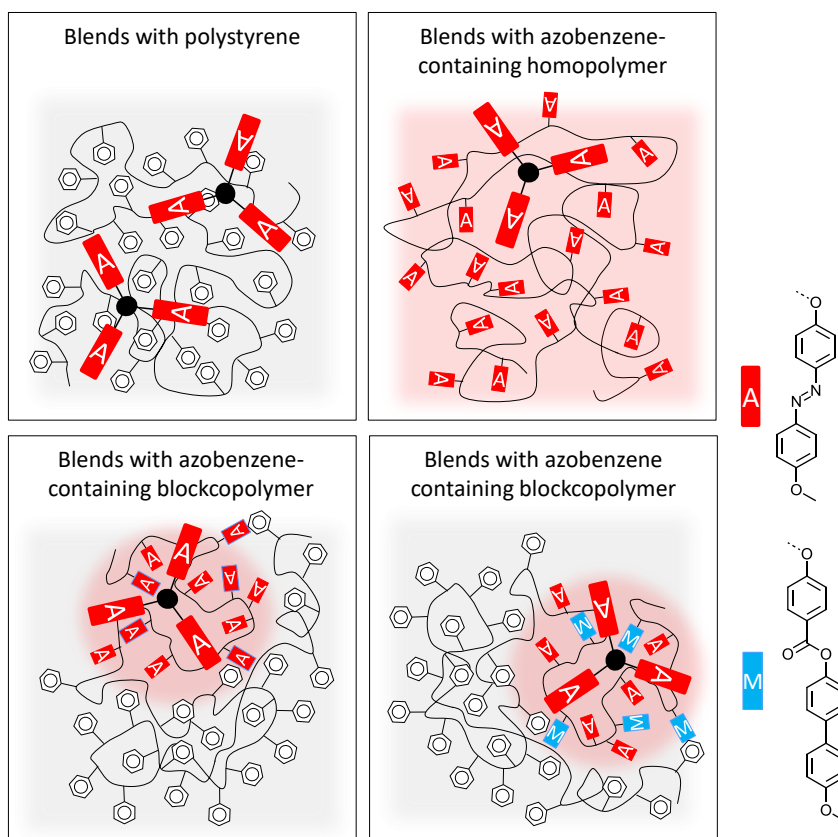


Figure 76: Schematic depiction of the general concept of improving the holographic performance of polymers by blending them with a photochromic molecular glass.

## 5.2 Materials

As materials, an azobenzene-functionalized molecular glass, three photo-orientable polymers (see Figure 77) and polystyrene were selected. To demonstrate how the orientation rate of azobenzene moieties in functionalized polymers is affected different photoactive are blended with photo-active **MG1**.

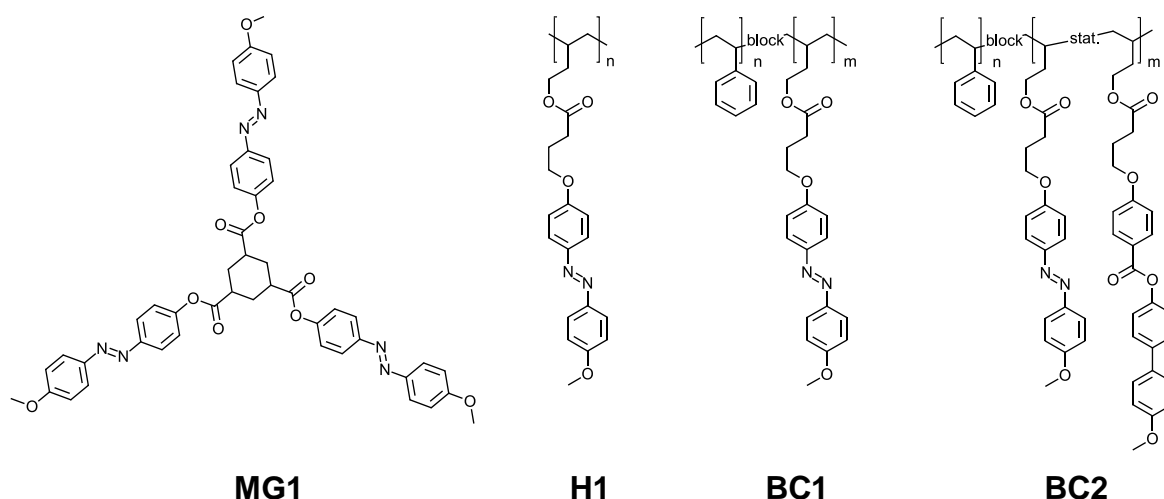


Figure 77: Chemical structure of the investigated methoxyazobenzene-functionalized molecular glass **1** of the investigated methoxyazobenzene-functionalized homopolymer **2** and block copolymers **3**. Block copolymer **4** comprises additional non-photoactive mesogenic side groups.

Compound **MG1** was synthesized by R. Walker and is based on a 1,3,5-substituted cyclohexane core with three azobenzene arms attached by an esterification reaction similar as reported previously.<sup>[142]</sup> The required hydroxyl-functionalized azobenzene moieties are accessible by a common azo-coupling reaction as described in basic literature.<sup>[85]</sup> Figure 78 depicts DSC traces of second heating and first cooling from 30°C to 250°C for **MG1**.

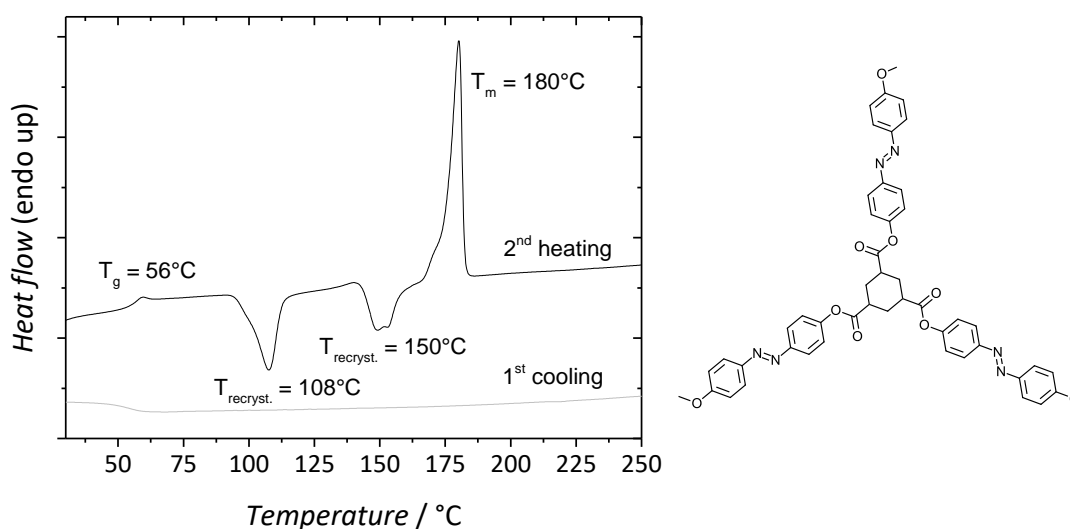


Figure 78: DSC traces of compound **MG1** during heating and cooling at a scan rate of 10 K/min under a N<sub>2</sub>-flow of 50 mL/min.

**MG1** features a glass transition temperature of 56°C. **MG1** tends to recrystallize between 90-120°C and 135-165°C and eventually melts at 180°C. During cooling, however, no crystallization occurs, so that the material can easily be quenched into a stable amorphous phase. It has been selected for its high orientation rate and its ability to form a stable amorphous phase at room temperature.<sup>[92]</sup> In the neat material, holographically inscribed gratings are not long-term stable.

The polymers were synthesized by R. Walker and were chosen to feature good processability to yield transparent thin films, and to possess a good miscibility with molecular glass **MG1**. The synthesis of these polymers has been described elsewhere.<sup>[38,143]</sup> All three selected photo-orientable azobenzene polymers feature methoxy-azobenzene chromophores, which were attached to the backbone as side groups. They exhibit good processability and yield transparent films. Azobenzene-containing homopolymer **H1** has a molecular weight  $M_n$  of 200000 g/mol, a PDI of 1.4 and a glass transition temperature of 47 °C. Azobenzene block copolymer **BC1** comprises a polystyrene majority block and a methoxy-azobenzene side group block. The molecular weight  $M_n$  of the block copolymer is 59000 g/mol, the PDI is 1.04. The weight fraction of the majority block and the azobenzene-containing minority block is 82.5 wt.-% and 17.5 wt.-%, respectively. Block copolymer **BC2** has a molecular weight  $M_n$  of 127000 g/mol and a PDI of 1.05. It features a polystyrene majority block and a minority block, which is composed of methoxy-azobenzene and non-photoactive mesogenic side groups. The weight fraction of the majority block and the azobenzene-containing minority block is 72 wt.-% and 28 wt.-%, respectively. Within the minority block, the ratio of azobenzene units to non-photoactive units is 46:54 mol.-%. Owing to the liquid-crystalline properties of the non-photoactive mesogenic side groups, the refractive-index modulation in block copolymers of this type is increased and, more importantly, also stabilized.<sup>[54]</sup>

As mentioned above, in polystyrene and homopolymer **H1**, the molecular glass is distributed randomly. Figure 78 depicts the differential scanning calorimetry scans of photoactive homopolymer **H1**. Upon heating, **H1** shows two melting points at 83°C and 115°C. After the first melting, the polymer recrystallizes at 95°C. Upon cooling, the polymer crystallizes at 94°C and 78°C. The DSC experiments in combination with polarization microscopy investigations did not show a liquid crystalline phase, which, owing to the form anisometric shape of the chromophore, could have been expected. Homogeneous transparent films with a stable amorphous phase at room temperature can be obtained via spin-coating.

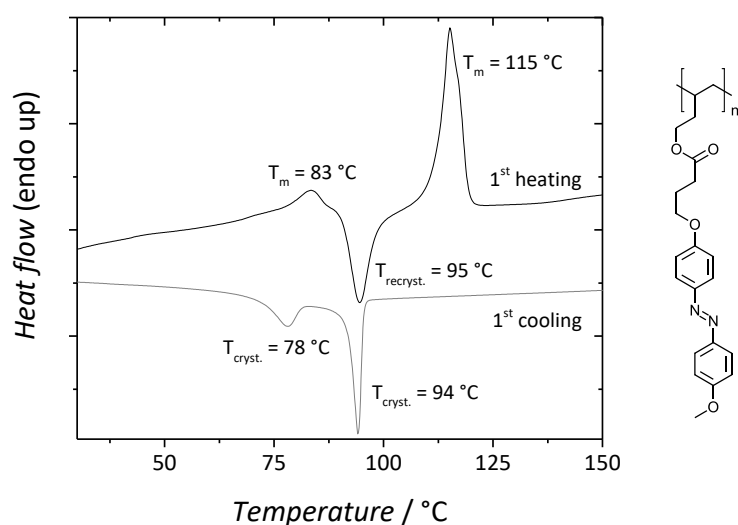


Figure 79: DSC traces of compound H1 during heating and cooling at a scan rate of 10 K/min under a N<sub>2</sub>-flow of 50 mL/min.

Block copolymer **BC1** features a non-photoactive polystyrene block and a methoxy-azobenzene-functionalized minority segment. The weight ratio of the polystyrene block is approximately 80 %. Figure 80 depicts DSC traces of **BC1** in the three heating and cooling cycles carried out from 30°C–150°C at a scan rate of 10 K/min. The first heating of the block copolymer reveals a broad melting peak, which is assigned to the minority phase. Moreover, the polymer features a glass transition at a temperature of 101°C caused by chain segment mobility of the majority block.

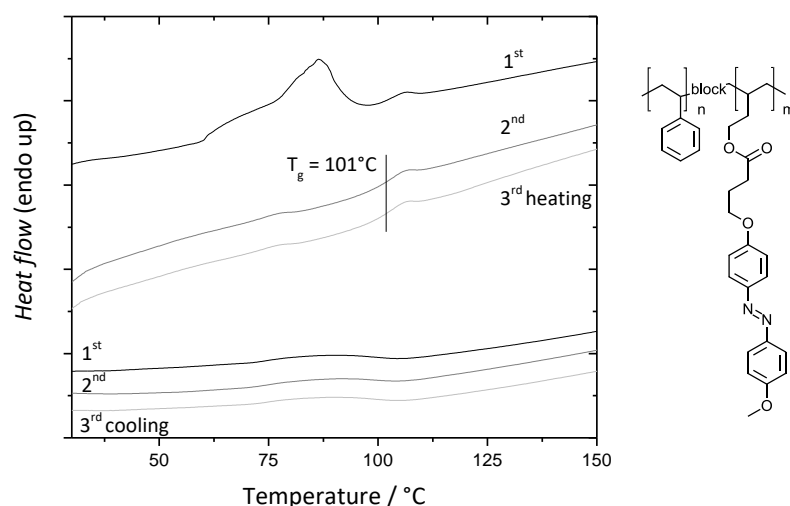


Figure 80: DSC traces of compound BC1 during heating and cooling at a scan rate of 10 K/min under a N<sub>2</sub>-flow of 50 mL/min.

Upon cooling, the polymer remains amorphous. The minor peak at 78°C during second heating can be allocated to the azobenzene-functionalized minority block and could might be assigned to the glass transition temperature of the same.

Besides photoactive azobenzene side groups, block copolymer **4** also contains non-photoactive mesogenic moieties in the minority block. Owing to these liquid crystalline moieties, the refractive-

index modulation in this block copolymer is increased and more importantly stabilized.<sup>[143]</sup> Figure 81 depicts the second heating and first heating DSC traces of **BC2** carried out from 30°C–250°C at a scan rate of 10 K/min.

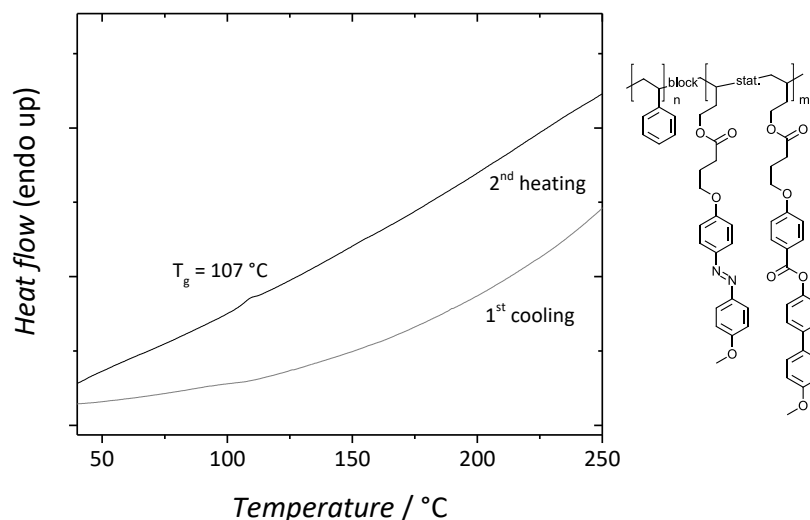


Figure 81: DSC traces of compound BC2 during heating and cooling at a scan rate of 10 K/min under a N<sub>2</sub>-flow of 50 mL/min.

The amorphous block copolymer has a glass transition temperature of 107°C, which is attributed to the PS block and can easily be transferred to homogenous, transparent films. Even though the weight of the minority block is about 30 %, the glass transition of the minority block is not visible in the DSC traces.

The thermal data of the compounds used in this chapter are summarized in Table 9.

Table 9: Characterization data of investigated azobenzene molecular glass MG1, photo-orientable azobenzene homopolymer H1 and the azobenzene block copolymers without (BC1) and with (BC2) additional non-photoactive mesogenic side groups.

Compound	T <sub>g</sub> / °C	T <sub>m</sub> / °C	M <sub>n</sub> / g/mol	PDI	w <sub>Minor</sub> / w <sub>PS</sub> / wt.-%	Azobenzene / mesogen content / mol-%
MG1	58	180	-	-	-	-
H1	47	115	2.0·10 <sup>5</sup>	1.4	-	-
BC1	101	-	5.9·10 <sup>4</sup>	1.04	17.5 / 82.5	100 / 0
BC2	107	-	1.27·10 <sup>5</sup> *	1.05	28* / 72	46 / 54

\* w<sub>Azo</sub> = 11 wt.-%; w<sub>Meso</sub> = 17 wt.-%

### 5.3 Influence of the molecular glass on the writing time

In holographic experiments, volume phase gratings were inscribed in thin films of the chosen materials with s:s-polarized beams with a wavelength of 488 nm to ensure efficient suppression of SRG formation.<sup>[144,145]</sup> Figure 82 shows an exemplary holographic grating inscription curve.

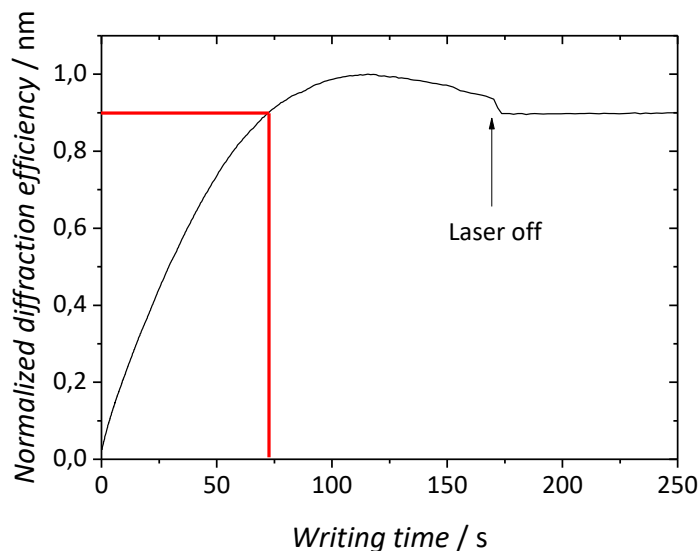


Figure 82: Example of a writing curve in a holographic experiment. The red lines indicate the point, at which 90 % of the diffraction efficiency is reached.

Typically, the evolution of the refractive index modulation  $n_1$  during exposure is characterized by a steep increase of  $n_1$ , followed by a broad maximum and a decay of  $n_1$  caused by overexposure of the illuminated areas. In certain cases, the time to reach the maximum refractive-index modulation  $n_1$  cannot be easily determined. Thus, for the sake of better comparability of experiments, the quantity  $t_{90\%}$  is introduced, which is defined as the time period required to reach 90% of the maximum diffraction efficiency. The highest achievable refractive-index modulation  $n_{1,max}$  is calculated from the maximum diffraction efficiency according to the scalar theory for thin volume holograms by Magnusson and Gaylord.<sup>[146]</sup>

To gain insight into the photophysical behavior of the low-molecular-weight compound **MG1** in blends with block copolymers, blends of polystyrene and the photoactive homopolymer with **MG1** were investigated first, as these two polymers represent the two blocks of the block copolymers investigated in this chapter. For that reason, a series of blends of commercially available polystyrene (BASF 165H) with azobenzene molecular glass **MG1** in a concentration range from 6 to 50 wt.-% of **MG1** is prepared by spin-coating from solution. The thin films feature a thickness of approx. 1.5  $\mu\text{m}$ . The good optical quality of the transparent samples is maintained throughout the entire concentration series, indicating a homogeneous distribution of the molecular glass in polystyrene. As reference sample, a thin film of the neat compound **MG1** featuring a thickness of about 300 nm is prepared by spin-coating from solution. Within the concentration series, the hologram writing time  $t_{90\%}$  is constantly below 1 s over a concentration range from 50 to 20 wt.-% being very similar to the performance of the neat sample. This result is in agreement with previously reported results from H. Audorff et al.<sup>[85]</sup> If the concentration of the photo-plasticizer is further decreased, however, the writing time increases significantly. Eventually, at a concentration of 6 wt.-%, the writing time  $t_{90\%}$  is 211 s. This corresponds to an increase of more than two orders of

magnitude compared to the higher concentrated blends and the neat sample (see Figure 83). This finding indicates that a cooperative effect, present between the azobenzene moieties at high concentrations of the same, extenuates significantly upon dilution of the chromophores in the PS matrix until the cooperative effect is lost.

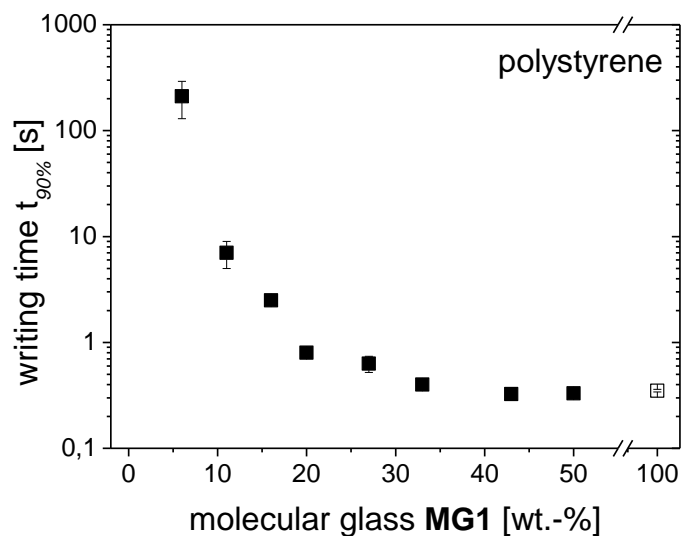


Figure 83: Time to reach 90% of the maximum diffraction efficiency as a function of the concentration of the molecular glass in non-photoactive polystyrene (filled squares) in comparison to the neat molecular glass **MG1** (open square).

In a similar manner, a concentration series of blends with weight fractions of **MG1** between 1 and 80 wt.-% in the azobenzene-containing homopolymer **H1** were prepared by doctor-blading exhibiting typical film thicknesses in the range of  $450 \text{ nm} \pm 200 \text{ nm}$ . All samples are highly transparent, homogeneous and do not show light scattering. In addition, a thin film of the neat homopolymer **H1** was prepared as reference sample. Since in this blend series two photoactive materials were chosen, the writing times  $t_{90\%}$  must lie between the performance of the neat individual materials, which are 0.35 s for the neat compound **MG1** and 6.9 s for neat homopolymer **H1** (see Figure 84). As in the previous blend series, at high concentrations of **MG1** (between 40 and 80 wt.-%), the writing times are almost equal to that of neat **MG1**, thus are largely dominated by the performance of the molecular glass. However, at a relatively low concentration of 10 wt.-% molecular glass in **H1**, the corresponding writing time  $t_{90\%}$  is still only 3.6 s. This means an improvement of a factor of 2 in the writing speed compared to the neat polymer. The writing time  $t_{90\%}$  of the polystyrene blend consisting 10 wt.-% of **MG1** is 7 s. These results indicate that in a blend comprising only a small weight fraction of compound **MG1** and a block copolymer with a photo-inactive polystyrene majority block and a photoactive block, the molecules of **MG1** located in the polystyrene segment, cannot significantly contribute to the overall holographic performance due to resulting overexposure of the photoactive segment. In addition to this insight, the improvement of writing speed in the examined blends with the homopolymer shows that the cooperative effect, which is important for both, the photo-plastification and the photo-orientation, is maintained in these systems.

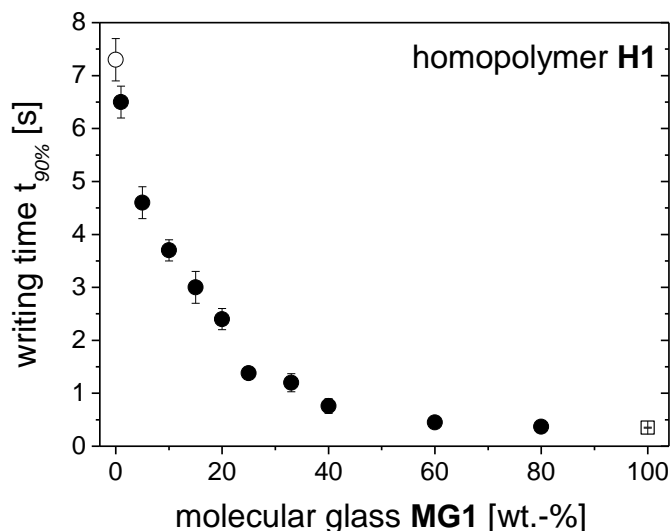


Figure 84: Time to reach 90% of the maximum diffraction efficiency as a function of the concentration of molecular glass **MG1** in photoactive homopolymer **H1** (filled circles), in comparison to the neat polymer (open circle).

Azobenzene-containing homopolymers are suitable for the inscription of thin holographic gratings. In contrast, photo-active block copolymers represent a promising concept to study thick gratings with a suitable optical density enabling angular multiplexing and high-density holographic data storage.<sup>[147]</sup> To further assess and apply the former findings, the photophysical behavior of photo-orientable block copolymer **BC1** were investigated. Therefore, blends with **BC1** with a content of photo-plasticizer **MG1** ranging from 0.25 to 40 wt.-% were prepared by doctor-blading. The average film thickness is 1.5  $\mu\text{m}$ . In addition, a thin film of neat block copolymer **BC1** with a film thickness of 1.7  $\mu\text{m}$  was prepared as a reference. As shown in Figure 85, all blends feature improved writing times compared to the neat sample. As demonstrated earlier, at concentrations higher than 10 wt.-%, the photophysical behavior of blends of **MG1** with polystyrene or photo-active **H1** cannot be clearly distinguished as the photophysical behavior of the molecular glass dominates. Again, at lower concentrations than 10 wt.-%, the amount of molecular glass molecules located in the inert PS majority block of **BC1** does not contribute to the holographic writing performance since the inscription time would be significantly higher than the inscription time of the minority block (see Figure 83). Compared to the neat sample, the writing time for the inscription of gratings into thin films of the block copolymer blend is nearly halved to 2.5 s at content of 5 wt.-% of **MG1** (see Figure 85). These results suggest that **MG1** accumulates in the photo-active minority phase of the block copolymer (compare to Figure 84). Consequently, the molecular glass is not distributed randomly within the different polymer segments. In addition to shortened grating inscription times, blending of block copolymer **BC1** with the molecular glass also leads to an improved homogeneity of the films. Accordingly, as indicated by the error bars, the writing times become more reproducible with increasing amount of **MG1**.

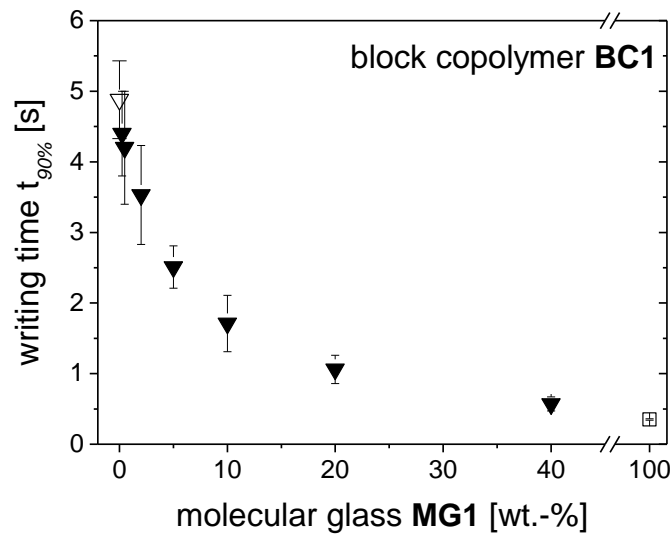


Figure 85: Time to reach 90% of the maximum diffraction efficiency as a function of the concentration of molecular glass **MG1** in photoactive block copolymer **BC1** (filled triangles) in comparison to the neat polymer (open triangle).

While block copolymer **BC1** provides fast inscription rates, it fails to store inscribed gratings for longer than a few days.<sup>[148]</sup> Recently, it was shown that polymer systems bearing mesogenic side groups can feature long-term stable gratings.<sup>[143]</sup> Due to the additional orientation of the non-photoactive mesogens, however, the orientation speed of the azobenzene moieties is quite low. In order to study the response characteristics of such kind of block copolymer in the presence of **MG1**, blends of photo plasticizer **MG1** and the photo-orientable block copolymer **BC2** with concentrations in the range of 0.5 to 15 wt.-% of **MG1** were prepared by spin-coating. The film forming technique yielded films of good optical quality with thicknesses of approx. 0.8  $\mu\text{m}$  on average. As in case of block copolymer **BC1**, the photochromic molecular glass is expected to migrate into the photoactive block and increase the orientation speed of the azobenzene side groups by plastification of their immediate surroundings. As stated earlier, the contribution of **MG1** to the holographic performance located in the inactive polystyrene block is negligible at concentrations below 10 wt.-%. Compared to the neat sample, all blends feature significantly improved writing times  $t_{90\%}$  even at very low concentrations of **MG1** (see Figure 86). The effect is even more pronounced than in block copolymer **BC1**. With 15 wt.-% of **MG1**,  $t_{90\%}$  is reduced by a factor of 15. Moreover, increasing content of **MG1** again leads to better reproducibility of the holographic experiment.

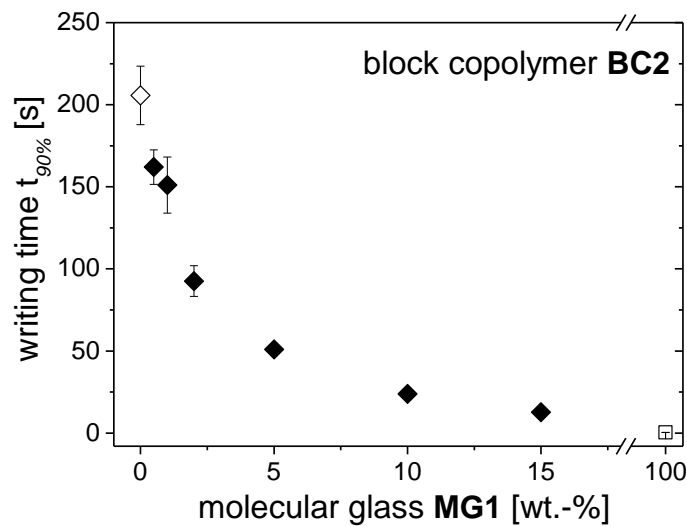


Figure 86: Time to reach 90% of the maximum diffraction efficiency as a function of the concentration of molecular glass **MG1** in photoactive block copolymer **BC2** (filled diamonds) in comparison to the neat polymer (open diamond).

#### 5.4 Influence of the molecular glass on the refractive-index modulation

The refractive-index modulation  $n_1$  is one of the most important holographic characteristics and is related to the photo-induced anisotropy. However, to compare the photo-induced anisotropy in a concentration series, the refractive-index modulation  $n_1$  must be normalized to the optical density at the writing wavelength,  $OD_{488}$ , divided by the sample thickness, since this parameter is proportional to the azobenzene concentration. The difference in the absolute refractive-index modulation and its normalized equivalent is demonstrated by the data obtained from the blends of **MG1** with polystyrene (see Figure 87). Whereas the normalized  $n_{1, \text{norm.}}$  values are roughly constant and comparable to the value of neat glass **MG1**, the absolute numbers ( $n_{1, \text{max}}$ ) decrease by an order of magnitude with decreasing concentration.

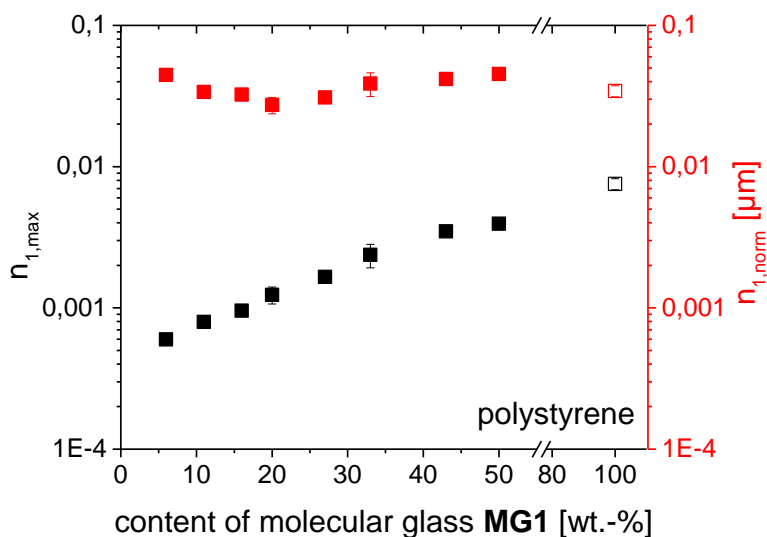


Figure 87: Maximum refractive-index modulation  $n_{1,max}$  and its normalized value  $n_{1,max}$  for different concentrations of molecular glass **MG1** in a) homopolymer **H1**, b) block copolymer **BC1** and c) block copolymer **BC2**. Data of the neat materials are shown with open symbols.

The blends with the photoactive polymers feature refractive-index modulations, which can approximately be described as linear combinations of the values of the respective polymer and compound **MG1**. Homopolymer **H1** has the highest  $n_{1,max}$  compared to the block copolymers and the molecular glass; hence,  $n_{1,max}$  of blends of homopolymer **H1** with **MG1** decreases from  $20.0 \cdot 10^{-3}$  to  $7.5 \cdot 10^{-3}$  (Figure 88 a). The refractive-index modulation of block copolymer **BC1** is lower than that of neat **MG1**. In blends with **MG1**,  $n_{1,max}$  increases from  $2.0 \cdot 10^{-3}$  to  $7.5 \cdot 10^{-3}$  with increasing concentration of **MG1** (Figure 88 b). Because the refractive-index modulation in neat block copolymer **BC2** is  $5.5 \cdot 10^{-3}$ ,  $n_{1,max}$  remains almost constant throughout the whole concentration series (Figure 88 c).

As it is the case for the absolute value  $n_{1,max}$  neat homopolymer **H1** features the highest normalized refractive-index modulation of all investigated systems of about  $0.16 \mu\text{m}$  (Figure 88 a). With increasing content of molecular glass **MG1**, however, this value decreases until the value of the neat compound **MG1** is reached. The values of  $n_{1,neat}$  for neat copolymer **BC1** and **BC2** are  $0.11 \mu\text{m}$  and  $0.10 \mu\text{m}$ , respectively, and, therefore, are almost identical to each other (Figure 88 b, c). As in case of homopolymer **H1**, this value decreases with increasing amount of **MG1**. From this results we conclude that photo-induced anisotropy in the photo-active polymers is generally higher than in the molecular glass. However, at concentrations as high as 40 wt.-% of **MG1** in the blends with the azobenzene polymers, the photophysical properties are mostly dominated by the behavior of the molecular glass.

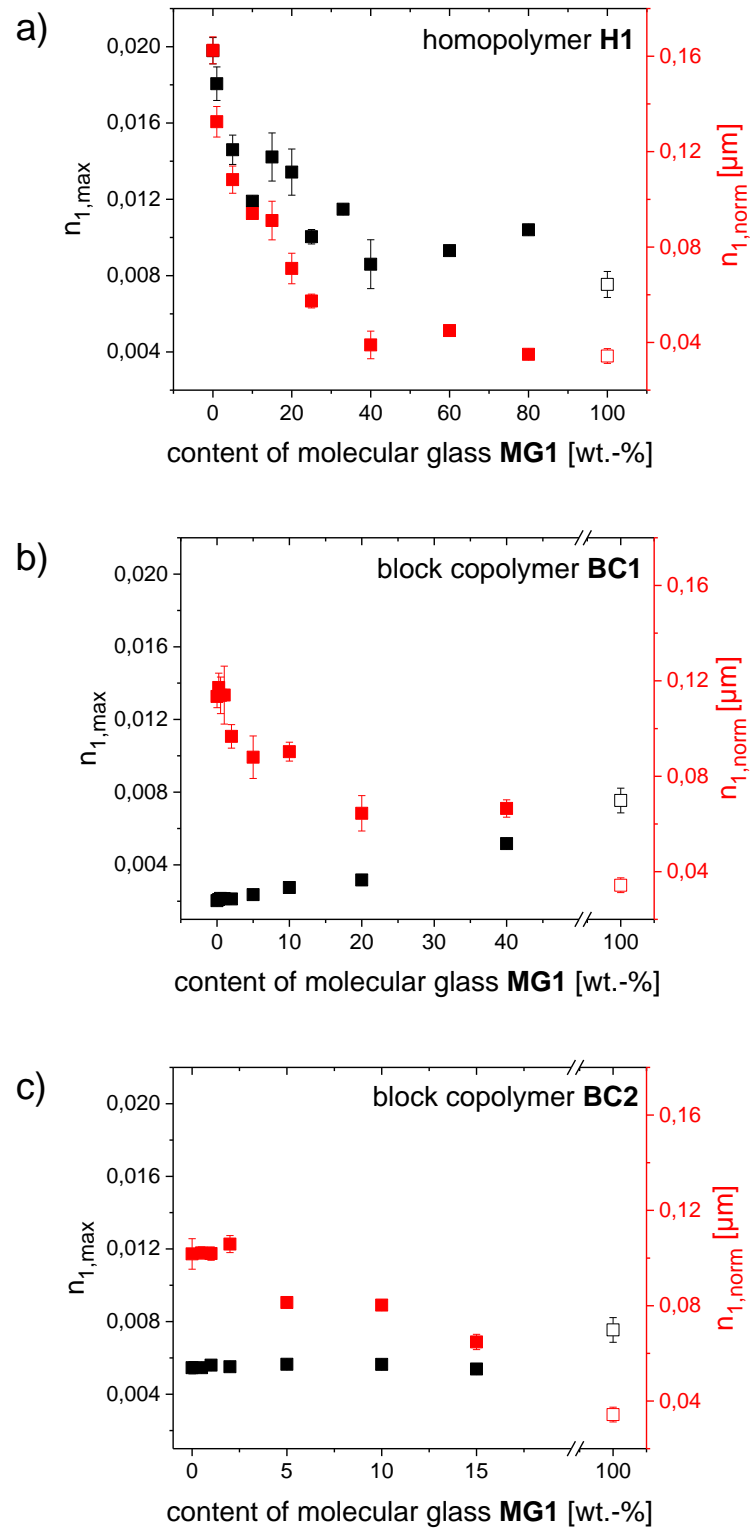


Figure 88: Maximum refractive-index modulation as a function of the concentration of molecular glass **MG1** in photo-orientable polymers **H1**, **BC1** and **BC2**. The data of the neat materials are indicated by open symbols. The open square corresponds to the neat glass.

## 5.5 Influence of annealing on writing time and refractive-index modulation

As shown previously, the molecular glass **MG1** accumulates in the photoactive block of the microphase-separated polymers. Partly, this accumulation occurs during the short period of the film preparation step. However, the diffusion might not be completed after this step. Hence, annealing of the thin films above the glass transition temperature of the PS majority block ( $T_g = 106^\circ\text{C}$ ) is expected to improve the phase separation and diffusion of **MG1** into the minority phase, and, consequently, leads to a more pronounced cooperative orientation. Therefore, a comparative study featuring two samples, a neat block copolymer **BC2** and a blend of **BC2** with 10 wt.-% of **MG1** is conducted. Each film is annealed for 3 h at a given temperature and subsequently cooled down to room temperature prior to the inscription of the volume gratings. This procedure is repeated in  $10^\circ\text{C}$  intervals in the range from  $70^\circ\text{C}$  to  $130^\circ\text{C}$ .

The maximum refractive-index modulation as a function of annealing temperature is studied in both samples (see Figure 89). Here, normalization of the refractive index data is not necessary, since the total number of azobenzene moieties in the sample is constant. Taking the large error bars into account,  $n_{1,\text{max}}$  is nearly constant in neat copolymer **BC2**. Since the number of azobenzene molecules in the illuminated volume of the intensity grating must be constant during the annealing process, this result was to be expected. Interestingly, the blend sample shows a slight drop of  $n_{1,\text{max}}$  at temperatures above  $100^\circ\text{C}$ . This can be attributed to an increasing disorder in the photoactive block caused by migration of the molecular glass from the polystyrene matrix into the minority phase of **BC2** upon annealing above the glass transition temperature of the PS block. This results correlates with an increasing content of **MG1** in the photoactive segment as shown in Figure 89.

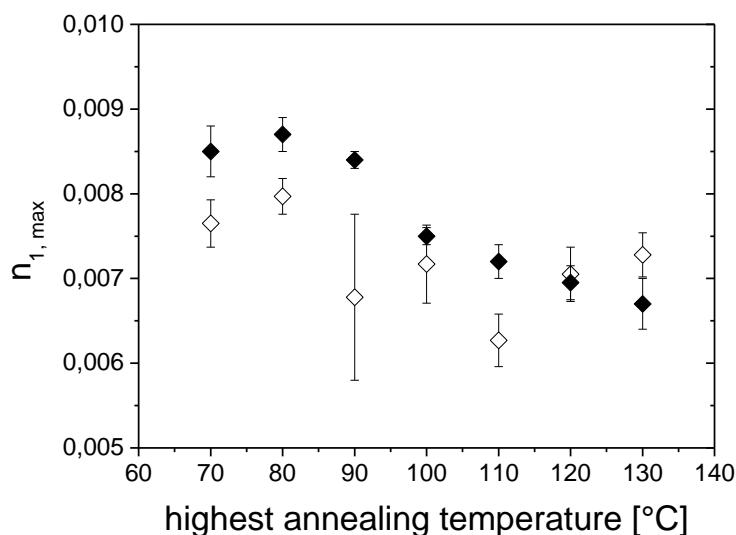


Figure 89: Maximum refractive-index modulation as a function of the annealing temperature in thin films of neat block copolymer **BC2** (open diamonds) and a blend with 10 wt.-% of molecular glass **MG1** (filled diamonds).

In addition to the refractive-index modulation, the evolution of writing times with increasing annealing temperatures is investigated. In the neat block copolymer  $t_{90\%}$  gradually decreases from 315 s to approx. 150 s and eventually, above the glass transition temperature of polystyrene, reaches a constant value (see Figure 90). At the same time, the holographic inscription becomes more reproducible as indicated by the smaller error bars. Both observations are attributed to an

improved microphase separation of the material resulting in enhanced cooperative effects between the azobenzene moieties. In contrast, the blend of **MG1** and **BC2** shows a considerably improved reproducibility of the writing times even for annealing temperatures below the glass transition temperature of the polystyrene matrix. The improved homogeneity of the holographic experiments in the blends compared to the neat polymers is in agreement with the previously shown results (see Figure 86). In similar manner, the writing times for the blend decrease to about the half of the initial value from 25 to 13 s if the annealing temperature is higher than the glass transition temperature of the majority segment. As  $n_{1,max}$  and, therefore, the order in the photo-active block decreases during annealing, the improved writing time in the blends upon annealing is not attributed to an enhanced microphase separation of the block copolymer, but to the migration of **1** into the minority segment.

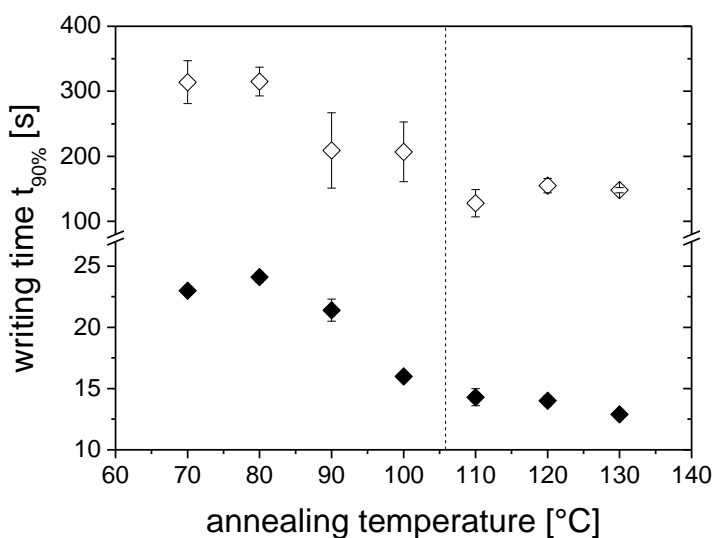


Figure 90: Writing time  $t_{90\%}$  as a function of the highest annealing temperature for neat photo-orientable block copolymer **BC2** (open diamonds) and a blend of **BC2** with 10 wt.-% of molecular glass **MG1** (filled diamonds). The glass transition temperature of the polystyrene segment is indicated at 106°C.

## 5.6 Influence of the molecular glass on the long-term stability of inscribed gratings

Inscribed holographic grating in the volume of the molecular glass **MG1** and the block copolymer **BC1** are not long-term stable and eventually decay within days or weeks.<sup>[85]</sup> In contrast, holographic gratings in thin films of photo-orientable polymers **H1** and **BC2** do not decay but show post-development of inscribed holograms, i.e., an increase of the refractive-index modulation after switching off the laser. Figure 91 depicts the temporal evolution of the normalized refractive-index modulation in blends of molecular glass **MG1** in homopolymer **H1** in a concentration range of 10–40 wt.-% of **MG1** after the inscription of a holographic grating. In this system, the optimum content of the molecular glass is around 25 wt.-%. At this concentration, the gain in writing speed is maximized ( $t_{90\%} \approx 1$  s) while, at the same time, the holographic gratings are long-term stable featuring a constant refractive-index modulation. At higher concentrations of **MG1**, the holograms begin to decay. At lower concentration of molecular glass, the post-development of the holographic gratings becomes increasingly pronounced. Thus, a blend of homopolymer **H1** with a content of 25 wt.-% of photo-plasticizer **MG1** exhibits excellent properties for volume holography in thin films.

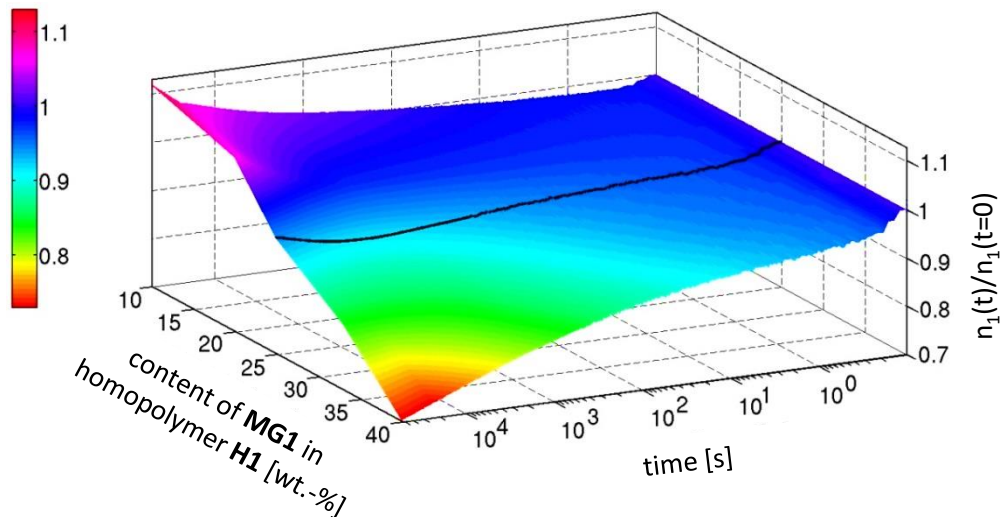


Figure 91: Temporal evolution of the normalized refractive-index modulation in blends of molecular glass **MG1** with photo-orientable homopolymer **H1** as a function of the content of **MG1** and the time after the end of hologram inscription. The refractive-index modulation has been normalized to its value immediately after the end of writing ( $t=0$ ). The black line indicates the blend with 25 wt.-% of molecular glass **MG1**, which still exhibits a positive slope of  $n_1(t)$  after 12 h. Here, the writing intensity is  $2 \text{ W/cm}^2$ .<sup>[132]</sup>

Photoactive block copolymers, such as **BC2**, possess the ability to store inscribed holograms for more than two years<sup>[143]</sup>, while being able to be processed to thick samples of suitable optical density. The stability of blends is examined on the basis of four samples with different concentrations of molecular glass **MG1** in the range from 5 to 15 wt.-% up to 21 hours (see Figure 92).

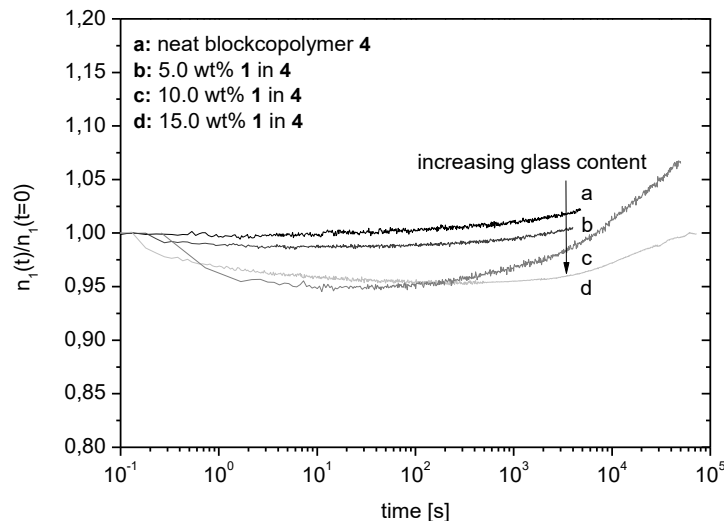


Figure 92: Temporal evolution of the refractive-index modulation after the end of the inscription process in neat block copolymer **BC2** and three blends with molecular glass **MG1**. All gratings are inscribed to the maximum refractive-index modulation.  $n_1(t)$  has been normalized to its value immediately after the end of writing  $n_1(t=0)$ . The data are presented on a logarithmic time axis.

In contrast to the neat block copolymer **BC2**, the blends exhibit a slight drop in  $n_1$  in the first few seconds after the inscription process. This effect is most pronounced for concentrations of **MG1** being higher than 10 wt.-%. At these concentrations a considerable amount of **MG1** in the PS

segment is oriented as well, which leads to a decay of the grating after a short period of time. After several seconds,  $n_1$  is constant, because the decay of **MG1** in the PS segments overlaps with the post-development in the minority block, which eventually is the solely process after some minutes. The data indicates an optimum composition of approximately 15 wt.-% of **MG1**, which combines a high writing speed with a stable  $n_1$ .

## 5.7 Summary of the chapter

In this chapter, the influence of blending photo-orientable polymers with an azobenzene molecular glass on the holographic recording performance is investigated. The photophysical behavior, in particular the holographic recording performance, of the neat molecular glass and its blends with photoactive and non-photoactive homopolymers is investigated first. In blends with non-photoactive polystyrene, the high writing speed of the molecular glass is retained for dilutions down to about 30 wt.-% demonstrating that a cooperative effect between the **MG1** molecules is present. In blends with the photo-orientable polymers, already small amounts of the molecular glass lead to significant shortening of the writing times. This improvement applies for the methoxy-azobenzene-substituted homopolymer as well as for the two investigated photo-active block copolymers. The results imply that the molecular glass mainly accumulates in the azobenzene minority phase of the block copolymers and interacts with the azobenzene groups attached to the polymer backbone, thus accelerating the reorientation process. At the optimum concentration of low-molecular compound, the photo-induced plastification reduces the writing times by a factor of 15 in the photo-orientable block copolymer bearing non-photoactive mesogens. Annealing the samples above the glass transition temperature of the block copolymer increases the writing speed even further. Although the microscopic order in the polymer systems appears to be reduced by the molecular glass, the refractive-index modulation is not affected. Moreover, blending the photo-orientable polymers with the molecular glass leads to an improved homogeneity of the films, resulting in more reproducible holographic experiments. Hence, photo-plasticizing molecular glasses are promising materials to improve the performance of azobenzene polymers in volume holography, making these materials suitable for applications such as holographic data storage or as carrier of forgery-proof security features.

## 6 Photoactive azobenzene-containing polymer nanoparticles

### 6.1 Introduction to core/shell block copolymer nanoparticles

Polymer nanoparticles are a versatile material class, which has raised the interest of numerous research groups in the past decades and can be found in a wide range of technologies and applications like e.g. biotechnology, photonics, sensors, electronics, medicine or environmental technology.<sup>[149–156]</sup> In general, nanoparticles are most often described as colloidal, solid particles in a size range from 10-1000 nm.<sup>[157,158]</sup> Polymer nanoparticles (PnPs) is a general term, which describes nano spheres, solid particles or hollow nano capsules made from polymeric material.<sup>[156]</sup> Despite in general the shape of these particles is spherical, in literature also non-spherical particles are described as PnP.<sup>[159]</sup>

Besides polymer nanoparticles, core/shell-type polymer nanoparticles have risen academic and industrial interest.<sup>[160]</sup> The properties of these multi-compartment structures are depending on the composition and the shape of the particle. Hard core-soft shell PnPs can be used as latex particle in paints, whereas soft core-hard shell PnPs see use as e.g. impact modifiers.<sup>[160]</sup> Among the synthesis strategies to obtain core/shell polymer nanoparticles, emulsion, miniemulsion, dispersion and suspension polymerization techniques are prominent examples. The dispersion polymerization is widely used because of its simplicity and the possibility to polymerize a great variety of monomers. However, self-assembly is the most relevant method for the preparation of core/shell PnPs from block copolymers. Amphiphilic block copolymers have the tendency to self-assemble in solution into micellar structures of various kinds if the solvent is chosen properly. A method to form micellar structures is to solve a block copolymer in a common solvent, i.e., a good solvent for both blocks, and subsequently exchange the common solvent by a selective solvent, which one of the blocks prefers for example by dialysis. The self-assembly process into micelles is driven by the endeavor to reduce the surface energy and is affected by several factors including the molecular weight of the blocks, the solvent chosen and the chemical structure. If a segment of the polymer is pH- or thermosensitive, the micellation can be induced by change of the pH value or the temperature of the solvent.<sup>[161–166]</sup> The exact control of the micelle morphology is, however, challenging, since block copolymers can assemble into a great number of morphologies, as for example cylinders<sup>[167]</sup>, disks<sup>[168]</sup> or toroids<sup>[169]</sup> that may feature sizes ranging from a few nanometers to micrometers.<sup>[170]</sup> Micelles are often used as templates for the synthesis of the final core/shell nanoparticles. This synthesis is done via crosslinking-reactions of the well-defined macromolecular architectures. For this purpose, crosslinkable groups must be present in the block that is to be crosslinked. After crosslinking, the resulting nanoparticles are resistant to variations in pH, temperature or solvent. Figure 93 schematically depicts the process of self-assembly of a block copolymer in a solvent mixture with subsequent stabilization of the core/shell structure via crosslinking is shown. Here, the amphiphilic block copolymer could be crosslinked owing to the photo-crosslinkable dimethylmaleimid-containing core.

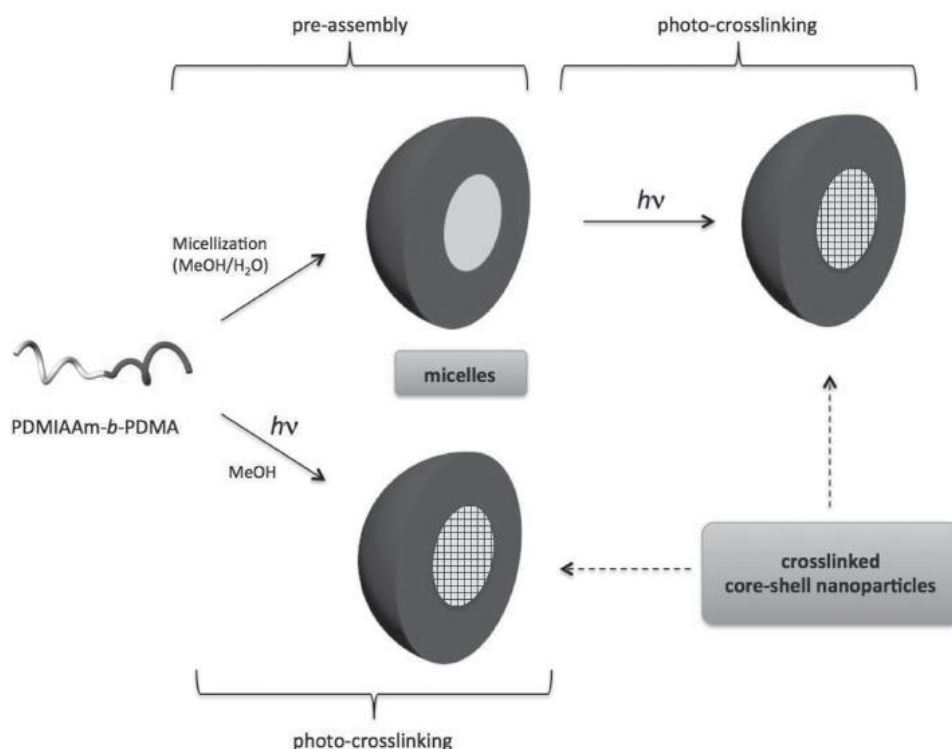


Figure 93: Schematic depiction of micellation of a block copolymer in a solvent mixture with subsequent intermolecular crosslinking of the core via UV light.<sup>[171]</sup>

In the example shown above, the core of the micelle is crosslinked. However, it is also possible to crosslink the entire shell, or at the interface between the solvent and the micelle.<sup>[160]</sup> pH sensitive polymeric micelles have the potential to see use as drug delivery system as they are able to carry hydrophobic drugs in their core and to release the drug at the targeted point.<sup>[172]</sup>

Microphase-separated structures are more stable in a bulk sample (film) than in solution. Thus, bulk crosslinking of self-assembled domains is superior to the preparation of core/shell particles via crosslinking of micelles in solution.<sup>[160]</sup> Using this synthetic route towards core/shell polymer nanoparticles, microphase separation of the block copolymer is a prerequisite. During block copolymer microphase separation, the interaction parameter  $\chi_{AB}$  (also referred to as Flory-Huggins parameter) between the monomers of type A and type B is a very important characteristic. The Flory-Huggins parameter is the driving force for the segments of the block copolymer to segregate. Along with the chain length  $N$  (degree of polymerization) and the composition  $f$  (monomer volume fraction of the minority block), it dictates the phase behavior.<sup>[173]</sup> In most cases, the interaction parameter is positive, meaning that the units A and B show repulsion between each other in order to minimize the contribution of interaction energy to the free energy.<sup>[174]</sup> Moreover, the Flory-Huggins parameter is inversely proportional to the temperature.<sup>[175]</sup> Hence, upon cooling, the blocks of the polymer are separating from each other to reduce the contact from each other. Owing to the chemical connection of the two blocks, the phase separation takes place on the micrometer scale and no macroscopic demixing occurs. Which kind of microphase morphology is formed is mainly determined by the volume fraction  $f$  and the product of  $\chi$  with the degree of polymerization  $N$ . In case of a sufficiently high degree of polymerization and repulsion of the building units A and B, spherical, cylindrical, gyroid, perforated lamellae or lamellae morphologies can be formed (see Figure 94).<sup>[176]</sup>

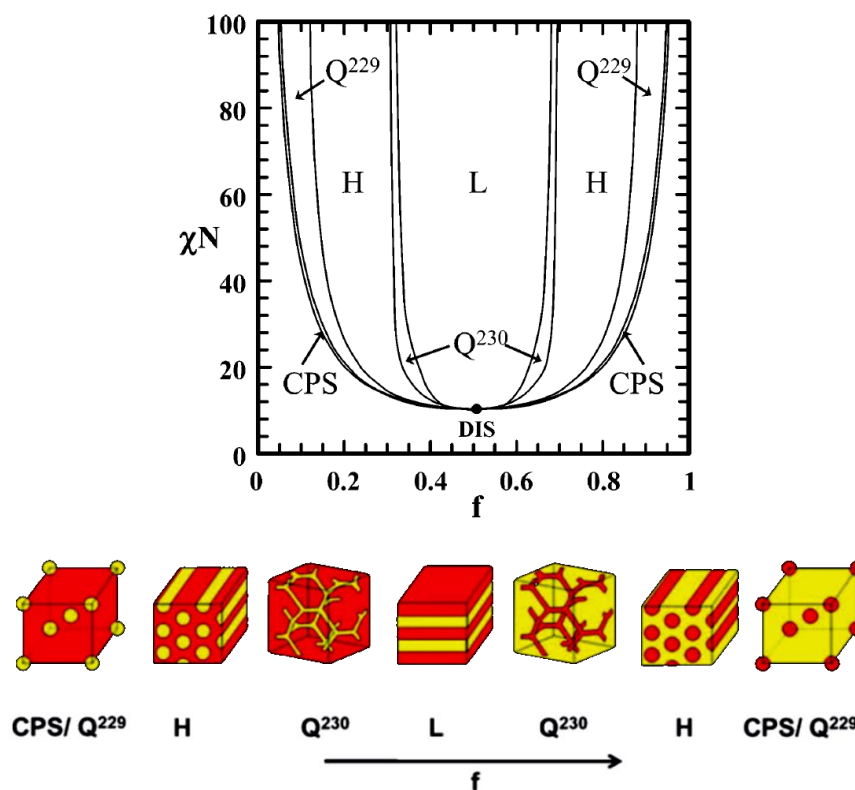


Figure 94: Top: Theoretical phase diagram for diblock copolymers. The phases are labeled as follows: L (lamellar), H (hexagonally arranged cylinders),  $Q^{230}$  (bicontinuous gyroid phase),  $Q^{229}$  (bcc spheres), CPS (close-packed spheres), and DIS (disordered phase). Below: Schematic illustration of the microphases.<sup>[177,178]</sup>

According to Landau theory, a block copolymer is expected to undergo a phase transition from disordered to the lamellar phase at a composition of  $f=0.5$  and  $\chi N=10.5$ .<sup>[175]</sup> The so-called mean-field theory, on the other hand, also allows for order-to-order transitions between the different phases by changing the product  $\chi N$ .

Crosslinking discontinuous domains of microphase separated block copolymers and subsequent dispersion in an appropriate solvent yields nano objects of controllable size and shape. These nano objects are intensively studied in various research groups. A prerequisite to generate such objects is a block which features functional groups that can be crosslinked. In literature, a great variety of suitable block copolymers have been proposed and appropriate crosslinking agents were investigated. Among the polymer systems, copolymers featuring crosslinkable blocks such as polybutadiene, polyisoprene, poly(3-(triethoxysilyl)propyl methacrylate), poly(2-cinnamoyloxyethyl methacrylate) have been studied comprehensively.<sup>[179–183]</sup>

In general, the theory of microphase separation of block copolymers can also be applied to block copolymers consisting of three blocks. Controlled microphase separation of these polymers with subsequent selective crosslinking allows for the synthesis of so-called Janus particles on the gram scale. The group of Prof. Dr. Müller has pursued this approach to generate a variety of different shaped Janus particles ranging from disk-like structures to cylindrical structures (see Figure 95).<sup>[184]</sup>

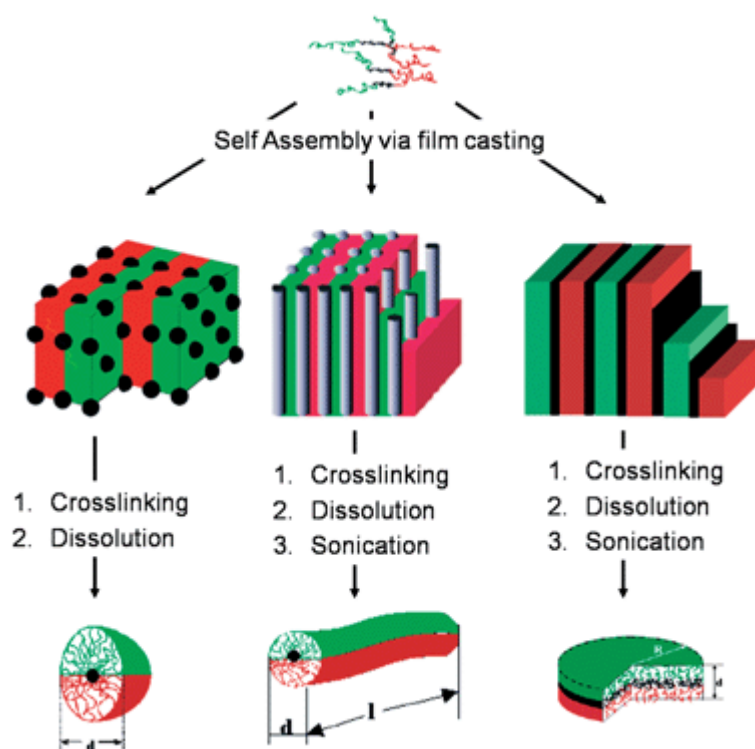


Figure 95: Schematic depiction of the preparation of so-called Janus particles via crosslinking of triblock copolymers in the bulk. The pathway to obtain Janus particles includes crosslinking of a microphase-separated triblock copolymer film and subsequent sonication.<sup>[185]</sup>

As polymer, a polystyrene-block-polybutadiene-block-poly(tert-butyl methacrylate) (SBT) triblock copolymer was chosen. The selective crosslinking of the polybutadiene block (PB) was performed either through radical crosslinking using azobisisobutyronitrile (AIBN) or by cold vulcanization with  $S_2Cl_2$ . In the first case, the triblock copolymer together with up to 5 wt.-% of initiator AIBN (related to the overall weight of all compounds) and 0-5 wt.-% of a trifunctional thiol (trimethylolpropane mercaptopropionate) to ensure a more complete crosslinking of the PB block are dissolved in  $CHCl_3$ . Afterwards, the solvent is evaporated in a desiccator for a period of about two weeks before a sonication treatment yielded the looked-for Janus particles. An alternative route towards these kind of particles is cold vulcanization using  $S_2Cl_2$ , of which about 1.5-5 vol.-% are introduced into a swollen film of the microphase-separated triblock copolymer.<sup>[186]</sup> In a similar manner, block copolymer nanofibers have been prepared from a polystyrene-block-polyisoprene block copolymer.<sup>[187]</sup> Here, however, the  $S_2Cl_2$  is introduced into the casted microphase-separated film by diffusion from the gas phase. The film is exposed to  $S_2Cl_2$  vapor for 1 week to ensure complete crosslinking of the polyisoprene cylindrical domains. During this period, a large excess of crosslinking agent is diffused into the approx. 5 mm thick film and yielded uniform crosslinking of the same. The nanofibers were obtained after dispersing the film in THF for a period of at least a week followed by several centrifugation steps to separate various length- and weight fractions from each other.

Crosslinking of segregated copolymer morphologies can also be performed using photo initiators. Schacher et al.<sup>[188]</sup> could obtain cylindrical nanoobjects from crosslinking a film of a polybutadiene-block-poly(2-vinyl pyridine)-block-poly(tert-butyl methacrylate) (BVT) block terpolymer casted together with up to 10 wt.-% of commercially available photo-initiator Lucirin-TPO<sup>®</sup> to crosslink the poly(butadiene) block. After successful crosslinking with an UV lamp for a period of 2 h, the film

was subjected to a sonication process and characterized via transmission electron microscopy and dynamic light scattering techniques (see Figure 96).

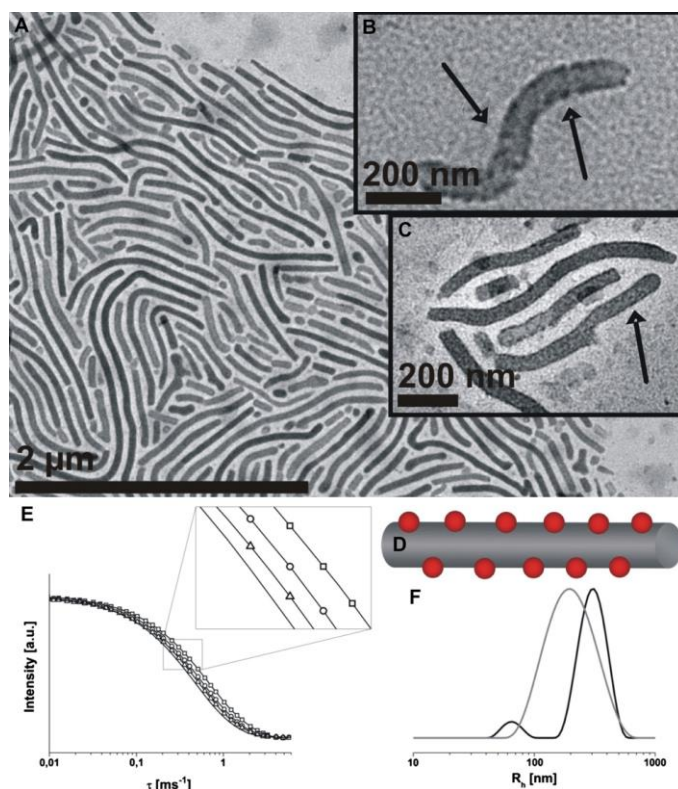


Figure 96: A, B and C: TEM micrographs of a crosslinked (BVT) block terpolymer after sonication and drop-coating from THF onto a TEM grid with enlargements after staining with iodine; D: illustration of the PB cylinder structure (grey) bearing poly(2-vinyl pyridine)-spheres (red) surrounded by a poly(*tert*-butyl methacrylate) matrix; E: DLS autocorrelation functions after sonication of the cross-lined film in THF for 1, 3, 5, and 10 min. F: DLS CONTIN plots for cylinders in THF after sonication for 1 min (black line) and 10 min (grey line).<sup>[188]</sup>

Besides non-functional objects, functionalized nanoobjects can also be obtained via diffusion-controlled crosslinking using a gaseous crosslinker.<sup>[189]</sup> In this case, the crosslinkable block consists of glycidyl methacrylate groups bearing an epoxy group, which can be crosslinked via ring-opening reactions using amines. The amines used for the crosslinking of the block copolymer can bear functional groups themselves, so that the properties of the final nanoobject can be adjusted. The schematic depiction of the synthesis of the functionalized polymeric nanoobjects is shown in Figure 97. The block copolymer chosen for this study is a poly(*tert*-butyl acrylate)-block-poly(glycidyl methacrylate) (PtBA-*b*-PGMA) copolymer, which is synthesized with different block ratios to enable the generation of different microphase morphologies and thus different shapes of nanoobjects. After crosslinking of the PGMA block under an atmosphere of amines, the PtBA block is hydrolyzed to poly(acrylic acid) so that the nanoobjects could be dispersed in water and show pH sensitivity. The amine used to crosslink the PGMA block is propargylamine bearing alkyne groups, which can be used to conduct click chemistry with the generated nanoobjects.

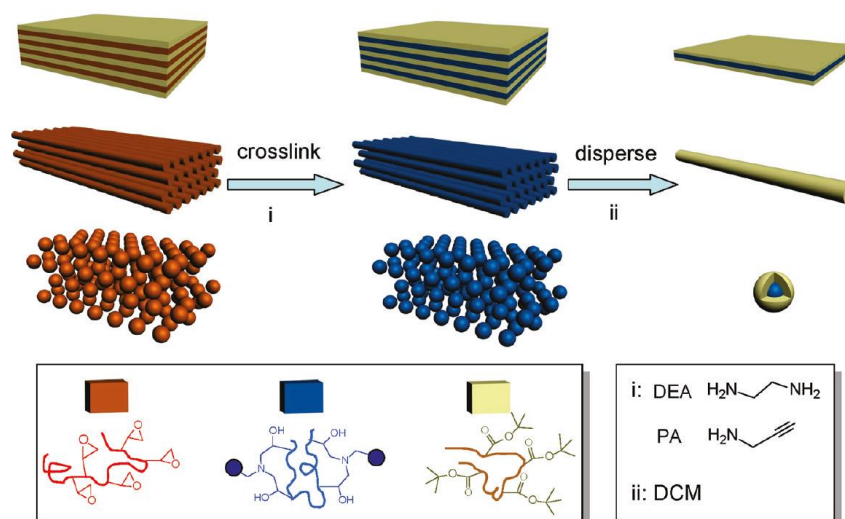


Figure 97: Schematic representation of the preparation of functionalized polymeric nanoobjects by crosslinking a microphase-separated poly(*tert*-butyl acrylate)-block-poly(glycidyl methacrylate) in the bulk using functionalized amines. The PtBA domains in the cylindrical and spherical phases are not shown in this scheme.<sup>[189]</sup>

### 6.1.1 Azobenzene-functionalized nanoobjects

In the past decade, azobenzene-containing micellar and crosslinked nanoobjects are becoming more and more interesting as drug delivery systems or photo sensors.<sup>[190,191]</sup> Especially drug delivery systems are the driving force for many research groups to investigate light responsive structures, among which non-crosslinked micelles are most prevalent. If the drug release upon excitation with light is possible on the target site, remote activation, thus, spatial and temporal control of the release are fascinating features.<sup>[192]</sup> Zhao et al.<sup>[193]</sup> were the first to report on an amphiphilic block copolymer micelle, which undergoes reversible assembly and disassembly upon exposure to light of a wavelength of 360 nm and 440 nm, respectively due to changes in the polarity of the azobenzene molecule when switched from the *trans*- to the *cis* form. This effect is based on an optically induced change of the hydrophilic – hydrophobic properties, caused by the photochemical reaction of azobenzenes - incorporated in the center of the micelle - upon exposure to light, resulting in an increased polarity of the hydrophobic block. This causes the self-assembled structure to disassemble into a block copolymer solution. Besides the ability to react on incident light, the synthesized micelles were also responsive to changes in the temperature, pH and ionic strength. The micelles were formed by self-assembly of the amphiphilic azobenzene-containing hyper-branched poly(ether amine)s in water. Upon UV irradiation, the obtained tetra-stimuli responsive micelles showed a lower cloud point, e.g. the point at which the surfactant phase separates, up to 5°C, which was attributed to an increased size of the micelles. This study spurred the motivation of academia to gain insight into the possibilities of light-responsive block copolymer micelles of this kind.<sup>[192][192,194–199]</sup>

Besides the well-investigated azobenzene-based micelles, various other types of organic and inorganic azobenzene-functionalized nanoobjects have been examined. Shu Seki et al.<sup>[200]</sup> have generated nanowires made from a dialkylfluorene-co-azobenzene random copolymer (abbreviated PFOAzo) using the single particle nanofabrication technique (SPNT) (see Figure 98). In SPNT, ultra-high-energy charged particles induce crosslinking reactions along the particle paths through an organic material film. During the crosslinking process, the trajectories of the particles are limited to nanometer-scaled cylindrical cross-sections. In this particular case, approx. 1 µm thick films of the

copolymer have been prepared, the PFOAzo featuring different ratios of di-n-octylfluorenyl-2,7-diyl to azobenzene units. The films were then exposed to an  $\text{Os}^{30+}$  ion beam. After exposure, the nanowires were developed by dipping the Si-wafers into a mixture of unipolar solvents. The crosslinking of the copolymer is attributed to the large number of alkyl side chains, in which radicals are formed leading to radical-radical coupling reactions resulting in insoluble nanowires attached to the substrate. With increasing content of alkylfluorene, more uniform and thick nanowires were obtained, which showed reversible shrinkage and change of their morphology upon exposure to an appropriate light wavelength and polarization.

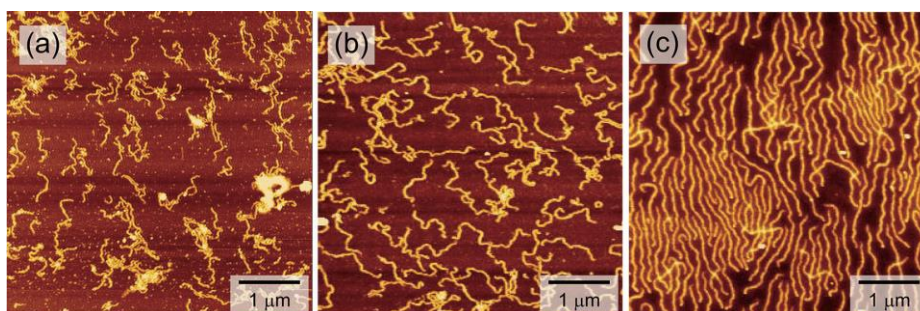


Figure 98: AFM topological images of nanowires fabricated using SPNT. The nanowires have different monomer ratios ranging from a) 1:1, b) 3:1, and c) 7:1 fluorene:azobenzene units in the PFOAzo copolymer.<sup>[200]</sup>

In the area of photoactive micro- and nanoobjects, the concept of Janus particles can be found, too. Very recently, Wang et al.<sup>[201]</sup> have reported on such non-centrosymmetric architectures consisting of a mixture of a methacrylate-based azobenzene-functionalized copolymer containing adamantyl groups and poly(methyl methacrylate) (PMMA). The generation of the Janus particles is performed by a straightforward method. In a first step, the two polymers are dissolved in dichloromethane (DCM). Subsequently, the solution is added to an aqueous solution of poly(vinyl alcohol) under constant stirring. Upon evaporation of the DCM, the initially spherical droplets change their shape to a “snowman-like shape” caused by a phase separation of the PMMA and the azobenzene-copolymer. When exposed to linear polarized light, the obtained photoresponsive Janus particles showed unique deformation behavior into e.g. “mushroom-like” and “snail-like” shapes.

Most azobenzene-containing micro- and nanoobjects discussed so far feature the azobenzene-content in the center of the structure. However, there is a large community, which is interested on functionalizing the shell of particles with azobenzene units to enable photo-triggerable property changes, traceability or even light-driven directed motion of polymer nanoparticles. Cannizzo et al.<sup>[202]</sup> have demonstrated a straightforward method to synthesize colored polymer nanoparticles by surface modification of chlorobenzyl-functionalized particles obtained from copolymerization of styrene and vinylbenzylchloride via microemulsion technique. The obtained nanoparticles of homogeneous size of about 20 nm were then functionalized with polyamines, which in a next step react with the azobenzene chromophore in an aqueous solution. This kind of particles has potential applications in labeling in the biomedical branch.<sup>[202]</sup> In a similar manner Brasselet et al.<sup>[203]</sup> have functionalized the surface of crosslinked polystyrene nanoparticles with azobenzene chromophores. Here, the microemulsion polymerized chlorobenzyl-functionalized particles serve as carrier for disperse red chromophores, which were covalently linked to the nanoparticles surface. By exposing the particles to a light intensity gradient, the group managed to move the 16 nm sized particles - at adjustable velocities - over tens of micrometers from the bright to the dark regions of the optical gradient with the mechanical work done by the azobenzene

chromophores during *trans-cis-trans* isomerization cycles. Since the nanoparticles can be doped with functional molecules, the study could spur the development of drug delivery nano machinery.<sup>[203]</sup>

Besides photoactive organic nanoparticles, emphasis has also been put on the research of azobenzene-functionalized inorganic nanoobjects. The most prominent examples of such kind of nanoobjects are azobenzene-coated gold particles. Recently, Zhao et al.<sup>[204]</sup> have synthesized Au nanoparticles, which are functionalized with a water-soluble azobenzene-containing random copolymer of N,N-dimethylacrylamide and N-4-phenylazophenylacrylamide on their shells. The copolymers' lower critical solution temperature (LCST) can be reversibly switched upon exposure to light, hence enabling photo-triggerable aggregation and re-dispersion of the Au particles in aqueous solution. As a consequence of photo-triggerable aggregation, a reversible shift of the surface plasmon resonance (SPR) of the particles is induced. The demonstrated tuning of the light-induced SPR renders the azobenzene-coated Au particles an interesting system for temporally and spatially controlled thermal therapy.<sup>[204]</sup>

Inorganic nanoparticles functionalized with azobenzenes can also be found in the field of holographic high density data storage or as material for optical magnetic recording media. The latter is addressed in a study from Einaga et al.<sup>[205]</sup>, in which FePt nanoparticles are coated with different low-molecular-weight azobenzene units and spacer ligands to realize optical switching of the magnetic material at room temperature. The examination of the photophysical behavior of the particles revealed that upon exposure to UV light a *trans-to-cis* isomerization occurs, leading to an increased magnetization of the composite FePt nanoparticles as a result of changes in the electronic polarization on the d electrons of the iron atoms on the surface of the particle. This photo-isomerization induced change of the magnetization is reversible and is reduced upon exposure of the particles to visible light. Due to the fact, that ferromagnetism at room-temperature is achieved in this system, it could be of great practical use in optical magnetic recording media. One of the most important characteristics in azobenzene-based holographic data storage media is the change in the maximal value of photo-induced birefringence. Inorganic ZnO particles have been used to improve this value in different amorphous and liquid crystalline CN-azobenzene functionalized polymeric systems.<sup>[206]</sup> Upon doping these polymeric systems with the approx. 50 nm sized nanoparticles, the birefringence, which is induced using a polarized laser beam at 400 mW/cm<sup>2</sup>, increased more than 40% while the writing time decreased about 30%. The increase of the birefringence is attributed to an increase of the mobility of the azobenzene side groups resulting from an increase in the free volume generated at the interface between the chromophores and the particles.

## 6.2 Azobenzene-functionalized core/shell polymer nanoparticles

Azobenzene-functionalized materials have been widely studied as potential material for reversible optical high density data-storage media.<sup>[28,48,53,126,207–212]</sup> In general, the materials investigated so far can be divided into two material classes: low-molecular-weight compounds and polymeric materials. Among the polymeric materials, to which homopolymers as well as statistical copolymers belong to, block copolymers are the material with the highest potential to be applied in reversible holographic data storage. Their main advantage over every other azobenzene-functionalized material is that the dilution of the azobenzene chromophores allows for the preparation of thick samples, which the laser light –used to inscribe the holographic gratings- can penetrate. Compared

to statistical copolymers and low-molecular-weight compounds, upon dilution, the spatial proximity of the azobenzenes is preserved in block copolymers owing to their tendency to microphase separate. The preserved spatial proximity is necessary to profit from the cooperative effect, i.e. a cooperative motion of the chromophores with –mostly mesogenic- azobenzene moieties in their surrounding leading to higher birefringence and stabilized inscribed gratings.<sup>[3]</sup> To realize high density data storage, these thick samples are a prerequisite, since solely samples of a thickness much higher than the thickness of the inscribed gratings are useable in angle-multiplexing, which allows for the inscription of several holograms in the same volume element.<sup>[33,213]</sup> This usually means a sample thickness in the millimeter range. However, for block copolymers featuring an azobenzene content of more than 10 wt.-%, the limit of the optical density the laser light can penetrate is reached within several micrometers.

The preparation of thick samples in the millimeter range is commonly performed via melt pressing, cell casting or injection molding. To reach an ideal optical density between 0.5 and 0.7, the azobenzene content of the 1-3 mm thick sample has to be reduced to about 0.2-0.4% (see Figure 99).<sup>[52]</sup> This can be achieved by blending the block copolymers with a non-photoactive matrix polymer that is chemically similar to the non-photoactive, amorphous block of the copolymer. In this case, to achieve 1 mm thick samples, the content of non-photoactive homopolymer in the blend has to be as high as approx. 95%. Blending an azobenzene-functionalized block copolymer with an amount of photo-chemically inert polymer means the formation of a spherical morphology. The size of the spheres comprising the azobenzene moieties is not affected by the amount of homopolymer blended with the photo-orientable block copolymer. However, a spherical morphology can come at the cost of stability of inscribed holographic gratings. This finding is demonstrated based on two different azobenzene-functionalized block copolymers.<sup>[52]</sup> Processed as neat material, one forms a cylindrical morphology, the other arranges in a lamellar microphase. To obtain a spherical morphology, the first block copolymer is blended with a non-photoactive homopolymer. In all three cases, the azobenzenes are oriented using two superimposed, polarized laser beams. During the inscription of the volume gratings and turning-off the lasers, however, significant differences have been observed. It turned out, that the highest value of induced birefringence is reached in samples of the block copolymer forming a lamellar microphase, whereas the cylindrical morphology showed a lower change in birefringence and the spherical morphology the lowest. When the laser is switched off, the birefringence in the lamellar arranged block copolymer increased, while the birefringence in the cylindrical morphology was stable. The birefringence in the sample with the spherically arranged block copolymer decreased after the inscription process. Even though the cylindrical and the spherical domains had the same size, only the holographic grating inscribed in the block copolymer forming the cylindrical morphology were stable.

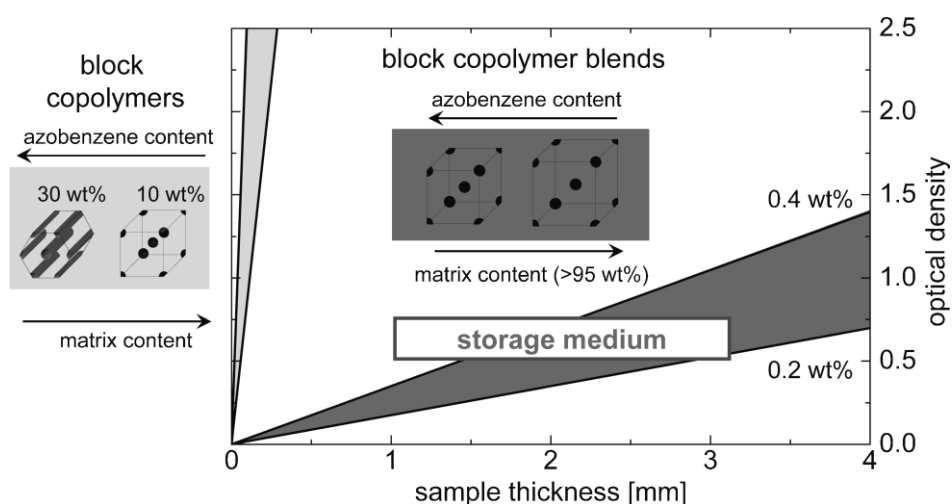


Figure 99: Increase of the optical density at the writing wavelength in dependency of the sample thickness. The light gray section represents the neat block copolymer; the dark grey section represents a blend of an azobenzene-containing block copolymer with a non-photoactive polymer, which corresponds to the block copolymers majority block.

As discussed above, block copolymers feature the possibility to process azobenzene-containing materials to samples with a thickness high enough to have the potential to be used in high density data storage by dilution in a non-photoactive homopolymer. Here, a novel dilution concept based on newly developed azobenzene-based polymer nanoparticles is presented. In this concept, the morphology of the neat block copolymer is fixed by crosslinking reaction in the bulk material, more precisely in the azobenzene phase. After the cross-linking reaction is performed, the cross-linked block copolymer is dispersed in a solvent, in which the non-photoactive majority block of the polymer is dissolved to yield azobenzene-functionalized polymeric core/shell nanoparticles in the shape of the microphase separation of the neat block copolymer. As a consequence, the material should maintain its morphology upon dilution with a non-photoactive polymer. The approach will be investigated using two different types of block copolymers. The difference in the chemical composition of these polymers is to be found in their non-photoactive majority block (see Figure 100).

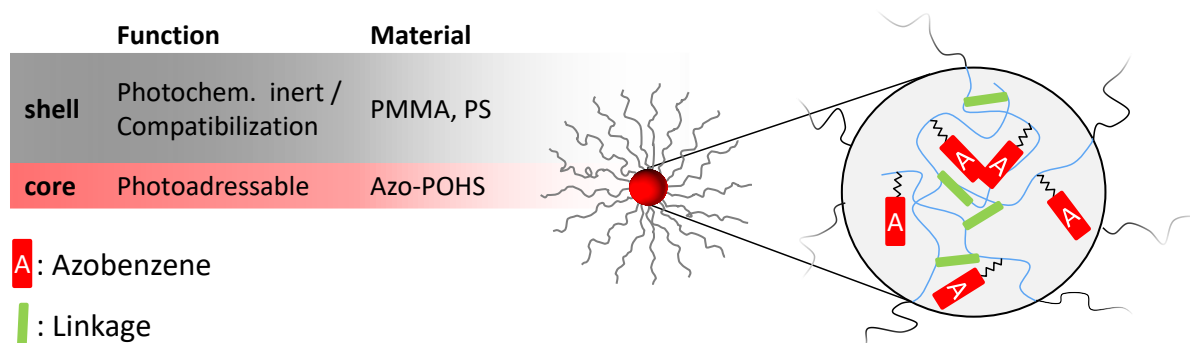


Figure 100: Schematic representation of an azobenzene-functionalized core/shell polymer nanoparticle. The core comprises an azobenzene-functionalized poly(4-hydroxystyrene)-core. The shell consists either of a poly(methyl methacrylate) or a polystyrene block.

The photoinactive, but azobenzene-functionalizable polystyrene-block-poly(4-hydroxystyrene) block copolymer will be synthesized via anionic polymerization. Another block copolymer was synthesized by Dr. R. Pettau (University of Bayreuth) and features a poly(methyl methacrylate) block and a functionalizable poly(4-hydroxystyrene) block. The azobenzene-containing phase

features azobenzene moieties and unreacted hydroxyl groups and is the one to be crosslinked. As a consequence, the prepared nanoparticles will feature a PS or a PMMA shell. Hence, the preparation of both, thick samples with PMMA and PS homopolymer will be possible. As crosslinking agent, the commercially available tetramethoxymethyl glycoluril (Powderlink 1174®) will be used. This compound is activated by protons and widely used to crosslink POHS systems. Here, for the first time, it is used as elegant way to crosslink the aromatic hydroxyl groups of the minority block to form polymer nanoparticles.<sup>[214–216]</sup> The system has the advantage to be very variable, as the protons can be incorporated into the block copolymer either by activation of a light- or temperature sensitive acid, or by diffusion of protons from the gas phase.

Azobenzene-functionalized core/shell polymer nanoparticles have not yet been discussed in the literature. However, there are literature-known ways to synthesize core/shell polymer nanoparticles. Here, the approach of crosslinking microphase-separated block copolymer architectures in the bulk, used by the research group of Prof. Dr. Müller<sup>[184]</sup> to obtain Janus particles of defined shape on a gram scale, will be applied. In the approach, the azobenzene-functionalized block copolymer is dissolved together with a crosslinking agent/crosslinking agent activator system (see Figure 101). In a next step, the solvent is slowly evaporated resulting in a microphase separated film, which in a next step is crosslinked by activation of the crosslinking system. Afterwards, the film is re-dispersed and azobenzene-functionalized core/shell nanoparticles are obtained. The solvent must be suitable to dissolve the both blocks of the block copolymer, as well as the crosslinking agent and the activator compound. The amount of crosslinking agent and activator must be low enough to not influence the microphase separation process negatively. To avoid the use of large excesses of crosslinking agent, the crosslinker should have an affinity to block, in which the OH-functionalities are located in. The same applies to the activator.

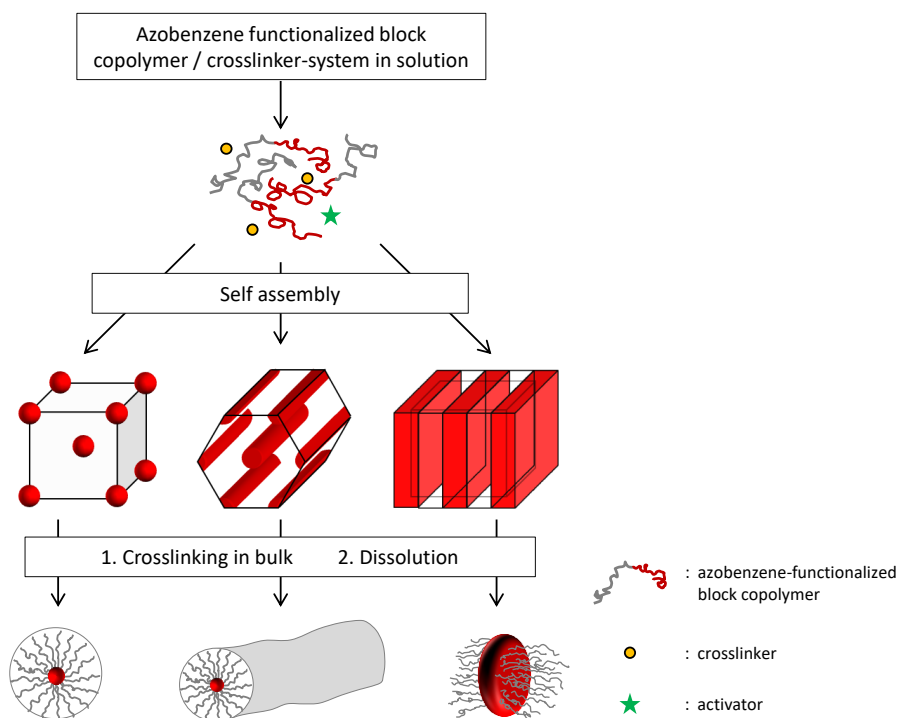


Figure 101: Synthetic strategy to obtain azobenzene-containing core/shell polymer nanoparticles. The photo-orientable block copolymer self-assembles from solution. In a next step, the microphase-separated film is crosslinked within the azobenzene-containing phase. Core/shell polymer nanoparticles are obtained after dispersion of the crosslinked block copolymer.

## 6.2.1 Materials

### 6.2.1.1 Polymers

Core/shell polymer nanoparticles were prepared from block copolymers bearing hydroxyl-styrene groups in one block and either a polystyrene or a poly(methyl methacrylate) block (see Figure 102).

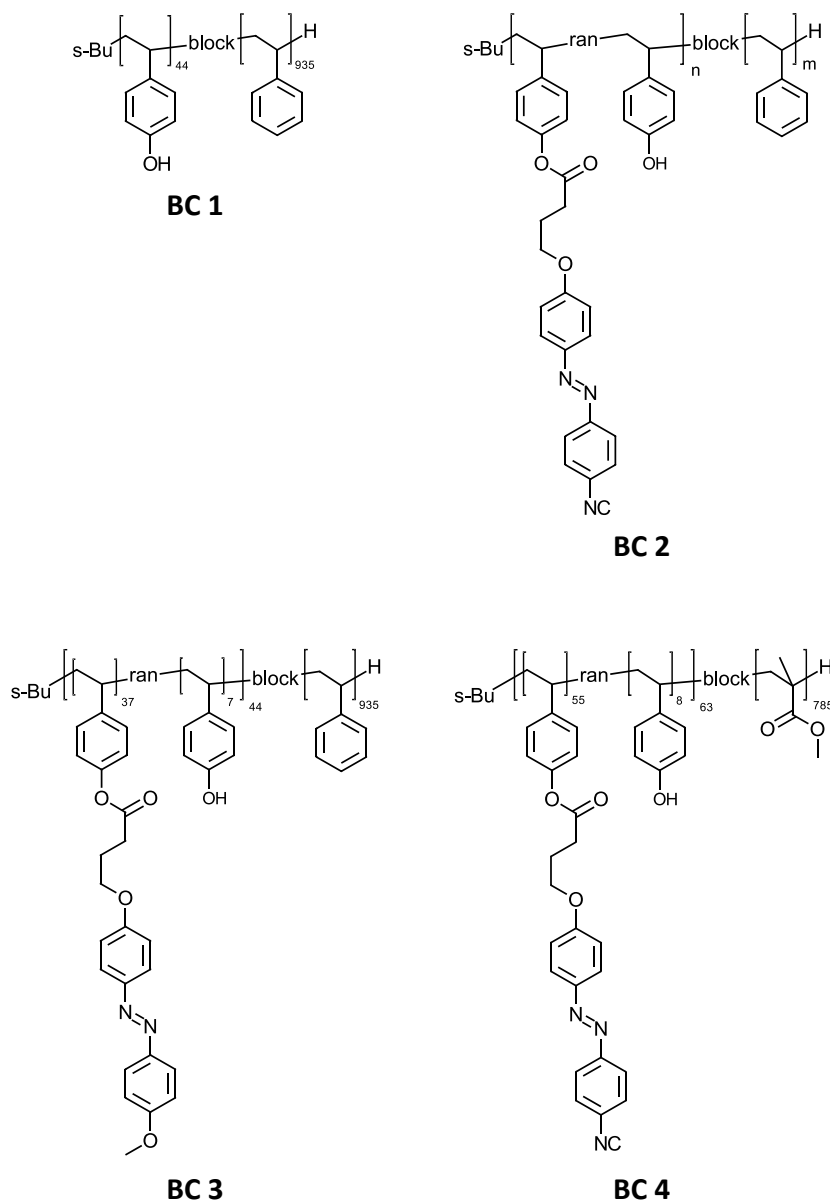


Figure 102: Chemical structures of the investigated block copolymers with hydroxyl-functionalization **BC1**, and of the investigated azobenzene-containing block copolymers **BC2-BC4**. **BC2** has been synthesized with different ratios of azobenzene-side groups to hydroxyl groups in the cross-linkable block.

The first block provides the ability for the block copolymer to be crosslinked via a substitution reaction at the hydroxyl group. Furthermore, this block can be functionalized with azobenzene side groups, so that the polymer becomes photo-orientable. The azobenzene moieties are substituted either with an electron acceptor group (CN) or an electron donor group (MeO), as both groups can induce liquid crystalline phases in azobenzene-functionalized polymers. This way, the induced birefringence, caused by interfering lasers in holographic experiments on thin films of such kind of polymers, can be much higher than in non-liquid crystalline block copolymers. The non-photoactive

block, which consists either of PS or PMMA block segments, provides miscibility with either a PS or a PMMA homopolymer to enable the preparation of samples of millimeter thickness by blending the block copolymers with the suitable homopolymer. The block ratio between the crosslinkable block and the non-photoactive block is tailored to be around 10-30 wt.-% of cross-linkable block and 70-85 wt.-% of non-photoactive block after the functionalization of the cross-linkable block. These ratios potentially yield spherical (10 wt.-%) and cylindrical microphase separation, so that eventually spherical and cylindrical polymer nanoparticles can be obtained. The exact degree of functionalization with azobenzene moieties, the weight ratios of the blocks (PS block to functionalized block) and the calculated number of repeating units  $r$  of the investigated block copolymers is listed in Table 10.

Table 10: Degree of functionalization of the P(OHS) block with azobenzene moieties, weight ratios of the blocks (PS block to functionalized block) and calculated number of repeating units  $r$  of the investigated block copolymers.

Name	BC 1	BC 2-1	BC 2-2	BC 2-3	BC 3	BC 4
<b>degree of functionalization P(OHS) block / %</b>	-	41	50	71	86	87
$r_{u,azo} / r_{u,OH}$	0/44	18/26	22/22	31/13	37/7	55/8
<b>P(OHS)-<math>r</math>-P(Azo) / PS / wt.-%</b>	5	9	11	13	15	23

The block copolymers have been synthesized via a sequential anionic polymerization. While the PMMA polymer was already available in our research group (synthesis by Dr. Pettau, University of Bayreuth), the PS functionalized block copolymer had to be synthesized. For the preparation of the block copolymers, an anionic polymerization was chosen since this type of polymerization allows for the exact adjustment of the molecular weight ratio in the resulting block copolymer. Furthermore, the reactor setup (with a reactor capacity of 1.6 L) allows for the preparation of polymers on the 100 g scale.

In a first step, a protected hydroxyl styrene monomer is polymerized followed by the polymerization of styrene in a one pot synthesis (see Figure 103). The synthesis was carried out in one single reactor with a connection to an adjacent THF distiller. Before starting the reaction, the reactor had to be flushed with a THF/*sec*-BuLi solution to avoid protic impurities. After cooling the reactor down to -68°C, the calculated amount of initiator (*sec*-BuLi) starts the anionic polymerization of *tert*-butoxy styrene (*t*-BS). After the reaction is finished, styrene was added to the solution and was allowed to react for 95 min with the precursor. The reaction was then terminated with MeOH.

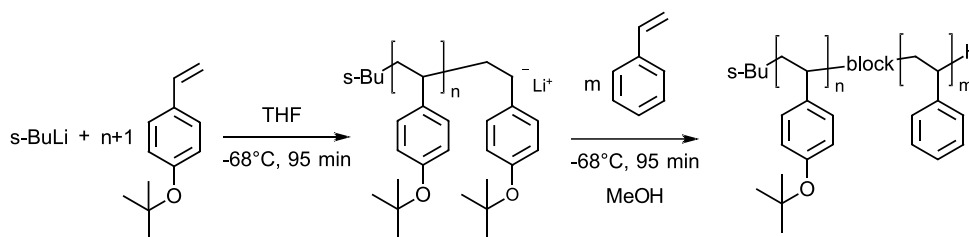


Figure 103: Polymerization of the PS-*b*-P(OHS) block copolymers via sequential anionic polymerization.

In a next step, the P(OHS) block was deprotected in an E1 elimination reaction (see Figure 104). Therefore, the block copolymer was dissolved in acetone at room temperature. To this solution, a large excess of HCl was added and the reaction mixture was heated and stirred vigorously overnight. The success of the reaction is indicated by the turbidity of the reaction solution, which is caused by the formation of a micellar solution. During the workup process, care had to be taken to circumvent crosslinking reactions. Therefore, the polymer was first precipitated in alkaline water (pH $\approx$ 10) and afterwards poured in slightly acidified water (pH $\approx$ 5). The deprotected block copolymer was stored at 4 °C as storage. A quantification of the success of this reaction step can be done by acetylation of the poly(hydroxy styrene)-containing polymer.

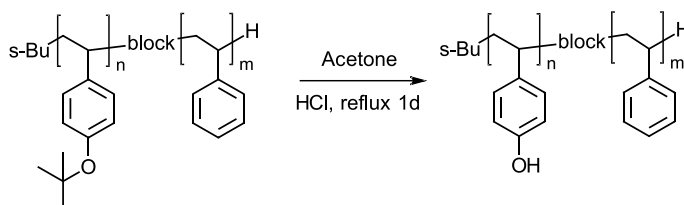


Figure 104: Deprotection of the hydroxyl group in the poly(*tert*-butoxy styrene) block of the block copolymer by acidic cleavage of the *tert*-butoxy group.

The reaction sequence allows for an easy polymer analogous side-chain reaction of the azobenzene moieties with the polymers backbone in a last reaction step (see Figure 105). The polymer analogous reaction of the acid chloride of the azobenzene carbon acid is an esterification S<sub>N</sub>2 reaction. To enhance the reactivity of the involved reaction partners, the polymer is dissolved in a dry polar aprotic solvent mixture consisting of a large excess of THF with DMF. Afterwards, the polymer solution has to be cooled to 0 °C to avoid side reactions. After the base triethylamine was added to the reaction mixture, the azobenzene acid chloride was admixed. Then the reaction was slowly heated up to room temperature. In a typical reaction, the mixture was stirred for 48 h, before the mixture was precipitated in MeOH. The precipitation was repeated several times until the MeOH does not become yellow-colored anymore. This indicates a complete removal of unreacted azobenzene molecules.

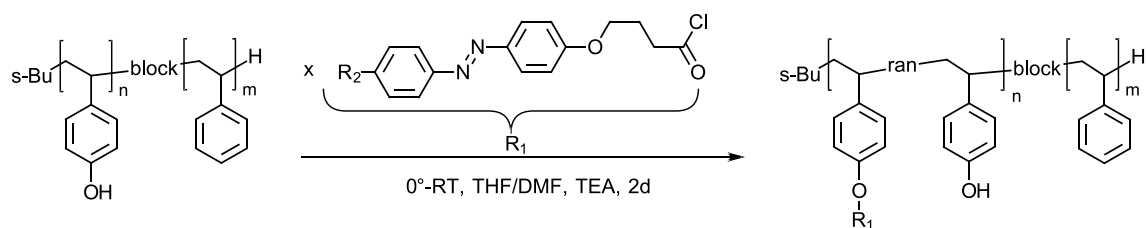


Figure 105: Partial polymer-analogous functionalization with azobenzene acid chloride in an esterification reaction. R2 is the substituent to the azobenzene molecule and can be either a CN or a MeO group.

### 6.2.1.2 Crosslinking agents and proton sources

As described in chapter 6.1, selective bulk crosslink of a polybutadiene block (PB) phase in microphase separated block copolymers can be achieved by radical crosslinking with AIBN or cold vulcanization with  $S_2Cl_2$ . To crosslink the hydroxyl groups of the partly azobenzene-functionalized POHS block in the present system, however, an approach with the tetra-functional glycoluril-based crosslinking agent Powderlink 1174<sup>®</sup> is chosen. The activation of the compound is performed by a Brønsted acid acting as catalyst (see Figure 106). Since the acid is regenerated during the crosslinking reaction, a single proton can initiate a cascade of reactions. This mechanism is also known as chemical amplification.<sup>[218]</sup> Owing to the cascade reactions and due to the four functional groups Powderlink 1174<sup>®</sup> has, a small amount of crosslinker is sufficient to efficiently crosslink a POHS phase.

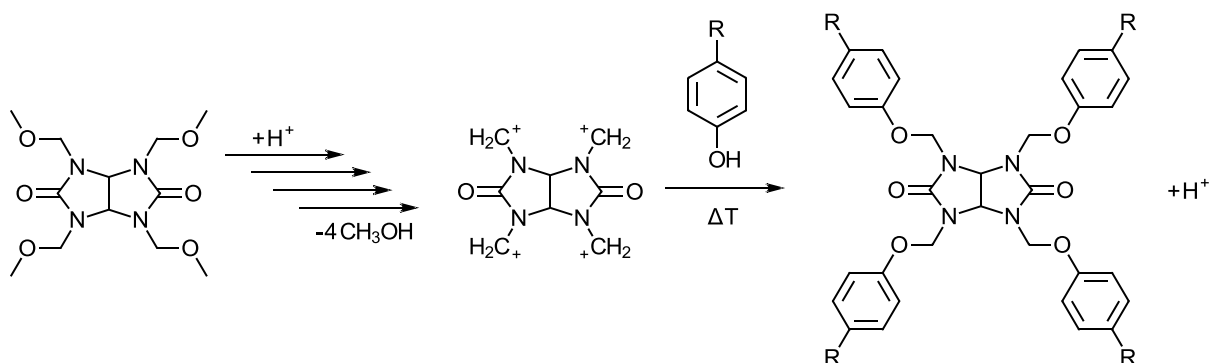


Figure 106: Activation of the crosslinking agent Powderlink 1174<sup>®</sup> in the presence of a Brønsted acid catalyst. The formed carbenium ions react with hydroxyl groups in their spatial proximity. The proton is regenerated.

As source of the protons, three different categories will be investigated (see Figure 107).

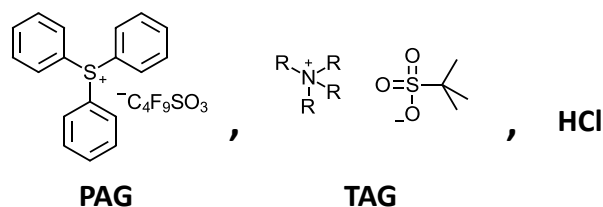


Figure 107: Chemical structures of the investigated proton sources for the crosslinking process. The photoacid generator (PAG) is activated upon UV irradiation. The thermal acid generator (TAG) generates a proton upon heating up to 100-120 °C. HCl vapor is an alternative source of protons.

One source is the commercially available photoacid generator (PAG) triphenylsulfonium perfluoro-1-butanesulfonate. This compound has been chosen for its good solubility in common solvents and

its stability at ambient conditions and high temperatures.<sup>[219,220]</sup> Upon irradiation with UV light ( $\lambda_{\text{max}}=278$  nm), the triphenylsulfonium chromophore decomposes and a sulfonic acid ( $\text{C}_6\text{F}_5\text{SO}_3\text{H}$ ) is generated. The thermal acid generator (TAG) is a quaternary ammonium blocked triflic acid, which is commercially available from King Industries under the trade name K-Pure TAG-2678. The TAG generates a proton when heated up to a temperature near its melting point of 100-120 °C. Both proton sources, the PAG as well as the TAG are ionic, thus polar molecules, which are expected to diffuse into the polar crosslinkable block of the polymers. The diffusion is driven by the so-called post-exposure bake, in which, in this case, the sample is treated at temperatures above the  $T_g$  of the polymer. Another way to introduce protons to the microphase separated block copolymer films is HCl vapor.

## 6.2.2 Synthesis of core/shell polymer nanoparticles

Figure 108 depicts a detailed insight into the synthesis of core/shell polymer nanoparticles using the crosslinker Powderlink 1174®.

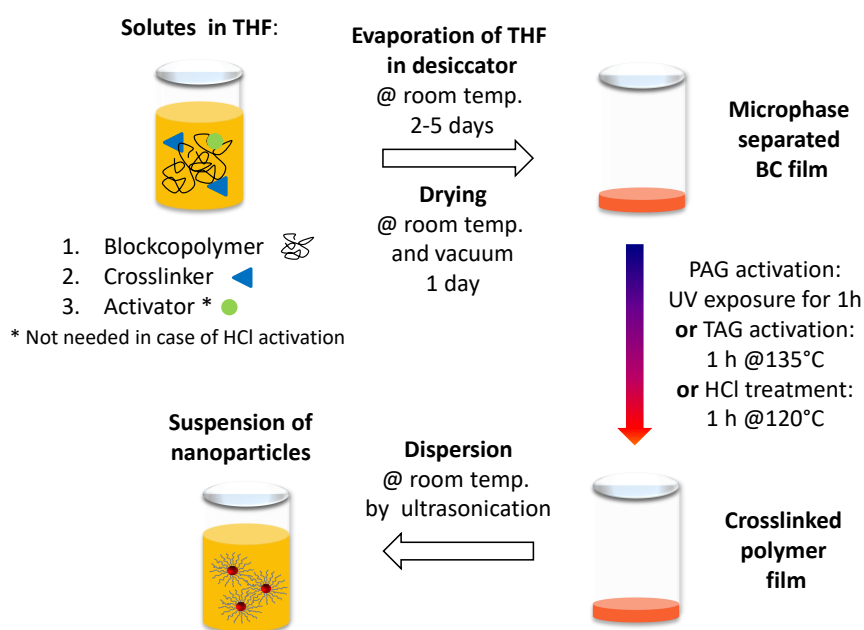


Figure 108: Synthesis of polymer core/shell polymer nanoparticles.

All investigated polymers, acid generators and the crosslinker are soluble in THF. In a first step, the block copolymer is dissolved in THF. The concentration is chosen to be in a range of 30-70 mg/ml. The amount of polymer used for the experiment is dependent on the form into which the polymer solution is casted. Usually, between 100-150 mg of block copolymer were used. To the polymer solution, the crosslinker is admixed. If a PAG or TAG is used to activate the crosslinker, the activator is added to this solution as last compound. The PAG is added under yellow light conditions and the evaporation is done in the dark to avoid early crosslinking reactions. The evaporation of the THF is performed in a desiccator to ensure that the solvent is in an equilibrium with THF vapor and that it is not evaporating too quickly, so that the microphase separation of the block copolymer can take place. This step is usually finished after 2-5 days. Afterwards, the film is dried under vacuum at room temperature for one day.

The obtained microphase separated film can be crosslinked in three different ways. If a PAG system is used, the film is exposed to UV light for 1 h and subsequently subjected to a post-bake step, at

which the film is heated up to 90 °C for 1 h to ensure diffusion of the formed protons through the entire film. A TAG system, however, is activated at a temperature of 135 °C for 1 h and no post-bake step, i.e. a thermal treatment to e.g. ensure diffusion of protons and crosslinker, is needed. Treatment with HCl vapor does not require post-bake either, since the film is heated up to 100 °C for 1 h during exposure to the HCl vapor.

In a next step, THF is added to the crosslinked block copolymer film. The THF is stirred for 1 day, so that the film can swell. In the final step, the swollen film in the THF is subjected to an ultrasonication step and the polymer nanoparticles are dispersed in the solvent.

### 6.3 Synthesis and characterization of non-photoactive poly(4-hydroxystyrene)-b-polystyrene core/shell nanoparticles

As a first block copolymer to be tested in the core/shell polymer nanoparticle synthesis using Powderlink 1174<sup>®</sup> as a crosslinker, the non-photoactive poly(4-hydroxystyrene)-b-polystyrene **BC 1** was chosen. Figure 109 shows transmission electron microscope (TEM) micrographs of a 50 nm thin films of the microphase separated block copolymer **BC 1** after the evaporation of THF in a desiccator and subsequent drying of the films in high vacuum at room temperature.

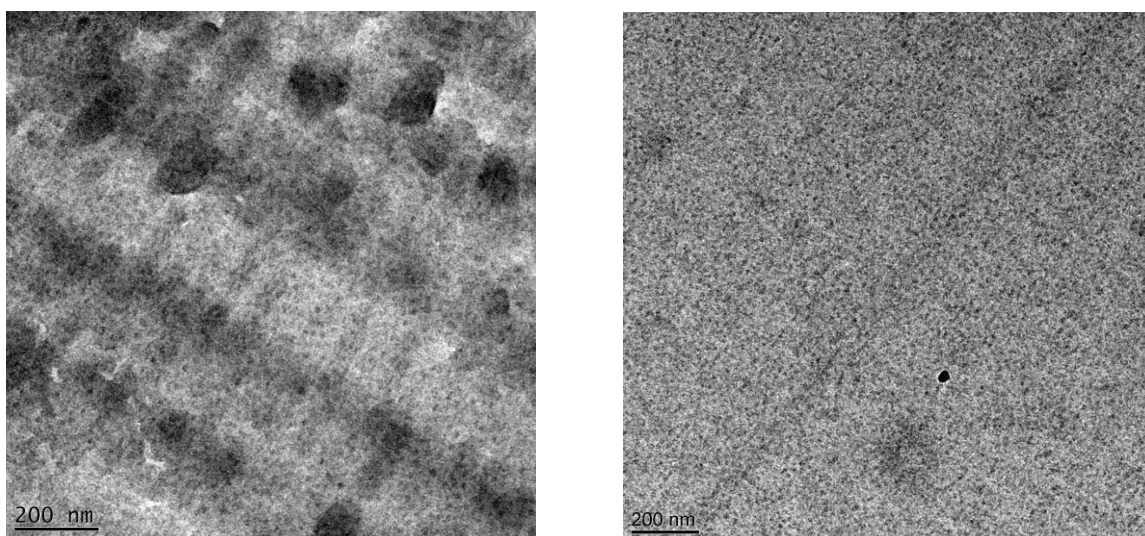


Figure 109: Transmission electron micrograph thin section of RuO<sub>4</sub>-stained 50 nm films of the non-photoactive block copolymer **BC 1** without added crosslinker (**left**) and with 5 wt.-% of Powderlink 1174<sup>®</sup> (**right**).

The left TEM image shows the neat block copolymer and the right image depicts the poly(4-hydroxystyrene)-b-polystyrene **BC 1** with additional 5 wt.-% Powderlink 1174<sup>®</sup>. Both films were stained with RuO<sub>4</sub>. The dark areas correspond to the hydroxy functionalized block, while the bright areas depict the polystyrene matrix. In both cases, the hydroxy functionalized domains form a spherical micro structure with an average size of about 10-20 nm. The addition of the crosslinker to the block copolymer has no noticeable effect on the microphase separation of the polymer. No conclusion whether the crosslinker preferably assembles in the hydroxy functionalized block or in the polystyrene block can be drawn from the images.

### 6.3.1 Photoacid generator system

The source of protons for the crosslinking reaction in the first set of experiments is the photoacid generator triphenylsulfonium perfluoro-1-butananesulfonate. A constant amount of 10 wt.-% of the PAG is added to the block copolymer/Powderlink 1174<sup>®</sup> mixture with respect to the weight of the crosslinker. Hence, the amount of PAG is between 0.05 and 0.3 wt.-% with respect to the weight of the polymer/crosslinker system and, thus, so low that no influence on the microphase separation of the block copolymer is expected. The amount of crosslinker is altered throughout the experiment series. Its amount is given in weight percent with respect to the weight of the block copolymer in the mixture. The crosslinking is performed by irradiation with UV light for 1 h in all experiments of this set. The generated polymer nanoparticles have been investigated via dynamic light scattering (see Figure 110).

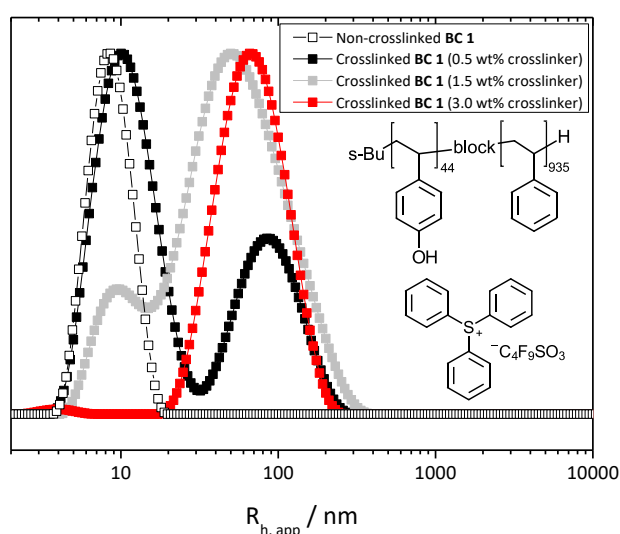


Figure 110: Dynamic light scattering CONTIN plots of pure **BC 1** and crosslinked **BC 1** using a photoacid generator with increasing content of crosslinker Powderlink 1174<sup>®</sup>. The amount of PAG is constant at 10 wt.-% with respect to the amount of crosslinker.

Prior to the DLS measurements, the re-dispersed polymer nanoparticles in THF were filtered using a Teflon filter with a pore size of 5  $\mu\text{m}$  to prevent dust from distorting the results of the experiment. The neat block copolymer **BC 1** shows a single peak at an apparent hydrodynamic radius  $R_{h,app}$  of 8 nm. Crosslinking with an addition of just 0.5 wt.-% Powderlink 1174<sup>®</sup> leads to the formation of a second species with a hydrodynamic radius of 86 nm. 1.5 wt.-% of crosslinker increases the height of the peak representing the crosslinked species and reduces the peak at  $R_{h,app} = 8$  nm representing the un-reacted block copolymer. At a concentration of 3 wt.-% crosslinker, the peak below at about 8 nm disappears and a single peak at  $R_{h,app} = 66$  nm remains. The results suggest that the amount of 3 wt.-% of Powderlink 1174<sup>®</sup> in combination with PAG (0.3 wt.-% with respect to the polymer/crosslinker mixture) is sufficient to efficiently generate polymer core/shell nanoparticles from a poly(4-hydroxystyrene)-b-polystyrene block copolymer. Owing to the tetra-functionality of the crosslinker, the amount of 3 wt.-% of crosslinker equals a ratio of 1 crosslinker molecule to 2 free hydroxy groups in the crosslinkable block of the polymer.

### 6.3.2 Thermal acid generator system

Besides the use of a photoacid generator/crosslinker system, the synthesis of polymer core/shell nanoparticles from a poly(4-hydroxystyrene)-b-polystyrene block copolymer is also tested using a thermal acid generator/crosslinker blend. As in case of the experiments using PAG, the amount of commercially available K-Pure TAG-2678 is constantly held at a value of 10 wt.-% with respect to the amount of Powderlink 1174®. The amount of crosslinker is changed in the experimental series. The crosslinking is performed by heating the microphase separated block copolymer film to 135 °C for 1 h. The generated polymer nanoparticles have been investigated via dynamic light scattering (see Figure 111). Prior to the DLS measurements, the re-dispersed polymer nanoparticles were filtered using a Teflon filter with a pore size of 450 nm to prevent dust from distorting the results of the experiment.

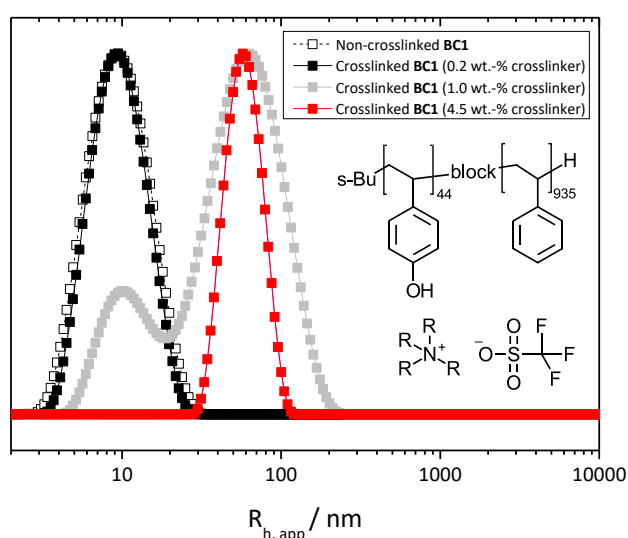


Figure 111: Dynamic light scattering CONTIN plots of pure **BC 1** and crosslinked **BC 1** using a thermal acid generator with increasing content of crosslinker Powderlink 1174®. The amount of PAG is constant at 10 wt.-% with respect to the amount of crosslinker.

The block copolymer **BC 1** has an apparent hydrodynamic radius  $R_{h,app}$  of about 9 nm. The addition of 0.2 wt.-% of crosslinker and subsequent crosslinking at 135 °C has no observable influence on the apparent hydrodynamic radius of the block copolymer in the THF dispersion. Upon the addition of 1 wt.-% Powderlink 1174® leads to the formation of polymer nanoparticles with a  $R_{h,app}$  60 nm. Besides these particles, another peak at 9 nm is still present representing the un-reacted block copolymer. At a concentration of 4.5 wt.-% crosslinker, only a single peak at  $R_{h,app}$  = 66 nm remains. Therefore, the amount of 4.5 wt.-% of Powderlink 1174® in combination with 0.45 wt.-% K-Pure TAG-2678 is sufficient to efficiently generate polymer core/shell nanoparticles from a poly(4-hydroxystyrene)-b-polystyrene block copolymer.

### 6.3.3 Hydrochloric acid treatment

As an alternative way to obtain polymer nanoparticles based on the poly(4-hydroxystyrene)-*b*-polystyrene block copolymer, the mixture of the crosslinker Powderlink 1174<sup>®</sup> with the microphase separated block copolymer is treated with HCl vapor as source of protons for the crosslinking reaction. As no thermally instable thermal acid generator or PAG is located in the dried block copolymer film, the film is annealed at 120 °C overnight prior to the crosslinking procedure to ensure a good micro phase separation. The crosslinking is performed by heating the microphase separated block copolymer film to 120 °C for 1 h while exposing it to HCl vapor. The generated polymer nanoparticles have been investigated via dynamic light scattering (see Figure 112). Prior to the DLS measurements, the re-dispersed polymer nanoparticles were filtered using a Teflon filter with a pore size of 450 nm to prevent dust from distorting the results of the experiment.

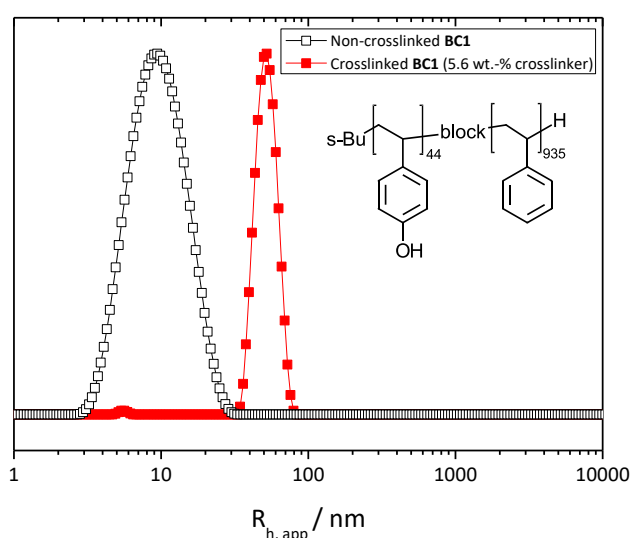


Figure 112: Dynamic light scattering CONTIN plots of pure **BC 1** and crosslinked **BC 1** using HCl with increasing content of crosslinker Powderlink 1174<sup>®</sup>. The amount of PAG is constant at 10 wt.-% with respect to the amount of crosslinker.

The block copolymer has an apparent hydrodynamic radius of 9 nm. Based on the results of the crosslinking experiments using PAG and TAG, the amount of 5 wt.-% of crosslinker is chosen for the crosslinking of the block copolymer with HCl vapor. The DLS measurement suggest that this amount is sufficient to create polymer nanoparticles with a radius of about 52 nm.

## 6.4 Synthesis and characterization of photoaddressable core/polystyrene shell polymer nanoparticles with polystyrene shell

The experience of crosslinking the non-photoactive poly(4-hydroxystyrene)-b-polystyrene (P(OHS)-b-PS) block copolymer is applied on the crosslinking of a partially functionalized azobenzene functionalized poly-(4-hydroxystyrene)-b-polystyrene block copolymer. Figure 113 shows 50 nm thin films of the microphase separated block copolymer **BC 2-2** with 50 % azobenzene functionalized P(OHS) block (11 wt.-% with respect to the total weight of the block copolymer) after the evaporation of THF in a desiccator and subsequent drying of the films in high vacuum at room temperature.

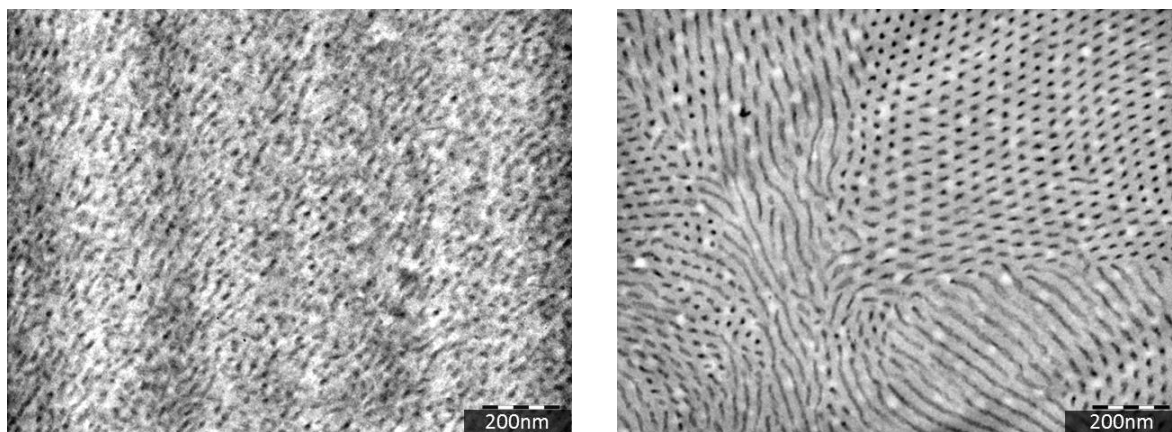


Figure 113: Left: Transmission electron micrograph of a 50nm thin section of a phosphotungsten acid stained block copolymer **BC 2-2** film placed on a Cu grid after annealing at 120°C for 12h. Left: Neat **BC 2-2**. Right: **BC 2-2** containing 6 wt.-% Powderlink 1174<sup>®</sup>. The dark areas correspond to the azobenzene functionalized block.

The left TEM image shows a thin section of microphase separated the neat block copolymer **BC 2-2** and the right image depicts the partially azobenzene-functionalized poly(4-hydroxystyrene)-b-polystyrene **BC 2-2** with additional 6 wt.-% Powderlink 1174<sup>®</sup>. Both films were stained with phosphotungsten acid. The dark areas correspond to the azobenzene-functionalized block, while the bright areas depict the polystyrene matrix. The neat **BC 2-2** forms a spherical micro structure with an average size of about 20 nm. The addition of the crosslinker to the block copolymer has leads to the formation of a cylindrical microphase separation of the polymer. This result suggests that the polar crosslinker preferably accumulates in the azobenzene phase, so that the volume of this phase is increased. By that, the microphase structure is changed from spherical to cylindrical.

### 6.4.1 Photoacid generator system

As a first crosslinking system to prepare azobenzene-functionalized core/shell polymer nanoparticles from a poly(4-hydroxystyrene)-b-polystyrene block copolymer, block copolymer **BC 2-1** is blended with Powderlink 1174<sup>®</sup> and a photo-acid-generator. After evaporating the solvent, the crosslinking is performed upon UV irradiation. To enable crosslinking with UV light, the maximum absorption of the PAG has to be chosen in a minimum of the absorption bands of the azobenzene units. Figure 114 depicts an absorption spectrum of a partially functionalized P(OHS)-b-PS block copolymer.

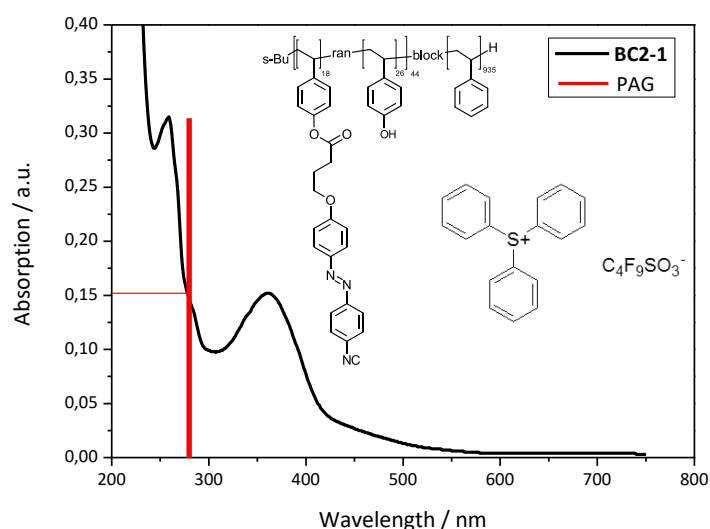


Figure 114: Absorption spectrum of a partially functionalized azobenzene functionalized poly-(4-hydroxystyrene)-b-polystyrene block copolymer film spin-coated on a quartz glass slide from a 5 wt.-% THF solution. The film thickness is 660nm. The red line depicts the wavelength of maximum absorption of the PAG (278 nm; data from PAG-supplier).

As can be seen from the absorption spectrum of the about 660 nm thick film of **BC 2-1**, the maximum absorption wavelength of the photoacid generator is located in a minimum of the absorption spectrum of the azobenzene block copolymer. The PAG therefore is suitable as a proton source in the experiment to crosslink the photoactive block copolymer. Three different amounts of crosslinker (between 1.1 and 4.2 wt.-%) were tested in this set of experiments. The amount of PAG was adjusted to be 10 wt.-% with respect to the amount of crosslinker used. The crosslinking of the partially functionalized polymer bearing 18 azobenzene units and 26 hydroxy groups in the crosslinkable block is carried out by irradiating the microphase separated film for 1 h. Afterwards, the about 3 mm thick film is post-baked at 90 °C for another hour to ensure a diffusion of the generated protons through the film to activate the crosslinker, which crosslinks the free hydroxy groups in the minority block of the polymer. After this procedure, the film is dissolved in THF using ultrasonication for 5 min. The dissolved block copolymer is then filtered through a 250 nm Teflon filter to allow for GPC analysis to be carried out (see Figure 115). During filtration, no noticeable pressure was built up.

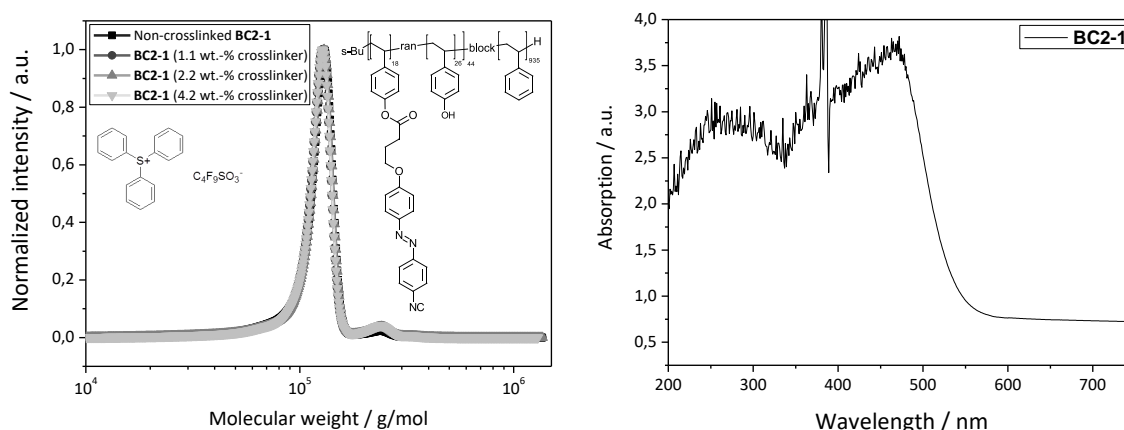


Figure 115: Left: GPC traces of non-crosslinked **BC 2-1**, and UV light irradiated **BC 2-1** with altering amounts of crosslinker from 1.1 to 4.2 wt.-% of Powderlink 1174<sup>®</sup>. Right: Absorption spectrum of a 3 mm thick film of **BC 2-1**.

The GPC analysis indicates that no crosslinking has occurred upon irradiation with UV light and subsequent post-bake of the azobenzene-functionalized **BC 2-1**. The GPC traces of the neat block copolymer equals those of the irradiated polymers blended with a crosslinker/PAG system. The reason for the failure of the crosslinking experiment could be explained by the high absorption of the 3 mm thick block copolymer in the region of the maximum absorption of the photoacid generator at 278 nm (see Figure 115). As the same system of crosslinker/PAG has worked for the non-photoactive block copolymer, a thinner, thus less absorbing azobenzene-functionalized block copolymer film could possibly solve this issue. However, films of a thickness of 500 nm or thinner would yield no sufficient amount of polymer particles per batch. Therefore, the crosslinking procedure by hydrochloric acid activated Powderlink 1174<sup>®</sup> is tested in the next step.

## 6.4.2 Hydrochloric acid treatment

### 6.4.2.1 Preparation and investigation of cyano-azobenzene-functionalized poly(4-hydroxystyrene)-b-polystyrene block copolymer nanoparticles

Since crosslinking thick films of microphase separated azobenzene-functionalized block copolymers using a photoacid generator failed, crosslinking with hydrochloric acid vapor is investigated next. Crosslinking experiments with non-photoactive block copolymer **BC 1** has shown that HCl vapor can penetrate even millimeter thick films and thus can activate the crosslinker within the film. Furthermore, crosslinking with HCl vapor means that no additional acid generator (PAG or TAG) is needed. By that, the chance of a distortion of the microphase separation of the block copolymer is reduced. Figure 116 depicts transmission electron micrographs of thin films of cyano-azobenzene-functionalized **BC 2-3** after evaporation from THF without and with additional crosslinker. In **BC 2-3**, the weight fraction of the azobenzene-functionalized block is 13 wt.-%. This amount is enough to promote the formation of a cylindrical microphase in the neat block copolymer. The white spots on the image may be caused by holes in the thin polymer film, which could originate from cutting the 50 nm thin film with a rough diamond knife. The addition of 6 wt.-% of crosslinker Powderlink 1174<sup>®</sup> has no observable influence on the micro structure of the polymer.

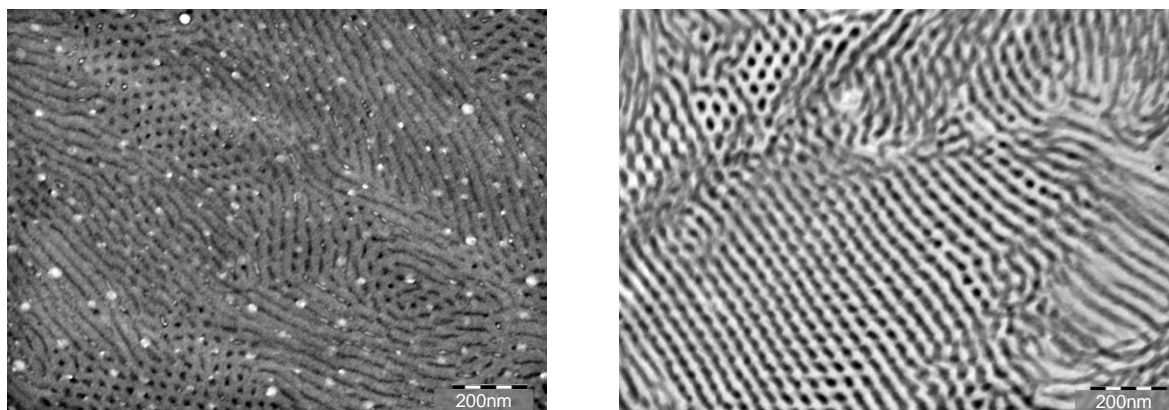


Figure 116: Transmission electron micrographs of 50nm thin sections of phosphotungsten acid stained block copolymer **BC 2-3**. Left: Neat block copolymer **BC 2-3**; Right: **BC 2-3** with additional 6 wt.-% Powderlink 1174®.

In the attempts of crosslinking non-photoactive **BC 1**, the time for exposing the microphase separated block copolymer film to HCl vapor was set to be 1 h. For the azobenzene-functionalized block copolymer **BC 2-3**, featuring a degree of functionalization of the poly(4-hydroxystyrene) block with azobenzene side groups of 70 %, an experimental series with different crosslinking times is conducted. The determination of the exact crosslinking time is performed to, if possible, lower the time of exposure of the block copolymer film to HCl to reduce possible side reactions potentially harming the azobenzene moieties. In the set of experiments, the amount of crosslinker is kept constant at 5 wt.-% with respect to the weight of the block copolymer. The film is exposed to HCl at a temperature of 120 °C to ensure good diffusion of the protons through the film. After 5, 15, and 30 mins a piece of the film is cut off and is swollen in THF. Prior to the DLS measurements, the particles are dispersed in THF via ultrasonication. The result of this experimental series is shown in Figure 117.

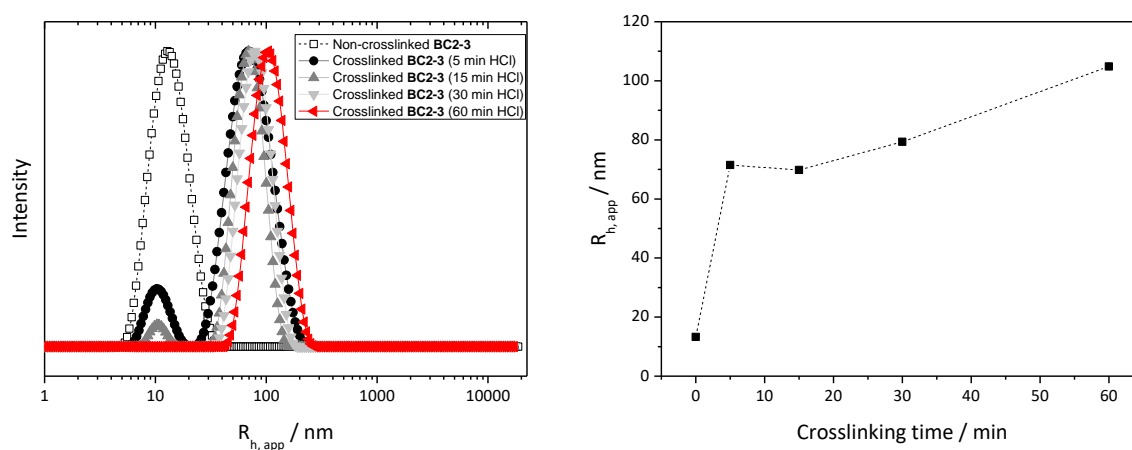


Figure 117: Left: Dynamic light scattering CONTIN plots of pure **BC 2-3** and crosslinked **BC 2-3** using HCl with increasing exposure time. The amount of Powderlink 1174® is kept constant at 5 wt.-% with respect to the weight of the block copolymer used. Right: Apparent hydrodynamic radius  $R_{h, app}$  as function of the crosslinking time.

The non-crosslinked block copolymer **BC 2-3** has an apparent hydrodynamic radius of 13 nm. Compared to the non-azobenzene-functionalized **BC 1** this is an increase in  $R_{h, app}$  of 5 nm. The DLS investigation implies that the crosslinking starts in the first minutes after exposing the film to HCl vapor. After 5 minutes, particles with a size of about 70 nm a formed. Within 30 minutes, the radius

of the particles increases to about 79 nm. However, a peak at an apparent radius of 13 nm indicates that still non-crosslinked block copolymer is present in the sample. When **BC 2-3** is crosslinked for 1 h, this peak vanishes and a single peak at an  $R_{h,app}$  of 105 nm indicates a complete crosslinking of the block copolymer.

The successful crosslinking of **BC 2-3** shows that the combination of Powderlink 1174® with exposure to HCl vapor for 1 h enables the synthesis of core/shell polymer nanoparticles from copolymers with a degree of functionalization with azobenzene units as high as 71 %. In an experimental series, the influence of the degree of functionalization with azobenzene moieties and hence, a lower amount of hydroxy groups in the minority block, is investigated. Therefore, three varyingly high functionalized block copolymers with a degree of azobenzene-functionalization between 41 wt.-% and 71 wt.-% are exposed to HCl vapor for 1 h. In all cases, 5 wt.-% crosslinker is added to the block copolymers. Figure 118 depicts the DLS CONTIN plots of the crosslinked particles and re-dispersed block copolymers as well as the non-crosslinked equivalents.

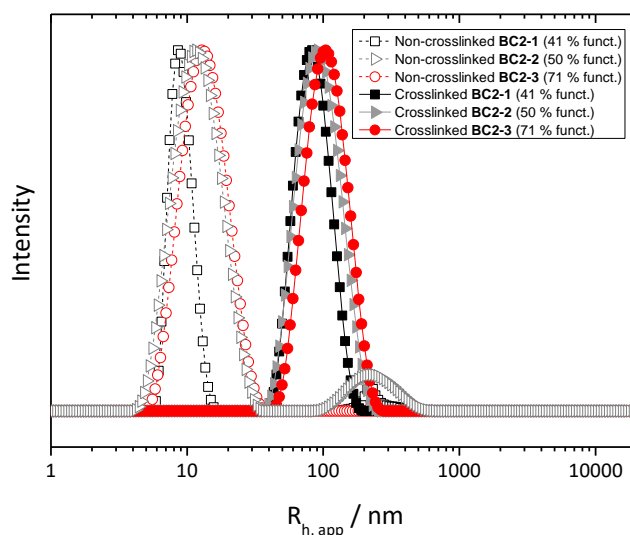


Figure 118: Comparison of crosslinking azobenzene-functionalized block copolymers with different degrees of functionalization. Dynamic light scattering CONTIN plots of pure **BC 2-1** – **BC 2-3** and crosslinked **BC 2-1** – **BC 2-3** using HCl vapor for 1 h. The amount of Powderlink 1174® is kept constant at 5 wt.-% with respect to the weight of the block copolymer used.

The non-crosslinked block copolymers feature radii between 9 and 13 nm in ascending order of the degree of azobenzene-functionalization. The same is true for the crosslinked equivalents. Here, the apparent hydrodynamic radii range between 82 and 105 nm.

The nanoparticles made from the cyano-azobenzene-functionalized block copolymer **BC 2-2** were also investigated via transmission electron microscopy. For this purpose, the re-dispersed particles are diluted with THF to a concentration of 1 mg/ml and then casted on a carbon-coated copper TEM-grid. The solvent is soaked-off by a tissue, which is located underneath the grid. The transmission electron micrographs of the unfiltered particle suspension of crosslinked block copolymer **BC 2-2** is depicted in Figure 119. The crosslinking of **BC 2-2** yields mostly cylindrical nanoparticles with a length up to 200 nm and a diameter of about 80 nm in the dried state. The crosslinked azobenzene-phase is about 10-20 nm wide. Besides the cylindrical-shaped

nanoparticles, also spherical nanoparticles have formed during crosslinking. These may have formed as a consequence of incomplete crosslinking.

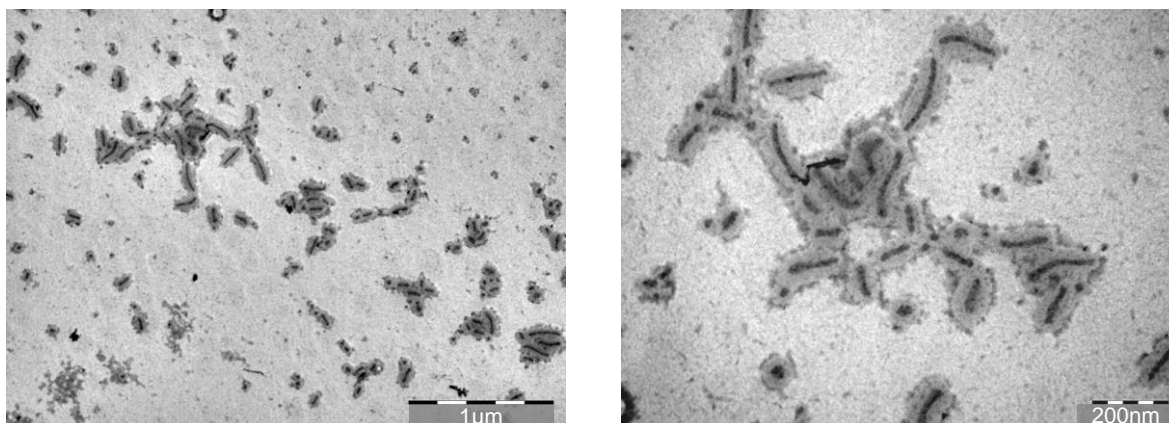


Figure 119: Transmission electron micrographs of an unfiltered particle suspension of crosslinked block copolymer **BC 2-2** stained with phosphotungsten acid on a carbon coated Cu grid. The dark areas correspond to the azobenzene functionalized block.

The photochemical behavior of crosslinked **BC 2-2** nanoparticles is investigated in a THF solution to determine if the crosslinking of the block copolymer minority block is distorting the *trans-cis-trans*-isomerization of the azobenzene moieties. For this purpose, a 0.1 mg/ml THF solution of nanoparticles from **BC 2-2** was prepared and an UV/Vis spectrum was taken. Afterwards, the solution was exposed to UV light for different times and subsequently an UV/Vis spectrum is measured again. Hereafter, the solution was stored in the dark and spectra are taken in different time intervals. Figure 120 depicts absorption spectra of the particles in THF solution before and during exposure with UV light as well as the absorption spectra of the particles after several hours in the dark.

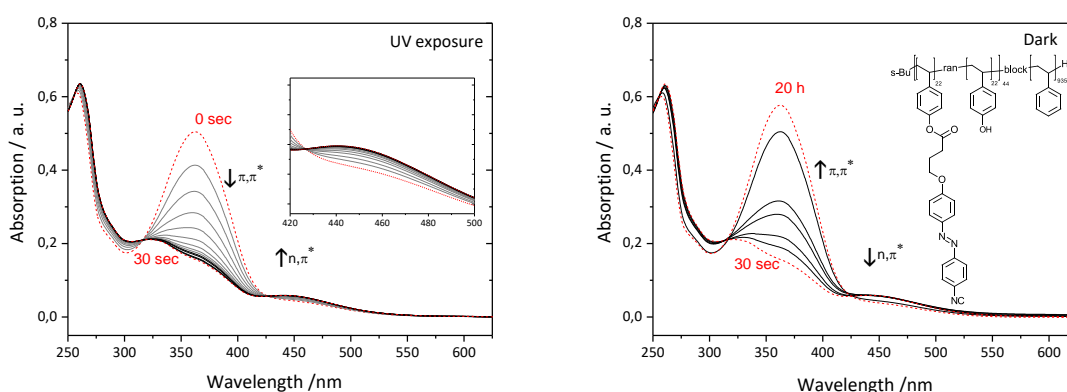


Figure 120: Left: Absorption spectra of **BC 2-2** nanoparticles before and after exposure to UV light at different exposure times. The inset shows a magnified section of the  $n,\pi^*$  absorption band of the azobenzene moieties. Right: Thermal back-relaxation of the azobenzene molecules in the dark.

The azobenzene polymer nanoparticles show a strong photo-response upon irradiation with UV light. Within 30 s, the  $\pi,\pi^*$  absorption band at 363 nm is decreased drastically, while, at the same time, the absorption band of the  $n,\pi^*$  absorption band at 454 nm increases. This observation is explained by a *cis-to-trans* isomerization of the azobenzene molecules upon exposure to non-polarized UV light. After just 30 s, a photo-stationary state is reached. When the solution is kept in the dark, the thermal back-relaxation from the thermodynamically less stable *cis*-form to the more

stable trans-form occurs. The back-relaxation takes 20 hours in this system. Despite the crosslinking reactions and the resulting confinement, cis-trans-isomerization cycles are still possible in within the particles.

The photoactive polymer nanoparticles are designed as a novel concept of diluting azobenzene molecules in a non-photoactive matrix, e.g. PS or PMMA, to achieve millimeter thick sample. At the same time the spatial proximity of the chromophores is expected to be retained to benefit from the cooperative effect between the azobenzenes. To compare the behavior of photoactive nanoparticles with non-crosslinked azobenzene-functionalized block copolymer upon dilution in a non-photoactive matrix, blends of PS shell nanoparticles **BC 2-2** with PS and non-crosslinked **BC 2-2** in PS at different concentrations between 25 and 1 wt.-% have been prepared. For this purpose, the photoactive particles and the non-crosslinked **BC 2-2** have been dispersed or dissolved in THF. To these solutions, PS in an amount of 75 wt.-%, 95 wt.-% and 99 wt.-% with respect to the total weight of the sample has been given. From the resulting six solutions, the THF has been evaporated off and the resulting films were cut in 50 nm thin films to be investigated with a transmission electron microscope (see Figure 121).

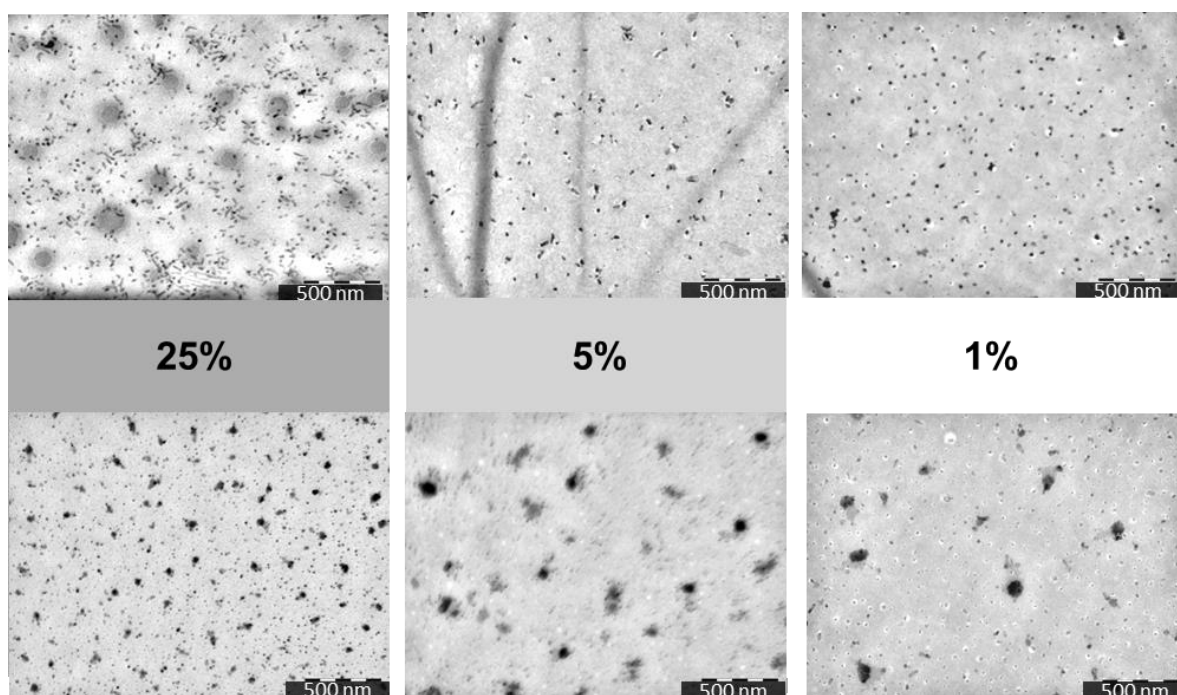


Figure 121: Transmission electron micrographs of blends of nanoparticles from block copolymer **BC 2-2** with PS (top) and blends of non-crosslinked block copolymer **BC 2-2** with PS (bottom) in different concentrations. Dark areas correspond to the azobenzene functionalized block. Stained with  $\text{RuO}_4$ .

Upon dilution of an azobenzene-functionalized block copolymer in a non-photoactive matrix, the azobenzene phase inevitably forms a spherical micro-structure.<sup>[52]</sup> This finding is confirmed when **BC 2-2** is diluted in polystyrene. The dilution of the block copolymer leads to spheres to be located further apart from each other. At a concentration of 25 wt.-%, the spheres are smaller than at higher dilutions. After diluting the block copolymer to an amount to 5 wt.-% with respect to the overall sample weight and below that, the size of the spheres is not changed anymore. The size of the nanoparticles, however, is not changed throughout the concentration series. In contrast to the non-crosslinked **BC 2-2**, the shape of the microstructure is preserved upon dilution, so that, besides nano spheres, also cylindrical nanoparticles are observable in the film. The nanoparticles are

distributed randomly and homogeneously within the sample. This finding suggests that the polystyrene shell of the particles ensures a good miscibility with the polystyrene.

#### 6.4.2.2 Preparation and investigation of methoxy-azobenzene-functionalized poly(4-hydroxystyrene)-b-polystyrene block copolymer nanoparticles

The concept of crosslinking azobenzene-functionalized block polymers with hydrochloric acid vapor is investigated on a methoxy-azobenzene-functionalized block copolymer next. In principle, the two azobenzene-functionalized block copolymers **BC 2** and **BC 3** differ not much from each other. In contrast to the **BC 2** copolymers, the azobenzene moieties carry methoxy instead of cyano substituents on the para-position of the chromophores. Furthermore, the degree of functionalization in **BC 3** is higher than in the other polymers. In **BC 3**, 37 of the 44 hydroxy groups are functionalized with azobenzene side groups yielding a degree of functionalization of 86 % and a weight of the functionalized block of 15 wt.-% with respect to the block copolymer weight. As a consequence of the high weight of the photoactive block, the microphase is expected to be cylindrical. Figure 122 depicts transmission electron micrographs of thin films of azobenzene-functionalized **BC 3** after evaporation from THF without and with additional crosslinker. As expected, neat **BC 3** forms a cylindrical microphase. The addition of 5 wt.-% of crosslinker Powderlink 1174<sup>®</sup>, however, seems to influence the micro structure of the polymer. While in case of the cyano-azobenzene-functionalized block copolymer **BC 2** the polar crosslinker seems to accumulate in the azobenzene phase, here, the crosslinker seems not to prefer the azobenzene phase. As a consequence, the cylindrical morphology is distorted. The formed micro-phase appears to be a kind of transition phase between a cylindrical and a spherical morphology. As a consequence, the crosslinking of **BC 3** should yield a mixture of cylindrical and spherical polymer nanoparticles.

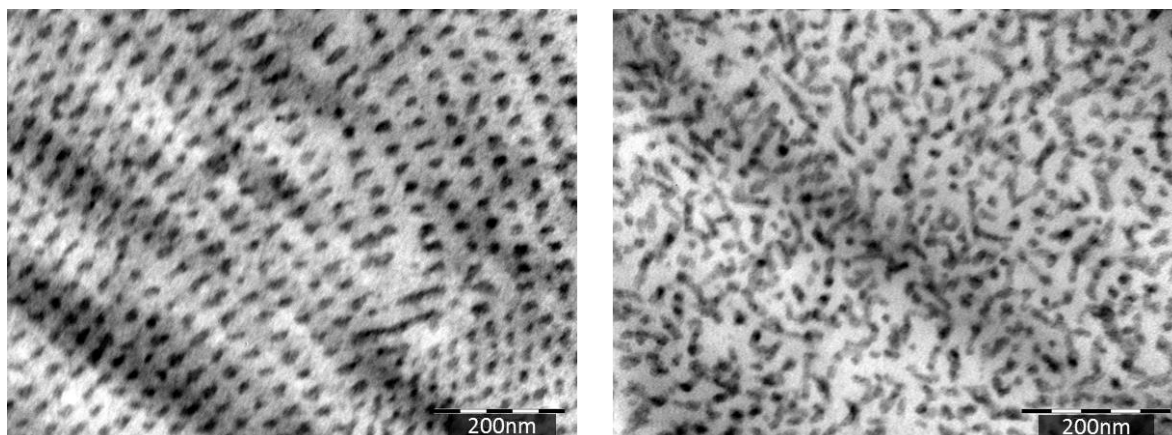


Figure 122: Transmission electron micrographs of 50nm thin sections of phosphotungsten acid stained block copolymer **BC 3**. Left: Neat block copolymer **BC 3**; Right: **BC 3** with additional 5 wt.-% Powderlink 1174<sup>®</sup>.

Since the combination of Powderlink 1174<sup>®</sup> as crosslinker and treatment with hydrochloric acid as proton source has been successful in the synthesis of polymer nanoparticles from cyano-azobenzene-functionalized block copolymers, **BC 3** has been crosslinked in the same way. For the experimental series, 5 wt.-% crosslinker has been added to the block copolymer in a THF solution. After evaporation of the solvent and microphase separation of the polymer, the polymer film has been exposed to HCl vapor at 120°C for different periods of time. The results of the DLS measurement of the re-dispersed particles in THF is shown in Figure 123.

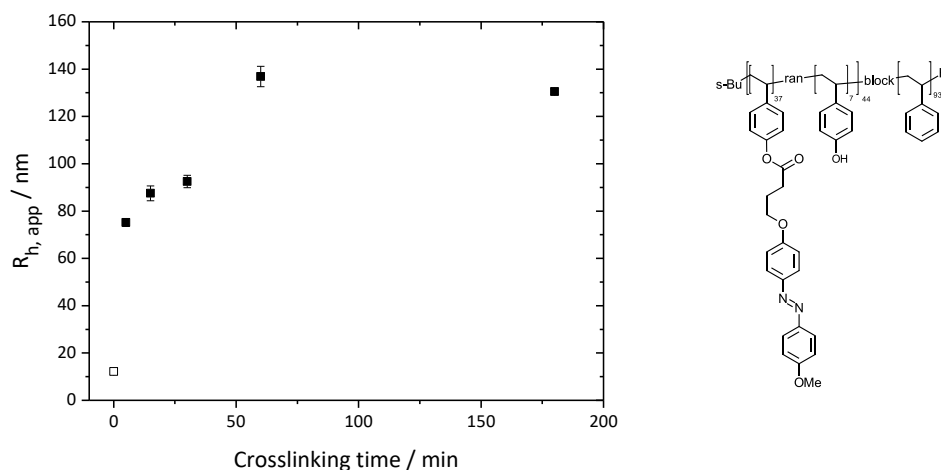


Figure 123: Apparent hydrodynamic radius  $R_{h, app}$  of BC 3 as a function of the crosslinking time. The open symbol represents the  $R_{h, app}$  of the non-crosslinked block copolymer.

The neat block copolymer features a hydrodynamic radius of about 13 nm. With increasing crosslinking time, the radius of the crosslinked polymer increases to about 90 nm after 45 min and increases further to 140 nm after 60 min of crosslinking. After 60 min, the hydrodynamic radius does not increase further, which suggests that the crosslinking of the block copolymer is completed after 60 min. In comparison to the cyano-azobenzene-functionalized, the  $R_{h, app}$  is about 40 nm larger.

The crosslinked core/shell polymer nanoparticles have been investigated using a TEM. For this purpose, the dispersed particles have been diluted to a concentration of 1 mg/ml. Subsequently, the dispersion is dropped on a carbon coated TEM grid. After staining the sample with phosphotungsten acid, the film has been dried at room temperature (see Figure 124).

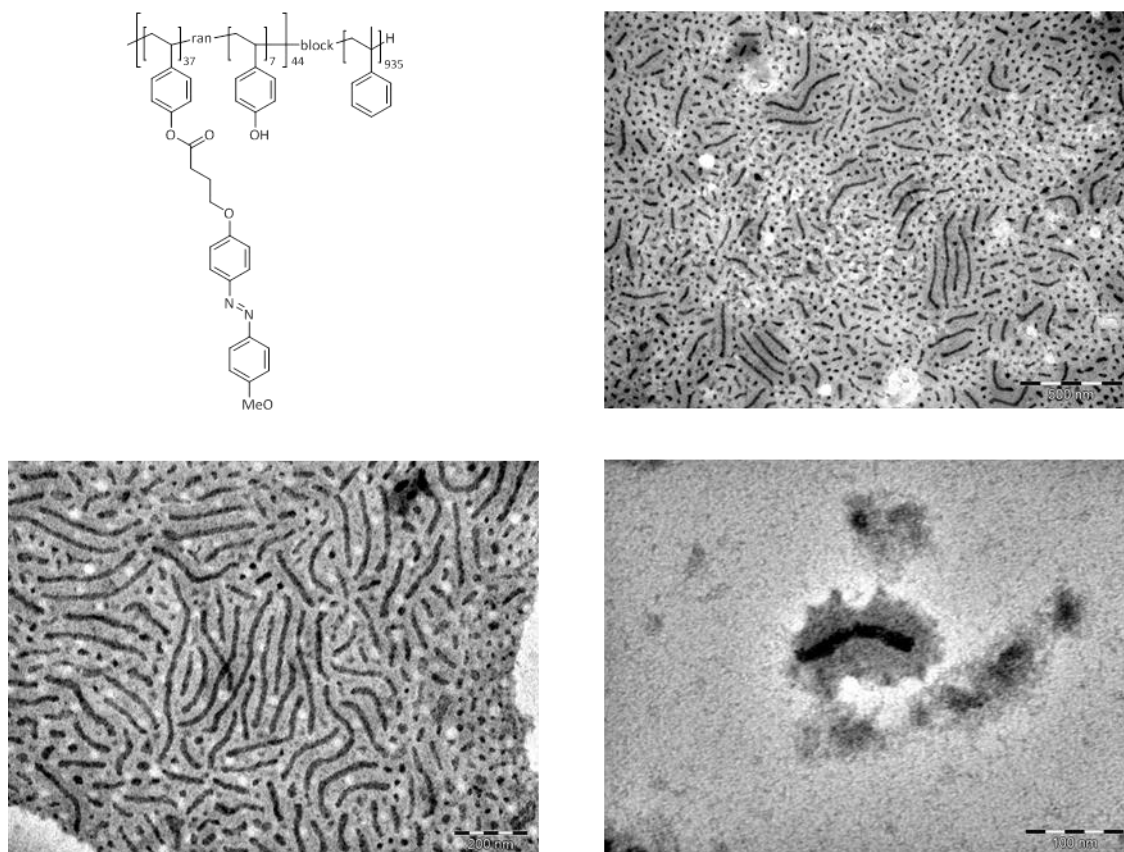


Figure 124: Transmission electron micrographs of an unfiltered particle suspension of crosslinked block copolymer **BC 3** stained with phosphotungsten acid on a carbon coated Cu grid. The dark areas correspond to the azobenzene functionalized block.

As expected from the investigation of the microphase of the block copolymer blend with Powderlink 1174<sup>®</sup>, a mixture of cylindrical and spherical nanoparticles are obtained. As in case of the particles obtained from **BC 2**, the azobenzene phase is about 10-20 nm wide. The cylindrical particles, however, are much longer. The longest particles feature a length of more than 500 nm.

#### 6.4.3 Holographic performance of azobenzene-functionalized poly-(4-hydroxystyrene)-b-polystyrene nanoparticles

The holographic performance of azobenzene-functionalized poly-(4-hydroxystyrene)-b-polystyrene nanoparticles is tested in 1.1 mm thick samples with a diameter of 2.5 cm prepared by injection molding. As reference material, the non-crosslinked block copolymer is investigated as thick sample in a holographic experiment. For this purpose, powder blends of azobenzene containing material with neat polystyrene polymer PS165H with a ratio of polystyrene:azobenzene-functionalized material of 99:1 wt.-% were prepared. The powder/powder blends are homogenized in a tumbling mixer for 12 h. Afterwards, the blends were compounded in a twin screw micro-compounder at a temperature of 230°C at a screw rotation speed of 50 rpm for 5 minutes. The extruded polymer was cut into pieces and subjected to injection molding. The polymer blend was injected into a surface-polished mold with a diameter of 25 mm and a thickness of 1.1 mm at a melt temperature of 210°C. The pressure was adjusted to 6 bar and the mold temperature was set to 70°C. The thick samples were annealed in a surface-polished annealing mold at 130°C in a vacuum oven for 20 h to reduce the shear birefringence, which was introduced into the specimen during injection molding.

As first material, the cyano-azobenzene-functionalized particles from block copolymer **BC 2-3** as well as non-crosslinked **BC 2-3** are investigated. The temporal evolution of the diffraction efficiency during the inscription process of a holographic grating is shown in Figure 125.

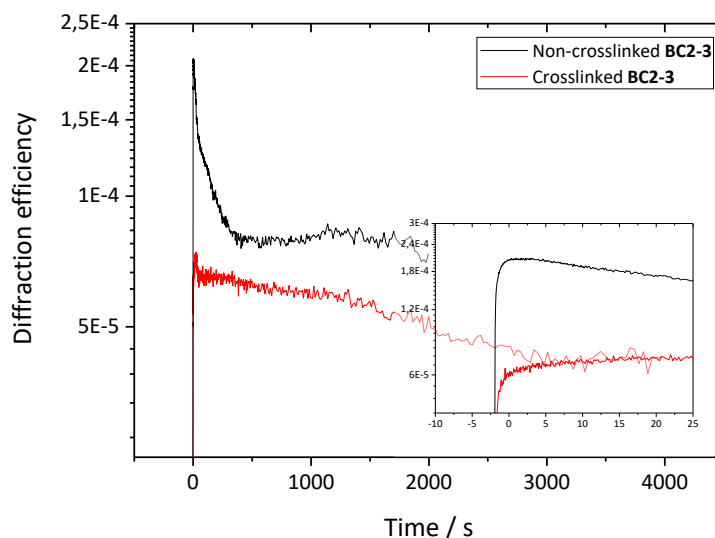


Figure 125: Temporal evolution of the diffraction efficiency during the inscription process of a holographic grating in a thick sample of crosslinked and non-crosslinked block copolymer **BC 2-3**. The inset shows the first 25 seconds of the inscription process.

The maximum diffraction efficiency in the non-crosslinked **BC 2-3** is reached after just about 2 s, while the maximum in the nanoparticle sample is attained after ca. 21 s. Besides the longer writing time, the reached value for the maximum diffraction efficiency is about 3 times lower than in case of the non-crosslinked block copolymer. The lower diffraction efficiency in the nanoparticle sample can be attributed to a higher degree in spatial confinement of the chromophores in the crosslinked azobenzene minority phase. The introduced linkages could lead to a restriction of the azobenzene moieties mobility, so that an orientation of the chromophores perpendicular to the polarity of the incident light is more limited resulting in a lower diffraction efficiency. The long-term stability of both samples seems to be not high. Even though cylindrical nanoparticles can be found in TEM images of the nanoparticle comprising thick sample, the negative influence of crosslinking the azobenzene phase seems to outweigh the potential positive aspects, i.e. better stability of gratings due to a cylindrical azobenzene phase.

The writing time and the reached diffraction efficiency in a holographic experiment is also investigated on methoxy-substituted azobenzene-functionalized poly-(4-hydroxystyrene)-b-polystyrene block copolymer and its nanoparticles (see Figure 126).

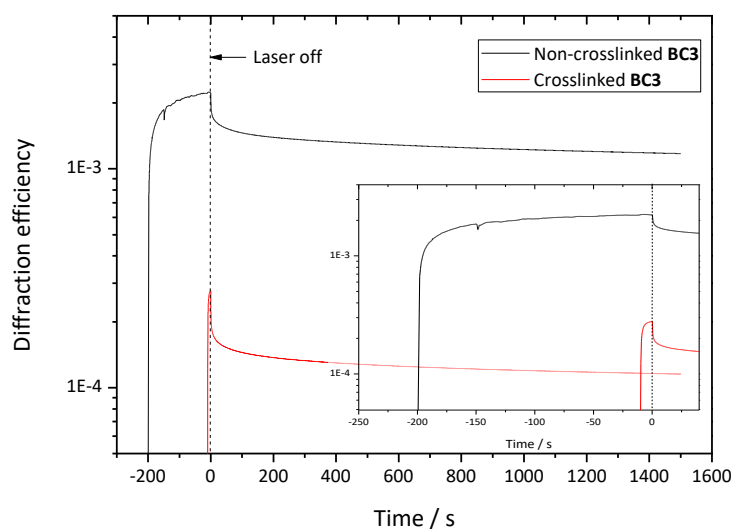


Figure 126: Temporal evolution of the diffraction efficiency during the inscription process of a holographic grating in a thick sample of crosslinked and non-crosslinked block copolymer **BC 3**. The inset shows the first 25 seconds of the inscription process. The dashed line depicts the time at which the laser is switched off.

In case of methoxy-azobenzene-functionalized block copolymer **BC 3**, the writing time in the nanoparticle sample is ca. 18 s. Compared to the writing time of non-crosslinked **BC 3**, this is about 10 times faster. However, the reached maximum diffraction efficiency in the sample comprising the nanoparticles is about 10 times lower ( $2.8 \cdot 10^{-4}$ ) compared to the block copolymer ( $2.3 \cdot 10^{-3}$ ). The reason for both observations, as in the former case, is most likely due to spatial restrictions of the chromophores. As in case of **BC 2-3**, the long-term stability of both samples does not differ significantly. To avoid light scattering, the nanoparticles were filtered using a  $5 \mu\text{m}$  pore size filter before subjecting the nanoparticles to the compounding process. As a consequence, the number and therefore the influence of cylindrical particles with potential positive effect on the long-term stability of the gratings is reduced.

## 6.5 Synthesis and characterization of photoactive polymer nanoparticles with poly-(methyl methacrylate) shell

In a next step, the concept of synthesizing polymer nanoparticles from a block copolymer with a poly(hydroxy styrene) minority block with a polystyrene shell using Powderlink 1174<sup>®</sup> as crosslinker with HCl as proton source is transferred to a partially azobenzene-functionalized poly(hydroxy styrene)-b-poly-(methyl methacrylate) block copolymer. The azobenzene-functionalized block of the investigated **BC 4** has a weight portion of 23 wt.-% and a degree of azobenzene functionalization of 87 %. The minority block feature 53 azobenzene units and 8 hydroxy groups, which are needed to crosslink this segment. The weight ratio of the two blocks suggests a cylindrical minority phase (see Figure 127).

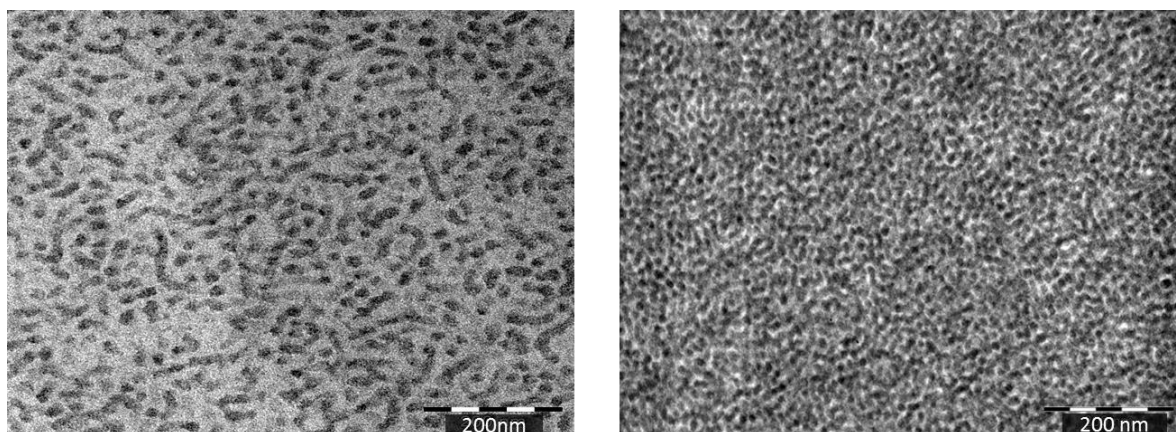


Figure 127: Transmission electron micrographs of left: a 50nm thin section of neat block copolymer **BC 4** film. Right: 50nm thin section of block copolymer **BC 4** film containing 6 wt.-% Powderlink 1174<sup>®</sup>. Dark areas correspond to the azobenzene functionalized block. The films were annealing at 120°C for 12h and stained with RuO<sub>4</sub>.

The left image shows a thin film of neat block copolymer **BC 4**. The right image depicts partially azobenzene-functionalized poly(4-hydroxystyrene)-b-poly-(methyl methacrylate) block copolymer **BC 4** with additional 6 wt.-% Powderlink 1174<sup>®</sup>. Both films were stained with RuO<sub>4</sub> and thus the dark areas correspond to the minority block, while the bright areas depict the poly(methyl methacrylate) matrix. In both cases, the azobenzene domains form a poorly ordered cylindrical micro phase. The addition of the crosslinker to the block copolymer increases the order of the microphase separation of the polymer as in some areas hexagonally arranged cylinders can be observed. As the order in the micro phase separation is poor, a prediction of the shape of resulting nanoparticles is difficult.

Since the azobenzene block copolymers from the former experiments feature similar block weight ratios and degrees of functionalization with azobenzene units, the time for exposure of **BC 4** to HCl vapor is set to be 1 h. Also, the amount of 6 wt.-% crosslinker Powderlink 1174<sup>®</sup> is similar to the amount used in the former experiments. Figure 128 depicts the DLS CONTIN plot of the crosslinked and re-dispersed block copolymer **BC 4** as well as the non-crosslinked equivalent.

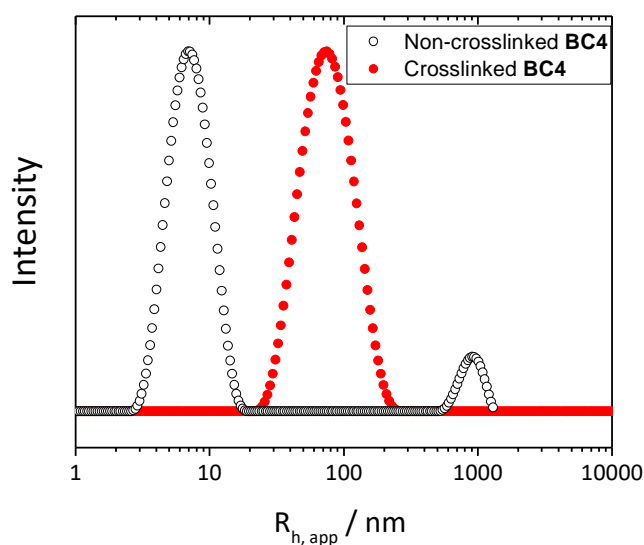


Figure 128: Dynamic light scattering CONTIN plots of neat **BC 4** and crosslinked **BC 4** using HCl and Powderlink 1174®.

The non-crosslinked block copolymer features an apparent hydrodynamic radius of about 7 nm. The peak at 900 nm most likely is an artifact since the investigated solutions were filtered with a 1-2  $\mu\text{m}$  PTFE filter before DLS investigation.  $R_{h,app}$  of the nanoparticles is 75 nm, thus comparable to the radius of nanoparticles formed from block copolymer **BC 2-1** with a low degree of functionalization. The low radius suggests the formation of spherical rather than cylindrical nanoparticles.

To identify the shape of the nanoparticles, the crosslinked **BC 4** is investigated with a transmission electron microscope. For this purpose, the re-dispersed particles are diluted with THF to a concentration of 1 mg/ml and then casted on a carbon-coated copper TEM-grid. The transmission electron micrographs of the particle suspension of crosslinked block copolymer **BC 4** is depicted in Figure 129. The dark areas correspond to the  $\text{RuO}_4$  stained azobenzene-functionalized minority block. The PMMA shell is transparent to electrons, thus is not visible on the images. The crosslinking of **BC 4** yields wormlike, often branched and spherical nanoparticles. The wormlike structures seem to have formed upon aggregation of several spherical particles rather than from the crosslinking of a cylindrical micro phase. The crosslinked azobenzene-phase is about 10 nm wide. The poorly defined shape of the particles may be a consequence of the poorly defined micro phase separation or of an incomplete crosslinking. Compared to the block copolymers with a polystyrene matrix, the PMMA matrix is relatively polar. The polarity of the matrix could have hindered a diffusion of the protons through the entire film thickness. Exposure to HCl at this high temperatures could have also lead to partial cleavage of the PMMA units. A change in the molecular weight, however, could not be determined via GPC analysis.

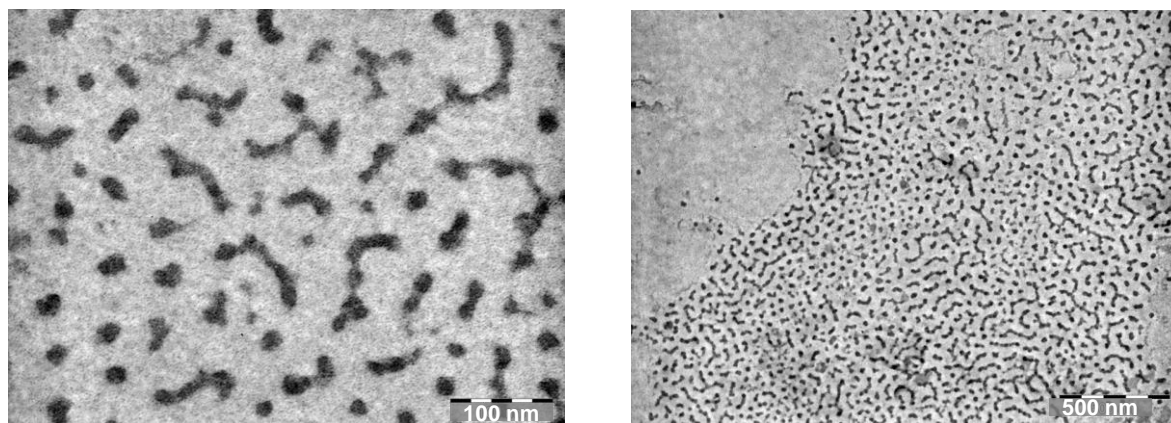


Figure 129: Transmission electron micrographs of an unfiltered particle suspension of crosslinked block copolymer **BC 4** stained with  $\text{RuO}_4$  on a carbon coated Cu grid. The dark areas correspond to the azobenzene functionalized block.

The photochemical behavior of crosslinked **BC 4** is investigated via UV/Vis spectroscopy to determine if the crosslinking of the block copolymer minority block is distorting the *trans-cis-trans*-isomerization of the azobenzene moieties. For this purpose, a 0.1 mg/ml THF of **BC 4** is exposed to UV light in different time intervals and then stored in the dark. Figure 130 depicts absorption spectra of the particles in THF solution before and during exposure with UV light as well as the absorption spectra of the particles after several hours in the dark.

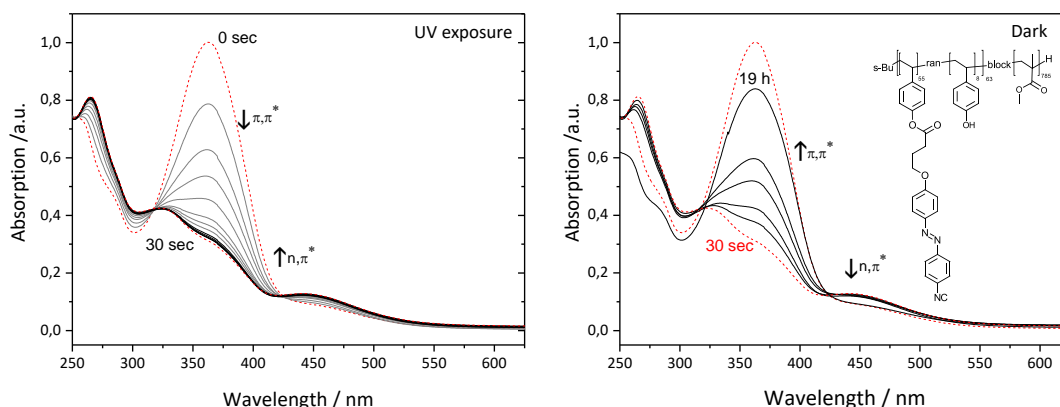


Figure 130: Left: Absorption spectra of **BC 4** nanoparticles before and after exposure to UV light at different exposure times. Right: Thermal back-relaxation of the azobenzene molecules in the dark.

The azobenzene-functionalized polymer nanoparticles show a photo-response upon irradiation with UV light. Within 30 s, the  $\pi,\pi^*$  absorption band at 360 nm is decreased, while, at the same time, the absorption band of the  $n,\pi^*$  absorption band at 455 nm increases. This observation is explained by a *cis*-to-*trans* isomerization of the azobenzene molecules upon exposure to unpolarized UV light. After just 30 s, a photo-stationary state is reached and the photochemical reaction stops. When the solution is kept in the dark, the thermal back-relaxation from the thermodynamically less stable *cis*-form to the more stable *trans*-form occurs. The back-relaxation takes more than 19 hours. Despite the crosslinking reactions and the resulting confinement, *cis-trans*-isomerization cycles are still possible in within the particles.

To compare the behavior of photoactive nanoparticles with non-crosslinked azobenzene-functionalized block copolymer upon dilution in a non-photoactive PMMA matrix, blends of PMMA

shell nanoparticles **BC 4** with PMMA and non-crosslinked **BC 4** in PMMA at concentrations of 25, 5 and 1 wt.-% have been prepared. For this purpose, the photoactive particles and the non-crosslinked **BC 4** have been dispersed or dissolved in THF. To these solutions, PS in an amount of 75 wt.-%, 95 wt.-% and 99 wt.-% with respect to the total weight of the sample has been added. From the resulting solutions, the THF has been evaporated off and the resulting films were cut in 50 nm thin films via an ultramicrotome cutting knife and then have investigated with a transmission electron microscope (see Figure 131).

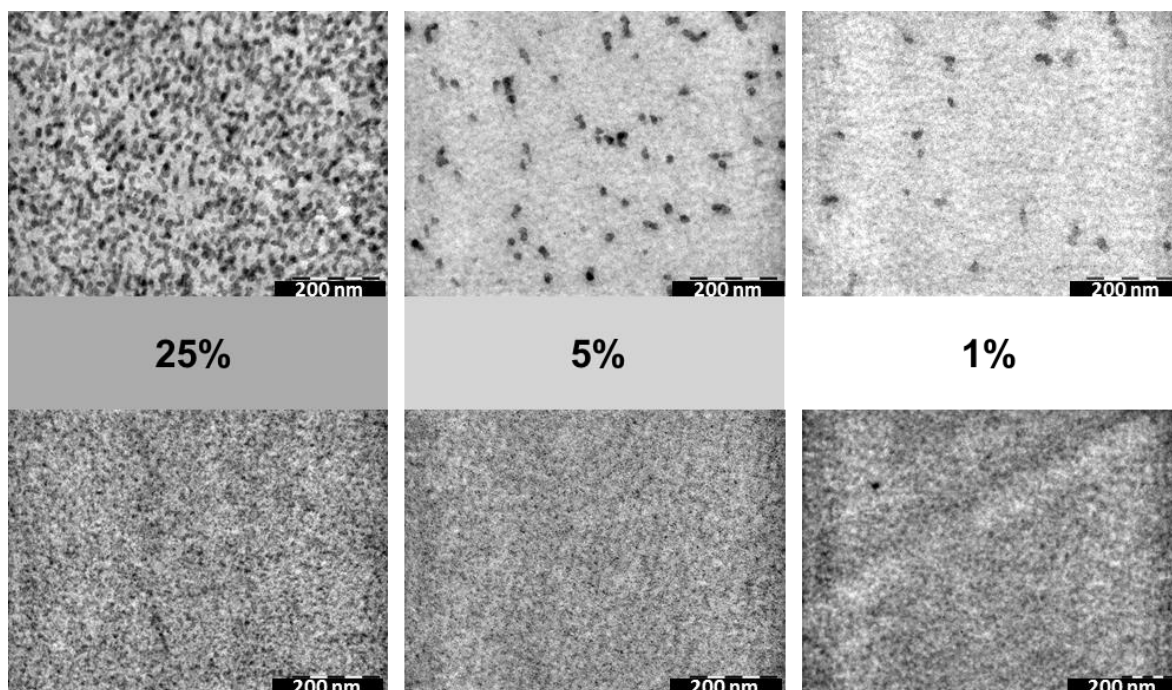


Figure 131: Transmission electron micrographs of blends of nanoparticles from **BC 4** with PMMA (top) and blends of block copolymer **BC 4** with PMMA (bottom) in different concentrations. Dark areas correspond to the azobenzene functionalized block. Stained with  $\text{RuO}_4$ .

Dilution of the azobenzene-functionalized block copolymer in the non-photoactive PMMA matrix must lead to a formation of a spherical micro-structure. However, the azobenzene-functionalize phase cannot clearly be identified in the dilution series of non-crosslinked **BC 4**. It seems as if the confinement of the azobenzene moieties is lost upon dilution. The confinement of the nanoparticles, on the other hand, is stable throughout the concentration series. In contrast to the non-crosslinked **BC 4**, the spherical shape of the microstructure is preserved upon dilution. The nanoparticles are distributed randomly and homogenously within the sample. Dilution of the particles just leads to an arrangement of the particles with greater distances to each other. This finding suggests that the PMMA shell of the particles ensures a good miscibility with the PMMA matrix.

### 6.5.1 Holographic performance of cyano-substituted azobenzene-functionalized poly-(4-hydroxystyrene)-b-poly(methyl methacrylate) nanoparticles

The holographic performance of azobenzene-functionalized poly-(4-hydroxystyrene)-b-polystyrene nanoparticles is tested in thin films of the neat material (thickness  $\approx 600$  nm) prepared by doctor blading. As reference material, the neat non-crosslinked block copolymer **BC 4** is investigated. The temporal evolution of the diffraction efficiency in thin films of cyano-azobenzene-functionalized particles from block copolymer **BC 4** as well as in non-crosslinked **BC 4** during the inscription process of a holographic grating is shown in Figure 132.

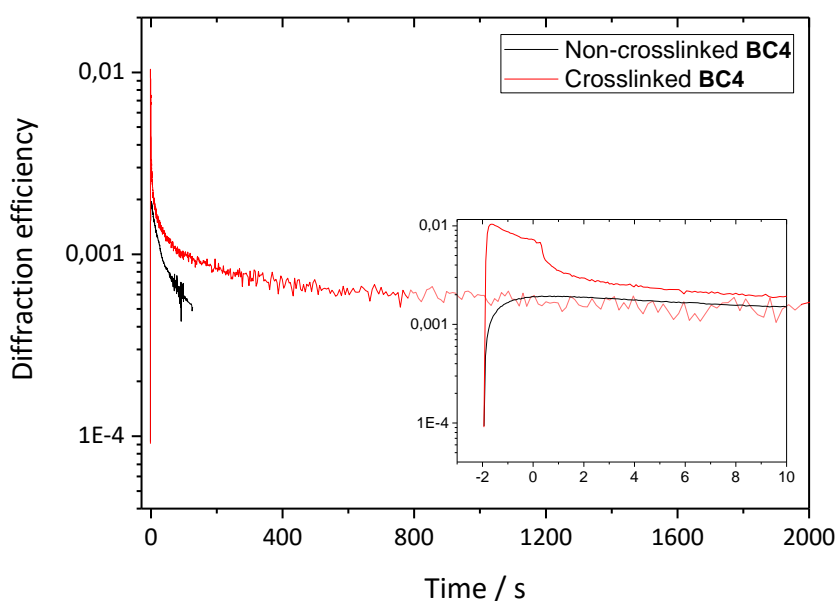


Figure 132: Temporal evolution of the diffraction efficiency during the inscription process of a holographic grating in a thin film sample of crosslinked and non-crosslinked block copolymer **BC 4**. The inset shows the first 10 seconds of the inscription process.

In the case of the non-crosslinked block copolymer **BC 4**, the writing time is about 2 s. The maximum diffraction efficiency in the sample comprising the nanoparticles from **BC 4**, however, the writing time is decreased to less than 0.3 s. In contrast to former studies of the holographic performance of nanoparticles, the reached maximum diffraction efficiency in is higher than in the block copolymer. Also, the long-term stability of the nanoparticle samples is slightly better than in the sample of non-crosslinked **BC 4**. These trends are in striking contrast to the results obtained in case of the other investigated nanoparticles made from **BC 2** and **BC 3** but could be explained by inhomogeneities in the film containing the nanoparticles as a consequence of the worsened film forming properties of the nanoparticles. As a result, a local variation in the film thickness can be obtained leading to higher film thicknesses than measured, which leads to incomparability of two films with allegedly featuring the same film thickness.

## 6.6 Summary of the chapter

A novel concept of diluting azobenzene-functionalized material in a non-photoactive matrix to yield millimeter thick samples for holographic applications is presented. The concept includes the synthesis of newly developed azobenzene-containing core/shell polymer nanoparticles with polystyrene and poly(methyl methacrylate) shell.

The polymer nanoparticles are crosslinked with the commercially available crosslinker Powderlink 1174®. For the first time, polymer core/shell particles are synthesized using this crosslinking agent. The crosslinking reaction takes place in the poly(4-hydroxystyrene) containing minority block. The tetra-functional crosslinking agent is activated by protons, which can be provided by thermal acid- or photoacid generators or by exposure with hydrochloric acid vapor.

All three proton sources have successfully been applied in the synthesis of non-photoactive poly(4-hydroxystyrene)-b-polystyrene polymer nanoparticles. For the synthesis of partially azobenzene-functionalized poly(4-hydroxystyrene)-b-polystyrene and azobenzene-functionalized poly(4-hydroxystyrene)-b-poly(methyl methacrylate) nanoparticles, the use of HCl vapor has proven to be suited best. TEM investigations showed that the crosslinker preferably accumulates in the azobenzene and hydroxy-functionalized minority phase and very efficiently crosslinks block copolymers with varying degrees of azobenzene functionality at a content of 5 wt.-% within 1 h of HCl exposure.

Investigations of the photophysical behavior of the azobenzene-functionalized nanoparticles via UV/Vis spectroscopy have shown that the crosslinking reaction has no negative impact on the *cis-trans* isomerization reaction of the chromophores.

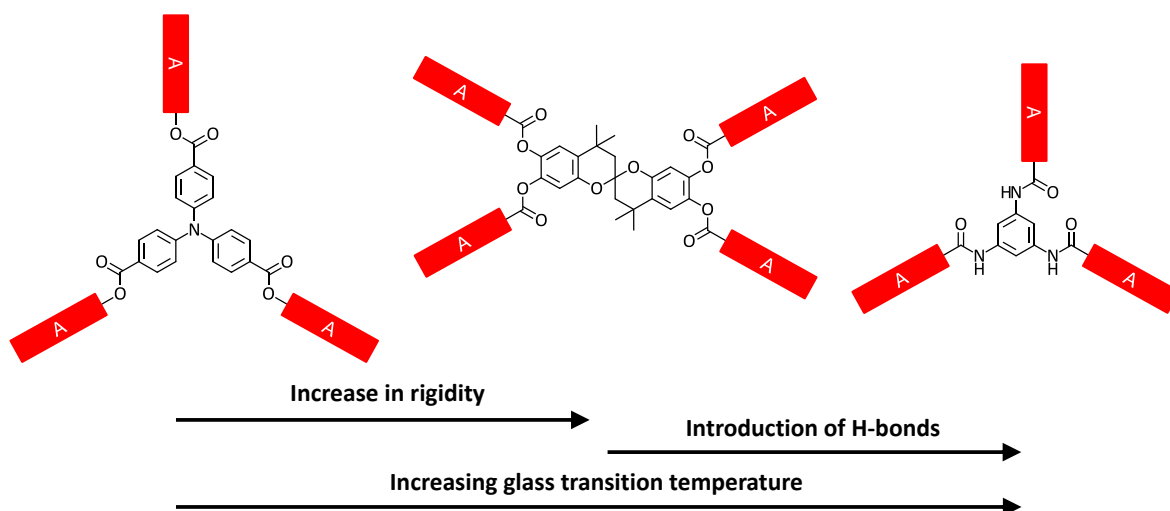
The obtained spherical and cylindrical nanoparticles were homogeneously incorporated in a non-photoactive PS or PMMA matrix and the holographic performance was evaluated based on injection molded millimeter thick samples. Experiments have proven that the holographic performance is not significantly altered.

## 7 Summary

Azobenzene chromophores possess unique photophysical properties and, therefore, have been subject to considerable research effort. The underlying mechanism is repeated *trans-cis-trans* isomerization, which renders azobenzene-functionalized materials useful in fascinating applications such as holographic data storage or surface patterning.

This thesis covers the design, synthesis and characterization of azobenzene-functionalized low-molecular-weight compounds, polymers and polymer nanoparticles as well as their application in holography and a newly developed azobenzene-based nanoimprint lithography.

The *first chapter* comprises the ***synthesis and characterization of azobenzene-functionalized molecular glasses*** based on 3 different cores with varying rigidity, steric demand and secondary interactions. The tri- or tetra-functional compounds feature triphenylamine, 1,3,5-benzenetrisamide or spirobichromane cores, to which azobenzene moieties are attached to. The azobenzene chromophores carry substituents on the para-position of the azo group to control the photophysical properties of the molecules.



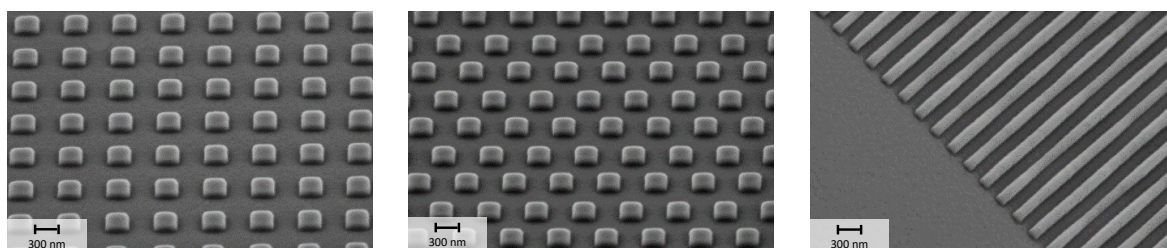
Schematic representation of the synthesized azobenzene-functionalized molecular glasses based on different cores. The rigidity of the cores is increasing from triphenylamine-based to spirobichromane-based molecular glasses. In case of 1,3,5-benzenetrisamide derivatives, intermolecular H-bond-formation capability is introduced. The glass transition temperature increases from left to right. The red rectangles represent the azobenzene chromophores.

Different azobenzene moieties are synthesized via the so-called “Mills reaction”, i.e. a condensation reaction of a para-nitrosobenzoic acid and an aniline derivative. The chromophores are attached to the corresponding core via esterification or amidation reactions. Thermal characterization was conducted via differential scanning calorimetry, thermal gravimetric analysis and polarization microscopy. Seven out of eleven compounds feature a glass transition temperature above 92 °C, increasing with the rigidity of the molecule core and with the introduction of strong secondary interactions (H-bonds) up to 136 °C. The low-molecular-weight compounds can readily be transferred into thin films with a very stable amorphous phase via, e.g., spin coating. UV/Vis spectroscopy in thin films and solution shows the adjustability of the photophysical properties of the molecular glasses by substitution with H, MeO or CF<sub>3</sub>-groups at the azobenzene moieties.

The *second chapter* covers the **development and optimization of a novel surface patterning method** based on azobenzene-functionalized materials allowing for the fabrication of non-periodic complex micro and nanostructures. For the first time, the unique properties of athermal photofluidization of azobenzenes are combined with the principles of nanoimprint lithography; hence, the technique is referred to as azobenzene-based nanoimprint lithography or azo-NIL. In azo-NIL, the negative-type pattern of a structured stamp is imprinted into a thin azobenzene film by exposure of the same to light of a suitable wavelength. Neither crosslinking reactions nor heat is needed and no phase transition occurs, so that shrinkage issues associated with established nanoimprint lithography techniques, e.g., thermal-NIL or UV-NIL, are avoided.

The most important parameters influencing the performance of azo-NIL, such as the wavelength of the incident light, the fluence or the film thickness and the stamp material are comprehensively studied. Imprinting experiments have revealed that biphotonic exposure with two LEDs featuring wavelengths of 365 nm and 455 nm is most beneficial for efficiently triggering *trans-cis-trans*-isomerization cycles and, thus, increasing the imprinting speed. It was also found that the fluence is directly proportional to the imprinting performance. Moreover it was demonstrated, that a resist film thickness of at least 500 nm results in the best imprinting performance, since the patterning of thinner films is restricted by capillary flow. Investigations on the influence of the pattern size revealed, that azo-NIL allows for the successful imprinting of structure sizes ranging from 10  $\mu\text{m}$  to 100 nm.

Subsequently, the influence of the resist material on the imprinting speed and quality of the imprinted structures was investigated using nine different azobenzene-functionalized molecular glasses and a poly(1,2-butadiene)-based photo-orientable homopolymer. It was found, that the fastest and most precise replication of various patterns can be realized with spirobichromane-based molecular glasses.

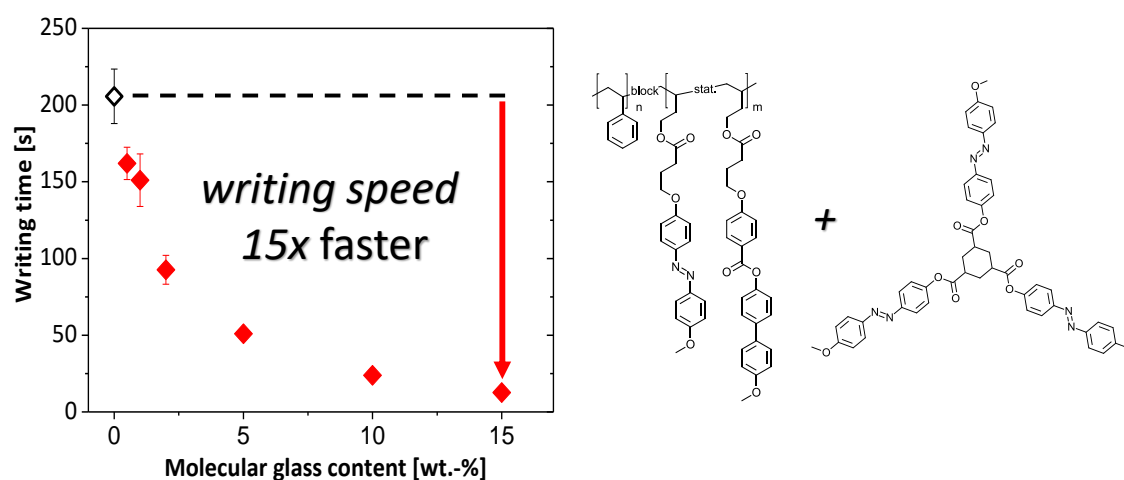


Tilted SEM micrographs of different 300 nm and 150 nm sized nanopatterns imprinted into films of an azobenzene-functionalized spirobichromane-based molecular glass.

The build-up constant  $\tau$ , i.e. the time at which 63 % of the maximum achievable structure height of 100 nm is reached, is 118 s in a film of a spirobichromane compound carrying H-substituted azobenzene moieties using biphotonic exposure. Owing to the tuned photophysical properties, the methoxy-substituted spirobichromane-based derivative features the best imprinting performance of all investigated compounds with just 64 s. This is about 5 times faster than the investigated homopolymer, which features a build-up constant of 308 s. Imprinting at elevated temperatures decreases the time to just 9 s. Even at temperatures just 10  $^{\circ}\text{C}$  below the  $T_g$  of the material, the amorphous phase is stable and no indications of crystallization are observed.

The *third chapter* covers the **improvement of the holographic recording performance of different photo-orientable azobenzene polymers by blending with molecular glasses**. In this chapter, holographic gratings are inscribed (or written) into the volume of thin films of azobenzene-functionalized materials by superposition of two polarized laser beams in the photoactive material, causing a reorientation of the chromophores in the illuminated areas.

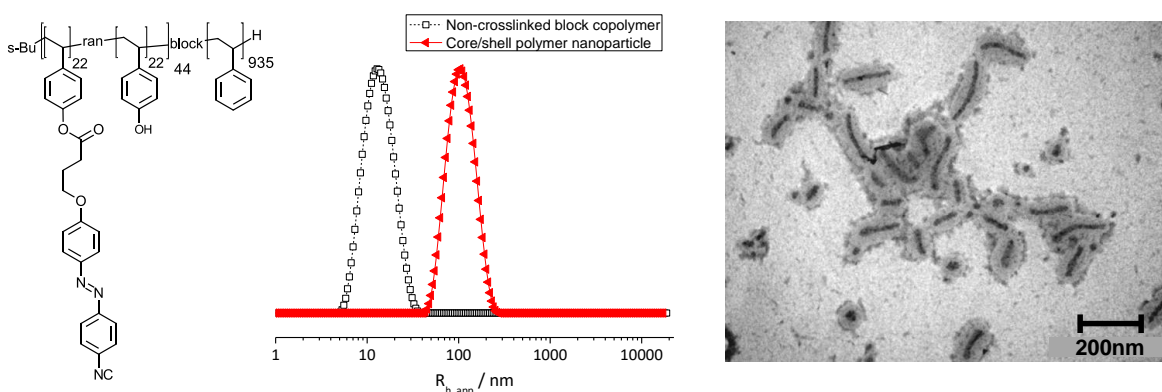
It was found, that the high writing speed of the investigated molecular glass in blends with non-photoactive polystyrene is retained down to molecular glass content of just 30 wt.-%. This demonstrates that the cooperative effect, which increases the writing speed and the stability of inscribed gratings, is still present between the azobenzene-functionalized molecules. Upon exposure, in blends with photo-orientable polymers the molecular glass reorients the azobenzene groups attached to the polymer backbone. This applies for the investigated poly(1,2-butadiene)-based methoxy-azobenzene-substituted homopolymer as well as for the two block copolymers featuring a polystyrene majority block and an azobenzene-functionalized poly(1,2-butadiene) minority segment. In addition to the azobenzene moieties, one block copolymer bears non-photoactive mesogens, which stabilize the inscribed gratings. It was found, that the molecular glass mainly accumulates in the azobenzene minority phase of the block copolymers, so that even small amounts of the molecular glass lead to significant shortening of the writing times when blended with a block copolymer. The addition of 15 wt.-% of azobenzene molecular glass results in a reduction of the writing time from 206 s to 13 s, which corresponds to an improvement by a factor of 15. Moreover, at this concentration, the long-term stability of the inscribed gratings is retained.



Time to reach 90% of the maximum diffraction efficiency as a function of the concentration of the molecular glass in the photoactive block copolymer (filled diamonds) in comparison to the neat polymer (open diamond).

In addition to the substantially improved imprinting speed, blending the photo-orientable polymers with the molecular glass leads to an improved homogeneity of the films, resulting in more reproducible holographic experiments. Hence, molecular glasses are promising materials to improve the performance of azobenzene polymers in volume holography, making these materials suitable for applications such as holographic data storage or as carrier of forgery-proof security features.

In the *fourth chapter* a novel concept of diluting an azobenzene-functionalized material in a non-photoactive matrix to yield millimeter thick samples while retaining the beneficial cooperative effect is presented. The concept is based on blending **core/shell polymer nanoparticles featuring an azobenzene-functionalized core** and non-photoactive shell with a photo-chemically inert polymer matrix. The polymer nanoparticles are based on block copolymers comprising a functionalizable poly(4-hydroxystyrene) (P(OHS)) minority block and a polystyrene (PS) or poly(methyl methacrylate) (PMMA) majority segment. The block ratios are designed to yield a spherical or cylindrical bulk morphology. The bulk morphology determines the morphology of the resulting nanoparticles, since crosslinking of the block copolymer is performed in millimeter thick films using the commercially available tetra-functional glycoluril-based crosslinker Powderlink 1174®. The crosslinking agent, which is used to crosslink aromatic OH functionalities in lithography, is here used to synthesize polymer nanoparticles for the first time. The crosslinking reaction takes place at the OH groups in the deliberately incomplete azobenzene-functionalized minority block. The tetra-functional crosslinking agent is activated by adding thermal acid- or photoacid generators or by exposure with hydrochloric acid vapor acting as proton source. All three proton sources have successfully been applied in the synthesis of non-photoactive P(OHS)-b-PS polymer nanoparticles. For the synthesis of partially azobenzene-functionalized nanoparticles with PS or PMMA shell, the use of HCl vapor has proven to be suited best. TEM investigations revealed, that the addition of crosslinker to the block copolymer results in a change of the morphology from spherical to cylindrical. It therefore can be concluded that the crosslinker preferably accumulates in the azobenzene and hydroxy-functionalized minority phase. This leads to a very efficient crosslinking of the block copolymers. It was demonstrated, that 5 wt.-% of crosslinking agent is sufficient to crosslink azobenzene-functionalized block copolymers within 1 h of HCl exposure to yield nanoparticles of approx. 50 to 200 nm in length.



Transmission electron micrographs and DLS measurements of a particle suspension of a crosslinked block copolymer. Staining was performed using phosphotungsten acid on a carbon coated Cu grid. The dark areas correspond to the azobenzene functionalized blocks.

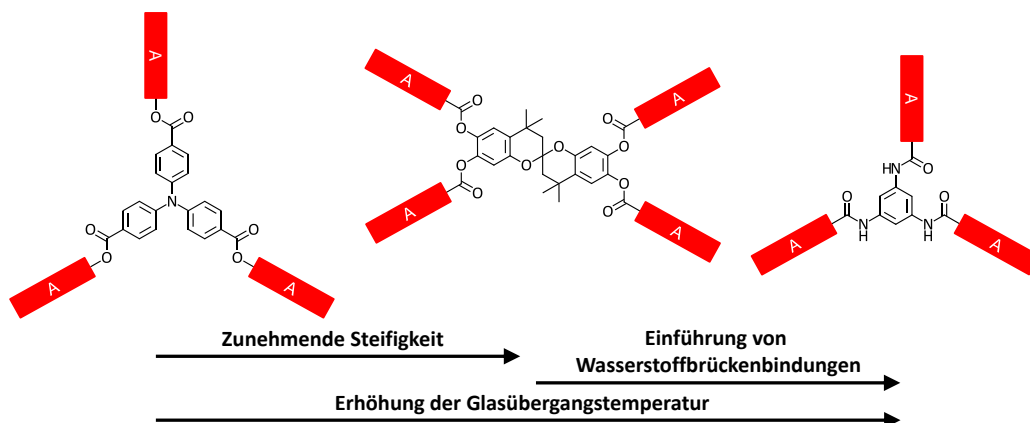
Investigations of the photophysical behavior of the azobenzene-functionalized nanoparticles via UV/Vis spectroscopy have shown that the crosslinking reaction has no negative impact on the *cis-trans* isomerization reaction of the chromophores. In addition, holographic experiments were conducted. Hereto, the obtained nanoparticles were incorporated in a PS matrix to yield injection molded millimeter thick samples. Experiments have proven that the holographic performance is not negatively affected. Consequently, a novel concept of diluting an azobenzene-functionalized material in a non-photoactive matrix to yield millimeter thick samples while retaining the beneficial cooperative effect was successfully demonstrated.

## 8 Zusammenfassung

Azobenzolchromophore besitzen einzigartige photophysikalische Eigenschaften und sind daher Gegenstand erheblicher Forschungsanstrengungen. Der Mechanismus, der azobenzolfunktionalisierte Materialien für Anwendungen wie zum Beispiel die holographische Datenspeicherung oder Oberflächenstrukturierungen interessant macht, ist die *cis-trans*-Isomerie.

Die vorliegende Arbeit umfasst das Design, die Synthese, und die Charakterisierung von azobenzolfunktionalisierten niedermolekularen Verbindungen, Polymeren und Polymernanopartikeln, sowie deren Anwendung in der Holographie und in der neu entwickelten azobenzolbasierten Nano-prägelithografie.

Das *erste Kapitel* enthält die **Synthese und Charakterisierung von azobenzolfunktionalisierten molekularen Gläsern**, die auf 3 verschiedenen Kerne mit unterschiedlicher Steifigkeit variierendem Raumbedarf und ungleichartigen sekundären Wechselwirkungen basieren. Die tri- oder tetrafunktionellen Verbindungen bestehen aus einem Triphenylamin-, 1,3,5-Benzoltrisamid- oder Spirobichroman-kern, an welchem Azobenzoleinheiten gebunden sind. Die Azobenzolchromophore tragen Substituenten an der para-Position der Azogruppe, die die photophysikalischen Eigenschaften der Moleküle steuern.



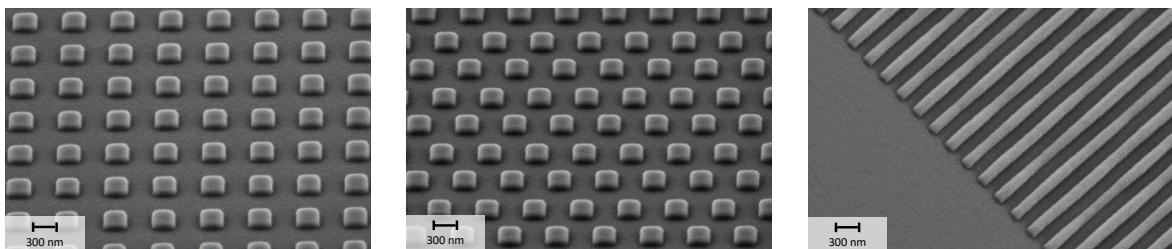
Schematische Darstellung der synthetisierten azobenzolfunktionalisierten molekularen Gläser auf Basis der verschiedenen Kerne. Die Steifigkeit der Kerne steigt von triphenylamin- zu spirobichromanbasierten molekularen Gläsern an. 1,3,5-Benzoltrisamidderivate besitzen zudem die Möglichkeit zur Ausbildung von intermolekularen Wasserstoffbrückenbindungen. Die Glasübergangstemperatur erhöht sich von links nach rechts. Die roten Rechtecke stellen die Azobenzolchromophore dar.

Die verschiedenen Azobenzoleinheiten werden mit der sogenannten "Mills Reaktion", einer Kondensationsreaktion einer para-Nitrosobenzoesäure mit einem Anilinderivat, synthetisiert. Die Chromophore werden mittels Veresterung oder Amidierung an den entsprechenden Kern angebunden. Die thermische Charakterisierung wurde mittels dynamischer Differenzkalorimetrie, thermogravimetrische Analyse und Polarisationsmikroskopie durchgeführt. Sieben von elf Verbindungen verfügen über eine Glasübergangstemperatur über 92 °C, die mit der Steifigkeit des Moleküllkerns und mit der Einführung Wasserstoffbrückenbindungen auf bis zu 136 °C erhöht wird. Die niedermolekularen Verbindungen lassen sich, beispielsweise durch Schleuderbeschichtung, leicht in dünne Filme mit einer sehr stabilen amorphen Phase überführen. Die UV/Vis-Spektroskopie im dünnen Film und in Lösung zeigt die Einstellbarkeit der photophysikalischen Eigenschaften der molekularen Gläser durch Substitution mit H, MeO oder CF<sub>3</sub>-Gruppen an den Azobenzoleinheiten.

Das zweite Kapitel behandelt die **Entwicklung und Optimierung einer neuartigen Oberflächenstrukturierungsmethode**, die auf azobenzolfunktionalisierten Materialien beruht und die Herstellung komplexer, nicht-periodischer Mikro- und Nanostrukturen erlaubt. Erstmals werden die einzigartigen Eigenschaften der athermischen Photofluidisierung von Azobenzolen mit den Prinzipien der Nanoprägelithografie verknüpft, weshalb diese Technik azobenzolbasierte Nanoprägelithografie oder kurz azo-NIL genannt wird. In dem azo-NIL-Verfahren wird durch Belichtung mit einer geeigneten Lichtwellenlänge das Negativ eines strukturierten Stempels in einen dünnen Azobenzolfilm geprägt. Für das Verfahren wird keine Hitze benötigt und es kommt zu keinen Phasenübergängen oder Vernetzungsreaktionen, sodass Schrumpfung, welcher in etablierten Nanoprägelithografieverfahren, wie zum Beispiel des t-NIL oder UV-NIL, auftritt, vermieden wird.

Die wichtigsten Parameter, die die Leistung des Verfahrens beeinflussen, wie zum Beispiel die Lichtwellenlänge, die Fluenz oder die Filmdicke, sowie das Stempelmaterial wurden eingehend studiert. Prägeexperimente haben gezeigt, dass biphotonische Belichtung mit zwei LEDs mit Wellenlängen von 365 nm bzw. 455 nm die wirkungsvollste Belichtungsmethode ist um die *cis-trans*-Isomerie und somit auch das Prägeverfahren möglichst schnell und effizient ablaufen zu lassen. Weiterhin konnte gezeigt werden, dass die Fluenz direkt proportional zur Prägegeschwindigkeit ist. Zudem hat sich herausgestellt, dass eine Filmdicke von 500 nm zu der höchsten Prägegeschwindigkeit führt, da das Strukturieren von dünneren Filmen sonst durch einen eingeschränkten Materialfluss behindert wird. Untersuchungen haben außerdem gezeigt, dass das azo-NIL Verfahren das Prägen von Strukturen mit einer Größe von 10  $\mu\text{m}$  bis zu 100 nm erlaubt.

Hiernach wurde, anhand von neun unterschiedlichen azobenzolfunktionalisierten molekularen Gläsern und eines auf Poly(1,2-butadien) basierenden photo-orientierbaren Homopolymers, der Einfluss des Filmmaterials auf die Prägegeschwindigkeit und die Qualität der geprägten Strukturen untersucht. Es wurde gezeigt, dass die schnellste und präziseste Replikation der unterschiedlichen Strukturen mit spirobichromanbasierten molekularen Gläsern möglich ist.

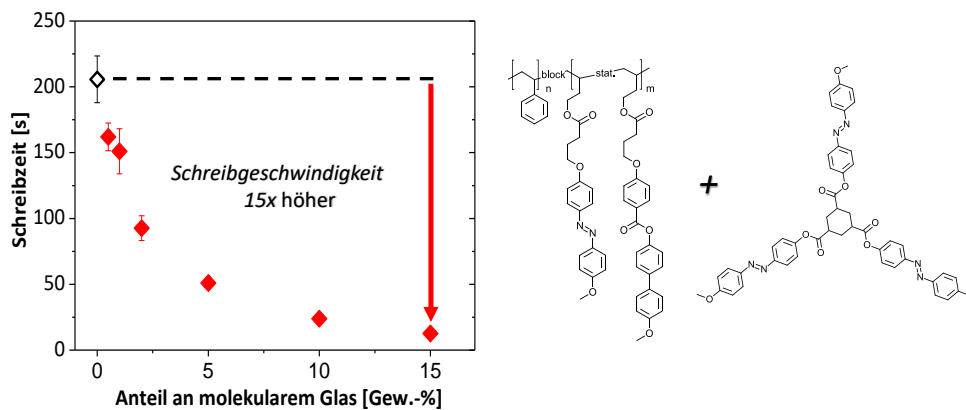


Gekippte Rasterelektronenmikroskopieaufnahmen unterschiedlicher Nanostrukturen in einem Film eines azobenzolfunktionalisierten spirobichromanbasierten molekularen Glases. Die Strukturen besitzen eine Größe zwischen 300 nm und 150 nm.

In einem Film eines spirobichromanbasierten molekularen Glases, an welchem H-substituierte Azobenzolchromophore angeknüpft sind, beträgt die Aufbaukonstante  $\tau$ , die für die Zeit steht in der 63 % der maximal zu erreichenden Strukturhöhe von 100 nm erreicht ist, bei biphotonischer Belichtung 118 s. Dank der abgestimmten photophysikalischen Eigenschaften des methoxy-substituierten spirobichromanbasierten Derivates, weist Dieses mit einer Zeit von nur 64 s die beste Leistung aller im Prägeverfahren untersuchten Verbindungen auf. Das ist fünfmal schneller als das untersuchte Homopolymer, das eine Aufbaukonstante von 308 s aufweist. Das Prägen bei hohen Temperaturen verkürzt die Zeit auf nur 9 s. Selbst bei Temperaturen die lediglich 10 °C unter dem  $T_g$  des Materials liegen, bleibt die amorphe Phase stabil und es sind keine Anzeichen einer Kristallisation zu beobachten.

Im dritten Kapitel wird die **Verbesserung der Leistung von photo-orientierbaren Azobenzolpolymeren im holographischen Schreibverfahren durch die Beimischung von molekularen Gläsern** behandelt. In diesem Kapitel werden durch Überlagerung zweier polarisierter Laserstrahlen holographische Gitter in das Volumen von dünnen, aus photoaktivem azobenzolfunktionalisiertem Material bestehenden Filmen eingeschrieben. Hierdurch wird eine Umorientierung der Chromophore in den belichteten Bereichen herbeigeführt.

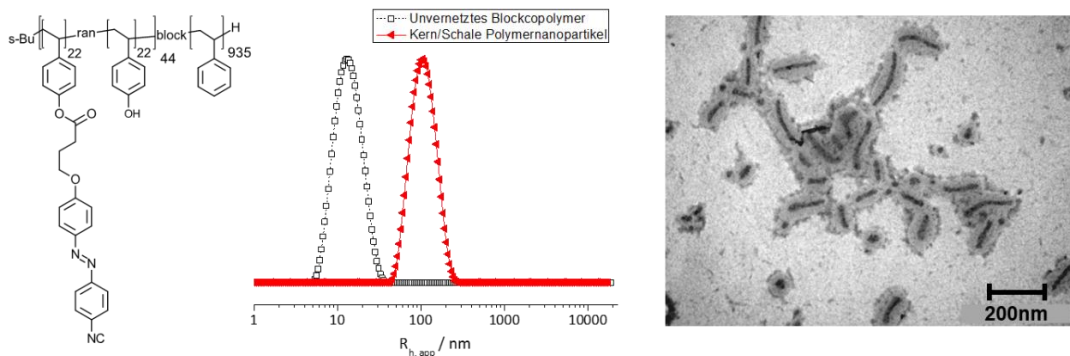
Es wurde gezeigt, dass die hohe Schreibgeschwindigkeit des untersuchten molekularen Glases in Mischungen mit dem photoinaktiven Polystyrol bis hin zu einer Verdünnung von nur 30 Gew.-% erhalten bleibt. Das zeigt, dass der kooperative Effekt, welcher die Schreibgeschwindigkeit und Stabilität der eingeschriebenen Gitter erhöht, immer noch zwischen den azobenzolfunktionalisierten Molekülen vorhanden ist. Bei Belichtung einer Mischung mit einem photo-orientierbaren Polymer orientiert das molekulare Glas die Azobenzoleinheiten, die an das Polymerrückgrat gebunden sind, mit. Dies trifft sowohl auf das untersuchte Poly(1,2-butdadien)-basierte methoxyazobenzol-substituierte Homopolymer, als auch auf die zwei Blockcopolymere mit je einem Polystyrolmajoritäts- und einem azobenzolfunktionalisiertem Poly(1,2-butdadien)-minoritätssegment zu. Zusätzlich zu den Azobenzoleinheiten, trägt eines der beiden Blockcopolymere photoinaktive Mesogene, welche die eingeschriebenen Gitter stabilisieren. Es wurde gezeigt, dass das molekulare Glas vorwiegend in der Azobenzolminoritätsphase akkumuliert, sodass, bei einer Beimischung zu einem Blockcopolymer, sogar kleine Mengen des molekularen Glases ausreichen um die benötigte Zeit für den Schreibvorgang deutlich zu verkürzen. Das Einbringen von 15 Gew.-% molekularem Glas resultiert in einer Verminderung der Schreibzeit von 206 s auf 13 s, was einer Verbesserung um einen Faktor von 15 bedeutet. Weiterhin bleibt bei dieser Konzentration die Langzeitstabilität der eingeschriebenen Gitter erhalten.



Die Zeit um 90 % der maximalen Beugungseffizienz zu erreichen als Funktion der Konzentration des molekularen Glases im photoaktiven Blockcopolymer (gefüllte Diamanten) im Vergleich zum reinen Polymer (offener Diamant).

Neben der deutlich gesteigerten Schreibgeschwindigkeit führt das Beimischen eines molekularen Glases zu einem photoaktiven Blockcopolymer zu einer verbesserten Homogenität des Films und somit zu reproduzierbareren holographischen Experimenten. Molekulare Gläser sind also ein vielversprechendes Material um die Leistung von azobenzolfunktionalisierten Polymeren in der Volumen holographie zu verbessern, was die Eignung solcher Materialien für deren Anwendung im Bereich der holographischen Datenspeicherung oder als Träger von Fälschungssicheren Sicherheitsmerkmalen steigert.

Im *vierten Kapitel* wird ein neuartiges Konzept zur Verdünnung von azobenzolfunktionalisierten Materialien in einer photoinaktiven Matrix zur Herstellung millimeterdicker Proben bei gleichzeitigem Erhalt des kooperativen Effekts vorgestellt. Das Konzept basiert auf dem Einmischen von **Kern/Schale Polymernanopartikeln mit azobenzolfunktionalisiertem Kern** und einer photoinaktiven Schale in eine photochemisch inerte Polymermatrix. Die Polymernanopartikel basieren auf Blockcopolymeren mit einem funktionalisierbaren Poly(4-hydroxystyrol) (P(OHS)) Minoritäts- und einem Polystyrol (PS) bzw. Poly(methyl-methacrylat) (PMMA) Majoritätssegment. Die Blockverhältnisse sind so gewählt, dass im Film eine sphärische oder zylindrische Morphologie erreicht wird. Die Filmmorphologie bestimmt die Form der entstehenden Polymernanopartikel, da die Vernetzungsreaktion, die mittels dem kommerziell erhältlichen, glycolurilbasierten Vernetzers Powderlink 1174 durchgeführt wird, in millimeterdicken Filmen stattfindet. Das Vernetzungsreagenz, welches zur Vernetzung aromatischer OH-Gruppen in der Lithographie verwendet wird, wird hier erstmalig zur Synthese von Polymernanopartikeln verwendet. Die Vernetzungsreaktion findet an den OH Gruppen in der absichtlich nur unvollständig azobenzolfunktionalisierten Minoritätsphase statt. Der tetrafunktionelle Vernetzter wird durch Hinzufügen eines als Protonenquelle dienenden thermisch- bzw. durch Licht aktivierbaren Säurebildners, oder durch Behandlung mit Salzsäuredampf, aktiviert. Alle drei Protonenquellen wurden erfolgreich in der Synthese von photoinaktiven P(OHS)-b-PS Polymernanopartikeln verwendet. In der Synthese der teilweise azobenzolfunktionalisierten Nanopartikel mit PS bzw. PMMA Schale hat sich die Behandlung mit HCl Dampf als beste Methode herausgestellt. Transmissionselektronenmikroskopische Aufnahmen zeigen, dass das Beimischen des Vernetzers zum Blockcopolymer zu einer Morphologieänderung von sphärisch zu zylindrisch führt. Hieraus kann geschlossen werden, dass das Vernetzungsreagenz vorzugsweise in der azobenzol- bzw. hydroxylfunktionalisierten Minoritätsphase akkumuliert. Dies führt zu einer sehr effizienten Vernetzung der Blockcopolymeren. Es wurde gezeigt, dass 5 Gew.-% Vernetzungsreagenz genügen, um die azobenzolfunktionalisierten Blockcopolymeren innerhalb einer Stunde mittels HCl Dampf zu vernetzen. Hieraus entstehen ungefähr zwischen 50 und 200 nm lange Nanopartikel.



Transmissionselektronenmikroskopische Aufnahme und DLS-Messungen einer Nanopartikelsuspension. Die Nanopartikel wurden mit Phosphorwolframsäure angefärbt und auf ein mit Kohle beschichtetes Kupfernetz getropft. Die dunklen Bereiche stellen den azobenzolfunktionalisierten Block dar.

UV/Vis Spektroskopie an azobenzolfunktionalisierten Nanopartikeln hat gezeigt, dass die Vernetzungsreaktionen keinen negativen Einfluss auf die *cis-trans*-Isomerie haben. Zusätzlich wurden holographische Experimente an millimeterdicken spritzgegossenen Proben durchgeführt. Die Experimente haben bewiesen, dass die holographischen Eigenschaften nicht negativ beeinflusst werden. Folglich ist das neuartige Verdünnungskonzept für azobenzolfunktionalisierte Materialien in einer photoinaktiven Matrix unter gleichzeitigem Erhalt des kooperativen Effekts erfolgreich.

## 9 Experimental part

### 9.1 Characterization methods (basics)

#### 9.1.1 Dynamic light scattering

Dynamic light scattering (DLS) is an analytical technique, allowing to determine the size of particles or macromolecules in the sub-micron region. The information about the size can be derived from the fluctuation of scattered light, which is constantly measured during the experiment. This fluctuation is caused by Brownian motion of the solute molecules, a random movement triggered by interaction with surrounding solvent molecules. Thus, the movement of solvent molecules is correlated with the solvent's viscosity, making an accurate temperature control necessary for DLS measurements. To analyze the fluctuation of the scattered light, a formalism called autocorrelation function  $g^2$  can be applied.<sup>[221–223]</sup> In this formalism, the intensity  $I$  at the time  $t$  is multiplied with the intensity of the time  $t+\tau$ . This operation is repeated for various times  $t$  and  $\tau$ 's (time delays) and a mean value is formed thereof. One obtains an exponentially decaying curve  $g^2(\tau)$ :

$$g^2(\tau) = \frac{\langle I(t) \cdot I(t+\tau) \rangle}{\langle I(t) \rangle^2} \quad (7.1)$$

with:  $I$ : intensity  
 $\tau$ : delay time

At short delay times  $\tau$ , the correlation is high, because the particles have not enough time to move long distances from their initial starting points. However, the correlation between two signals is decaying exponentially as the delay time is increasing (see Figure 133).

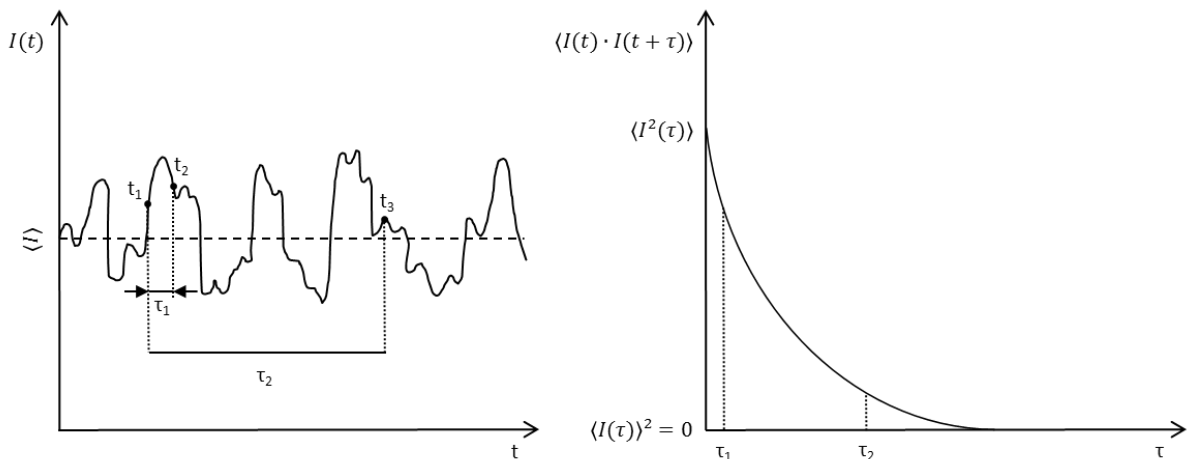


Figure 133: Left: fluctuation of the intensity of the scattered light. Right: Calculated second order autocorrelation function.<sup>[224]</sup>

The exponential decay is related to the diffusion coefficient of the particles. If the sample is monodisperse, the decay is a single exponential. Using the Siegert equation, a transformation of second-order autocorrelation function  $g^2(t)$  to the first-order autocorrelation function  $g^1(\tau)$  can be achieved:

$$g^2(\tau) = B[1 + |g^1(\tau)|^2] \quad (7.2)$$

with: B: correction factor (=1, in case of spherical particles)

For monodisperse, highly diluted systems containing only spherical particles and assuming no ion-ion interactions, no collisions between particles, the following approach to link the autocorrelation function with the translational diffusion coefficient D is applicable<sup>[225]</sup>:

$$g^1(\tau) = e^{(-\Gamma\tau)} \quad (7.3)$$

with:  $\Gamma$ : decay rate

$$\Gamma = q^2 D \quad (7.4)$$

and

$$q = \frac{4\pi n_0}{\lambda} \sin\left(\frac{\theta}{2}\right) \quad (7.5)$$

with:  $\lambda$ : wavelength of the laser  
 $n_0$ : refractive index of the sample  
 $\theta$ : angle between detector and sample cell  
D: diffusion coefficient  
q: wave vector

In most cases, however, the examined sample is polydisperse. Thus, the decay of the autocorrelation function is a sum of exponential decays<sup>[225]</sup>:

$$g^1(q, \tau) = \int_0^\infty G(D) e^{(-q^2 D \tau)} dD \quad (7.6)$$

with: G(D): distribution factor (proportional to relative scattering of each species)

G(D) depends on the amount, the mass and the form of each species and, thus, is angle dependent. Therefore, the determined translational diffusion coefficient is an apparent diffusion coefficient  $D_{app}$ :

$$D_{app} = \frac{\sum m_i M_i^2 G_i(q) D_i}{\sum m_i M_i^2 G_i(q)} \quad (7.7)$$

with: i: species  
M: molar mass  
m: mass fraction

By extrapolation of the apparent diffusion coefficients to 0 (form factor G(q)=1), it is possible to obtain the so-called "z-averaged" diffusion coefficient  $D_z$ . From this translational coefficient, the hydrodynamic radius  $R_h$  of a spherical solute molecule can be obtained from the Stokes-Einstein relation:

$$R_h = \frac{k_b T}{3\pi\eta D} \quad (7.8)$$

with:  $R_h$ : hydrodynamic radius  
 $k_b$ : Boltzmann's constant  
D: translational diffusion coefficient  
T: temperature  
 $\eta$ : viscosity

### 9.1.2 Holography

In holographic experiments a laser beam is split into two coherent laser beams, namely the object and the reference beam, which are superimposed within a photoactive material. The two beams are incident from different angles on the holographic media (off-axis). If the angle between the two laser beams ranges between  $0^\circ$  and  $90^\circ$ , a transmission hologram, for larger angles, a reflection hologram is generated. The object beam can, but must not, carry information. Is the object beam not carrying any information, a simple plane wave or hologram of no object experiment is performed.<sup>[226]</sup> In this case the two beams are creating a sinusoidal interference pattern or grating (see Figure 134).

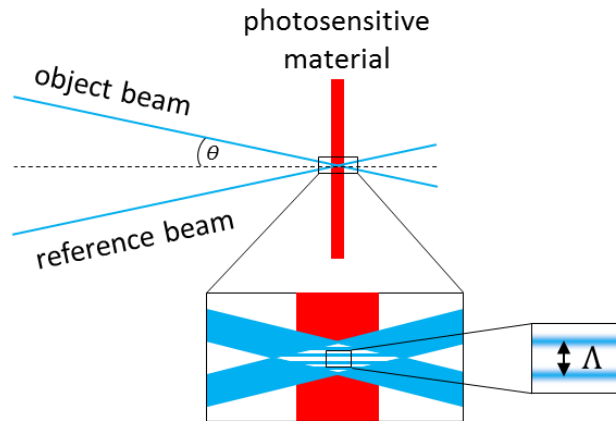


Figure 134: Scheme of an inscription process of a holographic grating into a photosensitive material in a holographic experiment. The grating constant  $\Lambda$  is the distance from maximum to maximum of the gratings. Referring to<sup>[217]</sup>.

The distance between the maxima (or minima) of the intensity grating is called grating constant  $\Lambda$  and is defined as:

$$\Lambda = \frac{\lambda}{2n_0 \sin\theta} \quad (7.9)$$

with:  $\Lambda$ : grating constant  
 $\lambda$ : writing wavelength  
 $\theta$ : half the angle between incident laser beams  
 $n_0$ : refractive index

These gratings can either be inscribed on the surface of the material due to mass transport (surface relief gratings), or in the volume due to orientation of the azobenzenes (volume holograms). Depending on which kind of photosensitive material is used, either a change in the absorption coefficient (amplitude hologram), or a local change in the refractive index (phase hologram) is generated in the photosensitive material. For phase holograms, mainly azobenzene-containing material or photopolymers are used. In this thesis, off-axis transmission volume holograms inscribed with plane waves are investigated only. Azobenzene-containing materials are expected to be affected mostly in the bright areas or regions of the intensity grating. Thus, the intensity grating leads to a change of the refractive index  $n$ .<sup>[226]</sup>

In the holographic experiments performed in this thesis, the inscription of gratings is done with a He-Ne-laser at 488 nm. The reading process had to be performed at a wavelength outside the absorption band of the dye (685 nm). Thus, in the reading process the reading beam is diffracted at the inscribed

grating without affecting the inscribed hologram. The quotient of the intensity of the diffracted reading beam into the first order  $I_1$  to its intensity at incident  $I_0$  is called diffraction efficiency  $\eta$ <sup>[226]</sup>:

$$\eta = \frac{I_1}{I_0} \quad (7.10)$$

When reading out a holographic grating, it must be distinguished if the hologram is *thick* or *thin*. Thin gratings diffract light in the Raman-Nath regime with multiple diffraction orders, and their theoretical maximum diffraction efficiency is 33.9 %. In thick gratings, all the light is diffracted into one order, for none of the others is fulfilling the Bragg condition. The theoretical diffraction limit is 100 %.<sup>[226]</sup> For thin gratings,  $\eta$  can be calculated according to the scalar theory for thin volume holograms by of Magnussen and Gaylord<sup>[227]</sup>, while the diffraction efficiency of thick gratings is determined by Kogelnick's<sup>[228]</sup> coupled wave theory. For small diffraction efficiencies, and if the light is incident at the Bragg angle, the diffraction efficiencies of both kinds of gratings are equal to:

$$\eta = \left( \frac{\pi n_1 d_0}{\lambda \cos \theta} \right)^2 \quad (7.11)$$

For the sake of comparability of different materials, one has to calculate the refractive index material  $n_1$ , which, in contrast to the diffraction efficiency, is independent of the thickness of the material. The refractive index modulation  $n_1$  can be calculated from the diffraction efficiency, that is obtained in the holographic experiment<sup>[229,230]</sup>:

$$n_1 = \frac{\lambda \cos \theta \sqrt{\eta}}{\pi d_0} \quad (7.12)$$

## 9.2 Characterization methods

### *Holographic setup*

The holographic setup for the inscription of volume gratings is depicted in Figure 135. Volume gratings are inscribed at room temperature using a 488 nm laser source with both writing beams being s-polarized. The angle  $2\theta$  between them is  $28^\circ$  which results in a grating period of  $1 \mu\text{m}$ . The intensity of each beam is adjusted at  $1 \text{ W/cm}^2$  while their diameter is about 2 mm. An s-polarized diode laser ( $145 \mu\text{W}$  overall intensity) at 685 nm is used for in-situ monitoring the diffraction efficiency without affecting the writing process. The signals of the 0<sup>th</sup> and the 1<sup>st</sup> diffraction orders are measured with photodiodes. The diffraction efficiency is calculated as the first-order signal divided by the overall power behind the sample (sum of 0<sup>th</sup> and 1<sup>st</sup> orders). A 10 kHz modulation of the red laser and lock-in detection are used to reduce noise. The refractive-index modulations were calculated according to (7.12).

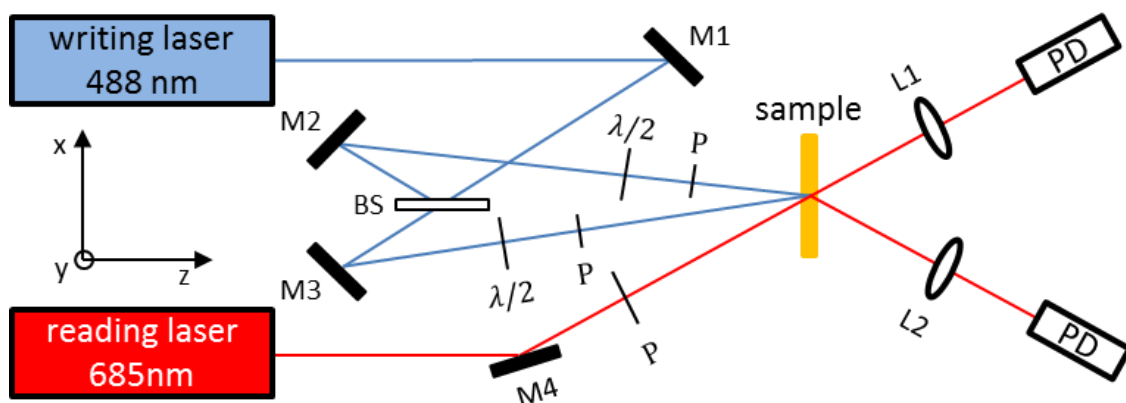


Figure 135: Scheme of the holographic experiment setup (L1-2: focus lens 1-2, P: polarizer, M1-4: mirror 1-4, BS: beam splitter, PD: photo diode,  $\lambda/2$ : half-wave plate).<sup>[231]</sup>

#### Dynamic light scattering setup

DLS measurements were performed on a temperature controlled ALV DLS/SLS-SP 5022F compact goniometer system with an ALV 5000/E correlator equipped with a He-Ne laser ( $\lambda = 632.8$  nm). The setup for the DLS measurements is shown in Figure 136.

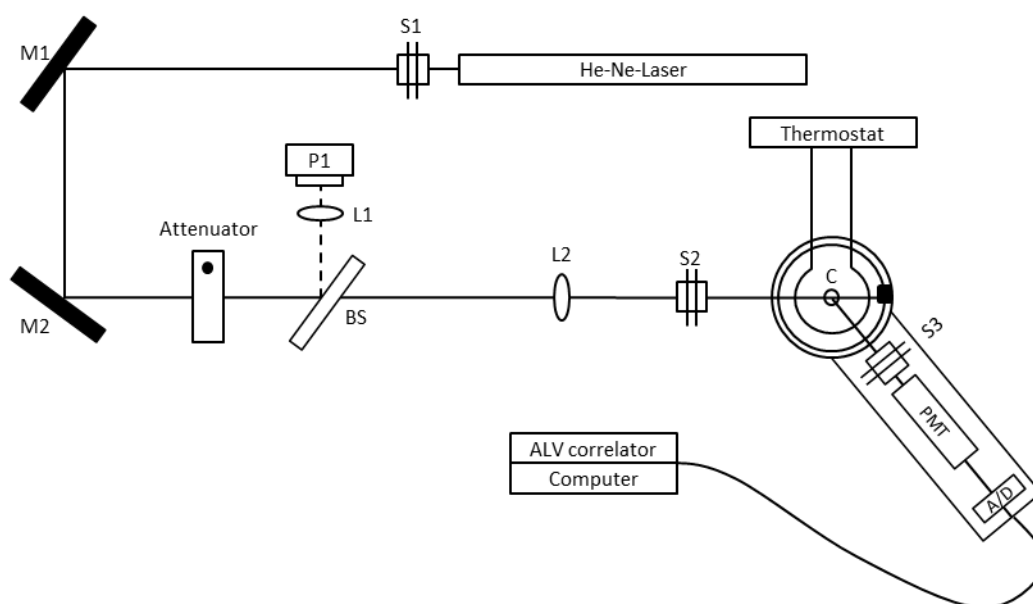


Figure 136: Schematic light scattering setup (S1-3: shutter 1-3, M1-2: mirror 1-2, BS: beam splitter, L1-2: focus lens 1-2, P1: photodetector (for  $I_0$ ), C: sample holder with cuvette, PMT: photo multiplier, A/D: signal converter).<sup>[224]</sup>

The DLS experiments in this thesis were performed on filtered and unfiltered samples. If the samples were filtered before the DLS experiment, teflon filters with PP hull and different diameters and pore sizes were used. The sample cuvettes were cleaned with acetone and dust free cloth prior to the experiment. The measurements were performed at a scattering angle of  $90^\circ$ . On the obtained autocorrelation function, a CONTIN analysis was carried out using ALV Correlator Software 3.0.

### *Differential scanning calorimetry (DSC)*

Differential scanning calorimetry was performed on a Perkin-Elmer DSC DIAMOND or METTLER DSC II. The heating and cooling runs were performed at a scan rate of 10 K/min under a constant flow of dry nitrogen (50 mL/min). Indium was used for calibration. 50  $\mu$ L (Perkin Elmer), or 40  $\mu$ L (METTLER) pans were filled with 3-12 mg of samples.

### *Stamp (replica) preparation*

Stamps were made of PDMS or a fluorinated polymer (EVG<sup>®</sup> polymer) and were prepared by casting a  $\mu$ m scale structured master or nm-scale structured master, respectively. In case of the nano-structured fused silica master, a silanization of the master's surface was carried out prior to the casting process. Therefore, approx. 10 mL hexamethyldisilazane (HMDS) was heated up to reflux and was condensed at the master's surface for 2h. PDMS replicas were prepared by mixing a temperature curable two component system (ELASTOSIL<sup>®</sup> RT 601, or SYLGARD<sup>®</sup> 184) in a ratio of prepolymer:initiator = 9:1 in a Hausschild SpeedMixer™ DAC 150 SP. The mixture was then casted onto the master and was allowed to crosslink at room temperature for 12 h. The crosslinking reaction was finished at 150°C for another 2 h. EVG<sup>®</sup> polymer replicas were prepared from a mixture of a UV curable prepolymer with 2 wt.-% UV initiator. Therefore, the prepolymer was mixed with the initiator for 30 min at room temperature in the dark. This mixture was then casted on the master and exposed to UV light (20 mW/cm<sup>2</sup>) for 100 sec using the mask aligner EVG<sup>®</sup> 620 at a wavelength of 365 nm. In a final step, the stamp was treated with ultrasonic in an isopropanol bath at room temperature for 15 min.

### *Size exclusion chromatography (SEC)*

Polymeric samples:

Size exclusion chromatography was performed utilizing a Waters 515 HPLC pump and stabilized THF as eluent at a flow rate of 0.5 ml/min. 20  $\mu$ l of a solution with a concentration of approximately 1 mg/ml was injected into a column setup comprising a guard column (Varian, 5  $\times$  0.8 cm, Resipore gel, particle size 3  $\mu$ m) and two separation columns (Varian, 30  $\times$  0.8 cm, Resipore gel, particle size 3  $\mu$ m). Polymer size distribution was monitored with a WATERS 2489 tunable UV detector at 254 nm and a Waters 410 differential RI detector. Molecular weight distributions were given with respect to PS calibration.

Oligomeric samples:

Oligomeric size exclusion chromatography (oligo SEC) were performed utilizing a Waters 515 HPLC pump and stabilized THF as eluent at a flow rate of 0.5 ml/min. 20  $\mu$ l of a solution with a concentration of approximately 1 mg/ml was injected into a column setup comprising a guard column (Varian, 5  $\times$  0.8 cm, Mesopore gel, particle size 5  $\mu$ m,) and two analytical columns (Varian, 30  $\times$  0.8 cm, Mesopore gel, particle size 5  $\mu$ m). Oligomeric compounds were monitored with a WATERS 486 tunable UV detector at 254 nm and a Waters 410 differential RI detector. Molecular weight distribution was given with respect to an oligo-styrene calibration.

### *<sup>1</sup>H-Nuclear magnetic resonance spectroscopy (<sup>1</sup>H-NMR)*

<sup>1</sup>H-NMR spectra were performed on a Bruker Avance 300 spectrometer. The operating frequency was 300 MHz using deuterated solvents and tetramethylsilane (TMS) as internal standard.

### *Transmission electron microscopy (TEM)*

Transmission electron microscopy was performed on a Zeiss CEM902 EFTEM electron microscope (CEM 902) operated at 80kV. Staining with phosphotungstic acid (PTA) was carried out according to the procedure proposed by M. G. Looney et al.<sup>[232]</sup> Therefore, the samples were treated for 5-30 min with a freshly prepared aqueous solution of 2 wt.-% PTA with 2 wt.-% benzyl alcohol. The samples were washed with distilled water and dried at room temperature.

Staining with RuO<sub>4</sub> was carried out in a desiccator. For this purpose, 13 mg of Ruthenium-III-chloride is weighed into a small pan. The TEM grids with the samples are placed in proximity to the pan. Then, 1 ml of sodium hypochlorite is added to the RuCl<sub>3</sub> powder and the desiccator is closed. The samples are exposed to the RuO<sub>4</sub> vapor for 30 min.

### *Ultramicrotome*

Thin sections (film thickness  $\approx$  50 nm) were cut at room temperature from as-cast films using a Leica UC7 Ultramicrotome equipped with a diamond knife. Sample films are placed on TEM gold grids with a mesh size of 150 $\mu$ m<sup>2</sup>.

### *Scanning electron microscopy (SEM)*

The examined azobenzene containing films were sputtered with approx. 1.3 nm platinum in a Cressington 208HR sputter coater and analyzed by SEM Zeiss LEO 1530 FESEM (Zeiss, Jena, Germany) at 3.0 keV.

### *Atomic force microscopy (AFM)*

Atomic Force Microscopy measurements were carried out in tapping mode under ambient conditions using a commercial scanning probe microscope (Digital Instruments NanoScope Dimension 3100) equipped with a Nanoscope IV Controller and Closed Loop XY Dimension Head. A silicon cantilever of the type OTESPA-R3, typical spring constant: 26 N/m was used for all measurements.

### *Fourier transform infrared spectroscopy (FT-IR)*

FT-IR measurements were performed in attenuated total reflectance mode (ATR) using a PerkinElmer Spectrum 100 with universal ATR equipment.

### *Thermogravimetric analysis (TGA)*

TGA experiments were conducted at a heating rate of 10 K/min under constant N<sub>2</sub> flow with a Mettler Toledo TGA/SDTA851<sup>e</sup>.

### *Thin film preparation*

Samples for the nanoimprint lithography and holographic experiments were prepared by spin-coating a filtered solution at 500-1500 rpm for 60s onto a commercially available glass substrate. The glass substrate was cleaned with THF and compressed argon prior to spin-coating. The annealing duration was 1 h for all films.

The film thickness of the samples varied from 40 nm to 600 nm; it was measured with a Dektak (Veeco 3300ST auto remote control stage profiler). All samples showed good optical properties and absence of light scattering.

### *Injection molding (thick sample preparation)*

Thick samples were prepared from compounded powder blends of azobenzene containing material with neat polystyrene polymer PS165H. The blends were compounded in a twin screw micro-compounder (DSM Xplore, 15 mL) at a temperature of 230°C at a screw rotation speed of 50 rpm. The dwell time was 5 minutes. The extruded polymer was cut into pieces and subjected to injection molding in a 12 mL injection molding machine (DSM Xplore). The polymer blend was injected at a melt temperature of 210°C into a surface-polished mold with a diameter of 25 mm and a thickness of 1.1 mm. The pressure was adjusted to 6 bar and the mold temperature was set to 70°C. The thick samples were annealed in a surface-polished annealing mold at 130°C in a vacuum oven for 20 h to reduce the shear birefringence.

## **9.3 Materials**

If not stated otherwise, all materials have been used as received.

## **9.4 Synthesis of azobenzene-functionalized molecular glasses**

### **9.4.1 General reaction procedures**

#### *General method for the preparation of para-substituted azobenzoic acids GM1<sup>[90]</sup>*

The 4-nitrosobenzoic acid (26 mmol, 1 eq.) was dissolved in DMSO (110 mL) and 70 mL acetic acid (AcOH) was added. To this solution the amino compound (26 mmol, 1 eq.) was added and the solution was stirred at room temperature for 24 hours. Full conversion of the educts was monitored by thin-layer chromatography (TLC). The precipitate was filtered off and washed with water and MeOH several times before drying in vacuum at 80°C overnight. The crude product was stirred in a KOH solution (0.1 M) for one hour and filtered off before it was acidified in an aqueous solution by slowly adding semi-concentrated HCl. The product was filtered off and dried at 80°C overnight.

#### *General method for esterification of carbon acid derivatives GM2*

The azobenzoic acid derivative (17 mmol) is added to a large excess of EtOH (750 mL, 12.8 mol). To this solution, 4 mL concentrated H<sub>2</sub>SO<sub>4</sub> was added and the reaction mixture was heated to reflux for 12h. Full conversion was monitored by TLC. After cooling to room temperature, approx. two-thirds of the solution was evaporated under reduced pressure. The precipitated was then filtered off and subsequently dried in vacuum overnight.

#### *General method for saponification of ester derivatives GM3*

The azobenzene ethyl ester (4.7 mmol, 1eq.) was suspended in a mixture of THF/H<sub>2</sub>O/MeOH (1:1:1, 48 mL). To this suspension, aqueous KOH (68.2 mmol, 14.4 eq.) was added. The reaction mixture was refluxed for 6h. Full conversion was monitored by TLC. The reaction mixture is poured into (HCl) acidified water (500 mL). The precipitate is filtered off and washed with water several times.

#### *General method for the preparation of acid chlorides GM4*

The reaction was carried out under inert atmosphere (e.g. dry argon) in a flame dried Schlenk flask. The azobenzoic acid derivative (8.1 mmol, 1eq.) was suspended in dry THF and 5 drops of dry DMF were added. The suspension was then cooled down to 0°C using an ice bath and COCl<sub>2</sub> (32.3 mmol,

4eq.) were added dropwise. The suspension was then allowed to stir at room temperature for 12h. After heating the reaction mixture to reflux for 2h, the mixture was cooled down to room temperature and the solvent, as well as the remaining  $\text{COCl}_2$  were evaporated under reduced pressure.

*General method for linking the perfluoroalkyl chains to azobenzene derivatives* **GM5**<sup>[233]</sup>

In a three neck round bottom flask anhydrous DMSO was deoxygenated by purging argon gas and stirring for 20 min. Subsequently, copper (61.6 mmol, 3 eq.) was added and the suspension was purged for another 10 min. To this suspension the azobenzoic acid ethyl ester derivative (20.5 mmol, 1 eq.) and the perfluoroalkyl iodide derivative (26.7, 1.3 eq.) were added. The reaction mixture was then heated to 110°C and stirred for 12h. The complete conversion was monitored by TLC. After cooling down to room temperature, diethyl ether (100 mL) and  $\text{H}_2\text{O}$  (100 mL) were added to the reaction mixture and the copper was filtered off. The ether phase was collected and washed with water several times. After evaporation of the solvent under reduced pressure, the crude product was recrystallized from methanol.

*General method the preparation of azobenzene functionalized 1,3,5-benzenetrisamides* **GM6**

The reaction was carried out under inert atmosphere (argon) in a flame dried Schlenk flask. The azobenzene acid chloride derivative (3.5 eq.) was dissolved in dry N-Methyl-2-pyrrolidone (NMP) and dried LiCl (spatula tip) as well as triethylamine (4 eq.) were added. The solution was cooled down to 0°C using an ice bath. To this solution 1,3,5-triaminobenzene (1 eq.) was added. The reaction mixture was then stirred at room temperature for 24h. Full conversion was monitored by TLC. Afterwards, the reaction mixture was precipitated in acidified ice water (HCl) and the precipitate was filtered off.

*General method the preparation of azobenzene functionalized spirobichromane derivatives* **GM7**

The reaction was carried out under inert atmosphere (e.g. dry argon) in a flame dried Schlenk flask. The azobenzene acid chloride derivative (4.5 eq.) was dissolved in dry THF and dried LiCl (spatula tip) as well as triethylamine (4 eq.) were added. The solution was cooled down to 0°C using an ice bath. To this solution 6,6',7,7'-tetrahydroxy-4,4',4'-tetramethylbis-2,2'-spirobichromane (1 eq.) was added. The reaction mixture was then stirred at 70°C for 48h. Full conversion was monitored by TLC. After cooling down to room temperature, the reaction mixture was precipitated in acidified ice water (HCl) and the precipitate was filtered off.

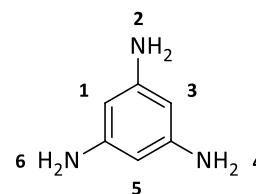
### 9.4.2 Synthesis of molecule cores

The triphenylamine-based molecular glasses were synthesized by R. Walker. The 6,6',7,7'-tetrahydroxy-4,4',4',4'-tetramethylbis-2,2'-spirobichromane molecule core was used as received from TCI.

#### Reduction of 3,5-dinitroaniline to 1,3,5-triaminobenzene<sup>[234]</sup>

A mixture of 3,5-dinitroaniline (6 g, 30 mmol), THF, MeOH and palladium (Pd/C) on activated charcoal (10% Pd) is stirred at 35°C in an autoclave with a H<sub>2</sub> pressure of 3.5 bar for 24 h. Afterwards, the catalyst was filtered through a short column of aluminum oxide (Alox N). Subsequently, the solvent was evaporated under reduced pressure and the product was dried in a high vacuum overnight to yield a white solid (yield: 2.95 g, 80%).

<sup>1</sup>H-NMR (DMSO-d<sub>6</sub>): δ (ppm) = 5.13 (s, 3H, Ar-H<sup>1,3,5</sup>), 4.32 (s, 6H, NH<sub>2</sub><sup>2,4,6</sup>).



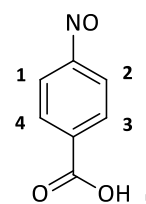
Chemical Formula: C<sub>6</sub>H<sub>9</sub>N<sub>3</sub>  
Molecular Weight: 123,16

### 9.4.3 Synthesis of azobenzene moieties

#### Oxidation of 4-aminobenzoic acid to 4-nitrosobenzoic acid<sup>[90]</sup>

To a solution of 4-aminobenzoic acid (72.9 mmol, 1 eq.) in DCM (110 mL), an aqueous solution of KHSO<sub>5</sub> (253.8 mmol, 3.5 eq.) was added under dry argon atmosphere. The reaction mixture was stirred at room temperature for one hour. The full conversion of the 4-aminobenzoic acid was monitored by thin-layer chromatography. The yellow precipitate was filtered off and washed with water several times. The crude product was dried in vacuum at 60°C overnight and is subjected to further reaction steps without further purification (yield: 10.45 g, 94 %).

<sup>1</sup>H-NMR (DMSO-d<sub>6</sub>): δ (ppm) = 8.26 (m, 2H, Ar-H<sup>3,4</sup>), 8.04 (m, 2H, Ar-H<sup>1,2</sup>)

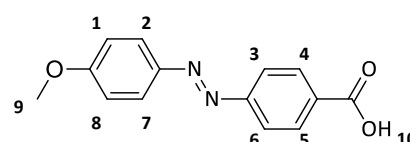


Chemical Formula: C<sub>7</sub>H<sub>5</sub>NO<sub>3</sub>  
Molecular Weight: 151,12

#### Preparation of 4-[(4-methoxyphenyl)azo]benzoic acid

The synthesis of the title product was carried out according to **GM1** using 4-nitrosobenzoic acid (66 mmol, 10.00 g), DMSO (150 mL), AcOH (200 mL), and p-anisidine (66 mmol, 8.15g). The crude product was recrystallized from EtOH (yield: 4.11 g, 24 %).

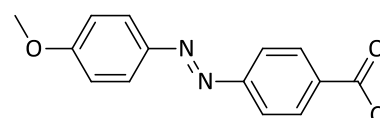
<sup>1</sup>H-NMR (CDCl<sub>3</sub>-d<sub>1</sub>/CF<sub>3</sub>COOD-d<sub>1</sub>): δ (ppm) = 8.35 (m, 4H, Ar-H<sup>4,5,1,8</sup>), 8.10 (m, 4H, Ar-H<sup>2,7,3,6</sup>), 4.32 (s, 3H, CH<sub>3</sub><sup>9</sup>)



Chemical Formula: C<sub>14</sub>H<sub>12</sub>N<sub>2</sub>O<sub>3</sub>  
Molecular Weight: 256,26

#### Preparation of 4-[(4-methoxyphenyl)azo]benzoic acid chloride

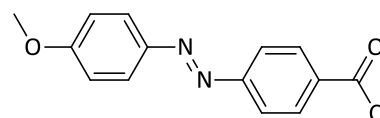
The synthesis of the title product was carried out according to **GM4** using 4-[(4-methoxyphenyl)azo]benzoic acid (16 mmol, 4.11 g), dry DMF (5 drops), dry CH<sub>2</sub>Cl<sub>2</sub> (50 mL) and COCl<sub>2</sub> (48.1 mmol, 6.10 g). The crude product was used as received.



Chemical Formula: C<sub>14</sub>H<sub>11</sub>ClN<sub>2</sub>O<sub>2</sub>  
Molecular Weight: 274,70

#### Preparation of 4-{4-[(4-cyanophenyl)azo]phenoxy}butyric acid chloride

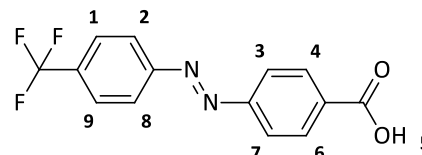
The synthesis of the title product was carried out according to **GM4** using 4-[(4-cyanophenyl)azo]benzoic acid (6.5 mmol, 2.00 g), dry DMF (5 drops), dry CH<sub>2</sub>Cl<sub>2</sub> (50 mL) and COCl<sub>2</sub> (48.1 mmol, 6.10 g). The crude product was used as received.



Chemical Formula: C<sub>14</sub>H<sub>11</sub>ClN<sub>2</sub>O<sub>2</sub>  
Molecular Weight: 274,70

#### Preparation of 4-[(4-trifluoromethylphenyl)azo]benzoic acid

The synthesis of the title product was carried out according to **GM1** using 4-nitrosobenzoic acid (71 mmol, 10.80 g), DMSO (250 mL), AcOH (150 mL), and 4-(trifluoromethyl)aniline (71 mmol, 8.97g) (yield: 13.0 g, 64 %).

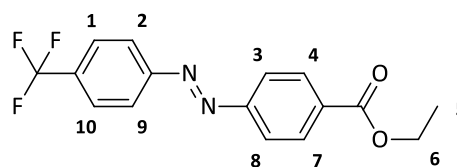


Chemical Formula: C<sub>14</sub>H<sub>9</sub>F<sub>3</sub>N<sub>2</sub>O<sub>2</sub>  
Molecular Weight: 294,23

<sup>1</sup>H-NMR (DMSO-d<sub>6</sub>): δ (ppm) = 13.38 (s, 1H, OH<sup>5</sup>), 8.17 (m, 2H, Ar-H<sup>4,6</sup>), 8.10 (m, 2H, Ar-H<sup>1,9</sup>), 8.03 (m, 2H, Ar-H<sup>3,7</sup>), 7.97 (m, 2H, Ar-H<sup>2,8</sup>)

#### Preparation of 4-[(4-trifluoromethylphenyl)azo]benzoic acid ethyl ester

The synthesis of the title product was carried out according to **GM2** using 4-[(4-trifluoromethylphenyl)azo]benzoic acid (28.4 mmol, 10.0 g), EtOH (500 mL), H<sub>2</sub>SO<sub>4</sub> (4 mL). The crude product was purified by column chromatography using toluene as eluent yielding an orange solid (yield: 4.76 g, 51 %).

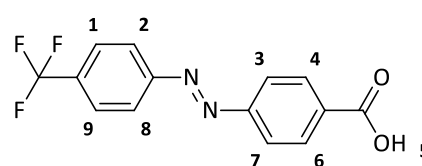


Chemical Formula: C<sub>16</sub>H<sub>13</sub>F<sub>3</sub>N<sub>2</sub>O<sub>2</sub>  
Molecular Weight: 322,28

<sup>1</sup>H-NMR (CDCl<sub>3</sub>-d<sub>1</sub>): δ (ppm) = 8.24 (m, 2H, Ar-H<sup>4,7</sup>), 8.06 (m, 2H, Ar-H<sup>1,10</sup>), 8.01 (m, 2H, Ar-H<sup>3,8</sup>), 7.82 (m, 2H, Ar-H<sup>2,9</sup>), 4.45 (q, 2H, CH<sub>2</sub><sup>6</sup>), 1.46 (t, 3H, CH<sub>3</sub><sup>5</sup>)

#### Saponification of 4-[(4-trifluoromethylphenyl)azo]benzoic acid ethyl ester to 4-[(4-trifluoromethylphenyl)azo]benzoic acid

The synthesis of the title product was carried out according to **GM3** using 4-[(4-trifluoromethylphenyl)azo]benzoic ethyl ester (14.7 mmol, 4.79 g), EtOH (150 mL), H<sub>2</sub>O (15 mL) and KOH (22.1 mmol, 1.24g). The crude product was washed with water thoroughly to yield an orange solid (yield: 4.34 g, quantitative).



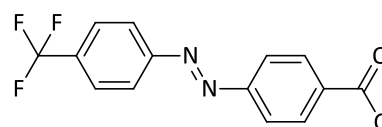
Chemical Formula: C<sub>14</sub>H<sub>9</sub>F<sub>3</sub>N<sub>2</sub>O<sub>2</sub>  
Molecular Weight: 294,23

<sup>1</sup>H-NMR (DMSO-d<sub>6</sub>): δ (ppm) = 13.37 (s, 1H, OH<sup>5</sup>), 8.17 (m, 2H, Ar-H<sup>4,6</sup>), 8.11 (m, 2H, Ar-H<sup>1,9</sup>), 8.04 (m, 2H, Ar-H<sup>3,7</sup>), 8.00 (m, 2H, Ar-H<sup>2,8</sup>)

EIMS (m/z): [M<sup>+</sup>] (calc.: 294.42), found: 294

#### Preparation of 4-[(4-trifluoromethylphenyl)azo]benzoic acid chloride

The synthesis of the title product was carried out according to **GM4** using 4-[(4-trifluoromethylphenyl)azo]benzoic acid (8.1 mmol, 2.5 g), dry DMF (5 drops), dry THF (20 mL) and COCl<sub>2</sub> (32.3 mmol, 4.1 g). The crude product was used as received.



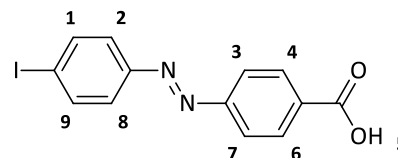
Chemical Formula: C<sub>14</sub>H<sub>8</sub>ClF<sub>3</sub>N<sub>2</sub>O  
Molecular Weight: 312,67

*Preparation of 4-[(4-iodophenyl)azo]benzoic acid*

The synthesis as well as the purification of the title product was carried out according to **GM1** using 4-nitrosobenzoic acid (99 mmol, 15.00 g), DMSO (350 mL), AcOH (220 mL), and 4-iodoaniline (99 mmol, 21.74g) to yield an orange solid (yield: 25.3g, 73 %).

$^1\text{H-NMR}$  (DMSO- $d_6$ ):  $\delta$  (ppm) = 8.13 (m, 2H, Ar-H<sup>4,6</sup>), 8.01 (m, 2H, Ar-H<sup>2,8</sup>), 7.95 (m, 2H, Ar-H<sup>3,7</sup>), 7.71 (m, 2H, Ar-H<sup>1,9</sup>)

EIMS (m/z): [M<sup>+</sup>] (calc.: 352.13), found: 352

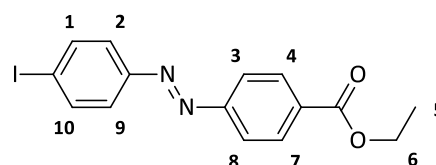


Chemical Formula: C<sub>13</sub>H<sub>9</sub>IN<sub>2</sub>O<sub>2</sub>  
Molecular Weight: 352,13

*Preparation of 4-[(4-iodophenyl)azo]benzoic acid ethyl ester*

The synthesis of the title product was carried out according to **GM2** using 4-[(4-iodophenyl)azo]benzoic acid (42.6 mmol, 15.0 g), EtOH (1000 mL), H<sub>2</sub>SO<sub>4</sub> (6 mL). The crude product was washed with water several times to yield an orange solid (yield: 13.56g, 84 %).

$^1\text{H-NMR}$  (CDCl<sub>3</sub>- $d_1$ ):  $\delta$  (ppm) = 8.22 (m, 2H, Ar-H<sup>4,7</sup>), 7.96 (m, 2H, Ar-H<sup>3,8</sup>), 7.91 (m, 2H, Ar-H<sup>2,9</sup>), 7.70 (m, 2H, Ar-H<sup>1,10</sup>), 4.44 (q, 2H, CH<sub>2</sub><sup>6</sup>), 1.45 (t, 3H, CH<sub>3</sub><sup>5</sup>)



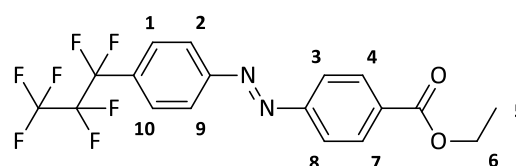
Chemical Formula: C<sub>15</sub>H<sub>13</sub>IN<sub>2</sub>O<sub>2</sub>  
Molecular Weight: 380,18

*Preparation of 4-[(4-perfluoropropylphenyl)azo]benzoic acid ethyl ester*

The synthesis of the title product was carried out according to **GM2** using 4-[(4-iodophenyl)azo]benzoic acid ethyl ester (20.5 mmol, 7.8 g, 1eq.), DMSO (200 mL), copper (61.6 mmol, 3 eq.) and perfluoropropyl iodide (26.7 mmol, 7.90 g, 1.3 eq.). The crude product was recrystallized from MeOH to yield an orange solid (yield: 4.98 g, 57 %).

$^1\text{H-NMR}$  (CDCl<sub>3</sub>- $d_1$ ):  $\delta$  (ppm) = 8.20 (m, 2H, Ar-H<sup>4,7</sup>), 8.14 (m, 2H, Ar-H<sup>2,9</sup>), 8.05 (m, 2H, Ar-H<sup>3,8</sup>), 7.96 (m, 2H, Ar-H<sup>1,10</sup>), 4.37 (q, 2H, CH<sub>2</sub><sup>6</sup>), 1.36 (t, 3H, CH<sub>3</sub><sup>5</sup>)

EIMS (m/z): [M<sup>+</sup>] (calc.: 422.30), found: 422

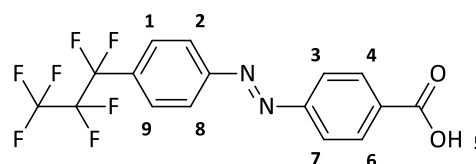


Chemical Formula: C<sub>18</sub>H<sub>13</sub>F<sub>7</sub>N<sub>2</sub>O<sub>2</sub>  
Molecular Weight: 422,30

*Preparation of 4-[(4-perfluoropropylphenyl)azo]benzoic acid*

The synthesis of the title product was carried out according to **GM3** using 4-[(4-perfluoropropylphenyl)azo]benzoic acid ethyl ester (11.7 mmol, 4.96 g), EtOH (100 mL), H<sub>2</sub>O (15 mL) and KOH (17.6 mmol, 1.0g). The crude product was washed with water thoroughly to yield an orange solid (yield: 4.6 g, quantitative).

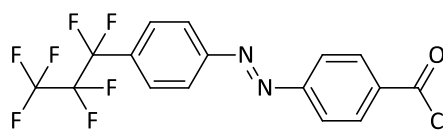
$^1\text{H-NMR}$  (DMSO- $d_6$ ):  $\delta$  (ppm) = 8.14 (m, 4H, Ar-H<sup>4,6,2,8</sup>), 7.98 (m, 4H, Ar-H<sup>1,9,3,7</sup>)



Chemical Formula: C<sub>16</sub>H<sub>9</sub>F<sub>7</sub>N<sub>2</sub>O<sub>2</sub>  
Molecular Weight: 394,24

### Preparation of 4-[(4-perfluoropropylphenyl)azo]benzoic acid chloride

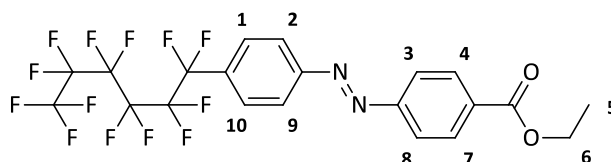
The synthesis of the title product was carried out according to **GM4** using 4-[(4-perfluoropropylphenyl)azo]benzoic acid (11.7 mmol, 4.6 g), dry DMF (5 drops), dry  $\text{CHCl}_2$  (60 mL) and  $\text{COCl}_2$  (35.0 mmol, 4.44 g). The crude product was used as received.



Chemical Formula:  $\text{C}_{16}\text{H}_8\text{ClF}_7\text{N}_2\text{O}$   
Molecular Weight: 412,69

### Preparation of 4-[(4-perfluorohexylphenyl)azo]benzoic acid ethyl ester

The synthesis of the title product was carried out according to **GM2** using 4-[(4-iodophenyl)azo]benzoic acid ethyl ester (21.0 mmol, 8.00 g, 1eq.), DMSO (200 mL), copper (63.1 mmol, 4.01 g, 3 eq.) and perfluorohexyl iodide (31.6 mmol, 14.08 g, 1.5 eq.). The crude product was recrystallized from MeOH to yield an orange solid (yield: 10.01 g, 83 %).

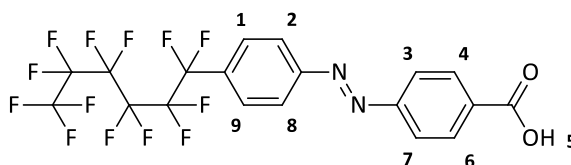


Chemical Formula:  $\text{C}_{21}\text{H}_{13}\text{F}_{13}\text{N}_2\text{O}_2$   
Molecular Weight: 572,32

$^1\text{H-NMR}$  ( $\text{CDCl}_3\text{-d}_1$ ):  $\delta$  (ppm) = 8.24 (m, 2H, Ar- $\text{H}^{4,7}$ ), 8.08 (m, 2H, Ar- $\text{H}^{2,9}$ ), 8.01 (m, 2H, Ar- $\text{H}^{3,8}$ ), 7.79 (m, 2H, Ar- $\text{H}^{1,10}$ ), 4.45 (q, 2H,  $\text{CH}_2^6$ ), 1.46 (t, 3H,  $\text{CH}_3^5$ )

### Preparation of 4-[(4-perfluorohexylphenyl)azo]benzoic acid

The synthesis of the title product was carried out according to **GM3** using 4-[(4-perfluorohexylphenyl)azo]benzoic acid ethyl ester (17.5 mmol, 10.00 g), EtOH (200 mL),  $\text{H}_2\text{O}$  (30 mL) and KOH (24.5 mmol, 1.37g). The crude product was washed with water thoroughly to yield an orange solid (yield: 7.5 g, 79 %).

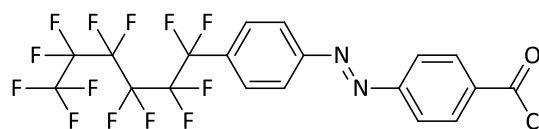


Chemical Formula:  $\text{C}_{19}\text{H}_9\text{F}_{13}\text{N}_2\text{O}_2$   
Molecular Weight: 544,27

$^1\text{H-NMR}$  ( $\text{DMSO-d}_6$ ):  $\delta$  (ppm) = 8.11 (m, 4H, Ar- $\text{H}^{4,6,2,8}$ ), 7.95 (m, 4H, Ar- $\text{H}^{1,9,3,7}$ )

### Preparation of 4-[(4-perfluorohexylphenyl)azo]benzoic acid chloride

The synthesis of the title product was carried out according to **GM4** using 4-[(4-perfluorohexylphenyl)azo]benzoic acid (9.0 mmol, 4.9 g), dry DMF (5 drops), dry  $\text{CHCl}_2$  (60 mL) and  $\text{COCl}_2$  (27.0 mmol, 3.42 g). The crude product was as received.

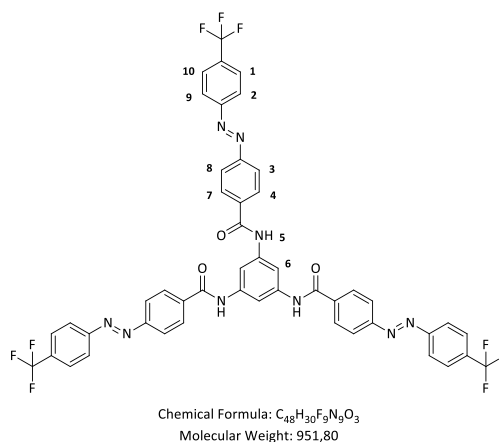


Chemical Formula:  $\text{C}_{19}\text{H}_8\text{ClF}_{13}\text{N}_2\text{O}$   
Molecular Weight: 562,71

### 9.4.4 Synthesis of azobenzene functionalized molecular glasses

#### Preparation of 1,3,5-tris-{4-[(4-trifluoromethylphenyl)azo]benzoyl}amino}benzene

The synthesis of the title product was carried out according to **GM6** using 1,3,5-triaminobenzene (1.4 mmol, 0.17 g), LiCl (spatula tip), dry NMP (25 mL), triethylamine (5.5 mmol, 0.56 g) and 4-[(4-trifluoromethylphenyl)azo]benzoic acid chloride (4.8 mmol, 1.51 g). The crude product was filtered off from hot EtOH to yield an orange solid (yield: 0.48 g, 37 %).



$^1\text{H-NMR}$  (THF- $d_8$ ):  $\delta$  (ppm) = 8.07 (s, 3H,  $\text{NH}^5$ ), 6.47 (s, 3H,  $\text{Ar-H}^6$ ), 6.39 (d, 6H,  $\text{Ar-H}^{4,7}$ ), 6.28 (m, 12H,  $\text{Ar-H}^{2,3,8,9}$ ), 6.09 (d, 6H,  $\text{Ar-H}^{1,10}$ )

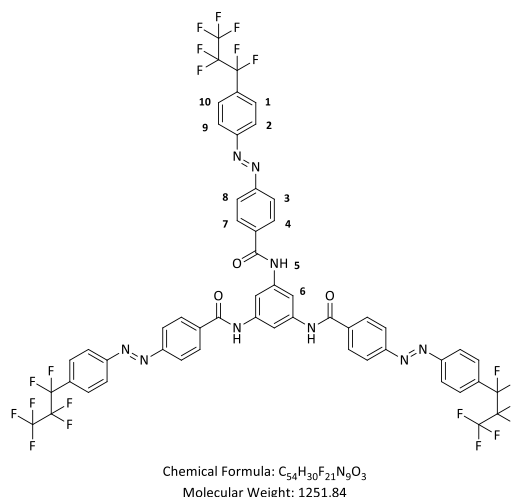
El. Vol. (Oligo-SEC): 15.49 mL

FT-IR (ATR):  $\nu$  ( $\text{cm}^{-1}$ ) 3306, 1788, 1654, 1612, 1535, 1424, 1320, 1261, 1167, 1101, 1062, 1011, 848, 762, 678

EIMS ( $m/z$ ): [ $\text{M}^+$ ] (calc.: 951.80), found: 951

#### Preparation of 1,3,5-tris-{4-[(4-perfluoropropylphenyl)azo]benzoyl}amino}benzene

The synthesis of the title product was carried out according to **GM6** using 1,3,5-triaminobenzene (1.1 mmol, 0.13 g), LiCl (spatula tip), dry NMP (25 mL), triethylamine (4.2 mmol, 0.43 g) and 4-[(4-perfluoropropylphenyl)azo]benzoic acid chloride (3.6 mmol, 1.48 g). The crude product was purified by column chromatography using THF as eluent yielding an orange solid (yield: 0.69 g, 52 %).



$^1\text{H-NMR}$  (DMSO- $d_6$ ):  $\delta$  (ppm) = 10.64 (s, 3H,  $\text{NH}^5$ ), 8.25 (s, 6H,  $\text{Ar-H}^{4,7}$ ), 8.11 (m, 15H,  $\text{Ar-H}^{2,3,6,8,9}$ ), 6.28 (m, 6H,  $\text{Ar-H}^{1,10}$ )

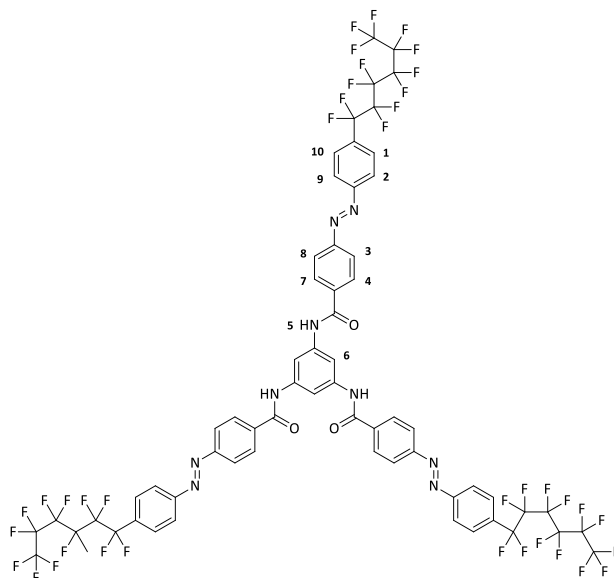
El. Vol. (Oligo-SEC): 15.08 mL

FT-IR (ATR):  $\nu$  ( $\text{cm}^{-1}$ ) 3309, 2963, 1657, 1614, 1539, 1426, 1348, 1262, 1167, 1201, 1178, 1114, 1071, 1011, 894, 749, 675

EIMS ( $m/z$ ): [ $M^+$ ] (calc.: 1251.48), found: 1251

*Preparation of 1,3,5-tris-{4-[(4-perfluorohexylphenyl)azo]benzoyl}amino}benzene*

The synthesis of the title product was carried out according to **GM6** using 1,3,5-triaminobenzene (0.9 mmol, 0.11 g), LiCl (spatula tip), dry NMP (25 mL), triethylamine (3.6 mmol, 0.36 g) and 4-[(4-perfluorohexylphenyl)azo]benzoic acid chloride (3.0 mmol, 1.71 g). The crude product was recrystallized from DMSO (yield: 0.53 g, 35 %).



Chemical Formula:  $C_{64}H_{33}F_{39}N_9O_3$   
Molecular Weight: 1697,94

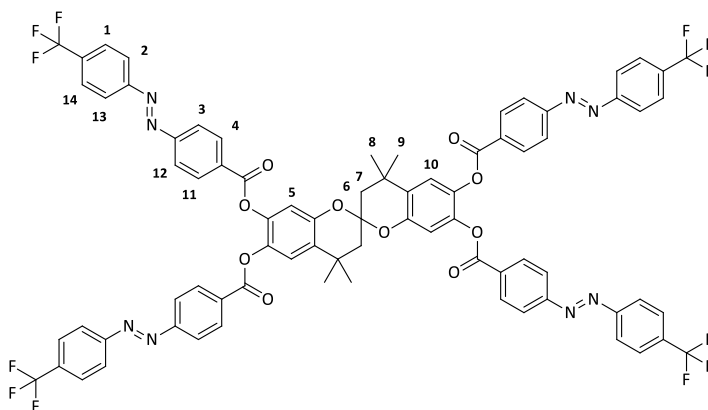
$^1\text{H-NMR}$  ( $\text{CDCl}_3\text{-d}_1/\text{CF}_3\text{COOD-d}_1$ ):  $\delta$  (ppm) = 8.50 (s, 3H, Ar- $\text{H}^6$ ), 8.25 (d, 6H, Ar- $\text{H}^{4,7}$ ), 8.09 (m, 12H, Ar- $\text{H}^{2,3,8,9}$ ), 7.83 (d, 6H, Ar- $\text{H}^{1,10}$ )

El. Vol. (Oligo-SEC): 14.62 mL

FT-IR (ATR):  $\nu$  ( $\text{cm}^{-1}$ ) 3318, 1657, 1614, 1538, 1426, 1348, 1282, 1193, 1120, 1103, 1091, 1037, 1012, 856, 688

*Preparation of 4,4,4',4'-tetramethyl-2,2'-spirobichromane-6,6',7,7'-tetrakis-4-[4-(trifluoromethylphenyl)azo]benzoate*

The synthesis of the title product was carried out according to **GM7** using 6,6',7,7'-tetrahydroxy-4,4,4',4'-tetramethylbis-2,2'-spirobichroman (3.0 mmol, 1.12 g), dry THF (80 mL), triethylamine (13.5 mmol, 1.37 g) and 4-[(4-trifluoromethylphenyl)azo]benzoic acid chloride (13.2 mmol, 4.13 g). The crude product was recrystallized from THF/EtOH to yield an orange solid (yield: 2.61 g, 59 %).

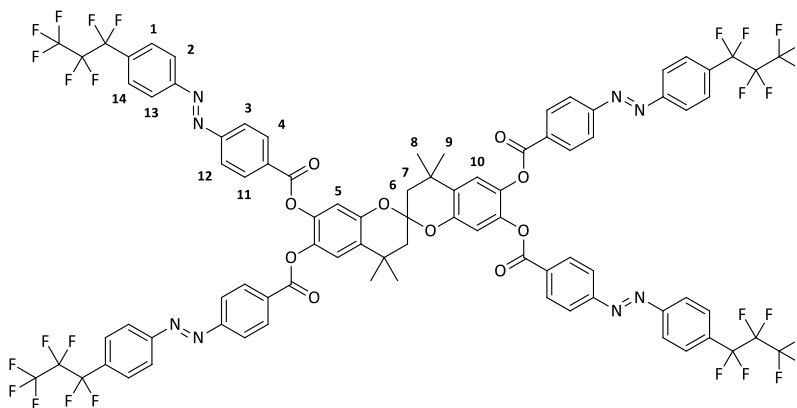


Chemical Formula:  $C_{77}H_{52}F_{12}N_8O_{10}$   
Molecular Weight: 1477,27

$^1\text{H-NMR}$ ( $\text{CDCl}_3\text{-d}_1$ ):	$\delta$ (ppm) = 8.25 (m, 8H, Ar- $\text{H}^{4,11}$ ), 8.00 (d, 8H, Ar- $\text{H}^{2,13}$ ), 7.93 (m, 8H, Ar- $\text{H}^{3,12}$ ), 7.78 (d, 8H, Ar- $\text{H}^{1,14}$ ), 7.39 (s, 2H, Ar- $\text{H}^5$ ), 6.89 (s, 2H, Ar- $\text{H}^{10}$ ), 2.25 (d, 2H, $\text{CH}_2^{6,7}$ ), 2.11 (d, 2H, $\text{CH}_2^{6,7}$ ) 1.70 (s, 6H, $\text{CH}_3^{8,9}$ ), 1.47 (s, 6H, $\text{CH}_3^{8,9}$ )
El. Vol. (Oligo-SEC):	15.13 mL
DSC (10K/min, $\text{N}_2$ , heating):	$T_g = 126^\circ\text{C}$
FT-IR (ATR): $\nu$ ( $\text{cm}^{-1}$ )	2963, 1732, 1603, 1492, 1410, 1326, 1320, 1253, 1235, 1124, 858, 848, 763, 688

*Preparation of 4,4,4',4'-tetramethyl-2,2'-spirobichromane-6,6',7,7'-tetrakis-4-[4-(perfluoropropyl)azo]benzoate*

The synthesis of the title product was carried out according to **GM7** using 6,6',7,7'-tetrahydroxy-4,4,4',4'-tetramethylbis-2,2'-spirobichroman (2.7 mmol, 0.99 g), dry THF (100 mL), triethylamine (11.93 mmol, 1.21 g) and 4-[(4-perfluoropropyl)azo]benzoic acid chloride (11.66 mmol, 4.81 g). The crude product was recrystallized from DMF to yield an orange solid (yield: 4.00 g, 80 %).

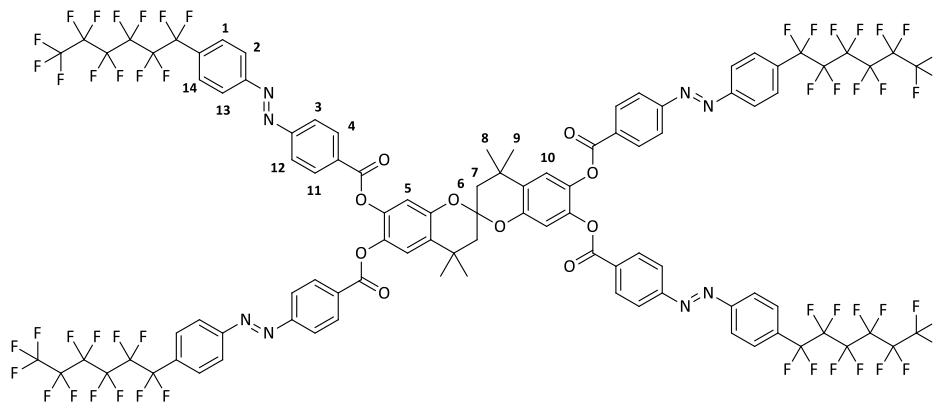


Chemical Formula:  $\text{C}_{85}\text{H}_{52}\text{F}_{28}\text{N}_8\text{O}_{10}$   
Molecular Weight: 1877.33

$^1\text{H-NMR}$ ( $\text{CDCl}_3\text{-d}_1$ ):	$\delta$ (ppm) = 8.25 (m, 8H, Ar- $\text{H}^{4,11}$ ), 8.02 (d, 8H, Ar- $\text{H}^{2,13}$ ), 7.94 (m, 8H, Ar- $\text{H}^{3,12}$ ), 7.75 (d, 8H, Ar- $\text{H}^{1,14}$ ), 7.39 (s, 2H, Ar- $\text{H}^5$ ), 6.89 (s, 2H, Ar- $\text{H}^{10}$ ), 2.24 (d, 2H, $\text{CH}_2^{6,7}$ ), 2.12 (d, 2H, $\text{CH}_2^{6,7}$ ) 1.70 (s, 6H, $\text{CH}_3^{8,9}$ ), 1.47 (s, 6H, $\text{CH}_3^{8,9}$ )
El. Vol. (Oligo-SEC):	14.79 mL
FT-IR (ATR): $\nu$ ( $\text{cm}^{-1}$ )	2966, 1737, 1603, 1492, 1412, 1347, 1260, 1224, 1203, 1115, 1161, 1030, 893, 862, 838, 748, 767, 676

*Preparation of 4,4,4',4'-tetramethyl-2,2'-spirobichromane-6,6',7,7'-tetrakis-4-[4-(perfluorohexylphenyl)azo]benzoate*

The synthesis of the title product was carried out according to **GM7** using 6,6',7,7'-tetrahydroxy-4,4,4',4'-tetra-methylbis-2,2'-spirobichroman (2.1 mmol, 0.76 g), dry THF (100 mL), triethylamine (9.2 mmol, 0.93 g) and 4-[(4-perfluorohexylphenyl)azo]benzoic acid chloride (9.0 mmol, 5.06 g). The crude product was recrystallized from DMF to yield an orange solid (yield: 3.68 g, 72 %).



Chemical Formula:  $C_{97}H_{52}F_{52}N_8O_{10}$   
Molecular Weight: 2477,42

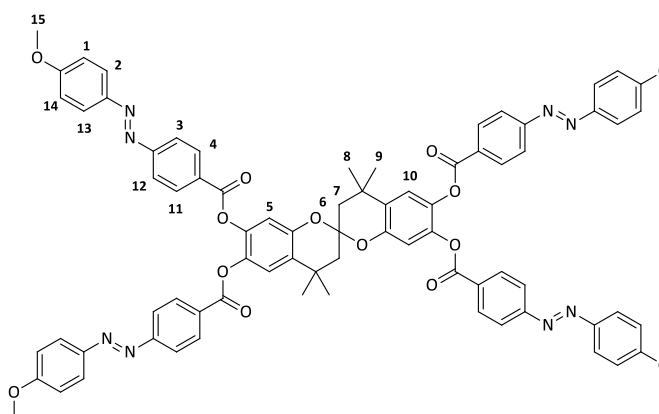
$^1\text{H-NMR}$  ( $\text{CDCl}_3\text{-d}_1$ ):  $\delta$  (ppm) = 8.25 (m, 8H, Ar- $\text{H}^{4,11}$ ), 8.02 (d, 8H, Ar- $\text{H}^{2,13}$ ), 7.93 (m, 8H, Ar- $\text{H}^{3,12}$ ), 7.75 (d, 8H, Ar- $\text{H}^{1,14}$ ), 7.40 (s, 2H, Ar- $\text{H}^5$ ), 6.89 (s, 2H, Ar- $\text{H}^{10}$ ), 2.24 (d, 2H,  $\text{CH}_2^{6,7}$ ), 2.12 (d, 2H,  $\text{CH}_2^{6,7}$ ), 1.70 (s, 6H,  $\text{CH}_3^{8,9}$ ), 1.47 (s, 6H,  $\text{CH}_3^{8,9}$ )

El. Vol. (Oligo-SEC): 14.42 mL

FT-IR (ATR):  $\nu$  ( $\text{cm}^{-1}$ ) 2962, 1738, 1604, 1493, 1413, 1364, 1285, 1233, 1197, 1121, 1089, 1031, 1011, 946, 907, 861, 844, 769, 689

*Preparation 4,4,4',4'-tetramethyl-2,2'-spirobichromane-6,6',7,7'-tetrakis-4-[4-(methoxyphenyl)azo]benzoate*

The synthesis of the title product was carried out according to **GM7** using 6,6',7,7'-tetrahydroxy-4,4,4',4'-tetramethylbis-2,2'-spirobichroman (3.6 mmol, 1.35 g), dry THF (60 mL), triethylamine (16.0 mmol, 1.62 g) and 4-[(4-methoxyphenyl)azo]benzoic acid chloride (16.0 mmol, 4.41 g). The crude product was purified by column chromatography using toluene/ $\text{CHCl}_3$  as eluent yielding an orange solid (yield: 1.60 g, 33 %).



Chemical Formula:  $C_{77}H_{64}N_8O_{14}$   
Molecular Weight: 1325,38

$^1\text{H-NMR}$  ( $\text{CDCl}_3\text{-d}_1$ ):  $\delta$  (ppm) = 8.21 (m, 8H, Ar- $\text{H}^{4,11}$ ), 7.92 (m, 8H, Ar- $\text{H}^{2,13}$ ), 7.85 (m, 8H, Ar- $\text{H}^{3,12}$ ), 7.38 (s, 2H, Ar- $\text{H}^5$ ), 7.01 (m, 8H, Ar- $\text{H}^{1,14}$ ), 6.87 (s, 2H, Ar- $\text{H}^{10}$ ), 3.91 (s, 12H,  $\text{CH}_3^{15}$ ), 2.22 (d, 2H,  $\text{CH}_2^{6,7}$ ), 2.09 (d, 2H,  $\text{CH}_2^{6,7}$ ), 1.69 (s, 6H,  $\text{CH}_3^{8,9}$ ), 1.46 (s, 6H,  $\text{CH}_3^{8,9}$ )

El. Vol. (Oligo-SEC):	15.61 mL
FT-IR (ATR): $\nu$ (cm <sup>-1</sup> )	2960, 1735, 1598, 1498, 1416, 1404, 1312, 1245, 1131, 1063, 1028, 1009, 905, 859, 835, 762, 685

## 9.5 Block copolymer synthesis

### 9.5.1 Purification of solvents and monomers

#### *Tetrahydrofuran (THF)*

Tetrahydrofuran was first refluxed over CaH<sub>2</sub> for 3 days and then distilled off. Subsequently, the THF was refluxed over potassium for another 3 days prior to use.

#### *Styrene (S)*

Styrene was purified in a flame dried flask under inert gas atmosphere using a dibutyl magnesium solution in hexane. For the synthesis of the block copolymer 50 mL of styrene were placed in a flask and 5 mL of the dibutyl magnesium solution were added until the solution turned yellowish. After stirring for 15 min in the dark, the solution was degassed by 3 freeze-pump-thaw cycles. Whereas cooling was realized by liquid nitrogen and the pump was a high vacuum turbo pump achieving pressures down to  $5 \cdot 10^{-6}$  mbar. The heptane was removed under vacuum carefully, cooling the solution in an ice bath. Subsequently, the styrene was condensed into an ampoule using high vacuum and stored in liquid nitrogen until usage.

#### *tert-Butoxystyrene (t-BS)*

tert-Butoxystyrene was purified in the same manner as styrene was using 1.5 mL dibutyl magnesium for 10 mL of t-BS. Due to its high boiling point, the t-BS could not be condensed directly into an ampoule, but had to be distilled at a temperature of 90°C using high vacuum and a micro distillation. After finishing the distillation, the purified monomer was stored in an ampoule using liquid nitrogen.

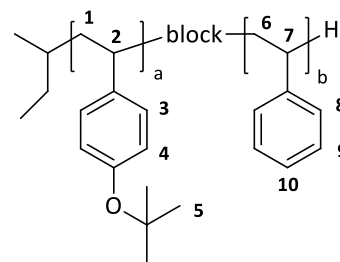
#### *General method for the polymer analogous functionalization of POHS-b-PS GM8*

Depending on the desired degree of functionalization different amounts of azobenzene acid chloride derivatives have been used. The reactions were carried out under inert atmosphere (argon) in a flame dried Schlenk flask. The POHS-b-PS block copolymer (2.5 g, 1.1 mmol, 1 eq.) is dissolved in dry THF (40 mL). Afterwards, pyridine (0.35 mL, 4 eq.) and dry DMF (2 mL) were added. The reaction mixture was then cooled down to approx. 0°C using an ice bath before the azobenzene acid chloride derivative (0.81 g, 2.5 mmol, 2.3 eq.) was slowly added. The mixture was allowed to react for 48h at room temperature and was then heated up to 50°C for another 2 hours. The reaction was then terminated by adding dry MeOH (approx. 5 mL). The solvent was then reduced to one third in vacuum and the reaction mixture then precipitated in MeOH. The precipitation process was repeated until the MeOH did not show any color anymore. The product was dried at high vacuum.

### 9.5.2 Synthesis of poly(4-tert-butoxystyrene)-block-polystyrene

The anionic block copolymer synthesis was carried out in a custom-made single reactor with a connection to an adjacent THF distiller. Before starting the reaction, the reactor was flushed with a THF/sec-BuLi solution that was pumped out afterwards. The THF needed for the reaction (700 mL) was

titrated with *sec*-BuLi to avoid protic impurities. Therefore, the reactor was cooled down to  $-68^{\circ}\text{C}$  and *sec*-BuLi was injected via a septum until the solvent turned yellow. Subsequently, the reactor was heated up to  $20^{\circ}\text{C}$  until the THF was colorless. After cooling the reactor down to  $-68^{\circ}\text{C}$  again, the calculated amount of *sec*-BuLi (0.28 mmol, 0.22 mL) was injected into the reactor using a syringe. In the next step, *t*-BS (15.90 mmol, 2.81 g, 1 eq.) was injected to the vigorously stirring THF.



The monomer was allowed to polymerize for 95 min at  $\text{N}_2$  overpressure. Afterwards, 100 mL of this reaction mixture were transferred into an adjacent reactor, in which 1 mL of dry methanol were filled before. In the next step, styrene (348.0 mmol, 36.24 g, 25.48 eq.) was added via a septum and a syringe at  $-53^{\circ}\text{C}$ . The second monomer was allowed to react for another 95 min with the precursor. The reaction was terminated with dry MeOH, injected via the septum with a syringe. After exhausting the polymer solution from the reactor, the block copolymer was precipitated in MeOH and dried for 72 h in a vacuum oven at  $50^{\circ}\text{C}$ .

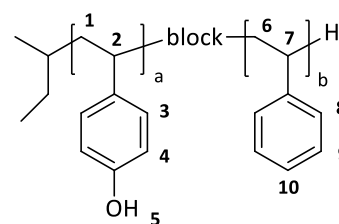
$^1\text{H-NMR}$ ( $\text{CDCl}_3\text{-d}_1$ ):	$\delta$ (ppm) =	7.25-6.89 (Ar-H <sup>9,10</sup> ),	6.89-6.23 (Ar-H <sup>3,4,8</sup> ),	2.27-0.98 (CH <sup>1,2,5,6,7</sup> )
El. Vol. (Poly-SEC):		16.23 mL		
DSC (10K/min, $\text{N}_2$ , heating):		$T_g = 105^{\circ}\text{C}$		
FT-IR (ATR): $\nu$ ( $\text{cm}^{-1}$ )		3026, 2923, 2850, 1601, 1493, 1452, 1365, 1237, 1163, 1069, 1028, 902, 842, 755, 697		

### 9.5.3 Polymer analogous reaction

Prior to polymer analogous azobenzene functionalization reactions, the hydroxyl group of the poly(4-*tert*-butoxystyrene)-block-polystyrene (PtBS-*b*-PS) block copolymer has to be deprotected. The degree of deprotection was checked in an acetylation reaction afterwards.

#### *Deprotection of poly(4-tert-butoxystyrene)-block-polystyrene*

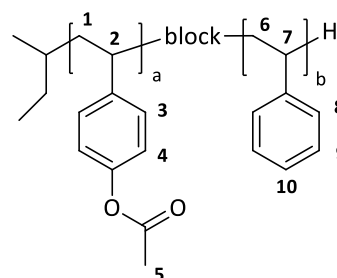
For the deprotection of the hydroxyl groups of the poly(4-*tert*-butoxystyrene) block, the poly(4-*tert*-butoxystyrene)-block-polystyrene (2.50 g, 0.9 mmol) was dissolved in 350 mL acetone. To this solution, an excess of hydrochloric acid (30-33%, 6.78 mL) was added and the reaction mixture was heated to reflux overnight. The obtained suspension is evaporated to approx. one third of its initial volume under reduced pressure and then precipitated in alkaline water (pH = 11). After filtration, the powder was given into slightly acidified water (pH = 5-6), stirred for 30 minutes at room temperature and filtered off again. After thorough drying at HV overnight, the block copolymer was dissolved in THF again and precipitated in MeOH. The product was then dried under HV.



$^1\text{H-NMR}$ ( $\text{THF-d}_8$ ):	$\delta$ (ppm) =	7.28-6.82 (Ar-H <sup>9,10</sup> ),	6.82-6.30 (Ar-H <sup>3,4,8</sup> ),	2.39-1.25 (CH <sup>1,2,6,7</sup> )
--	------------------	------------------------------------	-------------------------------------	------------------------------------

### Acetylation of poly(4-hydroxystyrene)-block-polystyrene (POHS-b-PS)

The reaction was carried out under inert atmosphere (argon) in a flame dried Schlenk flask. Prior to this reaction, the POHS-b-PS block copolymer (50 mg, 0.021 mmol, 1 eq.) was dried under HV for 3 days and then dissolved in 10 mL dry THF. Subsequently, dry pyridine (0.01 mL, 0.09 mmol, 4.5 eq.) was added and the reaction mixture was cooled down to approx. 0°C using an ice bath. Afterwards, triethylamine (0.01 mL, 0.08 mmol, 4.0 eq.) were slowly added via a syringe. The reaction was then stirred at room temperature overnight before it was heated to reflux for 1 h. The reaction was terminated by adding several drops of dry MeOH. The reaction mixture was then precipitated in MeOH and the precipitate was dried at HV.



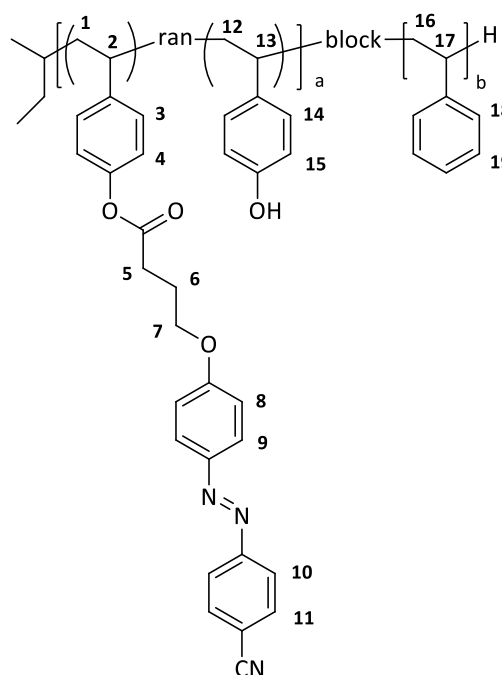
$^1\text{H-NMR}$  (THF- $d_8$ ):  $\delta$  (ppm) = 7.25-6.88 (Ar-H<sup>9,10</sup>), 6.82-6.21 (Ar-H<sup>3,4,8</sup>), 2.34-2.24 (CH<sub>3</sub><sup>5</sup>), 2.23-0.95 (CH<sup>1,2,6,7</sup>)

### Preparation of cyano-azobenzene functionalized poly(4-hydroxystyrene)-block-polystyrene (P(CNAzoOS)-b-PS)

The polymer analogous cyano-azobenzene functionalization reactions were carried out according to **GM8**. Depending on the desired degree of functionalization different amounts of azobenzene acid chloride derivatives have been used. The polymers with different degrees of azobenzene functionalization are listed in Table 11.

Table 11. Degree of functionalization of the P(OHS) block with azobenzene moieties, weight ratios of the blocks (PS block to functionalized block) and calculated number of repeating units  $r$  of the investigated block copolymers.

Name	BC 2-1	BC 2-2	BC 2-3
degree of functionalization P(OHS) block / %	41	50	71
$r_{\text{u,azo}} / r_{\text{u,OH}}$	18/26	22/22	31/13
P(OHS)- $r$ -P(Azo) / PS / wt.-%	9	11	13



$^1\text{H-NMR}$  (CDCl<sub>3</sub>- $d_1$ ):  $\delta$  (ppm) = 7.93-7.59 (Ar-H<sup>8,9,10</sup>), 7.24-6.12 (Ar-H<sup>3,4,11,14,15,18,19</sup>), 4.11-3.91 (CH<sub>2</sub><sup>5</sup>), 2.76-2.57 (CH<sub>2</sub><sup>6</sup>), 2.24-0.99 (CH<sup>1,2,7,12,13,16,17</sup>)

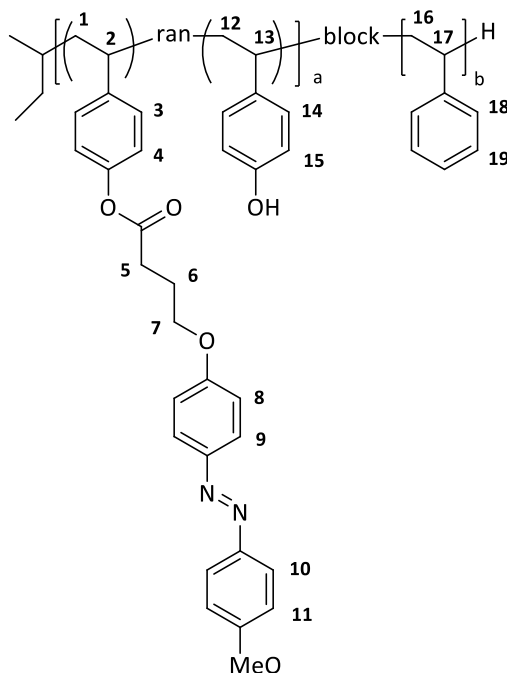
El. Vol. (Poly-SEC): 12.31 mL

DSC (10K/min, N<sub>2</sub>, heating):  $T_g$  = 104°C

FT-IR (ATR):  $\nu$  (cm<sup>-1</sup>) 3026, 2924, 2233, 1752, 1600, 1493, 1452, 1259, 1139, 1030, 907, 846, 801, 755, 698

*Preparation of methoxy-azobenzene functionalized poly(4-hydroxystyrene)-block-polystyrene (P(MeOAzOS)-b-PS)*

The polymer analogous methoxy-azobenzene functionalization reactions were carried out according to **GM8** using poly(4-hydroxystyrene)-block-polystyrene (1.30 g, 0.56 mmol, 1 eq.), 4-[4-[(4-methoxyphenyl)azo]phenoxy] butyric acid chloride (1.5 mmol, 0.50 g, 2.7 eq.), dry THF (35 mL), triethylamine (2.3 mmol, 0.23 g, 4 eq.) and dry DMF (0.80 mL). The crude product was precipitated in MeOH several times (yield: 1.10 g).



$^1\text{H-NMR}$  ( $\text{CDCl}_3\text{-d}_1$ ):  $\delta$  (ppm) = 7.76-7.59 (Ar- $\text{H}^{9,10}$ ), 7.22-6.11 (Ar- $\text{H}^{3,4,8,11,14,15,18,19}$ ), 3.96-3.76 ( $\text{CH}_2^5$ ), 2.20-0.79 ( $\text{CH}^{1,2,6,7,12,13,16,17}$ )

El. Vol. (Poly-SEC): 11.78 mL

DSC (10K/min,  $\text{N}_2$ , heating):  $T_g = 102^\circ\text{C}$

FT-IR (ATR):  $\nu$  ( $\text{cm}^{-1}$ ) 3025, 2923, 1752, 1600, 1493, 1452, 1373, 1315, 1250, 1148, 1029, 905, 840, 754, 696

## 10 References

- [1] H. Rau, *Ber. Bunsen-Ges. Phys. Chem.* **1968**, *72*, 408.
- [2] J. F. Rabek (Ed.), *Photochemistry and photophysics*, CRC Press, Boca Raton, Fla. **1990**.
- [3] Y. Zhao, T. Ikeda, *Smart light-responsive materials: Azobenzene-containing polymers and liquid crystals*, Wiley, Hoboken, N.J **2009**.
- [4] L. Lamarre, C. S. P. Sung, *Macromolecules* **1983**, *16*, 1729.
- [5] Y. Shirota, K. Moriwaki, S. Yoshikawa, T. Ujike, H. Nakano, *J. Mater. Chem.* **1998**, *8*, 2579.
- [6] S. A. Nagamani, Y. Norikane, N. Tamaoki, *J. Org. Chem.* **2005**, *70*, 9304.
- [7] I. K. Lednev, T.-Q. Ye, R. E. Hester, J. N. Moore, *J. Phys. Chem.* **1996**, *100*, 13338.
- [8] Z. F. Liu, K. Morigaki, T. Enomoto, K. Hashimoto, A. Fujishima, *J. Phys. Chem.* **1992**, *96*, 1875.
- [9] T. Naito, K. Horie, I. Mita, *Macromolecules* **1991**, *24*, 2907.
- [10] T. Fujino, S. Y. Arzhantsev, T. Tahara, *J. Phys. Chem. A* **2001**, *105*, 8123.
- [11] C.-H. Ho, K.-N. Yang, S.-N. Lee, *J. Polym. Sci. A Polym. Chem.* **2001**, *39*, 2296.
- [12] S. Xie, A. Natansohn, P. Rochon, *Chem. Mater.* **1993**, *5*, 403.
- [13] H. Audorff, K. Kreger, R. Walker, D. Haarer, L. Kador, H.-W. Schmidt, in *Complex Macromolecular Systems II*, Vol. 228 (Eds.: A. H. E. Müller, H.-W. Schmidt), Springer Berlin Heidelberg. Berlin, Heidelberg **2010**, p. 59.
- [14] H. Ringsdorf, H.-W. Schmidt, *Makromol. Chem.* **1984**, *185*, 1327.
- [15] M. R. Aguilar, J. San Román (Eds.), *Smart polymers and their applications*, WP Woodhead Publ./Elsevier, Amsterdam **2014**.
- [16] T. Seki, K. Fukuhara, M. Sano, M. Hara, S. Nagano, *Mol. Cryst. Liq. Cryst.* **2015**, *614*, 118.
- [17] C. L. van Oosten, C. W. M. Bastiaansen, D. J. Broer, *Nat. Mater.* **2009**, *8*, 677.
- [18] N. K. Viswanathan, D. Y. Kim, S. Bian, J. Williams, W. Liu, L. Li, L. Samuelson, J. Kumar, S. K. Tripathy, *J. Mater. Chem.* **1999**, *9*, 1941.
- [19] K. G. Yager, C. J. Barrett, *J. Photochem. Photobiol. A* **2006**, *182*, 250.
- [20] M. Moritsugu, S. N. Kim, T. Ogata, T. Nonaka, S. Kurihara, S. Kubo, H. Segawa, O. Sato, *Appl. Phys. Lett.* **2006**, *89*, 153131.
- [21] A. Natansohn, P. Rochon, *Chem. Rev.* **2002**, *102*, 4139.
- [22] H. Audorff, K. Kreger, R. Walker, D. Haarer, L. Kador, H.-W. Schmidt, *Adv. Polym. Sci.* **2010**, *228*, 59.
- [23] M. Eich, J. H. Wendorff, B. Reck, H. Ringsdorf, *Makromol. Chem., Rapid Commun.* **1987**, *8*, 59.
- [24] X. Meng, A. Natansohn, P. Rochon, *Polymer* **1997**, *38*, 2677.
- [25] V. Cimrová, D. Neher, S. Kostromine, T. Bieringer, *Macromolecules* **1999**, *32*, 8496.
- [26] H. Kogelnick, *Bell. Syst. Tech. J.* **1969**, *48*, 2909.
- [27] C. Berges, I. Díez, I. Javakhishvili, S. Hvilsted, C. Sánchez-Somolinos, R. Alcalá, *Opt. Mater.* **2014**, *36*, 845.
- [28] C. Berges, I. Javakhishvili, S. Hvilsted, C. Sánchez-Somolinos, R. Alcalá, *Appl. Phys. Lett.* **2013**, *102*, 193303.
- [29] P. Forcén, L. Oriol, C. Sánchez, F. J. Rodríguez, R. Alcalá, S. Hvilsted, K. Jankova, *Eur. Polym. J.* **2008**, *44*, 72.
- [30] H. Ringsdorf, H. W. Schmidt, G. Baur, R. Kiefer, F. Windscheid, *Liq. Cryst.* **1986**, *1*, 319.
- [31] T. Ikeda, S. Hasegawa, T. Sasaki, T. Miyamoto, M.-P. Lin, S. Tazuke, *Makromol. Chem.* **1991**, *192*, 215.

- [32] J. Stumpe, L. Müller, D. Kreysig, G. Hauck, H. D. Koswig, R. Ruhmann, J. Rübner, *Makromol. Chem., Rapid Commun.* **1991**, *12*, 81.
- [33] R. Hagen, T. Bieringer, *Adv. Mater.* **2001**, *13*, 1805.
- [34] S. J. Zilker, M. R. Huber, T. Bieringer, D. Haarer, *Appl. Phys. B* **1999**, *68*, 893.
- [35] S. Hvilsted, F. Andruzzi, C. Kulinna, H. W. Siesler, P. S. Ramanujam, *Macromolecules* **1995**, *28*, 2172.
- [36] C. J. Barrett, A. L. Natansohn, P. L. Rochon, *J. Phys. Chem.* **1996**, *100*, 8836.
- [37] T. Sasaki, M. Izawa, K. Noda, E. Nishioka, N. Kawatsuki, H. Ono, *Appl. Phys. B* **2014**, *114*, 373.
- [38] C. Frenz, A. Fuchs, H.-W. Schmidt, U. Theissen, D. Haarer, *Macromol. Chem. Phys.* **2004**, *205*, 1246.
- [39] P. Forcén, L. Oriol, C. Sánchez, R. Alcalá, S. Hvilsted, K. Jankova, J. Loos, *J. Polym. Sci. A Polym. Chem.* **2007**, *45*, 1899.
- [40] S. Gimeno, P. Forcén, L. Oriol, M. Piñol, C. Sánchez, F. J. Rodríguez, R. Alcalá, K. Jankova, S. Hvilsted, *Eur. Polym. J.* **2009**, *45*, 262.
- [41] X. Tong, L. Cui, Y. Zhao, *Macromolecules* **2004**, *37*, 3101.
- [42] C. Berges, I. Javakhishvili, S. Hvilsted, C. Sánchez-Somolinos, R. Alcalá, *Appl. Phys. Lett.* **2013**, *102*, 193303.
- [43] C. Berges, I. Díez, I. Javakhishvili, S. Hvilsted, C. Sánchez-Somolinos, R. Alcalá, *Optical Materials* **2014**, *36*, 845.
- [44] J. del Barrio, E. Blasco, L. Oriol, R. Alcalá, C. Sánchez-Somolinos, *J. Polym. Sci. A Polym. Chem.* **2013**, *51*, 1716.
- [45] G. Mao, J. Wang, S. R. Clingman, C. K. Ober, J. T. Chen, E. L. Thomas, *Macromolecules* **1997**, *30*, 2556.
- [46] T. Hayakawa, S. Horiuchi, H. Shimizu, T. Kawazoe, M. Ohtsu, *J. Polym. Sci. A Polym. Chem.* **2002**, *40*, 2406.
- [47] E. Yoshida, M. Ohta, *Colloid Polym Sci* **2005**, *283*, 521.
- [48] S. Gimeno, P. Forcén, L. Oriol, M. Piñol, C. Sánchez, F. J. Rodríguez, R. Alcalá, K. Jankova, S. Hvilsted, *Eur. Polym. J.* **2009**, *45*, 262.
- [49] Y. Zhang, W. Zhang, X. Chen, Z. Cheng, J. Wu, J. Zhu, X. Zhu, *J. Polym. Sci. A Polym. Chem.* **2008**, *46*, 777.
- [50] X. Tang, L. Gao, X. Fan, Q. Zhou, *J. Polym. Sci. A Polym. Chem.* **2007**, *45*, 2225.
- [51] H. Yu, A. Shishido, T. Ikeda, T. Iyoda, *Makromol. Rapid Commun.* **2005**, *26*, 1594.
- [52] A. H. E. Müller, H.-W. Schmidt (Eds.), *Complex Macromolecular Systems II*, Springer Berlin Heidelberg, Berlin, Heidelberg **2010**.
- [53] M. Häckel, L. Kador, D. Kropp, H.-W. Schmidt, *Adv. Mater.* **2007**, *19*, 227.
- [54] M. Häckel, L. Kador, D. Kropp, C. Frenz, H.-W. Schmidt, *Adv. Funct. Mater.* **2005**, *15*, 1722.
- [55] G. Tammann, *Z. Phys. Chem.* **1898**, *25*, 441.
- [56] Y. Shirota, *J. Mater. Chem.* **2000**, *10*, 1.
- [57] B. Rosenberg, *The Journal of chemical physics* **1959**, *31*, 238.
- [58] J. H. Magill, *The Journal of chemical physics* **1967**, *47*, 2802.
- [59] D. J. Plazek, J. H. Magill, *The Journal of chemical physics* **1966**, *45*, 3038.
- [60] Y. Sano, K. Kato, M. Yokoyama, Y. Shirota, H. Mikawa, *Molecular Crystals and Liquid Crystals* **1976**, *36*, 137.
- [61] P. Stroehriegl, J. V. Grazulevicius, *Adv. Mater.* **2002**, *14*, 1439.
- [62] Y. Shirota, T. Kobata, N. Noma, *Chem. Lett.* **1989**.
- [63] A. Higuchi, H. Inada, T. Kobata, Y. Shirota, *Adv. Mater.* **1991**, *3*, 549.

- [64] Y. Shirota, Y. Kuwabara, H. Inada, T. Wakimoto, H. Nakada, Y. Yonemoto, S. Kawami, K. Imai, *Appl. Phys. Lett.* **1994**, *65*, 807.
- [65] H. O. Wirth, *Angew. Makromol. Chemie* **1991**, *185*, 329.
- [66] K. Naito, A. Miura, *J. Phys. Chem.* **1993**, *97*, 6240.
- [67] Y. Shirota, *J. Mater. Chem.* **2005**, *15*, 75.
- [68] C. W. Tang, S. A. VanSlyke, *Appl. Phys. Lett.* **1987**, *51*, 913.
- [69] M. Grätzel, U. Bach, D. Lupo, P. Comte, J. E. Moser, F. Weissörtel, J. Salbeck, H. Spreitzer, *Nature* **1998**, *395*, 583.
- [70] J. Dai, S. W. Chang, A. Hamad, D. Yang, N. Felix, C. K. Ober, *Chem. Mater.* **2006**, *18*, 3404.
- [71] A. de Silva, N. M. Felix, C. K. Ober, *Adv. Mater.* **2008**, *20*, 3355.
- [72] C. Probst, C. Meichner, K. Kreger, L. Kador, C. Neuber, H.-W. Schmidt, *Adv. Mater.* **2016**.
- [73] J. V. Grazulevicius, P. Stroehriegl, J. Pielichowski, K. Pielichowski, *Progress in Polymer Science* **2003**, *28*, 1297.
- [74] L. M. Goldenberg, L. Kulikovskaya, O. Kulikovskaya, J. Tomczyk, J. Stumpe, *Langmuir* **2010**, *26*, 2214.
- [75] J. Aleksejeva, J. Teteris, A. Tokmakovs, *Physics Procedia* **2013**, *44*, 19.
- [76] D. Nagahama, T. Ujike, K. Moriwaki, S. Yoshikawa, H. Nakano, Y. Shirota, *J. Photopolym. Sci. Tec.* **1999**, *12*, 277.
- [77] H. Nakano, T. Takahashi, T. Kadota, Y. Shirota, *Adv. Mater.* **2002**, *14*, 1157.
- [78] E. Ishow, B. Lebon, Y. He, X. Wang, L. Bouteiller, L. Galmiche, K. Nakatani, *Chem. Mater.* **2006**, *18*, 1261.
- [79] E. Ishow, R. Camacho-Aguilera, J. Guérin, A. Brosseau, K. Nakatani, *Adv. Funct. Mater.* **2009**, *19*, 796.
- [80] H. Nakano, T. Takahashi, Y. Shirota, *J. Photopolym. Sci. Tec.* **2009**, *22*, 253.
- [81] M.-J. Kim, E.-M. Seo, D. Vak, D.-Y. Kim, *Chem. Mater.* **2003**, *15*, 4021.
- [82] E. Ishow, B. Lebon, Y. He, X. Wang, L. Bouteiller, L. Galmiche, K. Nakatani, *Chem. Mater.* **2006**, *18*, 1261.
- [83] A. Stracke, J. H. Wendorff, D. Goldmann, D. Janietz, *Liq. Cryst.* **2000**, *27*, 1049.
- [84] Y. Shirota, *J. Mater. Chem.* **2005**, *15*, 75.
- [85] H. Audorff, R. Walker, L. Kador, H.-W. Schmidt, *Chem. Eur. J.* **2011**, *17*, 12722.
- [86] K. Kreger, P. Wolfer, H. Audorff, L. Kador, N. Stingelin-Stutzmann, P. Smith, H.-W. Schmidt, *J. Am. Chem. Soc.* **2010**, *132*, 509.
- [87] M.-J. Kim, E.-M. Seo, D. Vak, D.-Y. Kim, *Chem. Mater.* **2003**, *15*, 4021.
- [88] C. Chun, M.-J. Kim, D. Vak, D. Y. Kim, *J. Mater. Chem.* **2003**, *13*, 2904.
- [89] T. Ujike, K. Moriwaki, H. Nakano, Y. Shirota, *J. Photopol. Sci. Technol.* **1998**, *11*, 33.
- [90] B. Priewisch, K. Rück-Braun, *J. Org. Chem.* **2005**, *70*, 2350.
- [91] H. Ando, T. Tanino, H. Nakano, Y. Shirota, *Mater. Chem. Phys.* **2009**, *113*, 376.
- [92] H. Audorff, R. Walker, L. Kador, H.-W. Schmidt, *Chem. Eur. J.* **2011**, *17*, 12722.
- [93] O. Lebel, T. Maris, M.-È. Perron, E. Demers, J. D. Wuest, *J. Am. Chem. Soc.* **2006**, *128*, 10372.
- [94] C. Probst, C. Meichner, K. Kreger, L. Kador, C. Neuber, H.-W. Schmidt, *Adv. Mater.* **2016**, *28*, 2624.
- [95] H.-P. Herzig, *Micro-optics: Elements, systems and applications*, Taylor & Francis, London **1997**.
- [96] G. M. Whitesides, E. Ostuni, S. Takayama, X. Jiang, D. E. Ingber, *Annu. Rev. Biomed. Eng.* **2001**, *3*, 335.
- [97] J. C. Whitaker, *Microelectronics*, CRC/Taylor & Francis, Boca Raton, FL **2006**.

- [98] Cen Shawn Wu, ChiiDong Chen, Yoshiyuki Makiuchi (Eds.), *High-energy Electron Beam Lithography for Nanoscale Fabrication*, INTECH Open Access Publisher **2010**.
- [99] S. Y. Chou, P. R. Krauss, P. J. Renstrom, *Appl. Phys. Lett.* **1995**, *67*, 3114.
- [100] B. Bhushan (Ed.), *Springer handbook of nanotechnology, third revised and extended edition*, Springer, Heidelberg, New York **2010**.
- [101] S. Y. Chou, *J. Vac. Sci. Technol. B* **1997**, *15*, 2897.
- [102] J. Taniguchi, *Nanoimprint technology: Nanotransfer for thermoplastic and photocurable polymer*.
- [103] W. Zhou (Ed.), *Nanoimprint Lithography: An Enabling Process for Nanofabrication*, Springer Berlin Heidelberg, Berlin, Heidelberg **2013**.
- [104] K. Y. Suh, Y. S. Kim, H. H. Lee, *Adv. Mater.* **2001**.
- [105] P. Rochon, E. Batalla, A. Natansohn, *Appl. Phys. Lett.* **1995**, *66*, 136.
- [106] A. Priimagi, A. Shevchenko, *J. Polym. Sci. Part B: Polym. Phys.* **2014**, *52*, 163.
- [107] K. Kreger, P. Wolfer, H. Audorff, L. Kador, N. Stingelin-Stutzmann, P. Smith, H.-W. Schmidt, *J. Am. Chem. Soc.* **2010**, *132*, 509.
- [108] R. H. Lambeth, J. Park, H. Liao, D. J. Shir, S. Jeon, J. A. Rogers, J. S. Moore, *Nanotechnology* **2010**, *21*, 165301.
- [109] P. Rochon, E. Batalla, A. Natansohn, *Appl. Phys. Lett.* **1995**, *66*, 136.
- [110] H. Audorff, R. Walker, L. Kador, H.-W. Schmidt, *J. Phys. Chem. B* **2009**, *113*, 3379.
- [111] L. J. Heyderman, B. Ketterer, D. Bächle, F. Glaus, B. Haas, H. Schiff, K. Vogelsang, J. Gobrecht, L. Tiefenauer, O. Dubochet, P. Surbled, T. Hessler, *Microelectronic Engineering* **2003**, *67-68*, 208.
- [112] J. Taniguchi, H. Ito, J. Mizuno, T. Saito (Eds.), *Nanoimprint technology: Nanotransfer for thermoplastic and photocurable polymers*, Wiley, Chichester **2013**.
- [113] B. Bhushan (Ed.), *Springer handbook of nanotechnology*, Springer, Berlin, Heidelberg **2007**.
- [114] F. Li, A. Nathan, Y. Wu, B. S. Ong, *Organic Thin Film Transistor Integration: A Hybrid Approach*, Wiley, Somerset **2011**.
- [115] A. Kravchenko, A. Shevchenko, V. Ovchinnikov, A. Priimagi, M. Kaivola, *Adv. Mater.* **2011**, *23*, 4174.
- [116] G. L. W. Cross, R. M. Langford, B. S. O'Connell, J. B. Pethica, *MRS Proc.* **2004**, *841*.
- [117] L. Heyderman, H. Schiff, C. David, J. Gobrecht, T. Schweizer, *Microelectronic Engineering* **2000**, *54*, 229.
- [118] Y. Hirai, T. Konishi, T. Yoshikawa, S. Yoshida, *J. Vac. Sci. Technol. B* **2004**, *22*, 3288.
- [119] H. D. Rowland, A. C. Sun, P. R. Schunk, W. P. King, *J. Micromech. Microeng.* **2005**, *15*, 2414.
- [120] J. Vapaavuori, A. Laventure, C. G. Bazuin, O. Lebel, C. Pellerin, *JACS* **2015**, *137*, 13510.
- [121] M. Houry, *J. Vac. Sci. Technol. B* **1996**, *14*, 75.
- [122] M.-J. Kim, E.-M. Seo, D. Vak, D.-Y. Kim, *Chem. Mater.* **2003**, *15*, 4021.
- [123] K. Y. Suh, Y. S. Kim, H. H. Lee, *Adv. Mater.* **2001**, *13*, 1386.
- [124] P. Stroehriegl, J. V. Grazulevicius, *Adv. Mater.* **2002**, *14*, 1439.
- [125] Y. Shirota, *J. Mater. Chem.* **2000**, *10*, 1.
- [126] C. Frenz, A. Fuchs, H.-W. Schmidt, U. Theissen, D. Haarer, *Macromol. Chem. Phys.* **2004**, *205*, 1246.
- [127] G. J. Fang, J. E. Maclennan, Y. Yi, M. A. Glaser, M. Farrow, E. Korblova, D. M. Walba, T. E. Furtak, N. A. Clark, *Nat. Commun.* **2013**, *4*, 1521.

- [128] Y. Y. Huang, W. Zhou, Hsia, K. J., E. Menard, J.-U. Park, J. A. Rogers, A. G. Alleyne, *Langmuir* **2005**, *21*, 8058.
- [129] H.-J. Lee, H. W. Ro, C. L. Soles, R. L. Jones, E. K. Lin, W.-I. Wu, D. R. Hines, *J. Vac. Sci. Technol. B* **2005**, *23*, 3023.
- [130] R. B. Bird, R. C. Armstrong, O. Hassager, *Fluid mechanics*, Wiley, New York **1987**.
- [131] F. You, M. Y. Paik, M. Häckel, L. Kador, D. Kropp, H. Schmidt, C. K. Ober, *Advanced Functional Materials* **2006**, *16*, 1577.
- [132] H. Audorff, *Holographic Investigation of Azobenzene-Containing Low-Molecular-Weight Compounds*, Bayreuth **2011**.
- [133] R. Walker, *Azobenzene-functionalized molecular glasses for holographic applications*, Bayreuth **2010**.
- [134] T. Farrell, C. I. Smith, A. L. Schofield, R. L. Williams, P. Weightman, *J. Phys. D: Appl. Phys.* **2010**, *43*, 245301.
- [135] K. G. Sharp, G. S. Blackman, N. J. Glassmaker, A. Jagota, C.-Y. Hui, *Langmuir* **2004**, *20*, 6430.
- [136] I. D. Johnston, D. K. McCluskey, C. K. L. Tan, M. C. Tracey, *J. Micromech. Microeng.* **2014**, *24*, 35017.
- [137] H. I. Bjelkhagen, in *Optical Imaging Sensors and Systems for Homeland Security Applications*, Vol. 2 (Ed.: B. Javidi), Springer Science+Business Media Inc. New York, NY **2006**, p. 385.
- [138] J. Kumar, L. Li, X. L. Jiang, D.-Y. Kim, T. S. Lee, S. Tripathy, *Appl. Phys. Lett.* **1998**, *72*, 2096.
- [139] G. J. Fang, J. E. MacLennan, Y. Yi, M. A. Glaser, M. Farrow, E. Korblova, D. M. Walba, T. E. Furtak, N. A. Clark, *Nat. Commun.* **2013**, *4*, 1521.
- [140] T. Sasaki, T. Shoho, K. Kawai, K. Noda, N. Kawatsuki, H. Ono, *Jpn. J. Appl. Phys.* **2014**, *53*, 62601.
- [141] T. Sasaki, T. Shoho, K. Kawai, K. Noda, N. Kawatsuki, H. Ono, *Jpn. J. Appl. Phys.* **2014**, *53*, 62601.
- [142] R. Walker, H. Audorff, L. Kador, H.-W. Schmidt, *Adv. Funct. Mater.* **2009**, *19*, 2630.
- [143] M. Häckel, L. Kador, D. Kropp, C. Frenz, H.-W. Schmidt, *Adv. Funct. Mater.* **2005**, *15*, 1722.
- [144] H. Nakano, T. Takahashi, T. Kadota, Y. Shirota, *Adv. Mater.* **2002**, *14*, 1157.
- [145] H. Audorff, R. Walker, L. Kador, H.-W. Schmidt, *J. Phys. Chem. B* **2009**, *113*, 3379.
- [146] R. Magnusson, T. K. Gaylord, *J. Opt. Soc. Am.* **1978**, *68*, 806.
- [147] M. Häckel, L. Kador, D. Kropp, H.-W. Schmidt, *Adv. Mater.* **2007**, *19*, 227.
- [148] K. Kreger, C. Löffler, R. Walker, N. Wirth, D. Bingemann, H. Audorff, E. A. Rössler, L. Kador, H.-W. Schmidt, *Macromol. Chem. Phys.* **2007**, *208*, 1530.
- [149] G. Schmid, *Nanoparticles*, Wiley-VCH Verlag GmbH & Co. KGaA, Weinheim, FRG **2003**.
- [150] K. E. Geckeler (Ed.), *Functional Nanomaterials*, ASP American Scientific Publ, Stevenson Ranch, Calif. **2006**.
- [151] M. Hosokawa (Ed.), *Nanoparticle technology handbook*, Elsevier, Amsterdam **2007**.
- [152] X. Wang, C. J. Summers, Z. L. Wang, *Nano Lett.* **2004**, *4*, 423.
- [153] H. Fudouzi, Y. Xia, *Adv. Mater.* **2003**, *15*, 892.
- [154] S. Brahim, D. Narinesingh, A. Guiseppi-Elie, *Anal. Chim. Acta* **2001**, *448*, 27.
- [155] Q. Zhang, K. T. Chuang, *Adv. Environ. Res.* **2001**, *5*, 251.
- [156] J. P. Rao, K. E. Geckeler, *Prog. Polym. Sci.* **2011**, *36*, 887.
- [157] J. Kreuter (Ed.), *Colloidal drug delivery systems*, Dekker, New York **1994**.
- [158] P. Couvreur, *Critical reviews in therapeutic drug carrier systems* **1988**, *5*, 1.

- [159] D. L. Wise (Ed.), *Handbook of pharmaceutical controlled release technology*, Dekker, New York **2000**.
- [160] V. Mittal (Ed.), *Advanced polymer nanoparticles: Synthesis and surface modifications*, CRC Press, Boca Raton, FL **2011**.
- [161] E. Lejeune, M. Drechsler, J. Jestin, A. H. E. Müller, C. Chassenieux, O. Colombani, *Macromolecules* **2010**, *43*, 2667.
- [162] M. Schmidt (Ed.), *Polyelectrolytes with Defined Molecular Architecture II*, Springer, Berlin, Heidelberg **2004**.
- [163] Y.-L. Luo, Y. Wang, X. Wang, F. Xu, Y.-S. Chen, *J. Biomater. Appl.* **2016**, *30*, 662.
- [164] H. Wei, S.-X. Cheng, X.-Z. Zhang, R.-X. Zhuo, *Prog. Polym. Sci.* **2009**, *34*, 893.
- [165] E. Lee, *J. Control. Release* **2003**, *91*, 103.
- [166] E. R. Gillies, J. M. J. Fréchet, *Bioconjugate Chem.* **2005**, *16*, 361.
- [167] G. Liu, Z. Li, X. Yan, *Polymer* **2003**, *44*, 7721.
- [168] Z. Li, Z. Chen, H. Cui, K. Hales, K. Qi, K. L. Wooley, D. J. Pochan, *Langmuir* **2005**, *21*, 7533.
- [169] Z. Chen, H. Cui, K. Hales, Z. Li, K. Qi, D. J. Pochan, K. L. Wooley, *J. Am. Chem. Soc.* **2005**, *127*, 8592.
- [170] C. Cheng, K. Qi, D. S. Germack, E. Khoshdel, K. L. Wooley, *Adv. Mater.* **2007**, *19*, 2830.
- [171] D. Roy, B. S. Sumerlin, *Macromol. Rapid Commun.* **2014**, *35*, 174.
- [172] Y. Chan, T. Wong, F. Byrne, M. Kavallaris, V. Bulmus, *Biomacromolecules* **2008**, *9*, 1826.
- [173] A. Chremos, A. Nikoubashman, A. Z. Panagiotopoulos, *J. Chem. Phys.* **2014**, *140*, 54909.
- [174] L. Leibler, *Macromolecules* **1980**, *13*, 1602.
- [175] N. Hadjichristidis, G. Floudas, S. Pispas, *Block copolymers: Synthetic strategies, physical properties, and applications*, Wiley-Interscience, Hoboken, N.J **2003**.
- [176] F. S. Bates, *Science* **1991**, *251*, 898.
- [177] E. W. Cochran, C. J. Garcia-Cervera, G. H. Fredrickson, *Macromolecules* **2006**, *39*, 2449.
- [178] Y. Mai, F. Zhang, X. Feng, *Nanoscale* **2014**, *6*, 106.
- [179] X. Yan, G. Liu, F. Liu, B. Z. Tang, H. Peng, A. B. Pakhomov, C. Y. Wong, *Angew. Chem. Int. Ed.* **2001**, *40*, 3593.
- [180] X. Yan, G. Liu, Z. Li, *J. Am. Chem. Soc.* **2004**, *126*, 10059.
- [181] R. Erhardt, A. Böker, H. Zettl, H. Kaya, W. Pyckhout-Hintzen, G. Krausch, V. Abetz, A. H. E. Müller, *Macromolecules* **2001**, *34*, 1069.
- [182] R. S. Yelamanchili, A. Walther, A. H. E. Müller, J. Brey, *Chem. Commun.* **2008**.
- [183] K. Zhang, L. Gao, Y. Chen, *Macromolecules* **2007**, *40*, 5916.
- [184] A. Walther, M. Drechsler, A. H. E. Müller, *Soft Matter* **2009**, *5*, 385.
- [185] A. Walther, A. H. E. Müller, *Soft Matter* **2008**, *4*, 663.
- [186] A. Walther, *Soft Compartmentalized Polymer Colloids: Janus Particles, Multicompartment Structures, Inorganic-Organic Hybrids and Applications.*, Bayreuth **2008**.
- [187] G. Liu, X. Yan, S. Duncan, *Macromolecules* **2002**, *35*, 9788.
- [188] F. Schacher, J. Yuan, H. G. Schoberth, A. H. Müller, *Polymer* **2010**, *51*, 2021.
- [189] J. Qin, X. Jiang, L. Gao, Y. Chen, F. Xi, *Macromolecules* **2010**, *43*, 8094.
- [190] J. Lai, K. Tu, H. Wang, Z. Chen, L.-Q. Wang, *J. Appl. Polym. Sci.* **2008**, *108*, 3305.
- [191] V. Ferri, M. Elbing, G. Pace, M. D. Dickey, M. Zharnikov, P. Samorì, M. Mayor, M. A. Rampi, *Angew. Chem. Int. Ed.* **2008**, *47*, 3290.
- [192] Y. Zhao, *Macromolecules* **2012**, *45*, 3647.
- [193] G. Wang, X. Tong, Y. Zhao, *Macromolecules* **2004**, *37*, 8911.
- [194] N. Feng, G. Han, J. Dong, H. Wu, Y. Zheng, G. Wang, *J. Colloid Interface Sci.* **2014**, *421*, 15.

- [195] T. Yuan, J. Dong, G. Han, G. Wang, *RSC Adv.* **2016**, *6*, 10904.
- [196] G. Wang, D. Yuan, T. Yuan, J. Dong, N. Feng, G. Han, *J. Polym. Sci. Part A: Polym. Chem.* **2015**, *53*, 2768.
- [197] W. Su, K. Han, Y. Luo, Z. Wang, Y. Li, Q. Zhang, *Macromol. Chem. Phys.* **2007**, *208*, 955.
- [198] J. del Barrio, L. Oriol, C. Sánchez, J. L. Serrano, A. Di Cicco, P. Keller, M.-H. Li, *J. Am. Chem. Soc.* **2010**, *132*, 3762.
- [199] O. Boissiere, D. Han, L. Tremblay, Y. Zhao, *Soft Matter* **2011**, *7*, 9410.
- [200] H. L. Cheng, M. T. Tang, W. Tuchinda, K. Enomoto, A. Chiba, Y. Saito, T. Kamiya, M. Sugimoto, A. Saeki, T. Sakurai, M. Omichi, D. Sakamaki, S. Seki, *Adv. Mater. Interfaces* **2015**, *2*, 1400450.
- [201] X. Zhou, Y. Du, X. Wang, *ACS Macro Lett.* **2016**, *5*, 234.
- [202] C. Cannizzo, S. Amigoni-Gerbier, M. Frigoli, C. Larpent, *J. Polym. Sci. A Polym. Chem.* **2008**, *46*, 3375.
- [203] J.-P. Abid, M. Frigoli, R. Pansu, J. Szeftel, J. Zyss, C. Larpent, S. Brasselet, *Langmuir* **2011**, *27*, 7967.
- [204] A. Housni, Y. Zhao, Y. Zhao, *Langmuir* **2010**, *26*, 12366.
- [205] M. Suda, M. Nakagawa, T. Iyoda, Y. Einaga, *J. Am. Chem. Soc.* **2007**, *129*, 5538.
- [206] L. Nedelchev, D. Nazarova, V. Dragostinova, *J. Photochem. Photobiol. A* **2013**, *261*, 26.
- [207] P. Forcén, L. Oriol, C. Sánchez, R. Alcalá, S. Hvilsted, K. Jankova, J. Loos, *J. Polym. Sci. A Polym. Chem.* **2007**, *45*, 1899.
- [208] P. Forcén, L. Oriol, C. Sánchez, F. J. Rodríguez, R. Alcalá, S. Hvilsted, K. Jankova, *Eur. Polym. J.* **2007**, *43*, 3292.
- [209] I. C. Khoo (Ed.), *Rewritable Bragg Holograms of Azobenzene Polymers with Fast Response*, SPIE **2009**.
- [210] Y. Naka, H. Yu, A. Shishido, T. Ikeda, *Mol. Cryst. Liq. Cryst.* **2009**, *498*, 118.
- [211] A. Sobolewska, S. Bartkiewicz, A. Miniewicz, E. Schab-Balcerzak, *J. Phys. Chem. B* **2010**, *114*, 9751.
- [212] M. Ishiguro, D. Sato, A. Shishido, T. Ikeda, *Langmuir* **2007**, *23*, 332.
- [213] S. Hvilsted, C. Sánchez, R. Alcalá, *J. Mater. Chem.* **2009**, *19*, 6641.
- [214] J. K. Bosworth, C. T. Black, C. K. Ober, *ACS Nano* **2009**, *3*, 1761.
- [215] M. Li, K. Douki, K. Goto, X. Li, C. Coenjarts, D. M. Smilgies, C. K. Ober, *Chem. Mater.* **2004**, *16*, 3800.
- [216] M. J. Madou, *Fundamentals of microfabrication and nanotechnology*, CRC Press/Taylor & Francis, Boca Raton, Fla. **2012**.
- [217] R. Pettau, *Synthesis, Characterization, and Properties of Tailored Functional Block Copolymers*, Bayreuth **2011**.
- [218] Cosima v. Salis-Soglio, *Untersuchung niedermolekularer Glasbildner Phenole und deren säureinitiierte Photostrukturierung*, Bayreuth **2005**.
- [219] J. Baltazar, H. Sojoudi, S. A. Paniagua, S. Zhang, R. A. Lawson, S. R. Marder, S. Graham, L. M. Tolbert, C. L. Henderson, *Adv. Funct. Mater.* **2014**, *24*, 5147.
- [220] E. Kapetanakis, A. M. Douvas, P. Argitis, P. Normand, *ACS Appl. Mater. Interfaces* **2013**, *5*, 5667.
- [221] R. Zwanzig, *Annu. Rev. Phys. Chem.* **1965**, *16*, 67.
- [222] B. Chu, *Laser Light Scattering*, Academic Press, New York **1974**.
- [223] K. S. Schmitz, *An Introduction to Dynamic Light Scattering by Macromolecules*, Academic Press, New York **1990**.

- [224] Universität Bayreuth, *Praktikumsanleitungen zum Modul 103 Polymer Science* **2008**.
- [225] S. B. Ross-Murphy, *Brit. Poly. J.* **1977**, *9*, 177.
- [226] H. Audorff, *Holographic Investigation of Azobenzene-Containing Low-Molecular-Weight Compounds*, Bayreuth **2011**.
- [227] R. Magnusson, T. K. Gaylord, *J. Opt. Soc. Am.* **1978**, *68*, 1777.
- [228] H. Kogelnick, *Bell. Syst. Tech. J.* **1969**, *48*, 2909.
- [229] T. Bieringer, *Optische Untersuchungen zur kollektiven Photoorientierung in flüssigkristallinen Seitenkettenpolymeren*, Bayreuth **1996**.
- [230] M. Huber, Bayreuth **2001**.
- [231] C. Meichner, *Holographische Speicherung zweidimensionaler Datenfelder in azobenzolhaltigen Materialien*, Bayreuth **2011**.
- [232] K. Magniez, B. L. Fox, M. G. Looney, *Polym. Int.* **2009**, *58*, 858.
- [233] M. Y. Paik, S. Krishnan, F. You, X. Li, A. Hexemer, Y. Ando, S. H. Kang, D. A. Fischer, E. J. Kramer, C. K. Ober, *Langmuir* **2007**, *23*, 5110.
- [234] F. Abraham, S. Ganzleben, D. Hanft, P. Smith, H.-W. Schmidt, *Macromol. Chem. Phys.* **2010**, *211*, 171.

## Danksagung

Die vorliegende Arbeit wurde in der Zeit von August 2011 bis Juni 2016 am Lehrstuhl für Makromolekulare Chemie I der Universität Bayreuth unter der Betreuung von Prof. Dr. Hans-Werner Schmidt angefertigt. Ihm möchte ich zuallererst für die sehr interessante, anwendungsbezogene Aufgabenstellung danken. Im besonderen Maße danke ich ihm weiterhin für die Bereitstellung eines gut ausgestatteten Labors und seine stete Bereitschaft zu wissenschaftlichen Diskussionen. Für die Fortwährende Unterstützung und Motivation danke ich ihm herzlich.

Besonders danke ich auch Dr. Klaus Kreger für seine stete Diskussions- und Hilfsbereitschaft, sowie für das Teilen seiner herausragenden fachlichen Kompetenz.

Christoph Meichner und Prof. Lothar Kador am Bayreuther Institut für Makromolekülforschung danke ich für die hervorragende und reibungslose Zusammenarbeit, sowie die Beantwortung auch schwieriger physikalischer Fragestellungen. Ich danke auch für die Durchführung der Belichtungs- sowie der holographischen Experimente an meinen Proben.

Bei Doris Hanft und Sandra Ganzleben bedanke ich mich ganz herzlich für die Unterstützung bei der Synthese und Aufreinigung einiger Verbindungen.

Bei Dr. Roland Walker bedanke ich mich für die Beteiligung an meiner Einführung in das Forschungsfeld der Azobenzole, sowie für die Synthese und Bereitstellung einzelner in dieser Arbeit verwendeten Verbindungen.

Martina Heider möchte ich bei der Unterstützung mit und bei einigen TEM Aufnahmen danken.

Bei Petra Weiss und Christina Wunderlich bedanke ich mich für ihre unermüdliche Unterstützung bei verwaltungstechnischen Problemen.

Für ihre Unterstützung bei IT Fragestellungen bedanke ich mich bei Alexander Kern und Jonas Mayer.

Meinen Laborkollegen Johannes Heigl, Andreas Haedler und Florian Richter danke ich für eine motivierende und sehr kollegiale Atmosphäre im Labor.

Dank gebührt allen Mitarbeitern des Lehrstuhls MCI, die durch ihre fachliche Kompetenz und Freundschaft zum Gelingen dieser Arbeit beigetragen haben.

Vor allem möchte meiner Familie für Ihre Unterstützung während des Studiums und der Promotion ganz herzlich danken.

## **(Eidesstattliche) Versicherungen und Erklärungen**

(§ 8 S. 2 Nr. 6 PromO)

Hiermit erkläre ich mich damit einverstanden, dass die elektronische Fassung meiner Dissertation unter Wahrung meiner Urheberrechte und des Datenschutzes einer gesonderten Überprüfung hinsichtlich der eigenständigen Anfertigung der Dissertation unterzogen werden kann.

(§ 8 S. 2 Nr. 8 PromO)

Hiermit erkläre ich eidesstattlich, dass ich die Dissertation selbständig verfasst und keine anderen als die von mir angegebenen Quellen und Hilfsmittel benutzt habe.

(§ 8 S. 2 Nr. 9 PromO)

Ich habe die Dissertation nicht bereits zur Erlangung eines akademischen Grades anderweitig eingereicht und habe auch nicht bereits diese oder eine gleichartige Doktorprüfung endgültig nicht bestanden.

(§ 8 S. 2 Nr. 10 PromO)

Hiermit erkläre ich, dass ich keine Hilfe von gewerbliche Promotionsberatern bzw. -vermittlern in Anspruch genommen habe und auch künftig nicht nehmen werde.

Bayreuth, den 24. Juni 2016

Christian Probst